QUANTIFYING STRUCTURAL CHANGE IN UK WOODLAND CANOPIES WITH A DUAL-WAVELENGTH FULL-WAVEFORM TERRESTRIAL LASER SCANNER

LUCY ANASTASIA SCHOFIELD

Ph.D. Thesis   2016

QUANTIFYING STRUCTURAL CHANGE IN UK WOODLAND CANOPIES WITH A DUAL-WAVELENGTH FULL-WAVEFORM TERRESTRIAL LASER SCANNER

LUCY ANASTASIA SCHOFIELD

Ecosystems and Environment Research Centre

School of Environment and Life Sciences

University of Salford

Salford, M5 4WT, UK

Submitted in Partial Fulfilment of the Requirements of the Degree of Doctor of Philosophy, March 2016

Contents

List of tables

List of figures

Acknowledgements

Declaration

I declare that the work presented in this thesis has not previously been submitted for a degree or similar award at Salford University or any other institution. To the best of my knowledge and belief, no material in this thesis has been previously published or written by another person, except where due reference is made.

Signed

Date

Abstract

Vegetation structure provides a direct link between forest ecosystem productivity and earth-atmosphere fluxes, and is both a result and driver of these interactions. Therefore, the ability to collect objective, quantitative and three-dimensional measurements of vegetation structure is essential, particularly in light of climate change. However, a significant challenge still remains as to how to best measure changes in forests and prepare for future climatic scenarios. Terrestrial Laser Scanning (TLS) has shown its potential to provide such measurements, offering a new approach to monitoring how forest systems change through time and space. The overall aim of this thesis was to improve the characterisation of the seasonal dynamics of UK woodland vegetation structure using the Salford Advanced Laser Canopy Analyser (SALCA), a research TLS with dual-wavelength full-waveform capabilities.

There were three key objectives to this research: (1) the development of a radiometric calibration for the SALCA instrument to produce an apparent reflectance product, (2) the separation of SALCA point clouds into leaf and wood on a tree and plot scale using dual-wavelength lidar, and (3) the examination of the seasonal dynamics of vegetation structure in a range of UK forest types. To address these objectives, two field campaigns were conducted. SALCA measurements of artificial reflectance targets were acquired from both field campaigns to generate a calibration dataset to address Objective 1. The two field campaigns comprised a tree-scale validation experiment at Alice Holt Forest (to address Objective 2), and a multi-temporal monitoring experiment using SALCA and hemispherical photography at Delamere Forest in five different plots (to address Objective 3).

Key findings relating to Objective 1 have highlighted the complexities of SALCA intensity response, such as the effect of internal temperature. As a result, a novel approach to radiometric calibration was developed using artificial neural networks which produced an apparent reflectance product with measured accuracy comparable with other approaches. A key conclusion of this research relating to Objective 2, is that dual-wavelength TLS has the potential to aid separation of leaf and wood material. However, there still remain significant ecological, instrumental, and processing challenges to be overcome. Temporally and vertically resolved plot measurements have provided a quantitative analysis of foliage

dynamics to address Objective 3 and results have shown how this differences between species. The research presented in this thesis has explored the use of dual-wavelength full-waveform TLS for improved characterisation of forest vegetation. Future research priorities should focus on the radiometric calibration and investigation of other methods for leaf-wood separation to extend and complement this research.

CHAPTER 1

Introduction

1.1   Research context

Forests are essential to life on Earth and amongst the wide range of ecosystem services that they provide (MEA, 2005), of particular significance is the role they play in regulating Earth's climate through the global carbon cycle. Forest vegetation absorbs and releases atmospheric carbon dioxide (CO_2) through photosynthesis and respiration. This activity alters atmospheric CO_2 concentration on time scales from seconds to millennia. The accumulation of CO_2 in its various forms has received significant attention over the last decade as a result of its status as a greenhouse gas responsible for absorbing long-wave terrestrial radiation leading to warming of Earth's atmosphere. Atmospheric CO_2 is currently increasing well beyond the projected natural accumulation level, making this the most important contributor to the enhanced climate effect (Broadmeadows & Matthews, 2003). The additional increase in atmospheric CO_2 is widely accepted to be the result of anthropogenic activities causing global 'climate change', the most significant environmental issue facing our planet today (IPCC, 2013), and the direct linkages between vegetation, climate, and carbon, mean that forests have a significant role to play.

In addition to their role in the atmospheric CO_2 balance, trees also retain large amounts of carbon in accumulated biomass in both long-lived woody structures and short-lived foliage and fine roots; approximately half the dry mass of this organic material is carbon (Broadmeadows & Matthews, 2003; Drake *et al*., 2003). The biomass of forests is particularly high, 20-50 times higher than established agricultural lands (Houghton, 2005), with forests globally holding 70-90% of terrestrial aboveground and below ground carbon (Houghton *et al*., 2009). It is for these reasons that forests have attracted attention for climate change mitigation strategies. In particular, retaining and enhancing carbon stocks and reducing greenhouse gas emissions, as detailed in global policies such as the Reducing

Emissions from Deforestation and forest Degradation (REDD) and REDD+ initiatives launched by the United Nations Framework Convention on Climate Change (UNFCCC).

Plants have evolved so that they are finely tuned to the seasonality of their environment. As a result, forests are also sensitive indicators of climate change, observed through vegetation phenology. This is because phenology, the timing of the seasonal cycles of foliage growth and senescence, is closely related to climate (Richardson *et al.,* 2009). This environmental sensitivity means that phenology is a significant resource with which to examine how species and ecosystems have responded to past temperature variation, and as an important indicator of ongoing and future climatic change (IPCC, 2007; Menzel *et al*., 2006; Sparks & Gill, 2002). The periodic accumulation and loss of photosynthetic biomass, observable in the phenological stages, is the driving force behind the annual flux of atmospheric CO_2 and ecosystem primary productivity, and varies between years based on patterns of weather and climate, as well as resource availability (Ahl *et al*., 2006; Haggerty & Mazer, 2008). Therefore, phenology can be considered a measure of the physical, chemical, and biological condition of the environment, as well as the "...most responsive aspect of nature to global warming" (Sparks & Menzel, 2002). The IPCC Working Group II report released in March 2014 attributed high confidence to earlier greening, leaf emergence and fruiting in temperate European trees (IPCC, 2014), as a result of the warming conditions predicted. However, large uncertainties remain as to how phenology, and therefore forest carbon fluxes, will respond to projected future climate change. In the UK, species potential distributions are likely to shift; the suitability and yield of species are already being incorporated into current management decisions, but a significant challenge remains as to how to best measure changes in forests and prepare for uncertain events (Read *et al*., 2009). It is clear that a key requirement to address these two concerns is to increase understanding of the interactions between site, species, and climate (Sparks & Gill, 2002; Ray *et al.*, 2010). By bridging the gap between these factors, vegetation phenology provides a measurable and quantifiable resource for this purpose.

In order to understand and respond to the two-way relationship between forests and climate, and how changes in one will affect the other, it is clear that we must be able to quantitatively measure both these systems in an accurate and robust manner. Current approaches exist that can measure atmospheric carbon flux measurements directly from the forest ecosystem, such as eddy covariance instruments mounted on flux towers above the

2

canopy (e.g. Mizunuma *et al.,* 2013). In contrast, the forest vegetation which drives these fluxes is not so easily measured. Forests represent dynamic heterogeneous ecosystems with diverse spatial, structural, and biological composition, making them among the most important global repositories of terrestrial biodiversity of plants, animals, and micro-organisms (MEA, 2005), but this complexity poses significant measurement challenges.

The ability to collect accurate and verifiable measurements of forest aboveground standing biomass has proved a technical barrier in the past. Reasons for this include the infrequency and non-standardisation of national forest surveys and the lack of appropriate methods such as adequate global forest monitoring systems (Baker *et al*., 2010). Space agencies are responding to the latter by planning future systematic data acquisition strategies. For example, the National Aeronautics and Space Administration (NASA) have announced proposals for two new instruments which will observe how forests and ecosystems are affected by changes in climate from the International Space Station platform. One is a multi-wavelength laser-based instrument due to be launched in 2018, the Global Ecosystem Dynamics Investigation Lidar (GEDI), anticipated to collect high spatial resolution observations of tropical and temperate forest structure for aboveground carbon quantification, habitat quality, biodiversity, and to study vegetation response to climate at the landscape level (NASA, 2015). The GEDI mission evolved from the result of recently proven abilities of Light Detection And Ranging (lidar) systems to collect revolutionary three-dimensional (3D) datasets with high detail and accuracy from airborne (Airborne Laser Scanners: ALS) and ground-based platforms (Terrestrial Laser Scanners: TLS) to characterise forest structure (e.g. Asner, 2009; Jupp *et al.,* 2009).

Recent advances in tree reconstruction modelling techniques now mean that total above-ground biomass (AGB) can be accurately estimated directly, and increasingly automatically, from a TLS 3D model (Raumonen *et al.,* 2013; Hackenberg *et al.,* 2015). Although currently only possible for individual trees or local plot scale, this is undoubtedly an exciting achievement that has the potential to set a new benchmark beyond the use of previously-accepted allometric equations. Data from Earth observation systems (such as from GEDI), innovative modelling techniques, and ground-based field measurements, have the potential to be incorporated into robust systems for global forest monitoring and accounting, such as fulfilling Measuring, Reporting, and Verification (MRV) objectives for REDD+ (Baker *et al.,* 2010).

However, challenges still remain that hinder the full characterisation of tree structures from laser scanning systems. One of these is the inability to distinguish between woody material and photosynthetically-active foliage. Carbon is allocated among plant organs to two main pools: slow decomposable carbon pools with low metabolic activity (woody material), and fast decomposable dynamic carbon pools (foliage) which control moisture, gas exchange, and radiation interception (Franklin *et al*., 2012). Carbon allocation is a topic of significant ecological interest. One of the reasons for this is that relationships between key ecological processes and Gross Primary Production (GPP) differs between these tree components, and therefore their potential effect on carbon sequestration in times of rising CO_2 (Litton *et al.,* 2007; Campioli *et al.,* 2010). It has been found that total biomass alone is not a good predictor of carbon flux in forests (Litton *et al*., 2007). Therefore, rather than assuming whole plant carbon use, it has been recommended that estimates are made by component (Litton *et al.,* 2007). Although the physiological mechanisms involved in each organ are relatively well understood, directly measuring how much of each pool is present at one time and their spatial and temporal variability still poses a significant challenge.

The work in this thesis tests the use of the world's first operational dual-wavelength TLS, the Salford Advanced Laser Canopy Analyser (SALCA) (Danson *et al.* 2014) to characterise structural change in a range of UK woodland canopies. The SALCA research instrument is an innovative full-waveform laser scanner developed by the University of Salford and Halo Photonics Ltd. for measuring forest environments. The dual-wavelength measurement characteristic of the system has the potential to separate foliage and wood, based on the spectral properties of these forest components at the wavelengths the instrument uses. This research will test this potential using high resolution 3D data acquired from the SALCA instrument over a full annual season of foliage growth.

1.2   Aim of Research

> The overall aim of this research project is to improve characterisation of the seasonal dynamics of UK woodland vegetation structure using dual-wavelength terrestrial laser scanning.

In order to achieve this aim, systematic multi-temporal monitoring is conducted using SALCA alongside hemispherical photography and destructive measurements to quantify

leaf change over an annual seasonal cycle in a range of UK forest types. Such information aims to provide a new approach for phenological monitoring in forest environments. This framework will allow integration of the complex three-dimensional (3D) structure of forest environments with multi-temporal data collection facilitating a four-dimensional (4D) analysis. Three key research objectives supporting this aim are detailed in the following sections.

1.2.1 Objective 1

Produce an apparent reflectance product for the SALCA instrument

In order to fully utilise the radiometric information recorded from a TLS instrument, a calibration to an apparent reflectance product is required. As this has not yet been developed for the SALCA instrument, the first stage of this research is to develop an approach in which this can be achieved. Although not a trivial task, the generation of an apparent reflectance product provides a basis for an increased level of ecological information to be derived from the TLS data, therefore potentially facilitating leaf-wood separation.

1.2.2 Objective 2

Assess whether dual-wavelength lidar can be used to separate leaf and wood returns

Developing an accurate method to allow isolation of foliage from woody components would considerably aid studies of carbon dynamics in forest ecosystems, increase accuracy in forest structural measurements, act as a validation tool for other indirect approaches, and has been identified as a current limitation of current TLS systems (Hosoi & Omasa, 2007). Dual-wavelength lidar provides a new opportunity for leaf-wood separation based on spectral properties of these materials at SALCA wavelengths.

Creating a vegetation product that relates only to photosynthetically-active biomass should allow improved estimates of leaf area index (LAI), the most important variable for modelling a range of ecological processes. Destructive sampling of foliage carried out at the Forestry Commission's research agency Forest Research UK site at Alice Holt, Farnham, in July 2014, provided a rare opportunity for assessment of accuracy of such a product.

1.2.3   Objective 3

Examine the spatial and temporal characteristics of foliage in a range of UK forest types

Phenology varies spatially across a canopy, both within and between individuals, and across communities. The phenology of individual plants plays a key role in determining how ecosystems are structured and how they function, but it is the canopy as a whole that defines ecosystem productivity. Current phenological studies lack detail of canopy structural change and fail to address such factors as the spatial distribution of green leaf area within the canopy. The scale and high resolution that TLS allows facilitates the retrieval of structural information from individual trees to a whole stand scale. Foliage profiles, a key structural metric describing canopy vertical structure, using only foliage (defined in objective 2) will be created and compared on a plot basis, along with gap fraction estimates from TLS and hemispherical photography.

Seasonal change in biomass reflects the functioning of the forest: the rates of photosynthesis, respiration, growth, and therefore rates of carbon accumulation and loss. A quantitative assessment of the development and loss of foliage throughout a full annual seasonal cycle in a range of forest types will be carried out to create a time-series of key biophysical parameters. This will aid understanding of the spatial characteristics of seasonal vegetation dynamics for a variety of UK forest types and will address some of the key limitations of current phenology studies, as discussed in the following chapter.

1.3   Structure of thesis

The thesis contains nine chapters. The current chapter, Chapter 1, has provided the context for the research and introduced the main aim and objectives. This is followed by a review of relevant literature in Chapter 2, together with an outline of specific research questions that this research addresses. Chapter 3 details the data collection protocols implemented and a description of the chosen study sites. The development and implementation of a radiometric calibration for the SALCA instrument (Objective 1) is outlined in Chapter 4. The focus of Chapter 5 is exploring the dual-wavelength full-waveform data and investigating methods of leaf-wood separation on a tree scale (Objective 2). This is extended in Chapter 6 to attempt a validation approach using direct measurements. Chapter 7 up-scales the leaf-wood separation to the plot scale for five differing forest types, and

explores methods of quantitative assessment of vertical distribution of plant material. The final research chapter, Chapter 8, applies the same approaches to the full time-series of plot scale measurements to allow the spatial and temporal characteristics of seasonal growth to be examined (Objective 3).

CHAPTER 2

Literature review

2.1 Introduction

The aim of this chapter is to establish a framework for the research, define relevant terms, and critically examine key published work in the field of study. This has been carried out using a systematic literature review and addresses the link between UK vegetation phenology, carbon dynamics, and climate change, before discussing relevant techniques for measuring seasonal vegetation growth. Finally, specific research questions key to fulfilling each objective are outlined.

2.2 Vegetation phenology and carbon dynamics in UK woodlands

Recent statistics from the National Forest Inventory show that woodlands comprise approximately 13% of the total land area of Britain, which equates to 3.1 million hectares (Forestry Statistics, 2013). Existing UK woodlands, including their soils, are both a store of carbon and a system that removes CO_2 from the atmosphere. In 1995 it was estimated that in the UK 80% of the carbon contained in terrestrial vegetation is found in forests and woodlands, amounting to around 91.9 million tonnes carbon (Cannell & Milne, 1995), showing that UK woodlands are a key component of the UK carbon store. One of the most important feedbacks between vegetation and the climate system is the influence of vegetation on atmospheric CO_2, which feeds through to global temperature (Richardson *et al.*, 2013).

The relationship between phenology and climate is represented in Figure 2.1, which illustrates the primary feedback between vegetation and the climate system driven by phenology. Of particular importance in this cycle is the role of the canopy - the interface between the vegetation surfaces and the atmosphere. The dynamic structure of the canopy controls trace gases (carbon dioxide and water vapour fluxes), exchanges of latent and

sensible heat (Bowen ratio), and substances such as volatile organic compounds (VOCs) (Richardson *et al*., 2013). Phenology determines the development and senescence of foliage and therefore drives all of the physiological activities in the canopy, which impact the structure and composition of the atmosphere which feeds through to the larger climate system (Figure 2.1).
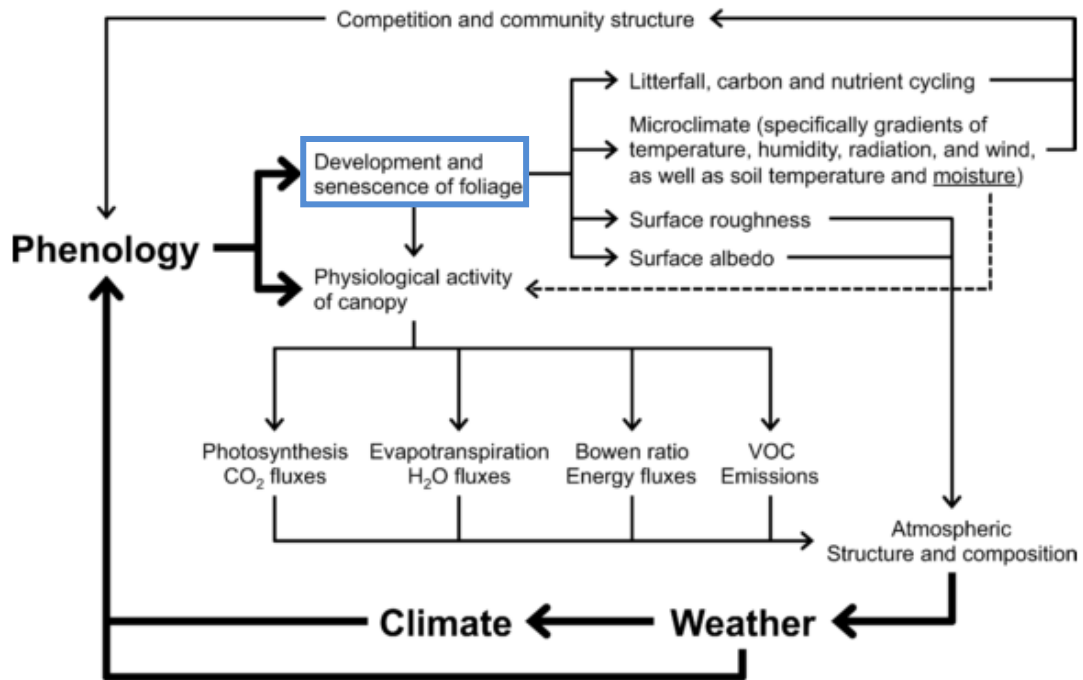
Figure 2.1. Conceptual model illustrating the primary feedbacks between vegetation and the climate system that are influenced by vegetation phenology (source: Richardson *et al*., 2013). The development and senescence of foliage is highlighted in blue.

The growth of woody plants is controlled by heredity and environmental factors operating through physiological processes. Genetic variations in physiological and growth characteristics are responsible for differences between tropical and temperate, and evergreen and deciduous trees, as well as differences among and within species (Kozlowski *et al.,* 1991). Trees in tropical rainforest grow continuously through growth cycles facilitated by environmental conditions favourable to all year round growth (Read & Frater, 1999). In temperate regions, such as the UK, the seasonal variations in temperature, light intensity, photoperiod (day-length), and rainfall, govern a regime that provides alternating favourable and unfavourable conditions for growth. In winter months, groundwater may be frozen and daylight hours are short, so trees risk losing water from the leaves while not producing adequate quantities of carbohydrates to survive (Packham *et al.*, 1992). Furthermore, leaf cells typically contain a large amount of water which is liable to freeze at low temperatures, posing a risk of damage to the protoplasm (Wareing &

Phillips, 1981). To address these issues trees may have leaves with a small surface area to limit water loss (needle-leaved evergreen) or lose their leaves during winter (deciduous) (Read & Frater, 1999). Thirty-six percent of UK woodland is deciduous broadleaved, 55% coniferous, and the remaining proportion is mixed (Forestry Statistics, 2013). All these woodland types show distinct annual seasonal cycles of CO_2 driven by the seasonal growth of the vegetation.

2.2.1   Deciduous phenology

In the UK, the most common broad-leaved deciduous species are oak (*Quercus robur*), ash (*Fraxinus excelsior*) and birch (*Betula spp.*) (Forestry Statistics, 2013). Figure 2.2 displays the daily CO_2 fluxes and cumulative Net Ecosystem Productivity (NEP) for a mixed oak deciduous woodland using data averaged over an eight-year period (Read *et al.*, 2009). Net Ecosystem Productivity is the difference between photosynthetic gain (NPP) and respiration loss from the ecosystem, representing the rate of accumulation of CO_2: the integral of the net CO_2 uptake in the growing season, and the loss during the winter leafless period (Morison *et al.*, 2012). This annual variation is striking and emphasises the impact of weather conditions on woodland CO_2 exchange. Richardson *et al.* (2007) attribute 40% of the variance in NEP directly to variation in environmental drivers such as increased soil respiration with increasing temperatures, and 55% to the physiological adjustments of the ecosystem to external conditions such as a warm spring causing earlier spring emergence, on an annual basis.
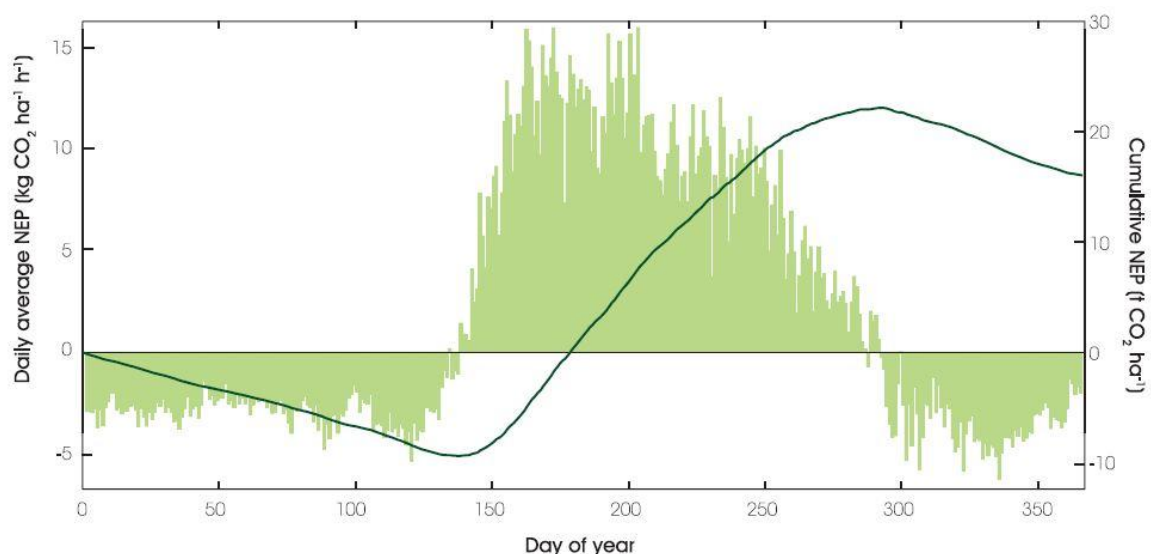
Figure 2.2. Daily net CO_2 fluxes (vertical columns) and cumulative Net Ecosystem Production (NEP) (solid line) of a mixed oak deciduous woodland at the Straits Enclosure, Alice Holt, Surrey, averaged over 8 years: 1999-2006 (Source: Read *et al.*, 2009).

The annual shifts in balance between canopy photosynthesis and ecosystem respiration govern relatively large fluxes into and out of the stand. The stand is a carbon sink when NEP is positive, and a source when NEP is negative. At the beginning of the year (Day of year = 0, Figure 2.2) deciduous trees are in a state of dormancy in which growth is temporarily suspended, the trees have no foliage, and therefore NEP is negative as CO_2 is released by maintenance respiration (Bonan, 2002; IPCC, 2013). Exposure to a period of cold temperatures is needed to break the dormancy in resting buds, referred to as the 'chilling requirement' which is met once environmentally unfavourable growing conditions remain for an extended period during winter; the optimal temperature for this is 5-7°C (Street & Opik, 1984; Polgar & Primack, 2011). As a protective mechanism to prevent the buds developing before the stable return of favourable growing conditions in spring, no growth occurs if warm weather occurs in winter before the plant satisfies its chilling requirement.

In spring, when air temperatures and day length (photoperiod) increase, the dormant resting buds begin to expand and green tissue emerges signalling budburst (Wareing & Phillips, 1981) at around 20th May (day 140) for the stand depicted in Figure 2.2. In deciduous ecosystems, the development of this new foliage is a pre-requisite for photosynthetic uptake to occur at the start of the growing season, and the stand becomes a carbon sink as the CO_2 balance is shifted. Following budburst, leaves continue to unfold and expand until a state of maturity is reached. The duration and warmth of the growing season strongly influences primary production (Packham *et al*., 1992). Throughout this time, the colour and nature of leaves can vary dependent on growing stage and species. For instance, beech leaves emerge in May a fresh bright green colour and mature to a darker green colour during summer (Read & Frater, 1999).

Mid-June to end of July (days 160-200) is the most productive time of the year; warm temperatures coupled with maximum photoperiod length lead to a state of maturity in the canopy. When this occurs, leaves are fully expanded and green leaf area is at its peak, facilitating maximum photosynthetic activity and as a result, maximum NEP (Peñuelas & Filella, 2001). In many species this period is accompanied by the development of closed dormant 'resting buds' in summer or autumn when temperatures and light conditions are still favourable (Lang *et al.,* 1987; Okubo, 2000; Arora *et al.,* 2003). This is the case for many common European woody plants including oak, ash, sycamore, and pine (Wareing &

Phillips, 1981). The onset of autumn in deciduous plants is clearly signified by the colour change (senescence) and fall (abscission) of leaves, driven by environmental factors such as decrease in day-length and temperature. Leaf senescence is characterised by the yellowing of the leaf, due to the breakdown of chlorophyll which causes other leaf pigments such as carotenes to become visible, and decline in leaf protein content and moisture (Street & Opik, 1984). This process typically starts at the ends of leaves and progresses towards their base. A thin plate of cells with soft cell walls is formed between the leaf stalk and the branch – the abscission layer – which is eventually broken by the wind causing the leaf to fall. These processes also occur in evergreen trees but the leaves have a longer life span and are shed gradually (Read & Frater, 1999). The nature of leaf fall that occurs can also depend on the growth stage of the tree species. In oak and beech, for instance, there is a tendency for the dead leaves to be retained on the shoots of juvenile trees during winter months, whereas they are normally shed in the adult stages (Wareing & Phillips, 1981). As a result, in autumn and winter, photosynthetic capacity slowly declines causes a decrease in NEP and the stand becomes a carbon source once more.

2.2.2 Coniferous evergreen phenology

Coniferous woodlands in the UK are dominated by Sitka spruce (*Picea sitchensis*) and pines (*Pinus spp.*) and hold their needles for a longer-lifespan than broad-leaved species (Forestry Statistics, 2013). The needle-leaves that are common in evergreen species have low photosynthetic capacity, low nitrogen concentration in foliage, and low leaf area per unit leaf mass (Bonan, 2002). Needles have a high initial carbon construction cost per unit photosynthetically active leaf area but as they have a longer lifespan and can photosynthesise all year round the high initial investment is recouped despite low photosynthetic capacity (Bonan, 2002). Figure 2.3 shows daily net CO_2 fluxes for a Sitka spruce stand in Scotland, and illustrates that coniferous woodlands have a longer photosynthetic season due to the ability to photosynthesise earlier in the spring and later into the autumn until photoperiod and temperature limits photosynthetic activity (Givnish, 2002; Read *et al.*, 2009). Recovery of conifer photosynthesis occurs when favourable environmental conditions return in spring. Despite averaging the data over a five year period, the high day to day variability in CO_2 exchange is clear, particularly in autumn.
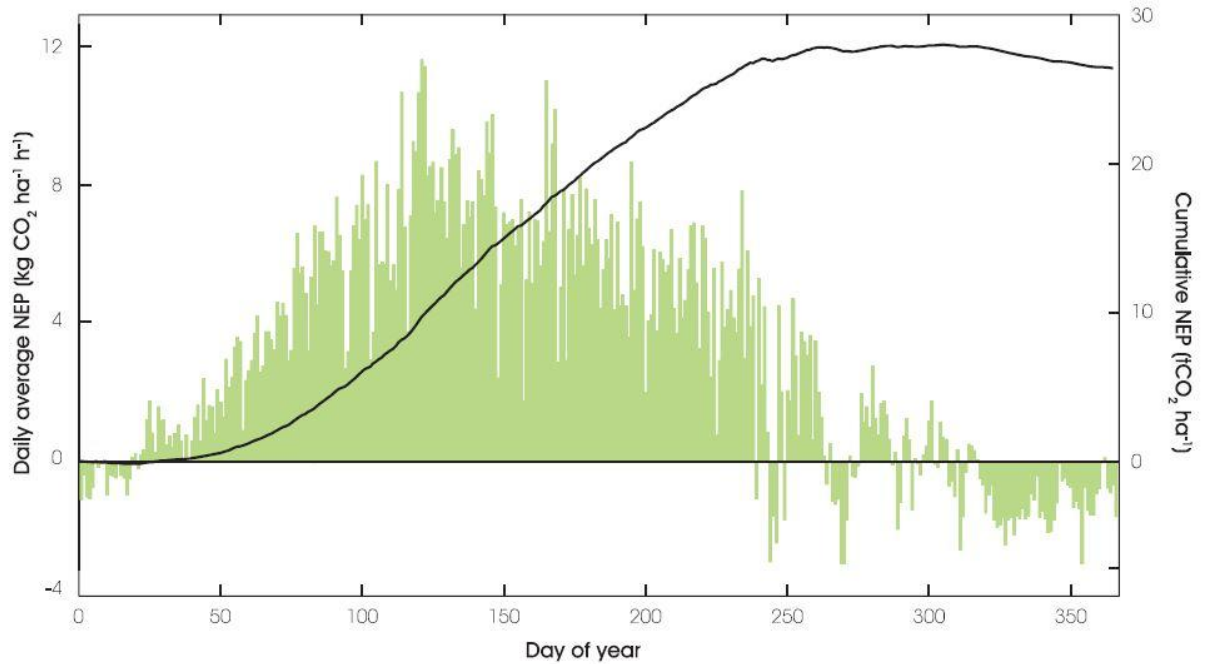
Figure 2.3. Daily net CO_2 fluxes (vertical columns) and cumulative Net Ecosystem Production (NEP) (solid line) of Sitka spruce woodland at Griffin Forest, Perthshire, averaged over 5 years: 1997-2001. (Source: Read *et al.*, 2009).

2.3 Vegetation phenology and climate change

Although woodlands in the UK are not faced with the same threats as many other regions of the world, such as large scale deforestation or wildfires, there are still many challenges that exist when attempting to sustainably manage such a significant resource. In light of the global concern for anthropogenic climate change, the UK Government issued a legally binding target to reduce the net UK carbon account by 80% in 2015 from the 1990 baseline (Climate Change Act, 2008). To assess these targets in a forestry context, and as a national response to the IPCC 4th Assessment Report, the Forestry Commission produced a UK based assessment compiled by leading experts in forestry and climate change chaired by Professor Sir David Read, commonly known as 'The Read Report' (Read *et al.*, 2009). This independent assessment examined the potential of UK woodlands to mitigate and adapt to our changing climate, and described how the impacts of climate change are becoming apparent in UK woodlands with effects on productivity, tree condition, leaf emergence, soil function, fauna and flora, and forest hydrology. However, the report noted that there is uncertainty about the likely severity and extent of these impacts (Read *et al.*, 2009). Several projected trends, supported by the UK Climate Projections by the Met

13

Office (UKCP09) for the UK were identified which would impact woodland vegetation growth:

- Increased temperature, lengthening of growing seasons, and rising CO_2 concentrations
- Increased precipitation in winter
- Increased frequency and severity of summer droughts
- Pests and diseases of forest trees representing a major threat

The report concluded that "clear, robust, research programmes" will be required to underpin the changes of forestry policy and practice to meet the challenges of the changing climate (Read *et al.*, 2009). However, an extensive body of literature provides compelling evidence that the climate has already changed considerably over the past fifty years and has affected the timing of vegetation phenophases (IPCC, 2013). In temperate regions, air temperature is considered to be most closely related to the phenological shift of vegetation (Menzel *et al*., 2006).

Sparks and Gill (2002) report changes of spring activity of several plant and animal species advancing by up to a month, and more marked in the UK than elsewhere in Europe. The Read Report documented that in the UK the leafing date has advanced by two to three weeks since the 1950s (Read *et al.*, 2009). The Forestry Commission confirm a clear temporal advancement in phenology for some species (Ray *et al.,* 2010).

Figure 2.4 suggests that leafing of pedunculate oak trees in Surrey is now around 25 days earlier than in the 1950s and has advanced by approximately 6 days for every 1°C increase in spring temperature (Ray *et al.*, 2010). However, the large variability in the data is clear and this may be attributed partly to the fact that the data is based on subjective visual observations. These studies highlight that spring phenology has responded to recent climate change in some measurable way, although large uncertainties remain as to how phenology will respond to projected future climate change such as scenarios depicted in UKCP09.
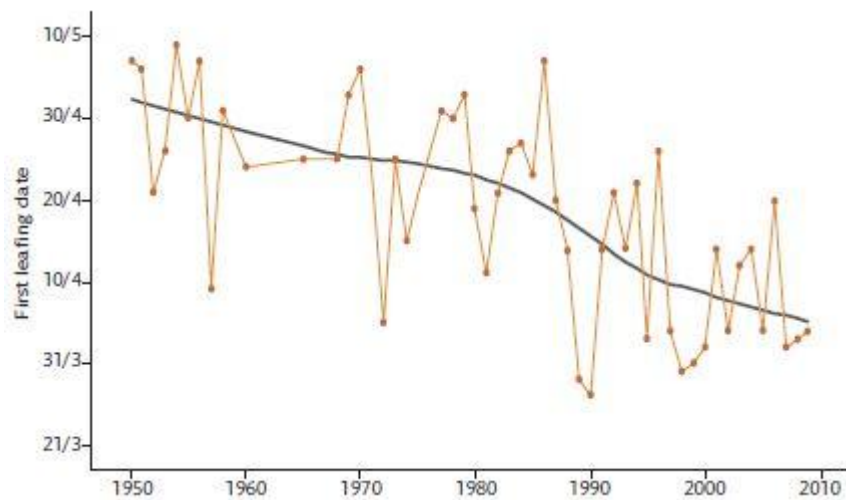
Figure 2.4. First leafing date of pedunculate oak trees (*Quercus robur*) in Surrey (source: Ray *et al*., 2010).

In the last decade the value of phenological data, particularly in climate change research, has been fully recognised. In 1999 (and reviewed in 2003), the timing of budburst of oak was identified as an official UK Government indicator of climate change (indicator 25 of 34) based on data from the UK Phenology Network (Cannell *et al*., 1999; Cannell *et al*., 2003). Climate science and the changes in vegetation phenology have entered more into public consciousness with the release of IPCC reports and media attention although the study of phenology has in fact a long history, in Europe dating back to early 1700s, with most developed countries having a recording scheme by 1850-1950 (Sparks & Menzel, 2002). This recent increase in public and scientific interest is marked by the emergence of a number of research and monitoring projects in the UK such as the UK Phenology Network (http://www.naturescalendar.org.uk/), the UK Environmental Change Network (http://www.ecn.ac.uk/), and the establishment of a UK-based International Phenology Garden (IPG) (http://www.forestry.gov.uk/fr/INFD-5ZZLRE). The IPG program was established in 1959 in Europe and the scheme uses cloned plants to minimise genetic variability (both within and among populations) to observe the timing of phenophases in a set of chosen species. An IPG site was established at Alice Holt Forest in Surrey, a long-term monitoring and experimental site of Forest Research UK, providing a useful international dataset. However, the scheme has received criticism for being unrepresentative of wild-grown native plants, which may be locally adapted to environmental conditions (Richardson *et al*., 2013).

2.3.1   Vegetation phenological monitoring by visual observations

Traditional methods of phenological data collection involve direct human visual observation of discrete phenological events, for instance, noting the date at which a certain tree shows the first sign of budburst. There are several accepted protocols available which provide guidance for observations (such as Koch *et al*., 2007, Miller-Rushing & Primack, 2008, and the IPG protocol). However, variations in definitions, criteria, sampling methods, and frequencies, often make the data difficult to compare (Denny *et al*., 2014). More recent methods, such as the protocol employed in the National Phenology Network in America (USA-NPN) phenology observation program, Nature's Notebook (www.nn.usanpn.org), also include an intensity/abundance measure (e.g. percentage of buds open) (protocol described in Denny *et al.,* 2014). However, estimating, or even being able to visualise, these fine scale changes in tall heavily occluded tree canopies poses obvious challenges.

Furthermore, all these methods are subject to the observer's skills and experience and only representative of the specific organism observed in the local site conditions. The observer can change from year to year, as can the plants measured, the amount of occlusion of the canopy, and day of year surveyed. Despite these significant limitations, the method of visual observations is still commonly adopted today and has been used to provide evidence to the IPCC and Read Report (IPCC, 2007; 2013; Read *et al.*, 2009).

The resultant data can best be described as a descriptive summary of phenological change and a requirement exists to quantify and gain more detailed information about vegetation growth dynamics to match the level of detail in carbon studies (such as Figures 2.2 and 2.3). This would ensure that these important interactions are accurately reproduced by models and further understood by forest managers, ecologists, and climate scientists.

2.3.2   Phenological modelling

There are two main model frameworks for phenological information: those that are used to predict the onset of a defined phenological event (usually budburst), and those that predict and analyse long term climatic data which incorporate phenology data as a primary input and/or a projected output.

The phenological stages of woodland phenology can be represented by a transitional date describing a discrete time where one phase ends and the next begins; for example budburst

signals the break of dormancy and the onset of leaf expansion. Models have been developed to predict these dates based on climatic conditions in order to forecast (and recreate past events) large area climate change impacts on phenology (such as Morin *et al.*, 2009) and to represent the seasonal course of foliage development and senescence, and associated physiological activity (Richardson *et al.*, 2012). Numerous models exist for predicting the onset of budburst based on temperature, such as the Bud Dormancy Release Model by Seeley (1996). The Forestry Commission research branch, Forest Research UK, have developed a budburst model for oak using day length and temperature, based on Hänninen (1990); the model uses observational data collected at IPG sites. Good agreement has been found between predicted and observed dates when datasets from multiple sites are combined, although variations in "observer performance" are noted (Forest Research, 2013), highlighting the issues raised in Section 2.3.1.

Numerous complex and sophisticated climatic models exist that are used to predict future climate scenarios and project likely environmental impacts, such as the Atmosphere-Ocean General Circulation Models (AO-GCMs), which have formed the core of IPCC report climate projections (IPCC, 2013). However, many of the land-atmosphere interaction models do not place sufficient emphasis on accurately modelling vegetation phenology or the seasonality of ecosystem processes (Richardson *et al.*, 2012); a factor that was reflected in the latest IPCC report for two key studies. Firstly, Pitman *et al.* (2009) compared the impact of land use change according to seven climate models which showed a wide range of results. It was reported that these discrepancies were "...mostly due to different assumptions on ecosystem albedo, plant phenology and evapotranspiration" (IPCC, 2013 ch8 pp32). Secondly, a study by Schwalm *et al.* (2010) found a difference between observations and simulations of ten times the observational uncertainty when comparing 22 terrestrial carbon cycle models to simulate the seasonal dynamics of land-atmosphere CO_2 fluxes from 44 eddy covariance towers. Again, poor simulation of spring phenology was listed in the model shortcomings (IPCC, 2013).

In another example, three carbon-climate models were examined (HadCM3LC, IPSL-CM2-C, and IPSL-CM4-LOOP) against measured CO_2 in the atmosphere to reproduce global growth rate, seasonal cycle, and the El Niño–Southern Oscillation, it was found that two out of the three models generally underestimate seasonal amplitude and suggests uncertainty in describing vegetation phenology (Cadule *et al.*, 2010). The Joint UK Land

Environment Simulator (JULES) land surface model, developed using UKCP (2009), and the Met Office HadCM3, acknowledges vegetation phenology as an important factor (Clark *et al*., 2011). In the current JULES model, phenology is characterised by scaling the maximum annual LAI by a temperature factor. When compared to using daily MODIS LAI, only very small improvements were observed (Slevin *et al*., 2015).

An important consequence of the poor representation of phenology in model simulations is that phenology, particularly budburst, drives primary feedbacks to the climate systems between vegetation and the atmosphere, and therefore uncertainty in the prediction of these events can feed forward to generate uncertainty in estimates of carbon and water cycling (Migliavacca *et al.*, 2012; Richardson *et al.*, 2013).

2.4   Canopy structural and biophysical parameters

Forest canopy structure, and seasonal dynamics of foliage growth, encompasses far more than solely the size and shape of the canopy over time. The spatial arrangement of stems, branches, and leaves, dictates the nature of the exchange surface including how much light can penetrate through gaps in the architecture (Pretzsch, 1997). Due to the structurally complex nature of forest canopies a number of biophysical variables have been developed to quantify and describe particular canopy elements – facilitating comparisons of one canopy to another. Estimates of biomass (that of standing wood and the seasonally dynamic foliage elements) are important inputs in carbon studies as well as a wide variety of other applications, however there are numerous other structural parameters that can also be quantitatively measured to give an insight into canopy structure, providing indicators of how open or dense the canopy is, or the spatial distribution of branch or leaf biomass. Structural and biophysical properties of vegetation, such as LAI, gap fraction, foliage profiles, clumping index, and leaf angle distributions are significant parameters related to ecosystem structure and function (Jonckheere *et al*., 2004; Danson *et al.,* 2007; Jupp *et al*., 2009). These properties can be used to describe vegetation dynamics over time with repeated measurements.

Leaf area is highly correlated with vegetation productivity (Webb *et al*., 1983). LAI is a biological parameter that defines the area that interacts with solar radiation and carbon dioxide exchange with the atmosphere (Kozlowski *et al.,* 1991; Clawges *et al*., 2007) and is therefore a primary factor controlling the optical properties and light transmission of the

canopy (Kozlowski *et al*., 1991). This information is essential for modelling and simulation of ecological and hydrological processes. LAI was first defined by Watson (1947) as the total one-sided area of photosynthetic tissue per unit ground surface area, but the definition has more recently been updated to the maximum projected leaf area per unit ground surface area (Jonckheere *et al*., 2004), to take into consideration the irregular form of needles and leaves. LAI is a dimensionless quantity and therefore independent of scale, appropriate to a canopy that forms a continuous and homogeneous layer. The LAI of forest stands varies widely depending on species, age, and site condition. In temperate deciduous forests LAI is typically in the region of 3-6 and temperate evergreen coniferous forests may reach an LAI of 11 or 12 (Kozlowski *et al.*, 1991). Seasonal LAI changes reflect phenological events such as leaf unfolding, expansion and senescence (Hertel *et al.,* 2012). The vertical distribution and availability of light is one of the most important factors for production of biomass (Hertel *et al*., 2012), and is quantified by the Foliage Area Volume Density (FAVD), also called leaf area density, defined as the total one-sided leaf area per unit of layer volume (Wilson, 2011). FAVD is a vertical profile of LAI where the integral of the FAVD gives the LAI (Morsdorf *et al*., 2006).

LAI can be estimated indirectly *via* the gap fraction; the probability of a ray of light passing the canopy without encountering any plant elements (Danson *et al*., 2007). Gap fraction is a key structural parameter in its own right which offers a measure of how open or dense a canopy is; gap fraction equals zero where there is a complete gap, and equals one when there is plant element present. The pattern of light absorption through a canopy often matches the logarithmic expectation of Beer-Lambert Law and has therefore been adapted for vegetation canopies (Monsi & Saeki, 1953). Beer-Lambert Law relates the attenuation of light to the properties of material through which the beam is travelling; absorbance is related to the concentration of the solution, the length of the light path through the solution, and an extinction coefficient. For vegetation canopies, a layer of leaves tends to absorb a fraction of incident light (depending on structural and reflectance factors). Light that passes through the first layer of leaves may be partially absorbed by the second layer, and so on. If each layer of leaves absorbs the same proportion of incident light, the resultant curve of light absorption as a function of leaf area will have logarithmic form. Under the assumption that gap fraction (Pgap) is equivalent to transmittance (T), Beer-Lambert Law can be adapted as follows:

$$Pgap = e^{-G.LAI.S}; \quad T = \frac{I_I}{I_o} \qquad (2.1)$$

$$where \; Pgap \equiv T$$

where I_I is the transmitted light intensity after travelling path length S through the canopy, I_o is the incident light intensity and G is the extinction coefficient, which is the fraction of foliage area projected onto a perpendicular plane ('G-function'; Ross, 1981), and LAI is the leaf area index.

Equation 2.1 then is inverted to solve for LAI. G is usually approximated to 0.5 to assume a spherical leaf distribution (Martens *et al.,* 1993). However in practise the extinction coefficient has been found to vary with solar elevation, canopy structure, and ratio of direct to diffuse beam irradiance and therefore generally varies between 0.25 and 0.75 (Jarvis & Leverenz, 1983). The main assumptions of this approach are that the foliage elements are randomly dispersed, the canopy is homogeneous, and the canopy elements exhibit isotropic canopy radiation (equal transmittance in all directions) (Hopkinson & Chasmer, 2007). However, rather than being randomly located, canopy elements are generally clumped in natural forest stands. This non-random arrangement of foliage is particularly common among many conifer species and can be described by the Clumping Index (Ω) (Walter *et al*., 2003). Clustering of canopy elements increases the transmittance of light and leads to underestimation of LAI, therefore the term 'effective LAI' is usually used (Clawges *et al*., 2007). To produce the 'true LAI', the effective LAI derived from the gap fraction inversion is combined with the clumping index where a Ω value near to zero indicates a very high clumped canopy whereas a value of one means a random spatial distribution (Chen & Cihlar, 1995).

2.4.1 Direct methods of measuring vegetation canopy structure

Direct or semi-direct measurement techniques for measuring vegetation structure are those made directly on canopy elements, such as stratified clipping (Hosoi & Omasa, 2009) or point-quadrant sampling (Warren-Wilson, 1959), and have been widely used for quantifying biophysical parameters in forests. One method of direct measurement is the felling and stripping of leaves of a single tree. After leaf collection, leaf area and dry mass is measured and the area divided by the measured mass to give an estimate of Specific Leaf Area, the projected area of fresh leaf per gram of dry leaf (SLA, cm^2 g^{-1}), a measure of leaf

thickness (Clawges *et al*., 2007). The remainder of the leaves are dried and the total dry mass is multiplied by the average SLA to give a value of LAI (Breda, 2003). This method can also be used to obtain a vertical leaf area density profile of the foliage of a tree based on harvesting plant elements within defined height levels (Clawges *et al.,* 2007). Light, and therefore SLA, scales with height in the canopy because sun-adapted foliage (compared with lower shady leaves) shows significantly higher photosynthetic activity (Marek *et al*., 1989).

These approaches are referred to as 'destructive' methods, as the plants being measured are damaged in some way as forest measurements are derived by active collection of plant material (Jonckheere *et al*., 2004). For this reason these methods clearly do not facilitate multi-temporal studies. The use of litterfall traps is a non-destructive direct method of calculating LAI of deciduous trees. This method collects leaves during leaf fall in traps of certain area distributed below the canopy and the area of collected leaves is measured and LAI determined by weight (Finotti *et al*., 2003). However, this method measures cumulative LAI rather than being an accurate measure at a single time, making it unsuitable for multi-temporal studies.

For evergreen species, a destructive sampling or allometric equations approach needs to be adopted. Direct methods derive information of high accuracy and therefore are often used as reference measurements to validate indirect estimates, such as remote sensing approaches (Baker *et al*., 2010). In fact, they are the only methods that measure 'true' LAI and associated variables as they directly separate the foliage. However, whilst direct methods are accurate for a specific location, they are inherently time consuming, labour intensive, and expensive, and therefore impractical for a wider level analysis (Lichti *et al*., 2002; Gibbs *et al.,* 2007). Furthermore, the destructive nature of these approaches mean that repeated readings are impossible, to assess seasonal change, for instance (Houghton *et al*., 2009). With direct methods, it is not always practical, or even possible, to measure biomass by cutting down trees, especially in an urban setting or protected area.

2.4.2   Indirect methods of measuring vegetation structure

Indirect methods collect information from the canopy without coming into physical contact with its elements. Based on radiative transfer theory, indirect methods infer LAI from the measurements of light transmission through the canopy (Ross, 1981; Breda, 2003). This is the case for specially designed instruments such as the LAI-2000 Plant Canopy Analyser

(Licor Inc., Nebraska) which measures diffuse radiation by means of a fisheye light sensor for five zenith angles (Jonckheere *et al.*, 2004). This instrument has been used to estimate LAI in coniferous (Gower & Norman, 1991) and deciduous stands (Cutini *et al.*, 1998). The Tracing Radiation and Architecture of Canopies (TRAC) (3rd Wave Engineering, Ontario, Canada) is a hand-held instrument which collects information on the gap size distribution of a canopy. This quantifies the effect of non-random spatial distribution of foliage (Ω), which can be used to convert effective LAI to true LAI (Jonckheere *et al.*, 2004). Although the LAI-2000 and TRAC are both portable and non-destructive, they rely on a number of assumptions and in fact measure Plant Area Index (PAI) as they cannot distinguish between leaves and woody material. They are also unable to retain a permanent record of the canopy structure. Other indirect optical methods for characterising vegetation structure such as satellite remote sensing, hemispherical photography, and terrestrial laser scanning, are outlined next.

2.5   Remote sensing of vegetation

Remote sensing interprets the interactions between electromagnetic energy and matter at selected wavelengths and offers a practical alternative for mapping aboveground biomass and other key biophysical variables related to seasonal vegetation growth at regional scales (Ji *et al.,* 2012). Offering a substantial departure from the traditional methods of measuring, remote sensing is able to map large areas efficiently, providing a valuable means of monitoring forests due to their complex widely distributed nature (Wulder, 1998). Remote sensing methods can be split into passive and active techniques. Passive techniques, such as optical imagery, rely on the availability of naturally occurring solar energy, whereas active methods provide their own energy source and so are independent of solar or terrestrial radiation (Campbell, 2002). Recent remote sensing advances for evaluating carbon and vegetation structure in forests primarily include optical remote sensors (satellite and near-surface sensors), radio detection and ranging (radar) and light detection and ranging (lidar). Remote sensing methods are based on the utilisation of the spectral properties of vegetation, as discussed below.

The radiation incident on a vegetation canopy is subject to three processes: reflectance, transmittance, and absorption, depending on characteristics of the radiation flux (wavelength, angle of incidence, polarisation) and of the vegetation target (surface

properties, cellular structure, composition) (Goel, 1988; Guyot, 1990). The success of remote sensing relies on the ability to relate reflectance measurements to vegetation properties. Due to the similarity in composition of pigments, other organic constituents, and water, leaves from a wide variety of plants possess similar optical properties. The spectral signature of a healthy green leaf is shown in Figure 2.5 and illustrates the proportion of reflected radiation at specific wavelengths of the electromagnetic spectrum (Malthus *et al*., 2002).

Radiation incident on a green leaf is strongly absorbed in the visible region of the electromagnetic spectrum (400-700nm), which means that the percentage of radiation reflected is low (Figure 2.5). This is caused by pigments, such as chlorophyll, carotenes, and xanthophylls, within the leaf (Jensen, 2006). Healthy green leaves absorb radiation efficiently in the blue and red regions of the spectrum where incident light is required for photosynthesis (Jensen, 2006) and these absorption features allow detection of stress in leaves (Carter, 1993). The relatively higher reflectance at green wavelengths is what causes healthy green foliage to appear green (Kozlowski *et al.,* 1991).
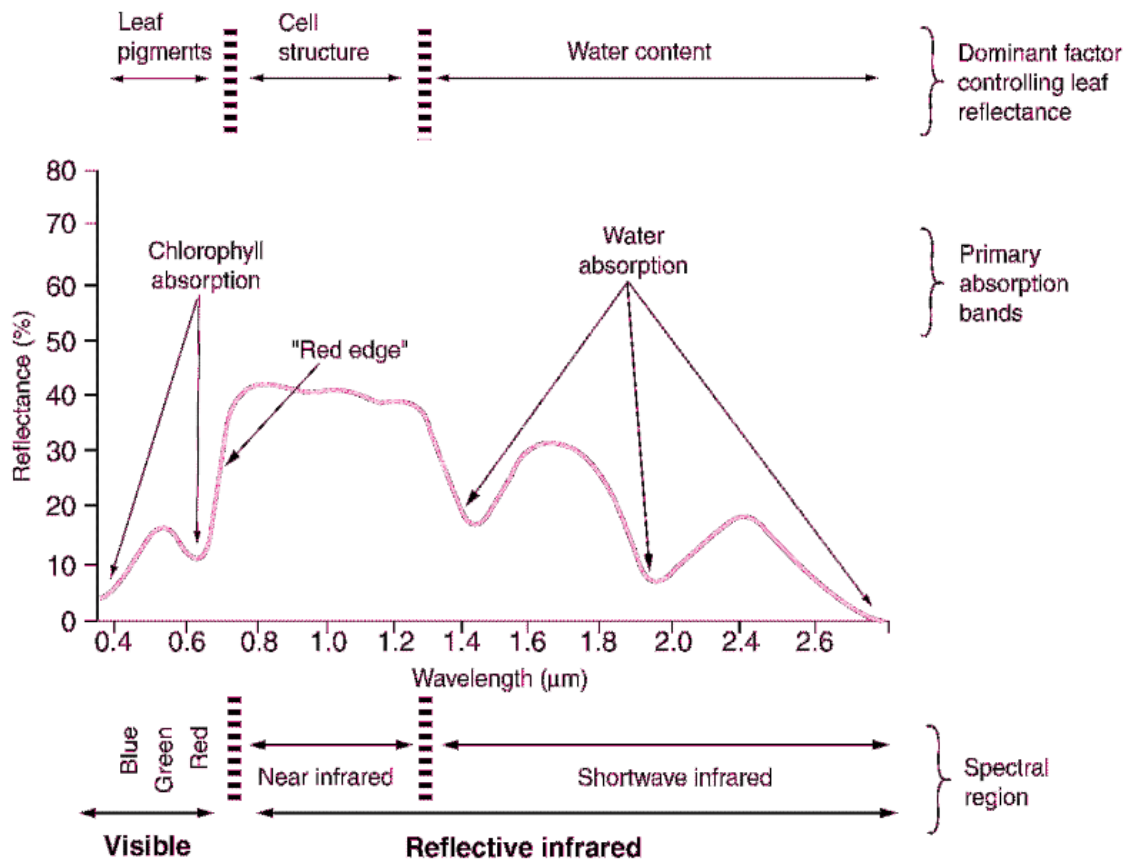
Figure 2.5. Optical properties for a typical leaf across the optical spectrum (source: Malthus *et al*., 2002).

The high reflectance of radiation in the near-infrared region of the spectrum is caused by cell structure within the leaf (700-1200nm) (Figure 2.5). The 'red edge' (700-750nm) describes a rapid rise in reflectance that can be related to chlorophyll concentrations and detection of senescence and dead vegetation (Jensen, 2006). Internal scattering at the cell wall-air interfaces within the leaf are responsible for the high reflectance (40-60%) and high transmittance (40-60%) in the near-infrared region (Jensen, 2006). The relationship between red and near-infrared canopy reflectance has resulted in the development of several vegetation indices from remote sensing data such as the Normalised Difference Vegetation Index (NDVI) (Guyot, 1990). The shape of the spectral signature in the shortwave infrared region is controlled by the absorption by leaf water (Figure 2.5). A strong relationship exists between the reflectance in the middle infrared and the amount of water present in the leaves of a plant canopy (Kozlowski *et al*., 1991).

Researchers have attempted to predict the reflectance of radiation in specific wavelengths for a given leaf or vegetation canopy. A number of factors have to be considered in these canopy reflectance models including the area and orientation of leaf components (LAI, leaf angle distribution), soil reflectance, illumination (amount of direct and diffuse light and angle of incidence), and sensor characteristics (Goel, 1988; Jensen, 2006). Furthermore, a vegetation canopy is not an ideal diffusely reflecting surface; instead it shows non-Lambertian characteristics which can be described by the bidirectional reflectance distribution function (BRDF). Canopy reflectance models are typically based on geometric-optics, radiative transfer theory, or average transmittance theory (Jensen, 2006). Examples include the Scattering from Arbitrarily Inclined Leaves (SAIL) model that use radiative transfer equations to model energy fluxes, and the geometric-optical Li-Strahler model (1985).

The physical principles described above provide the basis for mapping large areas with satellites. Satellite remote sensing has provided a framework for global up-scaling of phenology and to observe spatial patterns using the spectral reflectance of the Earth's surface. Annual time series using spectral indices such as NDVI or Enhanced Vegetation Index (EVI) can be related to transitional dates by using local minima and maxima values from the rate of change of the index (Schwartz *et al*., 2002; Naito *et al*., 2012). For example, Zhang and colleagues identified four key transitional dates: green-up, maturity, senescence, dormancy (also used by Ahl *et al.* (2006) in a similar MODIS study) using this

method from MODIS data for New England, USA. Although 'realistic results' were produced, no validation (ground or other) procedures were adopted (Zhang *et al.*, 2003).

Limitations to this approach include the spatial and temporal resolution of the data, quality and availability of images (clouds, shadow, etc), and inconsistent methods and definitions (White & Nemani, 2003). There is a critical need for accurate field data to understand and validate satellite-derived outputs, but traditional field data is not at scales compatible with coarse resolution remote sensing observations (Zhang *et al.*, 2003). A further limitation to this approach is the inability to separate understorey and overstorey phenology due to the restriction to two-dimensions in the image data. Understorey phenology can change throughout the season subject to a changing light environment and satellite based phenology cannot directly account for this, despite understorey being an important part of the woodland ecosystem (Liang *et al.*, 2011). For instance, a study by Ahl *et al.* (2006) and colleagues estimated an earlier onset of greenness from MODIS data than field measurements as observed understorey greened earlier than the canopy.

Due to heterogeneity in woodlands (such as species composition, type, age, site characteristics) and the inability to separate vertical strata (ground vegetation, understorey, canopy) the use of course resolution satellite data limits the evaluation of spatial variability in phenology. Furthermore, the spatial resolution and frequency of satellite-based monitoring makes it difficult to detect phenological events at the species or community scale and therefore this method is unsuitable for the fine scale analysis that this research project requires.

2.6   Current techniques for characterising seasonal vegetation growth

Recently, 'near-surface' optical methods such as digital cameras/webcams and hemispherical photography have been applied to derive information on vegetation phenology. These methods are discussed below, followed by an evaluation of laser scanning systems for this purpose.

2.6.1   Digital camera and webcam technologies
Methods for monitoring phenology from digital cameras and webcams have been developed in an attempt to fill the gap between spatially integrated information from satellite sensors that do not distinguish among individual tree species, and point

observations of phenological events at species level (Ahrends *et al.*, 2009). Photographs are taken repeatedly over time using high resolution commercial digital cameras (Sonnentag *et al.*, 2012; Ahrends *et al.*, 2008; Ide & Oguma, 2010), or real-time webcams (Richardson *et al.*, 2009), to provide a time course of vegetation indices analysed from red, green, and blue (RGB), or hue, saturation, and light (HSL) digital values. Mizunuma *et al.* (2013) found an improved correlation with vegetation colour indices from downward-facing digital camera images with GPP than between MODIS-derived NDVI and GPP, over two years (Mizunuma *et al.*, 2013). Ahrends *et al.* (2009) collected data from two forest sites using downward facing digital RGB cameras and CO_2 flux tower data. Daily green fraction taken from RGB values displayed a pronounced seasonal variation which were used to derive timing of vegetation development stages and followed the same trajectory as measured GPP (Ahrends *et al.*, 2009). In a recent study, Morris *et al.* (2013) piloted the use of networks of traffic monitoring cameras for automatic extraction of phenological metrics. However, there are certain limitations associated with using near-surface optical imaging such as changing illumination conditions and background effects (multiple trees and disturbances), limited image resolution, and changes in observation geometry, which lead to uncertainties and unreliability of this method.

2.6.2 Hemispherical photography

Hemispherical digital photography, also known as fish-eye photography, is an established technology for describing forest canopies frequently used by the ecological community (Leblanc *et al.,* 2005; Seidel *et al.,* 2012). This method involves a standard digital camera with a fish-eye lens attached, pointing upwards into the canopy (or sometimes downwards) and is the most widely used technique to provide estimates of gap fraction at multiple zenith angles (Zhang *et al.*, 2005; Danson *et al.*, 2007; Chianucci & Cutini, 2012). Photographs taken in this way provide a permanent 2D image of the forest at a given time, which allows information on forest gaps to be extracted, and has been used as a validation method, for example for terrestrial laser scanning (Danson *et al.,* 2007). A classification is carried out based on the contrast between sky (or ground) and canopy in the photograph. As such, the gap fraction ($Pgap(\theta)$) can be calculated using the ratio of pixels classified as canopy gap (N_{gap}) to the total number of pixels (N_{tot}) for a specific zenith angle (θ):

$$Pgap(\theta) = \frac{N_{gap}(\theta)}{N_{tot}(\theta)} \qquad (2.2)$$

As a result, correct exposure is important for accurate retrieval of canopy parameters and therefore photographs should ideally be taken under diffuse light such as an overcast day (Zhang *et al.,* 2005). Wang *et al.* (1992) found reasonable agreement between hemispherical photography and LAI-2000 Plant Canopy Analyser when studying the spatial variability of LAI in an oak forest. However, the limitations of using hemispherical photographs in this manner are that they are limited by sky conditions, an inability to distinguish foliage from woody material (i.e. measure PAI rather than LAI), and methodological errors can occur at any stage of image acquisition and analysis (Jonckheere *et al.,* 2004; Calders *et al.*, 2011; Chianucci & Cutini, 2012).

2.6.3   Light detection and ranging

LIght Detection And Ranging, commonly referred to as lidar, is a remote sensing approach that utilises the properties of scattered light to extract information on a target including its position in 3D space. A significant advantage of lidar systems is that they provide their own energy source making them 'active' sensors independent of solar and terrestrial radiation. They are not constrained by time of day or atmospheric conditions, unlike passive sensors that are sensitive to variations in solar illumination (Campbell, 2002). The application of lidar to vegetation studies is discussed here, while the physical principles behind lidar systems are discussed in Chapter 4.

Lidar systems can be classified according to the platform on which they operate: spaceborne, airborne, or ground-based systems. Spaceborne laser scanners (SLS) are those positioned on Earth-orbiting satellites from which measurements are taken from space. The Global Ecosystem Dynamics Investigation Lidar (GEDI) is a multi-spectral lidar system planned for launch in 2018. GEDI will collect high resolution observations of tropical and temperate forest structure at the landscape level (NASA, 2015). Lidar systems mounted on airborne platforms are referred to as airborne laser scanners (ALS): laser pulses are sent from the ALS towards the Earth's surface and positions are generated from the lidar sensor, the Inertial Navigation Unit (INU) of the aircraft, and a Global Positioning System (GPS) (Heritage & Large, 2009). ALS has been used to scan large areas in great detail leading to the production of high accuracy Digital Elevation Models (DEMs) (Wehr & Lohr, 1999), and more recently to forest canopy information (Drake *et al.*, 2003; Asner, 2009). Gap fraction has been estimated from discrete return ALS by measuring the penetration rates based on the fraction of laser returns from below the canopy to the total

returns (Lovell *et al*., 2003), or to derive gap fraction empirically from ALS metrics (Hall *et al.,* 2005), to give LAI (Morsdorf *et al*., 2006; Solberg *et al*., 2009).

Due to the fact that ALS systems operate from long ranges above the canopy, the spatial resolution of data acquisition, and inability to characterise full vertical structure of vegetation, means that ALS does not lend itself to phenology measurement as well as their ground-based alternatives. TLS cover a small area but point density can be very high (green points in Figure 2.6), and their position below the canopy facilitates characterisation of ground vegetation, understorey and full vertical profile. Returns acquired from ALS (black points in Figure 2.6) typically suffer from occlusion particularly in dense canopies. A lower spatial density and larger footprint size also restricts the amount of detail on the vegetation components that can be collected. It is for these reasons that this research is focussed on TLS, discussed in more detail in the following section.
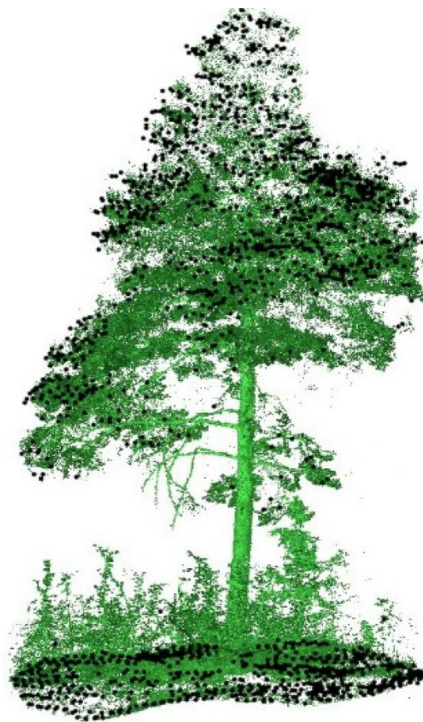
Figure 2.6. Combined point clouds from ALS (black dots) and TLS (green dots). Source: Holopainen *et al*., (2014).

2.7 Terrestrial lidar

TLS are lidar systems which operate from a ground-based platform and scan in increments of arc in both the vertical (zenith) and horizontal (azimuth) direction. TLS are capable of collecting accurate three-dimensional (3D) information on vertical structure and foliage

distribution, as well as understorey vegetation properties. This addresses many of the limitations of previously outlined methods, providing an opportunity for improving both the accuracy and level of information gathered on phenological characteristics and carbon dynamics in forests. Although only developed over the past decade, TLS have already been shown to accurately obtain tree diameter and stem density (Watt & Donogue, 2005), as well as LAI (Lovell *et al*., 2003; Jupp *et al.,* 2009), and gap fraction (Danson *et al*., 2007).

2.7.1   Gap fraction

Danson *et al.* (2007) developed an approach to estimate the gap fraction based on the ratio between the number of laser returns from a TLS and the total number of emitted beams, in a similar way that gap analysis on a DHP is done (Equation 2.2). This approach has been applied by others (Calders *et al*., 2011; Moorthy *et al*., 2011), including a modified approach for a waveform TLS (Lovell *et al*., 2003). Comparisons of gap fraction from TLS and hemispherical photography have shown both a good agreement (Danson *et al*., 2007) and an underestimation of gap fraction from TLS (Lovell *et al.,* 2003; Calders *et al.*, 2011). Data points around the edge of the canopy are more likely to be classified as vegetation rather than gap in TLS datasets due to partial hits (Vaccari *et al.,* 2013). Attempts have been made to correct for this by using return intensity (Ramirez, 2011) or apparent reflectance (Strahler *et al.,* 2008; Zhao *et al*., 2011). Returns have also been grouped into 3D volumetric pixels (voxel approach) with a pre-defined dimension (Hosoi *et al.,* 2010; Hosoi & Omasa, 2006) and then each voxel classified as occupied or empty (Henning & Radtke, 2006; Béland *et al*., 2014).

2.7.2   LAI

Estimates of LAI from gap fraction can be calculated in a number of ways, for instance, using Miller's integral approximation or inversion of the 'hinge angle'. Miller's integral is an adaptation of Beer-Lambert Law (Equation 2.1) and requires gap fraction measurements at a range of zenith angles, as follows:

$$LAI = -2\int_0^{\pi/2} \frac{\ln\big(Pgap(\theta)\big)\,cos\theta}{\Omega}\,sin\theta d\theta \tag{2.3}$$

where θ is the zenith angle. For a uniformly homogeneous canopy of height z, path length S (Equation 2.1) is equal to $z/cos(\theta)$. In Equation 2.3, gap fraction measurements at high zenith angles are usually neglected as they have been found unreliable (Jupp *et al.,* 2009;

Zhao *et al.*, 2012). A typical zenith value of 57.5°, also known as the hinge angle between vertical and horizontal facet effects, is also used to estimate LAI. This is convenient because the G-function is almost independent of the foliage angle distribution, and remains more or less constant (G=0.9) at different angles (Warren-Wilson, 1963). For hinge angle inversion, LAI is estimated as follows:

$$LAI = -1.1.\ln{(Pgap(57.5°))} \tag{2.4}$$

where $Pgap(57.5°)$ is the gap fraction at the hinge angle direction. The zenith ring between 55° and 60° is typically used to approximate the hinge region (Jupp *et al.*, 2009; Zhao *et al.*, 2011; Calders *et al.*, 2015). Jupp *et al.* (2009) also introduced a method of estimating LAI by separating the fraction of horizontal and vertical material in the canopy. The estimation is done by fitting a linear model to a plot of the following:

$$x = -\ln{\left(Pgap(\theta)\right)} \tag{2.5}$$

$$y = \frac{2}{\pi}tan\theta$$

The vertical component, L_v, is then equal to the gradient and the horizontal component, L_h, is the intercept on the y axis. The sum of L_v and L_v is then the LAI estimate. This method partially accounts for clumping, but still has some bias due to clumping effects (Jupp *et al.*, 2009).

2.7.3 Foliage profiles

Leaf area in a tree canopy is a three-dimensional attribute. LAI can be expressed as a vertical profile, known as a foliage profile. The foliage profile is defined as the total one-sided leaf area per unit of layer volume (Wilson, 2011), where the sum of the foliage profile over all the vertical layers is the LAI. Leaf area as a function of height is a key parameter to quantify vegetation structure, radiation interception, growth, and habitat. Typically, maximum rates of photosynthesis, and therefore leaf thickness (measured as SLA) are found in the highest section of the canopy and may be lower in leaves at the extreme external edge of the canopy (Woodman, 1971; Kozlowski *et al.,* 1991). Furthermore, the vertical distribution of components in a canopy has been identified as a major factor controlling canopy reflectance (Wang & Li, 2013). Kozlowski *et al.* (1991) identifies that the vertical distribution of canopy leaf area can be described by a normal distribution curve which shows maximum leaf area at an intermediate position within the

crown and gradually decreases upward and downward through the canopy. Millers integral can be calculated as a function of height, by introducing a vertical parameter (z) into Equation 2.3), to obtain vertically resolved gap fraction:

$$LAI(z) = -2 \int_0^{\pi/2} \frac{\ln(Pgap(\theta,z))cos\theta}{\Omega} sin\theta d\theta \qquad (2.6)$$

where z is height above the ground. Vertical plant profiles may also be derived from the vertically resolved directional gap probability ($Pgap(\theta, z)$) using the method of Jupp *et al.* (2009), which uses a solid angle weighted normalised profile:

$$FAVP(z) = LAI \frac{\delta}{\delta z} \left(\frac{\log(Pgap(\theta,z))}{\log(Pgap(\theta,H))} \right) \qquad (2.7)$$

where H is the height at which the laser pulse exits the canopy. The foliage area volume density, FAVD(z), is largely independent of clumping and is approximated from the hinge angle LAI (Equation 2.4). The solid angle weightings are calculated by the solid angle (mean zenith angle for each interval) subtended by the zenith bin size. This weighting gives zenith angles that represent a larger area in each height plane a larger weight than zenith angle bins that represents a smaller area (i.e. those directly above the scanner) (Jupp *et al.*, 2009). The idea here is to minimise the impact of clumping and sampling variation on the shape of the profiles. To enable this approach to be appropriate for sensors with multiple returns, the gap fraction at a zenith interval as a function of height (Pgap(θ,z)), is calculated as:

$$Pgap(\theta,z) = \frac{\sum w_i(z_i < z, \theta)}{N(\theta)} \qquad (2.8)$$

$$where \ w = 1/n_s$$

where $N(\theta)$ is the total number of outgoing laser pulses for the zenith angle interval. For multiple return instruments (discussed in Chapter 4), the assumption is made that for a specific transmitted laser pulse each return equates to a beam area interception of $1/n_s$ where n_s is the number of total returns for that transmitted laser pulse (Calders *et al.*, 2011).

A series of studies used TLS to estimate the vertical profile of foliage using voxel-based methods and showed that this can detect seasonal changes in broadleaved woody canopies

(Hosoi & Omasa, 2006; 2007; 2009; 2012). However, although this was a multi-temporal study, with only three visits in a year (May, August, November), it showed the potential of TLS to identify differences across seasons, but not phenological timings, or to give much insight into ecosystem processes. Furthermore, a significant conclusion was that the ability to separate foliage from woody material would increase the accuracy of forest measurements and that this is a current limitation of commercial TLS, as is the lack of validation in many TLS studies (Hosoi & Omasa, 2007). Current methods of separating foliage from woody components in a forest canopy using TLS involve scanning the trees at different stages of the seasonal cycle and assessing the leaf-off versus leaf-on results (Henning & Radtke, 2006; Hosoi & Omasa, 2009; Béland *et al*., 2011). However this method is clearly inapplicable for evergreen species, relies on multiple scans several months apart, and even then is not a true representation of the true foliage component. Calders *et al*. (2015) analysed a TLS time series of PAVD (plant area volume density; included woody material) of 48 measurement days of four plots in the Netherlands over spring 2014. Sigmoidal models were used to define the start of season, corresponding well with field observations and earlier than estimates from MODIS NDVI time series.

2.7.4   New sensors

Several new innovative TLS have recently been developed. The VEGNET *in-situ* monitoring lidar (Portillo-Quintero *et al*., 2014) is a portable TLS which measures vegetation at the hinge angle to generate PAI and PAVD in a rapid and repeatable way. Unlike other TLS, VEGNET was developed solely for vegetation and phenological monitoring applications, but the sensor still suffers from the inability to separate foliage from wood to enable true LAI, and FAVD, to be accurately quantified. However, the development of experimental multi-spectral TLS could overcome this limitation. There are currently four multi-spectral TLS systems in operation, their key features are summarised in Table 2.1.

Two research TLS systems currently exist which measure vegetation using two different laser wavelengths, the Salford Advanced Laser Canopy Analyser (SALCA), and the Dual Wavelength Echidna Lidar (DWEL). This dual-wavelength functionality has the potential to separate leaves and wood based on their spectral signatures (discussed in Chapter 4). If successful, these systems would allow for more accurate measurements of the forest environment, therefore reducing uncertainty in carbon, hydrological, and phenological

cycles. In addition, a recently developed Hyper-Spectral Lidar prototype (HSL) has full-waveform capabilities and uses a supercontinuum laser over a spectral range of 480-2200nm. Although still at the laboratory stage, early results have demonstrated the ability of the HSL for deriving information on vegetation targets using spectral indices, such as seasonal changes in chlorophyll content on pine specimens (Hakala *et al*., 2015).

Table 2.1. Key features of current multi-spectral TLS instruments.

Feature	SALCA	DWEL	HSL	MWCL
Status	Field operational	Field operational	Laboratory-based prototype	Laboratory-based prototype
Wavelengths	1063nm and 1545mn	1064nm and 1548nm	480-2200nm (supercontinuum laser)	555nm, 670nm, 700nm and 780nm
Measurement	Full-waveform digitisation	Full-waveform digitisation	Full-waveform digitisation	Photo-counting
Key reference	Danson *et al*., 2014	Douglas *et al*., 2014	Hakala *et al.,* 2012	Wei *et al*., 2012

Another recent development is a Multi-Wavelength Canopy Lidar (MWCL) which measures at four wavelengths: 555nm, 670nm, 700nm and 780nm, further exemplifies the growing popularity in developing custom research instruments for vegetation analysis. Results from the MWCL have shown that this system can detect small leaf-level changes in reflectance due to biochemical concentration (Wei *et al.,* 2012).

2.8   Conclusion

It is clear that the seasonal fluxes of CO_2 follow a distinct trajectory for both deciduous and coniferous woodland types, driven by the magnitude and physiological activity of plant leaf area in the canopy. Therefore, a method for systematic monitoring, accurate estimation, and generation of increased ecological information, is vital to study the carbon and water exchanges between forests and the atmosphere. The study of vegetation phenology needs to go beyond attributing a discrete phenophase and towards measuring the seasonal dynamics in forests as a continuous dynamic cycle with 3D characteristics. An effort to improve characterisation of these events would increase the information available for climate scientists, policy makers, land managers and forest ecologists. Recently, the study of vegetation phenology has become high profile and has received great public and

scientific interest as a tool for monitoring climate change. However, if this phenomenon is to be used as an indicator, it is vital that robust methods exist with which to accurately quantify fine scale changes in complex 3D canopies.

To carry out an ecologically sound study, it is important that the biological scale at which measurements are made is appropriate for the phenomenon being measured. Vegetation phenology varies within communities with local weather and site conditions, and the phenology of individual plants plays a key role in determining how ecosystems are structured and how they function (Cleland *et al*., 2007; Newnham *et al*., 2013). Furthermore, observing at a scale where individuals can be monitored within the context of the surrounding canopy will allow species in differing site conditions to be examined, and will provide a framework within which to establish which species will be best suited to the projected change of environmental conditions (Read *et al.,* 2009). The scale and resolution of TLS allows assessment of forest stands from individual leaves, to single trees, to plot level.

Long-term monitoring would require robust measurements of LAI, as do comparisons of LAI among stands or communities (Martens *et al*., 1993). TLS allow a quantitative and objective representation of a canopy at a single time. A time-series of repeated measurements allows for variation in these parameters to be analysed and related to phenological vegetation dynamics, such as the rate of expansion of leaf material, or the onset of senescence in the canopy, as well as being an indicator of plant condition. These variables may allow objective comparisons between single trees and stands.

The majority of studies tend to focus on isolated phenological events, particularly budburst in spring, and therefore fail to capture the full phenology as a cycle of which it is a part. Data has suggested a delay in autumn events in recent years (Sparks & Menzel, 2002), but this is not well understood (Richardson *et al*., 2013). In addition, many studies consider a single site and woodland type, with a clear emphasis on broadleaved deciduous species even though evergreen stands also exhibit a clear seasonal trend. Deciduous and evergreen woodlands comprise 91% (Forestry Statistics, 2013) of UK woodlands, with evergreen plantations making up the larger part. It is therefore important to consider and examine both types in a range of site conditions in order to aid understanding of the phenological cycle and response to a changing climate.

In conclusion, there is a requirement for a comprehensive frequent multi-temporal study that can monitor structural change and seasonal characteristics of UK woodland phenology as a dynamic 3D ecosystem throughout a full annual seasonal cycle. Dual wavelength TLS, together with direct destructive measurements, have the potential to allow a 4D approach to measuring the seasonal dynamics of foliage by quantifying the spatial locations (x,y,z) of foliage over time.

2.9   Research questions

As a result of the literature review a number of research questions have been developed to address each of the three key objectives (Chapter 1.2) and are presented in Figure 2.7. In order to complete these requirements two field campaigns are necessary: a direct destructive field experiment to provide TLS validation (conducted at Alice Holt, Surrey, UK), and a multi-temporal study (conducted at Delamere Forest, Cheshire, UK).

Objective 1 is concerned with generating an apparent reflectance product for SALCA data and is addressed in Chapter 4 by considering two key research questions. In order to develop a radiometric calibration procedure to derive apparent reflectance it is necessary to first understand the radiometric characteristics of the instrument, this is the focus of the first research question (Q1.1). The second (Q1.2) considers the accuracy of the approach. The input data for this objective are empirically derived measurements of SALCA intensity response. The desired output is a method to derive apparent reflectance which can be applied to all datasets to provide a basis for the following two objectives.

Objective 2, to investigate the classification of returns into leaves and wood, is examined by two research questions which address a key limitations of current studies outlined in the literature review. There are currently no commercial systems with dual-wavelength full-waveform functionality. Having full access to the instrument design and raw data for the SALCA system provides a unique opportunity to assess the potential benefits and applications to forest environments. The first research question (Q2.1) investigates if leaf-wood separation can be achieved on a tree (Chapters 5 and 6) and plot (Chapter 7) scale, using dual-wavelength datasets acquired by the SALCA instrument. An examination of these approaches to a range of different, but common, UK woodland species on a plot scale will be addressed in the second research question (Q2.2). The input data for Objective 2 is leaf-off and leaf-on TLS and direct measurements of individual oak trees (Alice Holt field

campaign) and leaf-off and leaf-on TLS measurements of five forest stands (Delamere Forest field campaign).

Aim To improve characterisation of the seasonal dynamics of UK woodlands using dual-wavelength terrestrial laser scanning		
Objective 1 Produce an apparent reflectance product for the SALCA instrument	**Objective 2** Assess whether dual-wavelength lidar can be used to separate leaf and wood returns	**Objective 3** Examine the spatial and temporal characteristics of foliage in a range of UK forest types
Question 1.1 What are the radiometric characteristics of the SALCA instrument? **Question 1.2** What is the accuracy of the apparent reflectance product?	**Question 2.1** Can leaf-wood separation be achieved on a tree and plot scale ? **Question 2.2** How does leaf-wood separation vary for different UK woodland species?	**Question 3.1** Does the spatial distribution of foliage vary between stands? **Question 3.2** Are there differences in the temporal characteristics of foliage growth between stands?
Input data: Empirically derived measurements of SALCA intensity response. **Output:** Method to achieve an apparent reflectance product which can be applied to all datasets.	**Input data:** (1) Individual trees at Alice Holt forest. (2) Five forest stands in winter and summer conditions at Delamere Forest. **Output:** Method to separate leaf-wood returns on multiple scales and species.	**Input data:** TLS and DHP Time-series of five forest stands at Delamere Forest. **Output:** Quantitative analysis of the seasonal dynamics of UK woodlands.
Chapter 4	**Chapters 5, 6, 7**	**Chapters 7 and 8**

Figure 2.7. Structure of research questions, inputs and outputs to address each objective. The thesis chapter numbers that relate to each objective are given at the bottom of the figure.

Objective 3, to examine the spatial and temporal characteristics of foliage, uses a time-series of SALCA and DHP data acquired at Delamere Forest in five forest stands. This quantitative analysis of foliage seasonal dynamics is addressed through the consideration

of two research questions. The first (Q3.1) uses vertical structural metrics (FAVD) to assess whether the spatial distribution of foliage varies between stands. The second (Q3.2) utilises LAI temporal profiles to examine whether there are differences in the temporal characteristics of foliage growth between stands. The creation of a time-series of quantifiable parameters derived for a full annual seasonal cycle for a range of plots will address some of the limitations outlined in the literature review, such as the majority of phenological studies focussing on isolated phenological events (predominantly budburst), inadequate temporal resolution of data collection, or incorporation of only one species or site. Rather than a set of discrete phenological events, the seasonal dynamics of foliage growth is a continuous cycle that has 3D spatial characteristics which change throughout the year. Hemispherical photography, and detailed visual observations will be considered alongside TLS data to examine the sensitivity to change, as well as the seasonal response of the TLS-derived parameters and apparent reflectance. As outlined in the review, LAI and foliage area volume density (FAVD) are important quantifiable biophysical parameters but are frequently estimated as plant area index (PAI) and plant area volume density (PAVD) profiles as robust methods to separate the foliage are lacking. There will be no direct validation of this objective although hemispherical photographs will provide coincident measurements. The results are presented in Chapter 7 and Chapter 8.

CHAPTER 3

Study sites and data collection methods

3.1   Introduction

This chapter describes the experimental design and methodological approaches adopted for this research. In order to fulfil the aim of this research, to improve characterisation of the seasonal dynamics of UK woodland vegetation structure using dual-wavelength TLS, a dataset is required that will allow for forest canopy TLS measurements to be made together with an opportunity for an assessment of the accuracy of those measurements. The only accurate method to validate indirect approaches such as TLS is to collect direct measurements which generally have a destructive nature. Due to the requirement for repeated measurements over time to facilitate a phenological study, together with the restrictions on felling trees, the validation dataset was collected at Alice Holt, and a separate field site used for the multi-temporal study at Delamere Forest. An overview of the approach at each site is given in Table 3.1. The following sections describe both study sites and the protocols implemented at each.

Table 3.1. Summary of objectives and methods applied for each study site.

Field campaign	1	2
Site name	Alice Holt	Delamere Forest
Location	Surrey, UK	Cheshire, UK
Scientific focus	Validation of TLS	Multi-temporal phenology
Scale	Tree (x3)	Plot (x5)
TLS	Leaf-on and leaf-off from multiple positions	Many throughout year
Hemispherical photos	No	Yes (coincident with TLS)
Destructive measurements	Yes (foliage and wood of 3 trees)	No
ASD spectrometry	Yes	Yes

3.2   Alice Holt study site

A destructive sampling fieldwork campaign was undertaken with Forest Research UK, the research agency of the Forestry Commission, as part of a collaboration between University College London, University of Newcastle, and University of Salford. The fieldwork was carried out at Alice Holt, located approximately 6.5km south of Farnham, Surrey, UK, a mixed deciduous and coniferous plantation forest. The forest is owned and managed by the Forestry Commission UK for timber production and recreation. A research station is based at Alice Holt and the forest contains long term monitoring plots, including the oak-dominated Straits Enclosure, a carbon flux measurement site where the destructive measurements took place. The location of the site is shown in Figure 3.1.
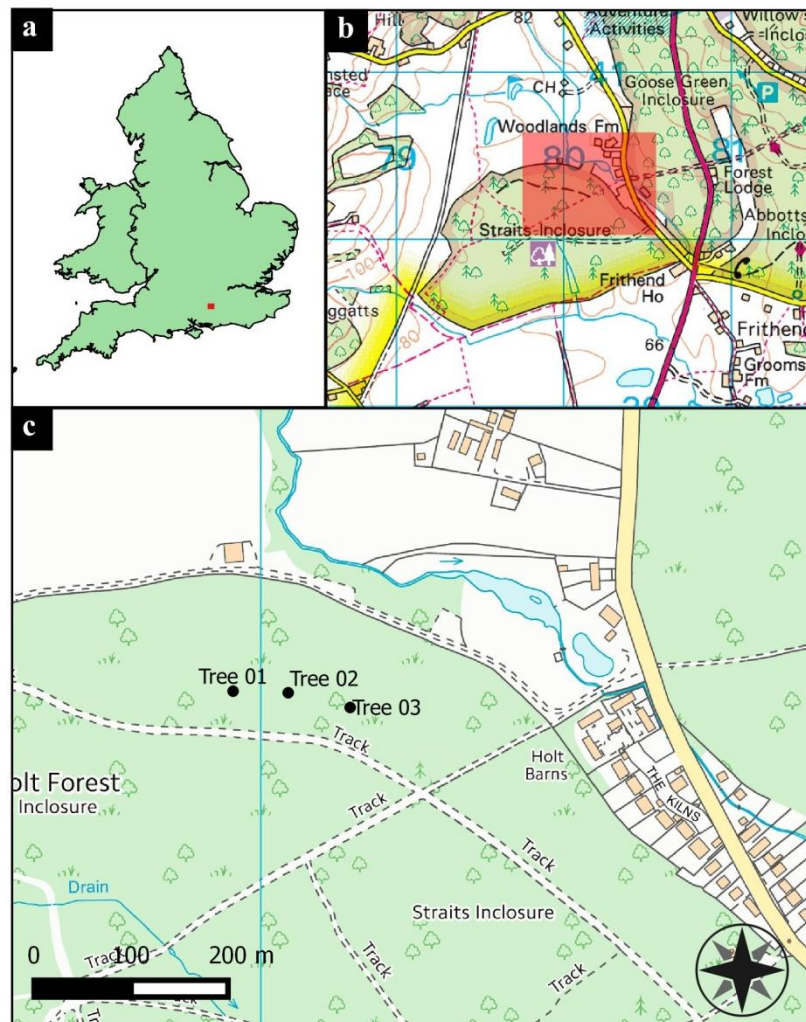
Figure 3.1. Site Location maps, showing: a) location of Alice Holt Forest within England, b) location of study site within the Straits Inclosure, and c) location of the three trees chosen for destructive sampling (Tree 01, Tree 02, and Tree 03). The red rectangles in a) and b) show the graphical extent of sub-figures b) and c), respectively.

3.2.1 Trees for destructive sampling

Three oak trees were chosen within Alice Holt forest for destructive field sampling. The trees were selected based on their accessibility and dimensions, so that a range of sizes were represented denoted by their diameter at breast height (DBH) and tree height, and are referred to as Tree 01 (large oak), Tree 02 (medium oak), and Tree 03 (small oak).

3.2.2 Experimental design

The TLS measurements at Alice Holt were acquired in two phases in order to achieve leaf-off and leaf-on measurements. The first visit occurred on 26-27th March 2014 when no foliage was present, and the second visit on the 2-3rd July 2014 in full-leaf conditions. On both visits, low resolution scans (0.24° in azimuth and 0.06° in zenith) of each of the three sample trees were acquired following the TLS protocol (described in Section 3.4.2). Due to the proximity of the scan positions (constrained by surrounding trees) from the target trees, the instrument was operated from the forest floor by placing it on the ground. This is due to the TLS instrument only scanning to -6° in elevation and therefore scanning from a tripod would omit the base of the tree. Conducting the scans from the ground ensured that the full tree was imaged in the scan. Three scans were carried out from different aspects of each tree (North, South-East, South-West), to ensure each section of the tree was adequately represented in the point cloud. To aid merging of the multiple scans, eight reflective targets were set out around each tree in positions enabling them to be viewed from multiple scanning positions.

The destructive sampling experiment (described in Section 3.4.1) took place during 7th – 10th July 2014, four days after the leaf-on TLS data acquisition while the trees were still in full-leaf. This was undertaken by a team from Forest Research UK, University of Salford, University of Newcastle, and University College London, coordinated by Dr. Eric Casella of Forest Research. Systematic spectral measurements were also acquired during the destructive experiment to include samples of leaves and tree bark.

3.3 Delamere forest study site

Delamere Forest, the largest wooded area in Cheshire, UK, is located approximately 40km south-west of Manchester and covers an area of 972ha. The forest is dominated by evergreen coniferous plantation (Scots pine *Pinus sylvestris*, Corsican pine P*inus nigra*) with patches of deciduous broadleaf (oak *Quercus*, sweet chestnut *Castanea sativa*, silver

birch *Betula pendula*, common beech *Fagus sylvatica*, rowan *Sorbus aucuparia*, ash *Fraxinus excelsoir*) and deciduous conifers (Japanese larch *Larix kaemferi*). The forest is owned and managed as a timber and recreational resource by the UK Forestry Commission and attracts a large number of leisure visitors from the North West of England. Permissions were obtained from the Forestry Commission to undertake the research. Information collected during site visits and from examination of stock maps confirmed Delamere forest as suitable for the multi-temporal field campaign for the following reasons:

- *Species composition* – the forest comprises a variety of common UK woodland tree species of both evergreen coniferous and deciduous broadleaf variety within close proximity of one another.
- *Site conditions and logistics* – relatively flat topography, forest tracks to aid movement of equipment, Forestry Commission office onsite, toilet and refreshment facilities. Parking facilities in the site allow easy transport of equipment to and from site.
- *Existing data* - established research site and therefore a record of previous data exists which may be useful to the study (e.g. Ramirez *et al*., 2013).
- *Location* –proximity to Manchester reduces travel and accommodation costs and maximises data collection time in the field.

3.3.1   Plots for multi-temporal data collection

Five locations were identified within Delamere forest at which data collection took place, referred to as *plots*. The location of the site and selected plots is shown in Figure 3.2. Several preliminary visits to the study site were undertaken in order to identify the site for each plot and a number of factors were taken into account including species composition, topography, understorey and ground vegetation, size and age of trees, access, and proximity to one another. Common UK broadleaf deciduous species are represented in **Plots 1, 2, and 3**. The relatively small number of key plots meant that they could all be scanned consecutively in a single field day, prioritising frequency and resolution of data acquisition over number of sites. **Plot 4** comprises evergreen conifer species which provides an opportunity to assess seasonal changes in the UK's most widely planted conifer forest type. Finally, **Plot 5** contains Japanese larch (*Larix kaempferi*), a deciduous conifer. This choice of data collection sites allows analysis and comparison of broadleaf

and needle-leaf species, and the presence of oak (Q*uercus petraea)* in Plot 1 provides a link between the destructive sampling conducted at Alice Holt. A basic overview of the characteristics of each plot is shown in Figure 3.3.
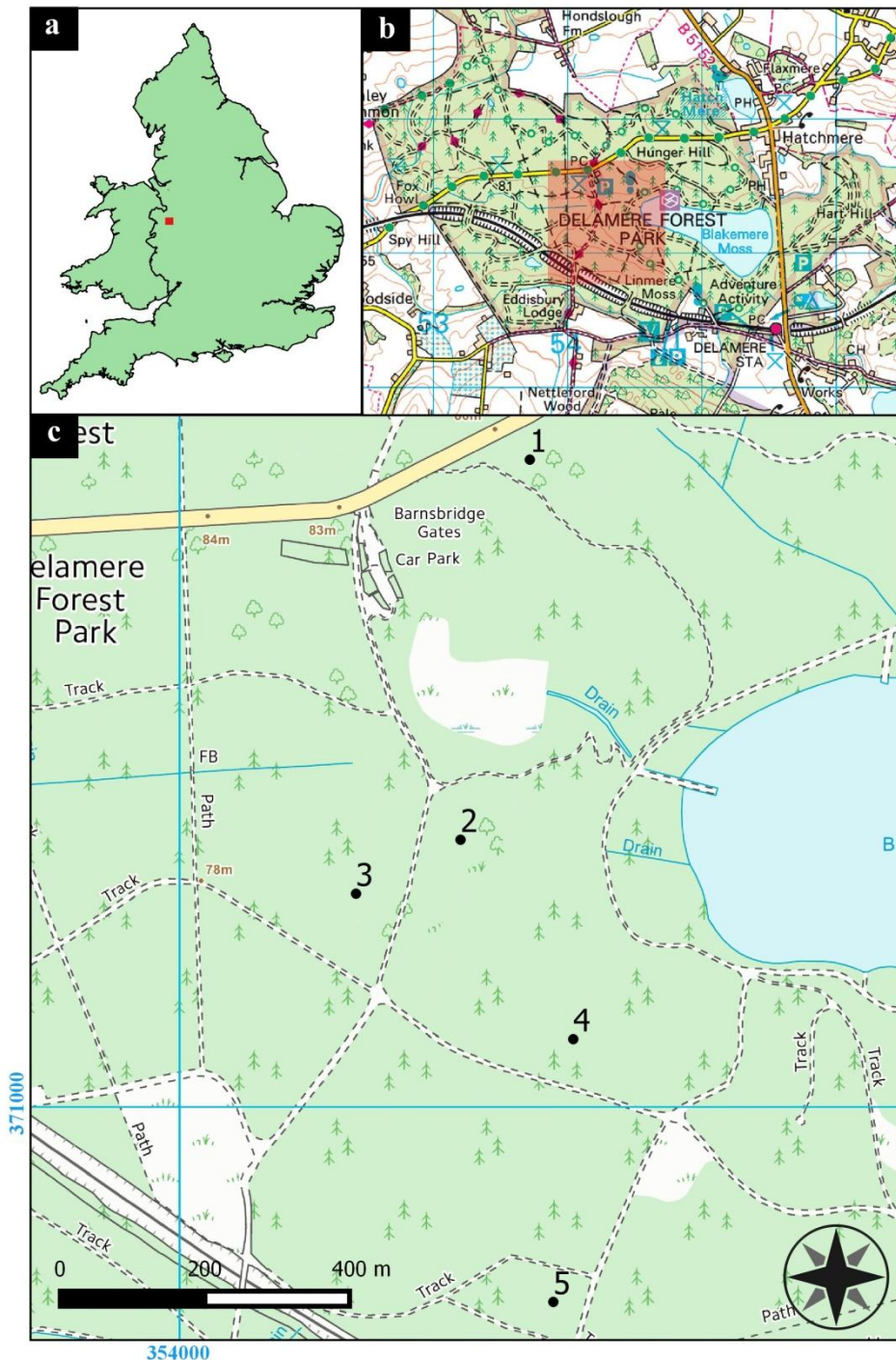
Figure 3.2. Site Location maps, showing: a) location of Delamere Forest within England, b) location of study site within Delamere Forest, and c) location of the five plots chosen for multi-temporal sampling (labelled 1-5). The red rectangles in a) and b) show the graphical extent of sub-figures b) and c), respectively.

Plot	Ground/understorey	Canopy	Description
1			**Broadleaf deciduous** Tree species: Sessile oak (*Quercus petraea*; common), Silver birch (*Betula pendula*; common), sweet chestnut (*Castanea sativa*; rare), ash (*Fraxinus*; rare). Ferns, bracken, leaf litter, moss. Near to road.
2			**Broadleaf deciduous** Tree species: Sweet chestnut (*Castanea sativa*; abundant), Rowan (*Sorbus*; rare). Multilayered canopy. Some young samplings. Slightly sloping to two sides. Dry soils.
3			**Broadleaf deciduous** Tree species: Common beech (*Fagus*; abundant), sweet chestnut (*Castanea sativa*; rare). Mostly bare ground, some small grasses patches. Open on West side and path to East.
4			**Conifer evergreen** Tree species: Corsican pine (*Pinus nigra*; common), Weymouth pine (*Pinus strobes;* common), Scots pine (*Pinus sylvestris*; common) Dense ferns, scrub. Damp. Slightly undulating ground.
5			**Conifer deciduous** Tree species: Japanese larch (*Larix kaempferi;* abundant) Sparse understorey and ground vegetation, mixture of bare ground and low laying vegetation.

Figure 3.3. Site description of plots, including the tree species present (Latin name, abundance).

3.3.2   Experimental design

The multi-temporal field campaign at Delamere forest was carried out during a full annual seasonal cycle between March 2014 and April 2015. The frequency of visits varied according to the amount of growth activity in the canopy. In spring (April through to June) visits were made around twice a week in order to capture budburst, leaf development, and leaf growth. In summer (July through to September) full leaf is reached in the canopy, during this time green leaf area stays relatively constant (Peñuelas & Filella, 2001) and therefore visits were scaled back to around twice per month. On each field visit visual phenological observations, hemispherical photographs, and TLS measurements were acquired according to the relevant data acquisition protocols described in the following sections. Thirty five field visits were carried out and the plots surveyed at each visit are shown in Figure 3.4. A revised optical filter combination was installed to the TLS instrument prior to 1st April, therefore the TLS data collected before this date (hashed areas; Figure 3.4) were not used as the output laser power differences mean that they are not comparable.

Due to the nature of TLS data collection, the weather can pose a significant limitation. Adverse weather conditions such as wind, rain, or fog, may reduce data quality considerably. For instance, the laser beam can be scattered by falling raindrops or suspended fog particles triggering a false return. Furthermore, the TLS instrument used is not fully watertight and any rain droplets that land on the external filter could also create erroneous returns. Therefore efforts were made to avoid adverse weather conditions by planning according to the Met Office weather forecast. However, weather patterns do change and rain can occur unexpectedly: if adverse weather was encountered in the field, TLS scanning was aborted and all electronic equipment covered. It is worth noting that due to the amount and weight of equipment involved in field scanning activity, a fieldwork assistant was required to accompany all of the field visits. These constraints on weather and resource availability did occasionally limit the frequency of visits. Furthermore, as Delamere Forest is actively managed as a timber resource by the Forestry Commission forestry works are routinely carried out throughout different areas of the forest. As a result, some plots were inaccessible during certain periods due to machinery present for thinning works and timber collection. This was the case for plot 5 and prevented visits to this plot during springtime. As a consequence, this plot was scanned once in summer and again the following winter to provide a leaf-on and leaf-off dataset.

Visit	Data visited		Plot number 1	2	3	4	5	Notes
X1	10	March						Generator broke – no scanning
X2	12	March	▨					
X3	13	March						Equipment failure – no scanning
X4	17	March		▨	▨			
X5	24	March						Equipment failure – no scanning
1	01	April	■	■				New optical filter combination
2	02	April			■			
3	08	April	■					Very windy so re-scanned on 9th April
4	09	April	■			■		
5	15	April	■					
6	17	April		■	■			
7	24	April	■	■	■			
8	28	April	■		■			
9	02	May	■	■				
10	07	May	■		■			Scan at plot 3 aborted before completion due to adverse weather
11	13	May		■				
12	14	May			■	■		
13	18	May	■					
14	19	May		■				
15	26	May		■				
16	30	May		■	■			
17	03	June	■					
18	13	June		■	■	■		
19	19	June	■					
20	26	June			■			
21	04	July	■	■				Scan at plot 2 aborted before completion due to adverse weather
22	17	July	■	■	■			
23	31	July	■	■	■			
24	07	August				■		
25	21	August	■	■	■			
26	02	September					■	
27	11	September	■	■	■			
28	27	October	■	■	■			
29	09	April	■			■	■	2015
30	21	April		■	■			2015

Figure 3.4. Details of fieldwork visits. The hatched areas (12th March and 17th March) indicate previous optical filters.

3.3.3 Defining plot size

To establish the area of interest in each plot, it is necessary to define a plot size. This can be done by consideration of the hinge angle. As introduced in Chapter 2, a zenith angle of 57.5° allows a convenient estimation of LAI as the G-function is approximately independent of leaf inclination angle (Warren-Wilson, 1963). For valid LAI estimation from the hinge region, the laser beams must be able to exit the top of the canopy. It is under this principle that the following protocol was adopted to define the plot size for each plot independently.

First, the maximum tree height was determined for each plot. This was done by examination of the height distribution of the entire scan in leaf-off conditions. Leaf-off datasets were used as opposed to leaf-on to limit foliage material from occluding the upper canopy and leading to an underestimation of top height. For each plot, histograms were drawn to show the frequency distribution as a function of the z-coordinate plus the height of the instrument optical centre (1m), and the height of the tallest tree was identified. Secondly, the horizontal distance that a beam from the outer edge of the hinge region (60°) can exit the top of the canopy was determined as follows:

$$D_{xy} = \frac{H_{plot}}{\tan(0.5236)} \tag{3.1}$$

where D_{xy} is the radial distance in metres projected on the xy plane that a laser beam at a zenith angle of 60° (elevation angle 0.5236 in radians) can exit the top of the canopy at a plot height of H_{plot}. Finally, the horizontal distance from the origin (scanner location) to each return was calculated and all returns with a distance larger than D_{xy} were discarded.

3.4 Protocols

This section describes the data collection protocols adopted for the field campaigns; not all outlined protocols are applicable for both sites as described in the experimental plans above.

3.4.1 Destructive sampling

Destructive measurements were only acquired at the Alice Holt survey site. After TLS scanning had been completed and photographs taken, each of the three trees (Tree 01, Tree 02, Tree 03) were felled by a Forest Research technician and measurements of DBH,

height, and lengths of stems and branches were taken using a tape measure and callipers. Each tree was divided into height levels referred to as strata. The large oak had four height strata, and the small and medium oak had two height strata due to their smaller size where the first stratum encompasses the low branches and the second stratum the main canopy. This facilitated the examination of the vertical distribution of leaf area. From the full height of each tree, wood discs from the main stem and branches were taken every 1m to be used to calculate woody biomass and bark-to-wood ratios. A detailed account of the woody biomass sampling protocol will not be given here as it is outside the interest of this research project which is focussed on quantifying the foliage component of the canopies.

The foliage sampling had two key components. The first involved manually stripping off each leaf from the branches and putting them into bags according to the height stratum to which they belonged. Several volunteers were involved with leaf collection. Each bag was weighed as fresh weight and then oven dried in potato sacks to obtain dry mass. The bag weights were subtracted from the final results. This method allowed total dry foliage mass estimation for each height stratum. The second component involved collecting a selection of leaves at random from each stratum on each tree, 90 samples were collected in total. Leaf area was calculated individually by classification with the GIS software ArcMap$^{©}$, and fresh weight was measured using a 0.001g precision balance. The leaf samples were then oven dried for 72 hours at 75°C and weighed to obtain dry mass. Specific Leaf Area (SLA) was derived for each of the samples by dividing the estimated one-sided surface area by the mass. Finally, the leaf area for each tree height stratum was estimated by multiplying the measured dry mass of all the leaves by the average SLA value calculated from the samples. This protocol is widely accepted for direct leaf sampling (e.g. Clawges *et al*., 2007; Béland *et al.,* 2011).

3.4.2   TLS

To ensure that the TLS data collection with the SALCA instrument was reliable, accurate, and repeatable, a protocol was followed as shown in Figure 3.5. Data were recorded and stored directly in the internal computer of the SALCA instrument. After a scanning day, the acquired data was transferred to an external hard drive. The SALCA instrument, data formats, and processing procedures are discussed in Chapter 4.

1. Risk assessment and permit approval

2. Survey planning

Identification of plot centres with white peg to allow repeat measurements from constant viewpoint.

3. Equipment setup

Level instrument, centre over white peg, and orientate board with magnetic North.

4. Instrument height

Delamere: Using a tape, measure 100cm from the ground to top of the board (130nm from ground to optical centre).

Alice Holt: Scanner placed on the ground

5. Set calibration panel

Erect calibration panel at same height relative to scanner and perpendicular to laser output.

6. SALCA operation

Connect to power and switch on. Use laptop to remote desktop to internal SALCA computer, set parameters and start scan.

7. Record calibration parameters

Log ambient air and laser temperatures every ten minutes throughout the scan.

Calibration panel

Handset with digital display to read laser temps from internal thermocouples

Laptop

100cm

Battery pack and connectors

Parameter	Setting	Justification
Azimuth resolution	Delamere: 0.06°	High resolution to achieve maximum point density for detecting very fine changes such as bud development and growth.
	Alice Holt: 0.24°	Low resolution as change detection not required so prioritised speed of data acquisition.
Maximum range	60m	Adequate for size of plots, limit wasted data and unnecessary storage capacity.

Figure 3.5. Workflow for TLS fieldwork setup and scanning procedure and parameters. Note setup differences between sites.

3.4.2.1 Calibration panel

Performing a radiometric calibration on the TLS raw data is the subject of the following chapter (Chapter 4). To facilitate the calibration and empirically measure the intensity response with range, reflectance, and temperature, an external reference target of known reflectance was used during field scanning. A medium-density fibreboard (MDF) panel (w500mm x h750mm x d9mm) was sourced and two undercoats applied of a water-based white matte emulsion (Crown Pure Brilliant White Matte Emulsion). The panel was divided into six equal sub panels of 250mm x 250mm. Matte black water-based emulsion (Colours by B&Q Matt Emulsion 'Jet Black') was mixed with the white paint using the measurements stipulated in Table 3.2 and two coats applied to the corresponding square using a roller. When dry, the reflectivity of each sub panel was measured 10 times with an ASD spectroradiometer using a contract probe to obtain the mean measured reflectance shown in Table 3.2. Sub-panel 5 was re-painted during data collection to a reflectance of 44.13% and 40.38% for the 1063nm and 1545nm wavelengths respectively, in order to ensure that this reflectivity region was sufficiently represented.

Table 3.2. Panel reflectance measured with an ASD spectroradiometer using a contact probe for each of the six 25cm by 25cm sub-panels. Mean values from 10 measurements at the two wavelengths of the SALCA instrument. Standard deviation shown in brackets.

Sub-panel	White (ml)	Black (ml)	Reflectance % λ1063	Reflectance % λ1545
1	200	0	88.78 (0.45)	80.36 (0.21)
2	160	40	27.61 (0.57)	24.50 (0.40)
3	120	80	17.08 (0.32)	15.24 (0.38)
4	80	120	9.99 (0.97)	8.77 (1.02)
5	40	160	6.15 (0.45), 44.13 (0.63)	5.55 (0.54), 40.38 (1.05)
6	0	200	3.46 (0.04)	3.53 (0.05)

This multi-reference panel was used in a large number of field scans to characterise intensity variation (Chapter 4). Previous deployment of the SALCA instrument exposed a drop in received power over time from the beginning of a scan; and this has been attributed to an internal thermal effect. To aid measurement of this effect thermocouples were attached to the casings of the two laser units inside the instrument as a proxy for laser temperature.

3.4.3   Spectral measurements

Spectral measurements were taking with an analytical spectral device (ASD) spectroradiometer (FieldSpec 4). The FieldSpec 4 measures the spectral range of 350-2600nm, allowing the reflectivity of materials at the wavelengths inherent to the SALCA instrument to be extracted. To operate in the field, the instrument is connected to an external battery and operated from a laptop. A contact reflectance probe was attached to the FieldSpec. Rather than relying on solar illumination, the contact probe provides an internal light source allowing for measurements to be made close to the 'hot spot' direction, and therefore analogous to lidar. A calibrated spectralon reference panel was measured frequently throughout the data collection to provide a 'white reference'. Then the measured samples were calibrated to absolute reflectance using the measured reflectance of the white panel. A leaf grip device, with integrated white and black background panels was connected to the contact probe, for measuring transmittance and reflectance, respectively. For each sample measured, a number of spectra were collected and an average taken.

To take the measurements a contact probe was held against the target surface. It is important that the probe sits flush against the surface and pressure is applied so that no extraneous light can enter the fibre. This was a simple task for wide flat broadleaf leaves but more of a challenge for pine needles (as the elements are smaller than the contact probe footprint) and for some bark (when rough and curved). A solution was to layer the fine needles into a dense bunch and apply pressure to the contact probe to achieve a satisfactory seal. Black tape was wrapped around the end of the contact probe to trap any escaped light. At Alice Holt, spectral measurements were acquired coincidently with the tree felling and destructive measurements. Leaf samples were chosen at random from a range of heights from each tree. The reflectance of both the upper and lower surfaces and the transmission of each leaf were measured using a leaf clip as described above. Bark reflectance was taken at a range of height intervals up the trunk and branches of different sizes. At Delamere Forest, spectral measurements were acquired on a single summer (full-leaf) date. Reflectance of the upper surfaces was measured for five semi-randomly selected (had to be accessible) leaves for each species, and bark reflectance was taken of the main trunks.

3.4.4 Phenological observation protocol

On each field visit to Delamere forest, detailed visual observations were noted based on the observational protocols set out by the International Phenological Gardens (IPG). There is a subset of 18 plant species which are planted at all new IPGs (Figure 3.6), and the Delamere fieldwork plots contained three of these key species.

IPG-No.	Plant species		Phenological Phases							
	Botanical name	English name	BO	M	B	AB	J	F	LV	BF
111	*Larix decidua*	European larch	x		x	x			x	x
122	*Picea abies (late)*	Norway spruce		x	x	x				
131	*Pinus silvestris*	Scotch pine, Fir		x	x	x				
211	*Betula pubescens*	White birch,	x		x	x			x	x
221	*Fagus sylvatica* 'H'	Common beech	x		x	x		x	x	x
241	*Prunus avium* 'B'	Wild cherry	x		x	x		x	x	x
256	*Qercus robur* 'W'	Common oak	x		x	x	x	x	x	x
261	*Robinia pseudoacacia*	Common robinia	x		x	x		x	x	x
271	*Sorbus aucuparia*	Mountain ash	x		x	x	x	x	x	x
281	*Tilia cordata*	Small-leafed lime	x		x	x		x	x	x
311	*Ribes alpinum*	Alpine currant	x		x	x	x	x	x	x
323	*Salix acutifolia*	Pussy willow	x		x	x	x		x	x
324	*Salix smithiana*	Smith's willow	x		x	x			x	x
326	*Salix viminalis*	Basket willow	x		x	x			x	x
331	*Sambucus nigra*	Common elder	x		x	x		x	x	x
411	*Corylus avellana*	Common Hazel	x		x	x		x	x	x
421	*Forsythia suspensa*	Forsythia	x		x	x			x	x
431	*Syringa vulgaris*	Common lilac	x		x	x			x	x

Figure 3.6. Eighteen species part of the IPG Standard-Observation-Programme, three of which are represented in fieldwork plots (highlighted). Phenological phases: Beginning of leaf unfolding (BO), May shoot (M), Beginning of flowering (B), St. John's sprouts (J), First ripe fruits (F), Autumn colouring (LV), Leaf fall (BF). Source: Koch et al. (2002).

The phenological observations in this study were extended to include noting the stages of leaf development and growth in more detail (Figure 3.7). Where possible, the amount and spatial distribution of activity was also recorded with the aid of binoculars and photographs taken from a number of angles. The collection of this information was particularly useful during the transitional phases of spring and autumn and provides a descriptive reference for each dataset.
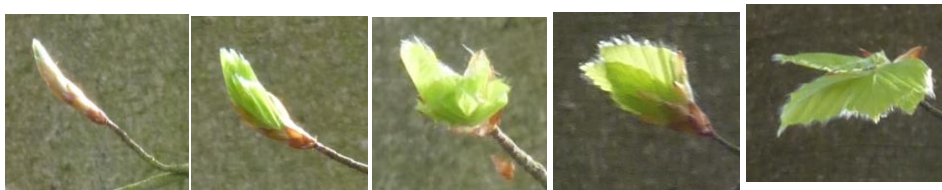
Figure 3.7. Five individual buds from a single beech tree located in Plot 3 on 15th May 2014. From left to right: closed bud, bud burst, leaf unfolding, leaf expansion, full leaf.

3.4.5   Hemispherical photography

Hemispherical photographs were obtained on each scanning occasion at Delamere forest using a Nikon D70s digital SLR camera with a Nikon 10.5mmf/2 8DX rectangular fish eye lens. Two photographs were taken in the zenith direction in each plot – one on the North-South axis and one on the East-West axis, this was to account for the lens not being a full circular fish eye. The fish-eye lens has been calibrated in a previous study (Ramirez, 2011) based on the methodology proposed by Baret (2004). For the data to be optimal the sky conditions should be uniform when the photographs are taken, these conditions are usually seen early or late in the day or during overcast conditions (Welles & Cohen, 1996). The procedure for taking hemispherical photographs was as follows:

i.   Attach fish-eye lens to camera and mount the camera on photography tripod.
ii.   Align camera lens with ground peg (plot centre) to ensure that the photographs were taken from the same position as the scans.
iii. Measure and adjust the height of the camera to 132cm to coincide with the height of the TLS instrument.
iv.   Use a compass to orientate camera to North-South direction.
v.   Use a bubble level to level the camera.
vi.   Turn camera on and take a picture with automatic exposure and infinity focus.
vii. Move to the East-West axis, re-level, and check height, acquire second photograph.

The hemispherical photographs were processed using CanEye (version 6.1), a free software package downloadable from http://www6.paca.inra.fr/can-eye (Weiss *et al*., 2004) which works in conjunction with Matlab. The software can be used to extract canopy structure properties (such as LAI and gap fraction) from true colour images (Weiss *et al*., 2004). These biophysical characteristics can then be compared with estimates derived from TLS data from SALCA. The first stage of image processing is to import the true colour hemispherical image and define the processing parameters described in Table 3.3.

The next stage in the processing is to classify the image into classes representing sky (gaps) or vegetation. This is an interactive step where the user can manually adjust the allocation of pixels to either class. Once this step is complete the outputs are generated to include a binary image and statistical biophysical parameters (Figure 3.8). For each date

and plot, both the NS and EW hemispherical photograph are processed and the average of the two results adopted.

Table 3.3. Processing parameters used for hemispherical photographs in Caneye

Parameter	Setting	Description
Image size (pixels)	4662, 4662	Determined automatically by software
Optical centre (pixels)	2331, 2331	Centre point of image
Zenith angular Resolution	5°	Angles for which the Gap Fraction will be computed. Balance between resolution and computational time
Azimuth angular resolution	5°	Angles for which the Gap Fraction will be computed. Balance between resolution and computational time
Sub-sampling factor	3	Computational time. One pixel out of three
Circle of interest	60°	Limit of the image used during the processing. Zenith angles higher >60° are not taken into account due to large occurrence of mixed pixels in these areas. Commonly used in gap fraction analysis
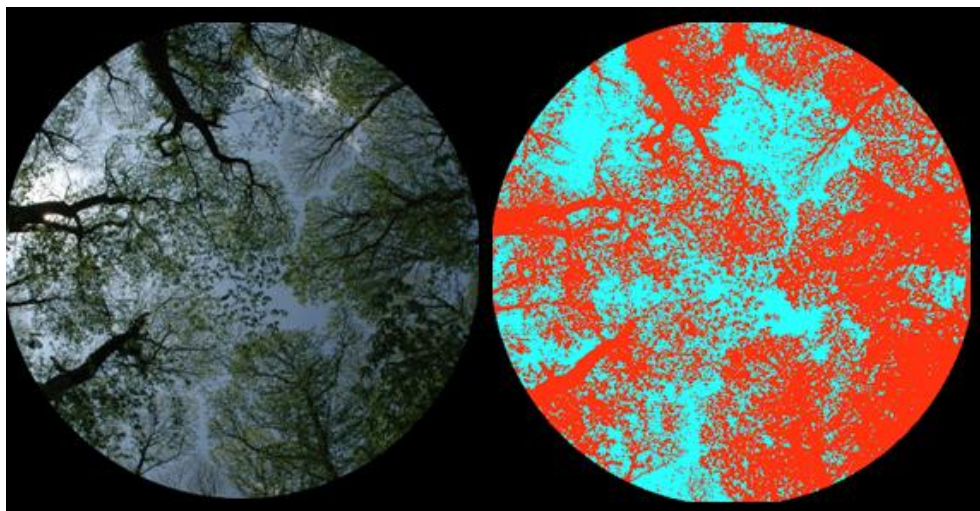
Figure 3.8: Image processing in Caneye. Image on left is input true colour image of 60° circle of interest. Image on right is binary image following classification to sky or vegetation

3.5 Conclusion

In order to fulfil the objectives of this research, two study sites were selected for data collection. Forest Research UK long-term monitoring and research site, Alice Holt, facilitated a collaborative destructive sampling campaign of three oak trees, combined with leaf-on and leaf-off TLS measurements. Five plots within Delamere Forest were selected,

based on tree species, stand composition, and logistical factors, for a multi-temporal study focussing on plot scale phenology. This chapter presented descriptions of both field campaigns including the experimental designs and data collection protocols. SALCA, the TLS instrument at the focus of this research, is the subject of the following chapter.

CHAPTER 4

SALCA instrument description and radiometric calibration

4.1   Introduction

The Salford Advanced Laser Canopy Analyser (SALCA) is an experimental Terrestrial Laser Scanner (TLS) developed to measure forest environments. This chapter starts with a discussion of the physical principles that underpin LIght Detection And Ranging (lidar) technology, followed by a description of the characteristics of the instrument. The remaining sections of this chapter outline and test a new approach to convert the intensity data recorded by the instrument into units relating to the forest target reflectance, addressing research Objective 1. This is carried out by performing a radiometric calibration using artificial neural networks (Schofield *et al*., 2016).

4.2   Principles of lidar

Lidar systems operate on the same physical basis as that of Radio Detection And Ranging (radar) except that a laser (with a wavelength between 532nm and 1.5µm) is used instead of radio waves; we can therefore apply the measurement principle first introduced in radar remote sensing to describe the flow of radiant energy in lidar systems using the radar equation (Wagner *et al*., 2006):

$$P_r = \frac{P_t D_r^2}{4\pi R^4 \beta_t^2} \sigma \tag{4.1}$$

where P_r is the received power, P_t the laser pulse energy at the transmitter, D_r the aperture diameter of the receiver optics, R the distance from the laser to the target, β_t^2 the beam divergence, and σ is the backscatter cross-section, computed as:

$$\sigma = \frac{4\pi}{\Omega} \rho A_s \qquad\qquad (4.2)$$

where Ω is the angle defining a backscattering cone in relation to surface roughness, ρ the reflectivity of the scatterer and A_s is the illuminated area of the scattering element. These equations were developed from Baltsavias (1999) but disregard atmospheric effects as these can have negligible effect on the measurements over the short ranges measured in a forest environment (Campbell, 2002; Wagner *et al.*, 2006).

Assuming that all variables in the radar equation are constant except distance from the target, and that the target fills the entire beam footprint, the return power intensity P_r can be simply expressed as:

$$P_r = \frac{1}{R^2} \qquad\qquad (4.3)$$

There are two main types of lidar system, 'time-of-flight' and 'continuous-wave' (CW). The time-of-flight method, as the term suggests, measures the travel time of light from a laser transmitter to a target and back to a laser receiver. This method is based on the principle that light travels at known constant velocity and therefore the time for the pulse to return to the sensor translates directly to distance, that is - the *range* (Rees, 1990; Lefsky *et al.*, 2002; Jensen, 2006). CW lidar systems offer an alternative approach in which the phase shift between the transmitted and backscattered light of a continuous laser beam of known wavelength is used to measure delay and obtain the range (Campbell, 2002). Although CW systems are usually quicker to operate than those of time of flight, they only facilitate one range return measurement: deeming them unsuitable for structurally complex environments such as forests, and so this method will not be considered further here.

The main features of the time-of-flight method can be described as follows. A pulse of strongly collimated light energy, the laser beam, is emitted in a systematic pattern from a transmitter within the lidar instrument (Pfeifer & Briese, 2007). Rotating mirrors inside the sensor head deflect the beam out of the instrument to travel through the atmosphere and interact with objects in its path. The beam footprint increases in size with the distance dictated by the laser beam divergence angle (Jiang *et al.*, 2012). Typical beam divergence values are between 0.03 and 8 mrad (Lim *et al.*, 2003; Mallet & Bretar, 2009). When the beam hits an object, the light energy is reflected, absorbed, or transmitted; the proportions of each depend on the nature of the surface, the wavelength of the energy, and the angle of

illumination (Campbell, 2002). The reflected energy that travels the same path from the reflecting surface back to the sensor, the *backscattered energy,* is detected within the instrument (Pfeifer & Briese, 2007). Recorded return energy is sampled to a discrete 'bin' by range; the size of which is predetermined by the frequency with which the digitiser can sample the signal and governs the 'range resolution'.

Different target materials have spectral reflectance curves of different shapes, their *spectral signature,* and this forms the basis for identifying the material type from lidar data (see Chapter 2.5: Remote sensing of vegetation). The reflectance of vegetation, for instance, is governed by the presence of absorbing pigments, water content, and other physical and chemical factors (Rees, 1990). The nature of the backscattered energy also depends on the sizes of surface irregularities (roughness or smoothness) in relation to the wavelength of the radiation (Campbell, 2002; Lichti *et al.,* 2002). The range (R) is derived once the return pulse energy crosses an internally defined threshold, and is computed by the time (t) for a lidar pulse travelling at the speed of light (c) to travel to and return from a target, according to:

$$R = \frac{ct}{2}$$

(4.4)

As a result, the accuracy of the range measurement is dependent on the time counting accuracy of the digitiser and the accuracy of detecting the backscattered energy above a noise level (Pfeifer & Briese, 2007). As lidar measurements work on a 'line of sight' principle, depending on the scene and the orientation of the laser scanning system, near-range objects in the path of the laser beam can obscure sampling of surfaces leading to occlusion (Kirchhof *et al.,* 2008). This can be a significant limitation, particularly in TLS.

The range and direction to reflecting surfaces is determined by the lidar scanner, which creates a *3D point cloud* data set in relation to the scanners internally defined coordinate system; for instance the direction of the pulse is stored from the orientation of the internal mirror at the time of pulse emission. Therefore, the data is typically processed to transform the acquired measurements to a standard coordinate system, translating the output data from 'scanner space' to 'object space' (Heritage & Large, 2009).

In the case of pulsed lidars the energy returning to the sensor can be recorded according to several schemes; *first return*, where the first point at which the signal intensity rises above a defined threshold is recorded signalling the first 'hit'; *last return*, where the furthest point

is recorded; *discrete return*, where a number of ranges are recorded for each pulse *full waveform*, in which all the energy reflected from a target is recorded.

4.2.1 Intensity measurement

Along with the acquisition of range, some laser scanning systems also offer a quantitative measure of the return signal – the *intensity*: a measure of the strength of the backscatter recorded defined by the echo amplitude (Pfeifer & Briese, 2007; Vain *et al.,* 2010). Intensity can be related to laser power, recorded as a sensor-specific digital number (DN), and can provide an insight into the material properties of the reflected surface (Lichti *et al.,* 2002; Lefsky *et al.*, 2002; Mallet & Bretar, 2009). However, it is dependent on many factors (as defined in equation 4.1) including: *target characteristics*, such as the reflectance of the intercepted surface at the lasers wavelength or the 'roughness' of the surface; *atmospheric conditions*, such as weather conditions during an airborne flight campaign; *lidar instrument characteristics*, such as the total power of the transmitted pulse conforming to eye-safety and; *scan geometry*, such as range from target or angle of scan. Due to these factors, calibration of intensity values is commonly performed to allow measurements to be compared.

4.3   Instrument description and data processing

The Salford Advanced Laser Canopy Analyser (SALCA) is the world's first dual-wavelength laser scanning instrument. The sensor was designed at the University of Salford and built by Halo Photonics Ltd as an experimental research TLS instrument to measure forest canopies using pulsed time-of-flight lidar technology (Danson *et al.*, 2014). SALCA's full-waveform capabilities, hemispherical scanning rotation, and high angular sampling resolution mean that it is well-suited to measuring forest environments. The fixed speed of the internal rotational mirror fixes the zenith resolution to 0.06°, however, the angular displacement in azimuth is tuneable to 0.06° (high resolution), 0.12° (medium resolution), and 0.24° (low resolution). The key specifications of the instrument are described in Table 4.1 and the significance of the functionalities is discussed further below.

The two lasers are fired sequentially as the head rotates on two axes, the 1545nm laser is output first followed by the 1063nm. The lasers are intercepted by forest targets and create the 3D point cloud (Figure 4.1) by sampling the full hemisphere over specified ranges of

zenith and azimuth angles defined by the resolutions. The fine beam sizes and low

divergence angle are suited to detecting the small components in forest canopies.

Table 4.1. System characteristics of the SALCA instrument, modified from Danson *et al.,* 2014 ('Description' column added).

SALCA system specifications:		Description
Centre wavelengths	1. 1545.4 nm	Shortwave infrared pulsing laser
	2. 1063.4 nm	Near-infrared pulsing laser
Pulse length	3 ns and 1 ns	Length of time each pulse lasts
Pulse rate	5 kHz	Rate of output: 5000 pulses/second
Beam width at sensor	3.6 mm and 2.4 mm	Diameter of each beam as it exits the instrument
Beam divergence	0.56 mrad	Half angle to describe the increase in beam diameter with distance
Laser output energy	5 μJ and 0.5 μJ	Strength of each laser beam
Detector field of view	5 mrad	Angle over which the detector is sensitive to receiving return energy
Sampling rate	1 GHz	Records data 1 billion times/second
Range resolution	15 cm	Records data in 15cm discrete range bins
Maximum range	105 m	Maximum recordable range of lasers (adjustable)
Azimuth resolution	0.06°/0.12°/0.24°	Variable azimuth resolution defined by operator
Zenith resolution	0.06	Zenith resolution fixed (1.05 mrad)

Figure 4.1. Examples of a 3D point cloud from SALCA at high resolution (0.06° in azimuth and 0.06° in zenith), plotted in 3D (left image) and 2D (right images). Datasets are from the λ1545nm laser and are coloured by raw intensity (white is high intensity, dark grey is low intensity, black is no returns).

Currently, two optical filters are fitted to the instrument, one internally and one externally.

The internal filter is fitted inside the instrument in the path of the 1545nm laser. The

purpose of this filter is to balance the power between the lasers by tuning the stronger

SWIR laser down to an output level closer to the 1063nm laser. The external filter is

attached to the outside of the instrument at the exit point of the lasers. The purpose of the external filter is to reduce the outgoing power of both lasers to reduce saturation of signal. The current filter combination is shown in Table 4.2.

Table 4.2. Current Thorlabs optical filter combination used for the SALCA instrument.

Filter	Description	Transmission 1063nm	Transmission 1545nm	Notes
Internal	NENIR06B Ø25 mm Unmounted NIR Absorptive ND Filter, Optical Density: 0.6	N/A	26.31%	Internal filter has one-way transmission
External	NENIR202B 2" x 2" Unmounted NIR Absorptive ND Filter, Optical Density: 0.2	52.49%	65.71%	External filter has two-way transmission

4.3.1   Dual-wavelength measurements

The application of the dual-wavelength and full-waveform capabilities is now discussed. Figure 4.2 shows a spectral signature for a typical green leaf and bark measured using an ASD spectroradiometer. These reflectance properties in vegetation are governed by the presence of absorbing pigments, water content, and other physical and chemical factors as discussed in Chapter 2.5. At a wavelength of 1063nm green leaf and bark have a similar reflectance whereas at 1545nm bark has a distinctively higher reflectance as it is in the region of water absorption for vegetation (Danson & Bowyer, 2004). These spectral properties provide an opportunity for the separation of foliage from woody material, addressing a significant research gap.
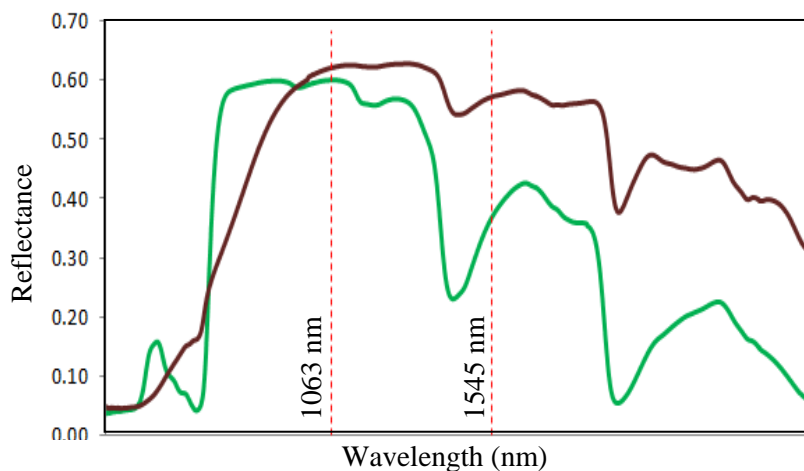
Figure 4.2. Spectral signatures of green leaf (green line) and bark (brown line) from this study, SALCA wavelengths 1063nm and 1545nm shown with dotted lines.

Based on the reflective principles of leaf and woody components in the wavelengths present in SALCA and demonstrated in Gaulton *et al.* (2013) and Danson *et al.* (2014), taking a ratio of the wavelengths at each point should potentially allow separation of these components as well as other applications such as assessing tree health and measuring vegetation moisture content. The ratio can be calculated according to a Normalised Difference Index (NDI) where ρ is the reflectance (Gaulton *et al.*, 2013):

$$NDI = \frac{(\rho 1063 - \rho 1545)}{(\rho 1063 + \rho 1545)} \qquad (4.5)$$

Since the water content of leaves is higher than that of bark, taking ratios in this manner should be sensitive to moisture content and allow a threshold to be applied to classify the point cloud as 'leaf' or 'wood'. Assuming that the beam footprints are fully aligned a ratio would be independent of amount of material within the laser beam, beam incidence angle, illumination conditions, and range.

4.3.2 Full-waveform data recording

Full-waveform lidar systems, such as SALCA, digitise and record the entire backscattered signal of each emitted pulse, and therefore allow the user to determine the range distribution of targets hit by a single laser pulse. Multiple hits occur when the first object in the beams' path only partially fills the beam footprint (such as the edge of a leaf) and the remaining portion of the beam carries on to the next object; this can happen multiple times for each laser pulse. The received signal is recorded as a function of time containing one or more peaks which correspond to interceptions of the laser beam. Full-waveform digitisation provides a greater amount of control and flexibility over the point extraction process, and therefore has the potential to improve measurement reliability (Chauve *et al.,* 2009).

In a forest environment, where there is a highly complex 3D architecture of small structures, the chance of multiple returns is increased. Most commercial systems only record data for a limited number of discrete returns, with the exception of the Riegl VZ400. Having access to the full waveform for each laser pulse may allow improved accuracy for many biophysical measurements such as gap fraction, leaf area index, as well providing an extra level of detail on 3D canopy structure. Multiple returns occur most frequently in the canopy where target elements are small, and around the edge of features, rather than hard solid targets such as stems and branches.

4.3.3 Data description

For each laser pulse, the backscatter is recorded as an 8-bit digital number (0-255) at 15cm intervals and stored as a set of binary files. Each binary file contains 3200 waveforms (number of pulses per azimuth position) for both wavelengths for a given azimuth scan line. In the 'low resolution' mode there are 750 azimuth positions in a full hemisphere scan. The binary files are numbered with the azimuth scan number 0-749. In the 'high resolution' mode there are 3051 azimuth scans, numbered 0-3050. The SALCA instrument contains an onboard 150GB hard drive for data storage. This raw data is then transferred from the instrument and processed according to a set of algorithms written in Matlab$^{©}$, which can be found in the Appendix.

4.3.4 Waveform processing

The waveform of a laser scanner refers to the shape of the backscattered energy against time (Campbell, 2002). By decomposing the waveform into a series of individual echoes, further physical and geometrical properties can be derived for each detected target. Useful surface features that can be extracted from the waveform of a reflected lidar signal include range, roughness, and reflectance. Waveform properties corresponding to these surface features are: time, width and amplitude (Jutzi & Stilla, 2005; Wagner *et al*., 2007). For the SALCA instrument, three primary processing steps were developed in this research, as shown in Figure 4.3 and described below.
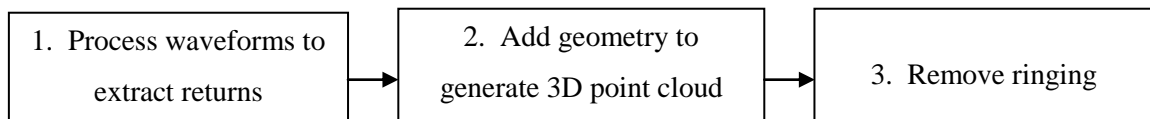
Figure 4.3. Primary processing steps for the SALCA instrument.

4.3.4.1 Processing waveforms

The first stage is to process the raw binary files, decompose the waveform into a set of individual echoes, and extract information on each return (Figure 4.4). First, the binary files are read into Matlab$^{©}$ and split into the two wavelengths: the first 1000 rows in each binary file is the recorded backscatter from the 1545nm laser (150m max range divided by the sampling resolution of 0.15m). The remaining rows are the recorded backscatter from the 1063nm laser, the number of rows for this wavelength is defined by the maximum range set during data acquisition. Second, background instrument noise is removed, leaving only DN above the noise threshold, assumed to be the result of 'valid' returns.

Finally, for data in consecutive range bins, the DN is summed to provide an intensity value for a given return. The range is calculated by weighting each range bin by the DN and dividing by the sum of the DN, and the range of the outgoing pulse is subtracted. This approach is known as the 'centre of gravity' method and has been found to be the optimum data extraction method for SALCA for two primary reasons: it facilitates sub-bin range resolution and has a higher signal to noise ratio, as demonstrated in Hancock *et al*. (2015). The resultant output data generated by this processing step is shown in Table 4.3.
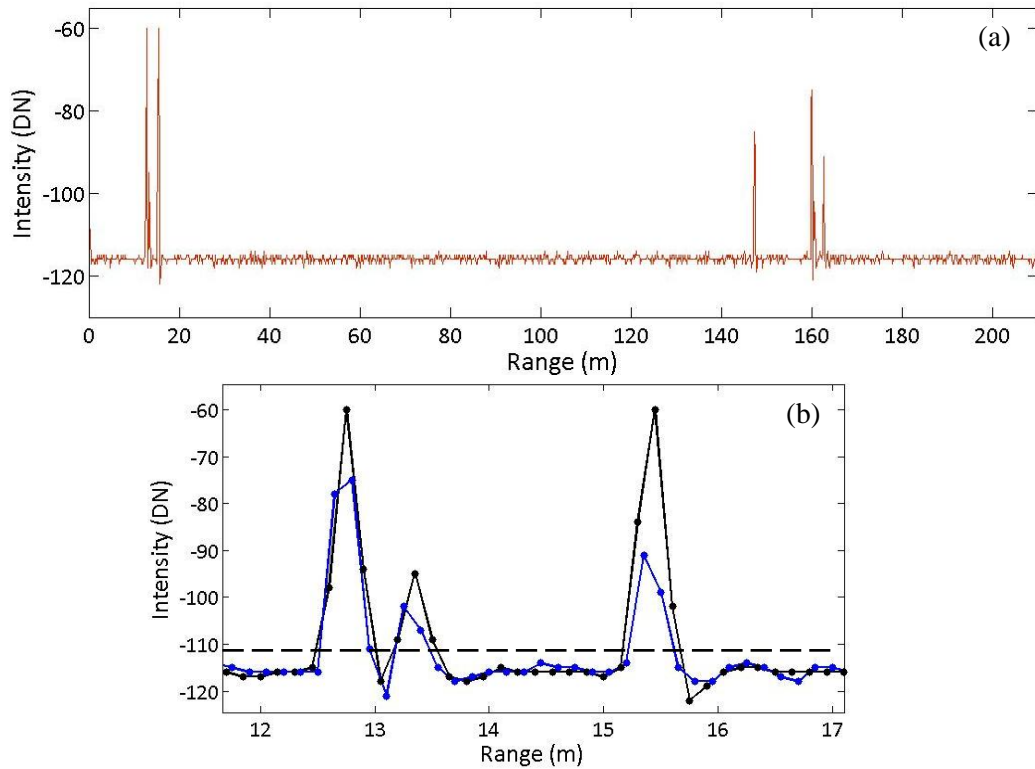
Figure 4.4. Waveform processing, (a) raw SALCA waveform, and (b) 1063nm waveform (blue) and 1545nm waveform (black), dotted line shows location of noise thresholding.

Table 4.3. Output of the first processing stage.

Parameter	Description	Justification
Return number	For each pulse: first return (1), second (2), third (3), etc.	Allows filtering by return number
Intensity (DN)	Digitised signal returned for each return, calculated by centre of gravity method.	Related to target reflectance
Width	Number of range bins for each return	Related to target characteristics
Range (m)	Distance between instrument and target.	Facilitates 3D reconstruction
Azimuth index	Variable according to scanning resolution and start and stop angles defined during data acquisition. Always starts at 0.	Used to calculate geometry
Zenith index	1-3200	Used to calculate geometry

4.3.4.2 Add geometry

The second stage is to calculate and attach geometrical information for each return. Using the azimuth and zenith indices and the range, Cartesian coordinates (x,y,z) are generated along with azimuth and zenith angles (in degrees and in radians). The returns can then be visualised and analysed in 3D using the x,y,z (left-hand image in Figure 4.1) or in 2D using the azimuth and zenith angles or indices (right-hand images in Figure 4.1). Previous experiments with the SALCA instrument revealed that the lasers are not emitted precisely perpendicular to the laser output view direction. As a consequence, a blind region is present directly above the scanner. To reduce the quantity of missing data, the instrument operation was modified to 'over-scan' by 7° in azimuth which fills in some of the missing slice at low elevation angles. The resultant geometry is illustrated in Figure 4.5. Due to this 'squinting' of the laser beams, a new geometry configuration was developed by S. Hancock based on iterative fitting to measured data.
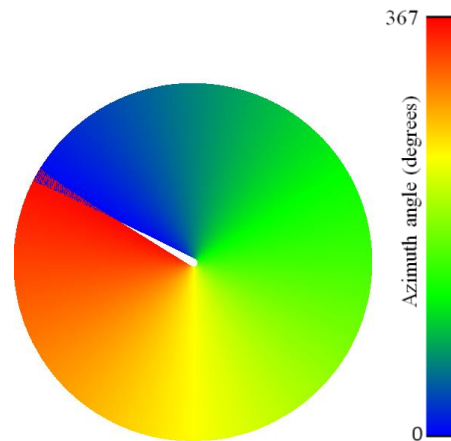
Figure 4.5. 2D (x,y) visualisation of the overhead blind region.

4.3.4.3 Removing ringing

The final stage in the primary SALCA data pre-processing workflow is to remove returns resulting from ringing. Ringing can occur as echoes behind hard solid objects (e.g. tree stem) where the signal oscillates with decreasing amplitude (Hakala *et al*., 2012). These unwanted oscillations can then produce false returns (Figure 4.6). In order to characterise the ringing response in the SALCA instrument returns were extracted from the centre of solid targets that should only have one return. In pulses where a second return occurred (i.e. ringing), the intensity of the first return was noted. First return intensities where ringing occurred ranged from 310DN to 467DN in the 1063nm wavelength and 311DN to

502DN in the 1545nm wavelength (n=30). Therefore, a threshold of 310DN was adopted for both wavelengths where subsequent multiple returns were removed if the first return exceeded the threshold. The method was tested on a number of scans with successful results (Figure 4.6). This approach relies on the assumption that to reach 310DN a return would have to be a solid and/or close range object; therefore, it is highly unlikely to have any subsequent returns. Although this is an adequate approach within the scope of this research it is rather rudimentary which may mean that a small number of valid multiple returns are omitted.
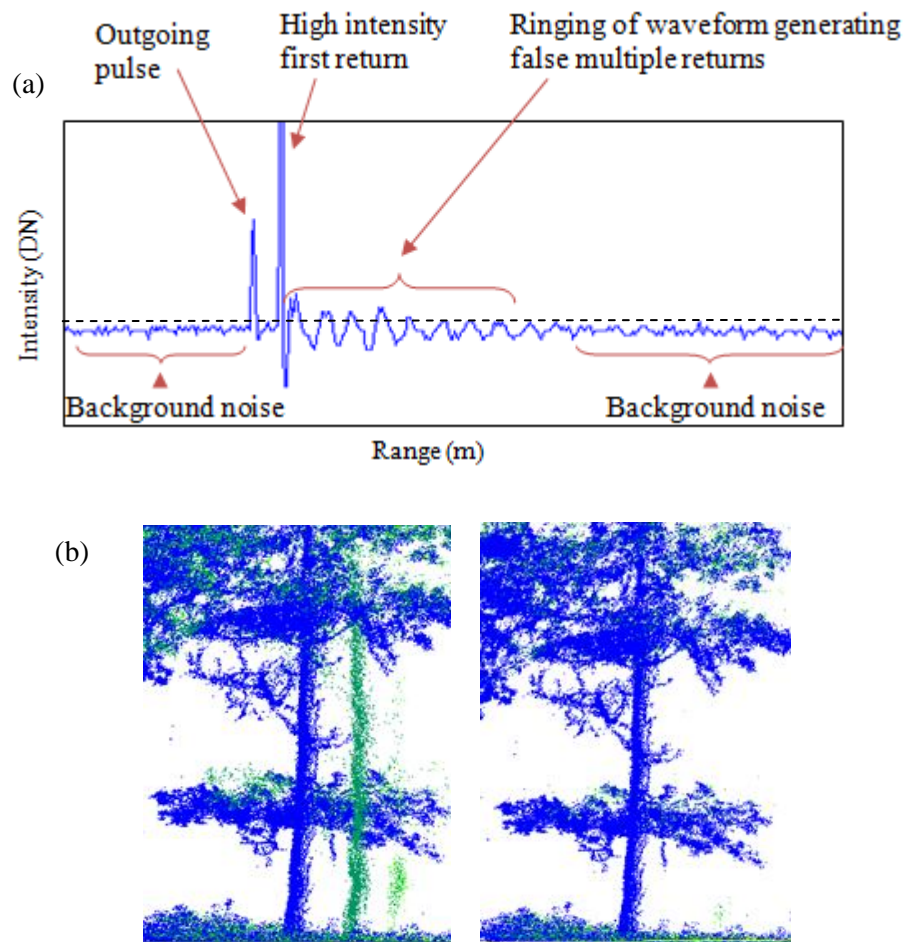
Figure 4.6. (a) shows a ringing waveform. (b) illustrates the ringing removal: Original point cloud (left image) and point cloud after applying ringing algorithm (right image). Blue points represent first returns and green are multiple returns.

4.4 Background to calibration

The accurate correction of SALCA intensity data is a first step required to fulfil all three objectives of this research project. Intensity has been most commonly used to support the visual analysis of a point cloud or to increase accuracy in lidar measurements. Among the

latest advances in laser scanning is the application of intensity data to extract information about the target properties through the interpretation of physical backscattering characteristics (Pfeifer & Briese, 2007; Wagner *et al., 2008*). Therefore, the reliability of the intensity measure and the application of correction methods is increasingly becoming an important area of study to allow for an effective use of this information (Kaasalainen *et al*., 2009). In order to convert raw DN recorded by the instrument into physical units related to target reflectance, it is necessary to apply a radiometric calibration procedure. In remote sensing, this is typically implemented by applying a sequence of corrections to translate the DN into a value proportional or equal to target reflectance, usually with the aid of known external reference targets (Kaasalainen *et al*., 2009; Pfeifer & Briese, 2007) The calibrated output, the *apparent reflectance*, has applications in object classification, change detection, and in point cloud processing algorithms for both airborne laser scanner (ALS) and TLS datasets.

Very few published studies exist on TLS radiometric calibration methods. One of the reasons for this is that the design of commercial laser scanners is often undisclosed by the manufacturers and some systems have proprietary calibration routines that are performed within the system software. As a consequence, uncertainties remain which hinder the interpretation of data from many systems (Pareja *et al.,* 2013) and limit the utilisation of recorded intensity.

4.4.1   Factors requiring correction

Assuming the sensor configuration for a given TLS instrument remains constant, the return intensity of a laser pulse is governed by the range, reflectance properties of the target, incidence angle, and area of beam occupied. Atmospheric effects can also play a part but are only significant over ranges of 100m or more (Wagner *et al*., 2006).

4.4.1.1 Range

The theoretical range-dependence of laser return power can be expressed in terms of $1/R^2$ where R is the range of the target measured, deduced from Equation 4.1. Although this has been shown to be mostly valid for ALS (Höfle & Pfeifer, 2007), the inverse square law does not fully apply for many TLS systems due to detector response and telescope optics. Typically, close to the scanner, the recorded intensity increases with range: a strong deviation from the inverse square law of the lidar equation and an artefact identified for several TLS instruments (Höfle, 2014; Koenig *et al.,* 2013). This can be the result of

system software such as a brightness reducer in the detector for short distances, as is the case for Faro and Leica instruments (Kaasalainen *et al.,* 2011), or the incomplete overlap of the laser beam and detector field of view (FOV) which restricts the amount of energy reaching the detector through the optics (Höfle, 2014). Figure 4.7 is the result of a simulation by Pfeifer *et al.* (2008) and describes the effect of the partly overlapping footprints and illustrates that, depending on the geometrical configuration and the range, the overlap of the beam footprints causes the received energy to increase with range as a larger proportion of the outgoing beam footprint is 'seen' by the detector FOV. For larger ranges received energy starts decreasing as the $1/R^2$ effect becomes dominant.
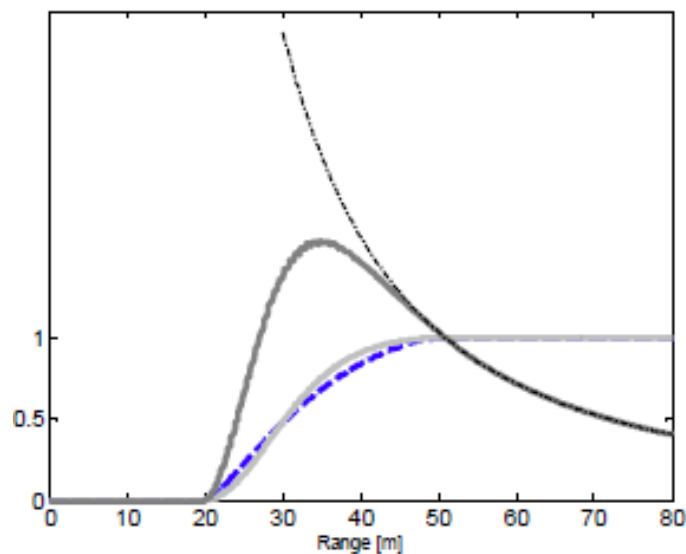
Figure 4.7: Simplified simulation of the effect of partly overlapping footprints. *Dashed* curve shows the portion of the visible footprint in the detector FOV, *solid light grey* line shows portion of footprint energy visible in the detector FOV, *black dash-dot* curve shows theoretical $1/R^2$ decay of received power according to the lidar equation, *dark grey* curve is the combined effect. From Pfeifer *et al*. (2008) pp.1046.

4.4.1.2 Reflectance

The reflectance properties of the target are a significant factor controlling the amount of backscatter returned to the sensor, together with the phase function, which describes reflectance as a function of angle of incidence. Assuming that the target fills the entire footprint of the laser beam and incidence angle remains constant then the recorded intensity should increase as the reflectance of the object increases (Wagner *et al*., 2006).

4.4.1.3 Laser temperature

A third factor to consider is the influence of laser temperature. It is well documented in manufacturer guidelines that many commercial TLS sensors will only function properly

when used within a certain range of external temperatures. Temperatures inside the scanners may be considerably higher than the surrounding atmosphere due to operational activity and external radiation, and this heating of the lasers can influence outgoing (P_t) laser pulse energy. Previous deployment of the SALCA instrument exposed a drop in received power over time from the beginning of a scan, and this has been attributed to an internal thermal effect. In an effort to cool the system, fans were installed within the scanner but a decrease in recorded intensity over time was still observed. The influence of internal temperature of the sensor on intensity has not been openly reported for other TLS systems. However, the dependence of laser power on temperature is well known (e.g. Welford & Mooradian, 1982) and therefore commercial laser scanning companies must account for this effect within their algorithms, although these remain inaccessible due to commercial sensitivity.

4.4.2 Approaches to calibration

There are two broad approaches that can be adopted to perform radiometric calibration of TLS data. The first involves applying a series of corrections based on theoretical laws and relationships in Equation 4.1. These known characteristics of laser devices give the received power as a function of sensor parameters, measurement geometry, and the scattering properties of the target. Wagner *et al.* (2008) demonstrated this approach on full-waveform ALS data collected with the RIEGL LMS-Q560 instrument. However, the complex interaction of the TLS optics and electronics make it difficult to derive an entirely theoretical calibration. This has meant that a second approach to calibration, a data-driven method, has often been preferred (Pfeifer *et al*., 2008). Data-driven approaches fit statistical models to empirically measured data such as using simple or complex non-linear fitting. For instance, Balduzzi *et al*. (2011) corrected TLS intensity from a Faro LS880 with regard to distance and angle of incidence with leaf surfaces. In addition, Kaasalainen *et al*. (2008) describe a calibration procedure using reference targets in both laboratory and field conditions for TLS compared with ALS. Semi-empirical approaches have also been adopted, combining empirical methods to physical principles of lidar systems (Kaasalainen *et al.,* 2011). A calibration model has been developed for the Dual-Wavelength Echidna Lidar (DWEL; Douglas *et al.,* 2014) which combines a function to remove the effects of telescope efficiency with the inverse square law (Li *et al.,* 2015a).

The radiometric properties of the SALCA instrument are characterized by non-linearity in reflectance and temperature response, and a near-field peak in intensity followed by the inverse square form with range. Correcting for these artefacts with a function fitting approach would not be a trivial task. In contrast, neural networks offer an empirical data-driven framework that allow for non-linear relationships between inputs and outputs developed by supervised learning. Artificial neural networks (referred to as 'neural networks') provide a very powerful and flexible computational tool, which can solve complex problems with a high degree of accuracy whilst being relatively quick and easy to implement (Nahar, 2012). The following sections provide background to the neural network approach before describing its implementation.

4.5   Neural networks

Neural networks are adaptive statistical models inspired by the way in which biological nervous systems, such as the brain, process information (Abdi *et al*., 1999). The network structure is typically arranged in layers with interconnected 'nodes'. The raw information is presented to the network through the input layer, which links to one or more hidden layers where the processing is done through a system of weighted connections. The hidden layers then link to an output layer where the output is produced (Nahar, 2012) (Figure 4.8). Supervised learning is used to train the network until a particular input leads to a specific target output by adjusting the connection weights. This functionality allows application to complex systems that are not easily modelled with a closed-form equation such as the radiometric properties of some TLS sensors.
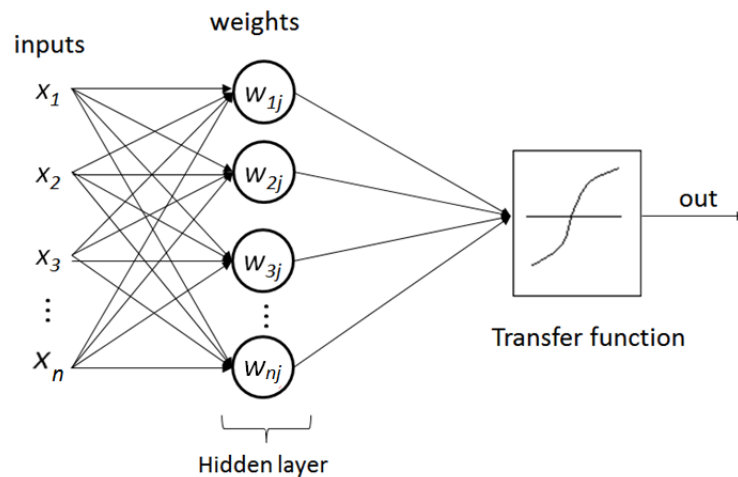
Figure 4.8. Graphical representation of the layer structure of a feed-forward neural network.

One of the most common types of neural network is a *feed-forward* network where the signals are sent forward from input, through the hidden layer(s), and to the output layer. The difference between output and the target are analysed using a back propagation learning algorithm which iteratively improves the fit of the network (Abdi *et al*., 1999). The hidden layers between the input and output and the process of error back propagation allow the network to solve non-linear problems through the implementation of non-linear transfer functions. The ability to learn non-linear relationships between pairs of input and output patters is a significant advantage of this approach (Demuth & Beale, 2002) and allows application to complex systems that are not easily modelled with a closed-form equation. However, a notable disadvantage of neural networks is that they do not have the ability to accurately extrapolate beyond the range of inputs for which they have been trained (Demuth & Beale, 2002).

4.6   SALCA reflectance calibration experiment

This section describes the data collection protocol and implementation of the neural network. This work builds on a reflectance calibration experiment undertaken in July/August 2013 as part of an international TLS instrument inter-comparison experiment with the Terrestrial Laser Scanning International Interest Group (TLSIIG, http//tlsiig.bu.edu).

4.6.1   Field measurements

In order to correct for the effects of range, reflectance, and temperature, outlined above, it is necessary to collect data with which characterise these effects. A homogeneous reflectance target can be used to do this. The calibration panel described in Chapter 3.4.2.2 was mounted on a tripod and imaged at different ranges during the acquisition of full hemisphere high resolution scans at Delamere forest. This was achieved by moving the panel around the scanner as the scan progressed so that it was imaged multiple times at multiple ranges, during each scan. The panel was erected at approximately the same height relative to the scanner and visually aligned perpendicular to the laser output to reduce incidence angle effects. Ambient air temperatures and the laser case temperatures were logged at ten minute intervals throughout the scans.

4.6.2 Information extraction

The raw binary files recorded by the SALCA instrument were processed following the processing workflow described in Section 4.3.4. Each scan was visualised in order to identify the locations of the panels. The returns corresponding to each sub-panel were extracted from the point cloud as shown in Figure 4.9. The intensity values were averaged over each selected sub-panel for both wavelengths. The mean range to the centre line of each panel was also extracted and recorded. Each sub-panel was then attributed an air and laser case temperature value linearly interpolated from the recorded logs, based on the time at which the panel was imaged. A summary of the information extracted is shown in Figure 4.9 which includes: scan number, sub-panel number, upper left and lower right coordinates, measured reflectance of the sub-panel, intensity (mean) and standard deviation, time through the scan the sub-panel appears, range (m), laser case temperature, and air temperatures (°C).
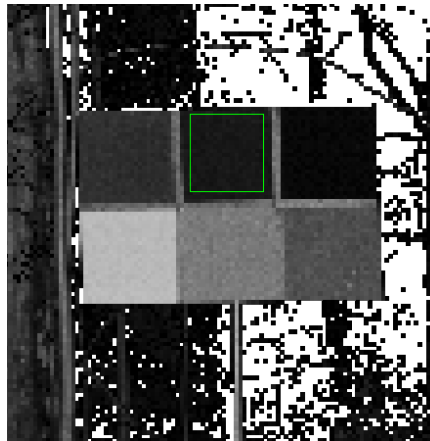
		UL x	UL y	LR x	LR y	1063 ref	1545 ref	1063 i	1063 std	1545 i	1545 std	Time	Range	t1545	t1063	air
3232	1	447	201	464	183	0.0388	0.03926	53.0018	4.4567	94.3585	7.6840	17.1746	10.14	23.1	23.9	13.5
3232	2	424	199	440	182	0.0615	0.0555	93.5895	6.0366	147.1049	9.7121	16.2885	10.14	23.1	23.9	13.5
3232	3	399	197	416	180	0.1108	0.09693	152.0059	8.7259	229.2682	13.6225	15.3648	10.14	23.1	23.9	13.5
3232	4	450	176	466	160	0.1896	0.16404	208.2800	8.7711	285.0201	10.9227	17.2689	10.14	23.1	23.9	13.5
3232	5	428	175	441	159	0.2984	0.26014	267.0245	5.4611	361.2097	7.4523	16.3828	10.14	23.1	23.9	13.5
3232	6	402	173	418	157	0.8923	0.86973	317.5742	4.2085	447.5671	6.3476	15.459	10.14	23.1	23.9	13.5

Figure 4.9. Top Image: SALCA point cloud showing the calibration panel coloured by raw intensity (white is high intensity, and black is low intensity), a green square illustrates the data extraction process for each sub-panel. Bottom image: summary of the information extracted.

The protocol outlined above provides a robust method to acquire data to characterise the range, reflectance, and temperature effects. However, there are two factors which could introduce noise into the data. The first is the incidence angle between the laser pulse and

the surface of the panel and the second is using a single range measurement measured from the centre of each panel. Both of these effects are described in Figure 4.10 which shows that these factors quickly become negligible. For instance, an edge sub-panel at 7.5m range would have a maximum range error of 1cm and maximum incidence angle of 3°.
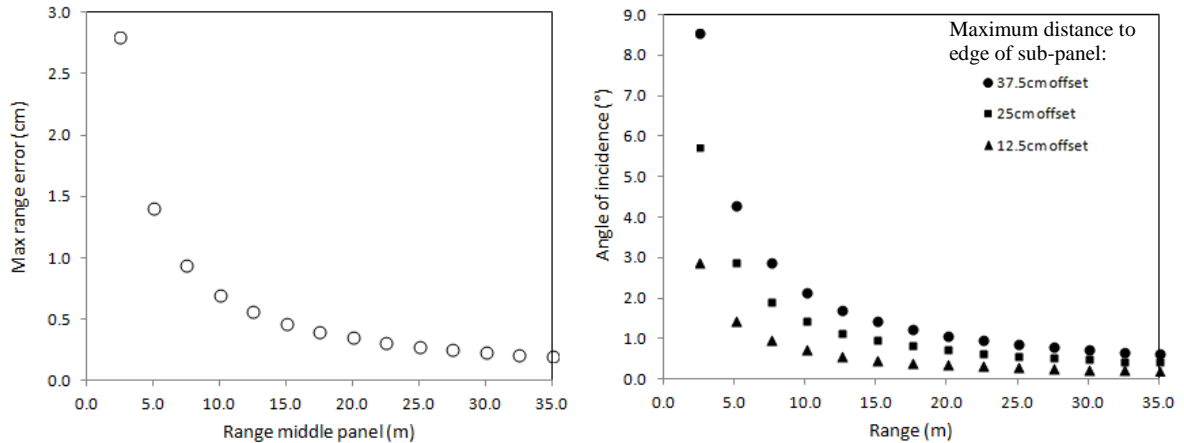
Figure 4.10. Maximum range error (left) and angle of incidence (right) for sub-panel measurements.

To reduce noise and errors in data acquisition there were a number of actions implemented. Care was taken to avoid extracting points too close to the edge of each sub-panel to avoid partial hits or 'mixed pixels' and the point cloud was filtered by range in order to remove any noise in front of the panel. The panel was visually aligned perpendicular with the laser exit point on the SALCA instrument and kept at approximately the same height relative to the scanner. Furthermore, data was not extracted from panels that did not appear rectangular in the point cloud as this would indicate it had spun around in the wind, increasing the incidence angle. The reflectance panel was a flat smooth matte target and therefore Lambertain scattering properties was assumed. Averaging the footprints for each sub-panel meant that the values were more representative of the mean sub-panel reflectance.

4.7 Developing a neural network

The creation, training, and simulation of neural networks in this study were carried out within a Matlab® environment with the Neural Network Toolbox®. There are four key steps in the implementation of a neural network technique: assemble the training data,

create the network object, train the network, and simulate the network response to new inputs. These elements are described below.

4.7.1 Assemble training data

The first step is to collect and format the data to train the network using supervised learning. The *inputs* to the network were (1) mean sub-panel intensity, (2) range, (3) laser case temperature, and (4) air temperature. The *target output* for the network was measured sub-panel reflectance. The training dataset was then randomly divided into three subsets with varying proportions for: Training (70%), to initiate the gradients and adjust the network weights; validation (15%), to minimise over-fitting, and; testing (15%), to test the final network solution (Demuth & Beale, 2002). In total, the resultant dataset contained 868 sub-panel measurements collected over 42 scans, covering the ranges, air temperatures, and laser case temperatures shown in Figure 4.11. The larger number of measurements acquired at 10m was to allow a relationship to be examined between intensity and temperature, and intensity and reflectance, independent of range.

A necessary condition for the good generalisation of the network is that the training data is a sufficiently large and representative sample of the population dataset that it will be used to generalise. Interpolation can often be done reliably within the network, but extrapolation is generally unreliable. Due to the size of the reflectance panels and the dense forest environment it proved challenging to make measurements beyond 32m in range (with limited measurements beyond 25m). In order to have sufficient training data to avoid the need for extrapolation, longer range estimates between 25m and 60m (the maximum range set during data acquisition) were included by an extrapolation of the measured results for each sub-panel. To achieve this, near-range effects were ignored (by excluding points closer than 8m) and a power function was fitted to the observed range-intensity relationship. The resultant equations were then used to estimate expected intensity values between 25m and 60m. This process was repeated for each sub-panel in both wavelengths. Extrapolated data made up a small proportion of the training set (approximately 7%).
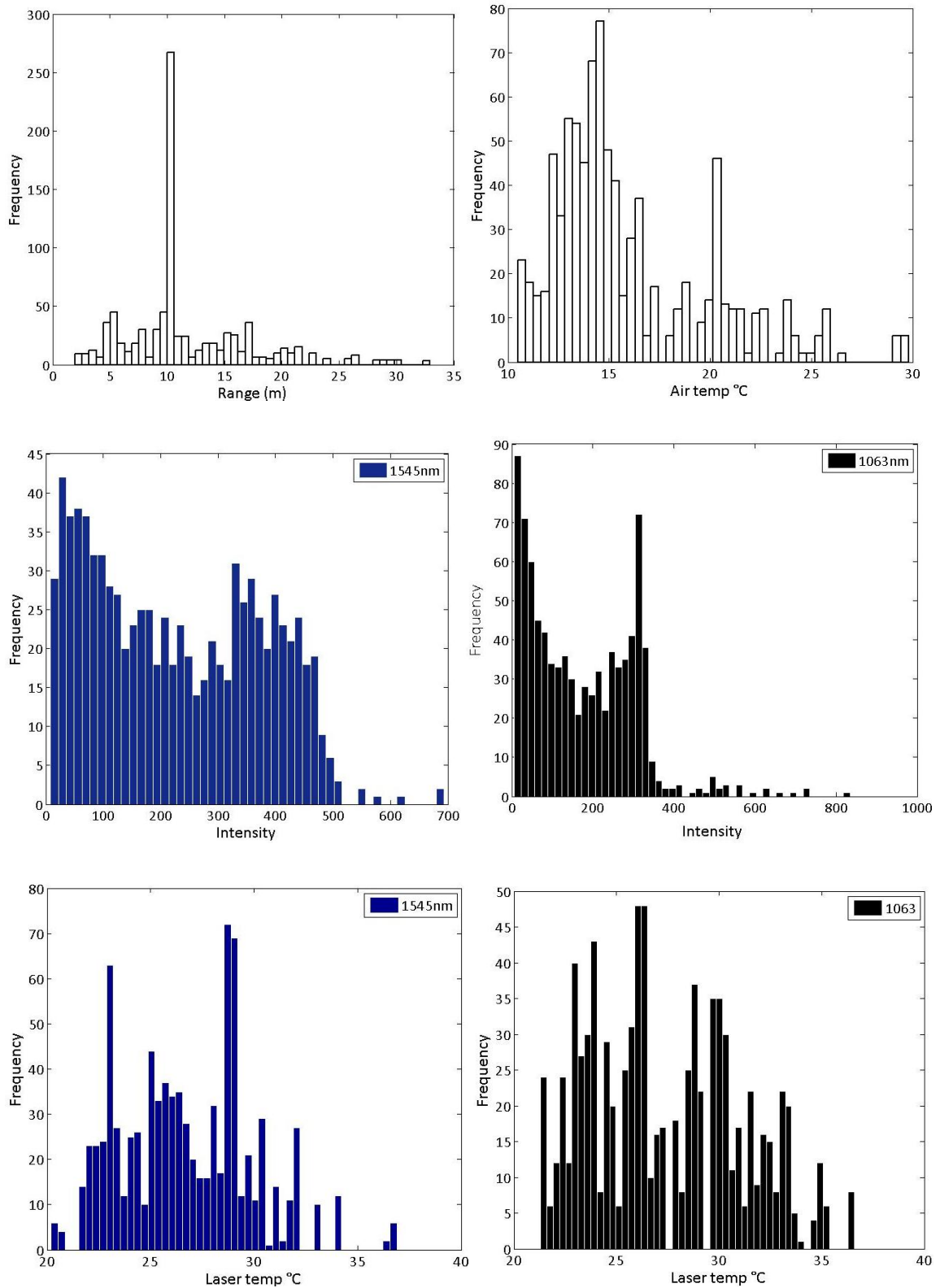
Figure 4.11. Histograms showing the frequency distribution of input training data: range, air temperature, and intensity and laser case temperatures for both wavelengths.

4.7.2 Create network object

The general architecture of a network was created from a set of user-input parameters. The parameters for the initial setup of the neural network is given in Table 4.4, this architecture have been chosen to allow for robust supervised learning, non-linear relationships, and a workable balance between power of network versus computation speed and over-fitting. The lasers were calibrated independently, therefore separate networks were developed.

Table 4.4. Parameters chosen for setup of initial neural networks

Parameter	Input	Justification
Network type	Feed-forward	Allow supervised learning, non-linear relationships, learns by example, very robust (Svozil *et al*., 1997).
Number of neurons	15	Dependent on complexity of problem, will be investigated iteratively to determine the optimum number.
Transfer function	Tan-sigmoid	Non-linear transfer function
Number of hidden layers	6	Balance between increasing power of network vs. computation and over-fitting
Training algorithm	Gradient descent	Default algorithm which is known for its robustness and versatility (Demuth & Beale, 2002)

4.7.3 Train the network and simulate with new data

The training of a neural network is achieved by tuning the values of the weighted connections to optimise the performance (Demuth & Beale, 2002). The default function used to assess the performance of a network is the root mean square error (RMSE), which describes the average squared error between the network outputs and the target outputs. Throughout the training process a training window is updated in Matlab to allow the performance and validation checks to be monitored by the user. The training data is used to train the network until the validation data indicates to stop training (when the RMSE in validation set stops decreasing); the test dataset is an independent dataset which is then used to test the network. A regression plot is created to show the relationship between the outputs of the network and the targets. The network is retrained several times to improve accuracy. Following satisfactory training, testing, and validation, the neural network can be used to calculate a response to new inputs. In order to prepare the full field scans for input to the network each azimuth scan line was attributed a laser case and air temperature

measurement by linear interpolation with extrapolation of the recorded logs (Figure 4.12). The neural network was simulated with the full field scans to produce an apparent reflectance output.
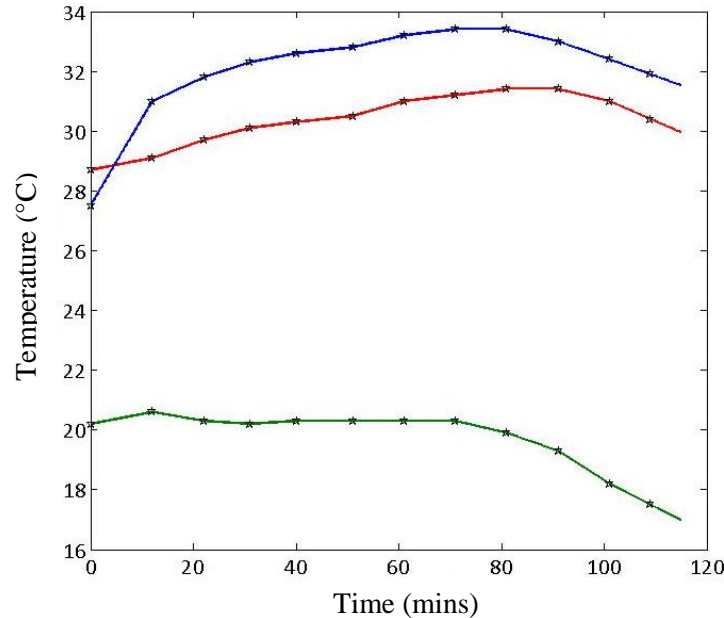
Figure 4.12. Example of linear interpolation with extrapolation of measured air temperature (green line) and laser case temperatures (red line = 1545nm laser, blue line = 1063nm laser). Observed measurements plotted as stars and lines represent linearly interpolated/extrapolated values. A high resolution full hemisphere scan takes 115minutes.

4.7.4 Optimising the network

There are several ways in which a network can be optimised to increase its performance. One problem that occurs when the neural network is trained is over-fitting. This happens when the error on the training set is very low but it has poor generalisation ability to new data. As a result, the development of a successful neural network seeks to balance the power of the network to learn complex problems, but not to over-fit to the training data (Tarrasenko, 1998). Some methods which can be implemented to improve the performance of a network are outlined below.

Inputs: A necessary condition of an effective neural network is that the inputs to the network contain sufficient information on the target, which can be described with a mathematical function relating correct outputs to inputs, with the desired degree of accuracy (Wolpert, 1996). This means that selection of optimal inputs is a crucial first step.

Training algorithm: Many different algorithms exit that can be implemented to train a network, and the optimum one is dependent on the characteristics of the training data and

their relationships with the output. The default algorithm in Matlab$^{©}$ is the gradient descent method which generally works well for most cases (Demuth & Beale, 2002). An alternative is the Bayesian regularisation algorithm which has been shown to improve generalisation capacity (Neal, 1996).

Neurons: Neural networks are sensitive to the number of neurons in the hidden layer. Too few can lead to under-fitting; increasing the number of neurons gives the network more flexibility but can lead to over-fitting.

Each time a neural network is trained the result is different due to different initial weight and bias values, and random divisions of data into training, validation, and test sets. As a result, different neural networks trained on the same problem can lead to different solutions for the same inputs. Neural networks should be retrained several times to ensure that good accuracy has been found. To test the performance of each network simulation the root mean square error (RMSE) of the 'test' dataset was analysed. As discussed previously, the test dataset is an independent subsample of the panel data. The RMSE measures the difference between the targets (measured reflectance of the sub-panel) and the output estimated from the network (apparent reflectance) to give an indication of the magnitude of error in terms of reflectance. For example, an RMSE of 0.05 gives an average error of 5% reflectance. As the RMSE decreases, more confidence can be given to the ability of the neural network to generalise well to new data.

4.8 SALCA radiometric characteristics results

This section describes the radiometric properties of the SALCA instrument, specifically the intensity (DN) response to temperature (ambient air and laser case), range, and reflectance.

4.8.1 Temperature

A negative relationship was observed between the recorded laser temperature and the intensity response of all six sub-panels. Figure 4.13 shows the results of 190 sub-panel measurements at 10m range. A steeper slope for the 1545nm wavelength was evident with a stronger correlation (R^2 values 0.85, 0.87, 0.90, 0.78, 0.84, 0.92, 0.85; second order polynomial) compared with the 1063nm wavelength (R^2 values 0.72, 0.77, 0.82, 0.68, 0.70, 0.65, 0.73; linear fitting).
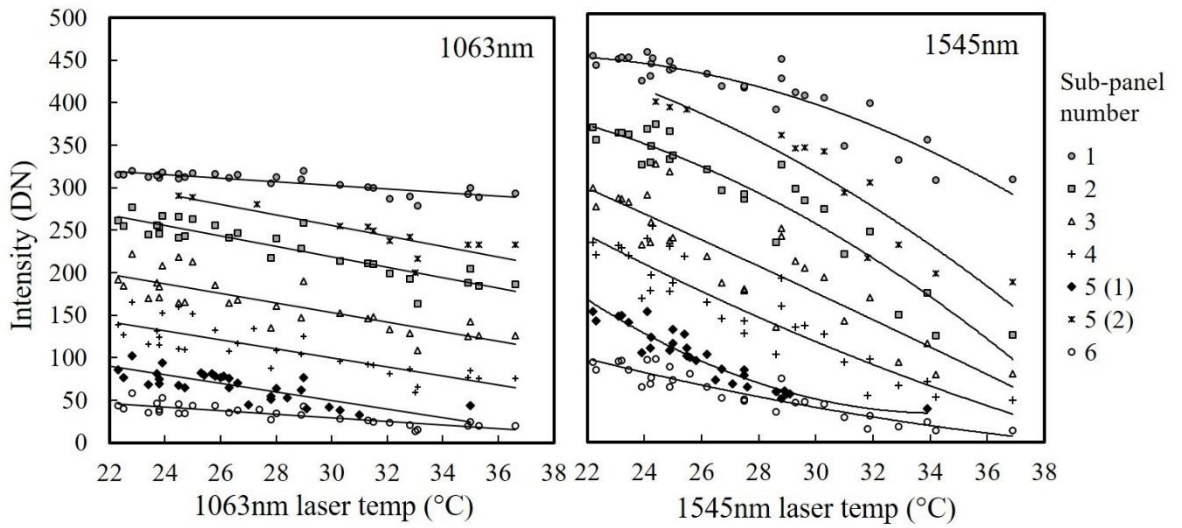
Figure 4.13. Relationship between laser case temperature and intensity for the six sub-panels at a range of 10m for wavelength 1063nm (left) and 1545nm (right). Each sub-panel is represented by a different symbol. The 1063nm wavelength displays a linear trend whereas the 1545nm wavelength was best described with non-linear fitting (2nd order polynomial).

4.8.2   Range

Intensity as a function of range is displayed in Figure 4.14 for both wavelengths showing the results of 122 measurements of sub-panel 3 ($\rho1063$=17%, $\rho1545$=15%). At close ranges, the flattened top is caused by the incomplete overlap of the laser beam and the detector field of view and then the inverse square effect becomes dominant from around 8m. The vertical spread of data at each range can be attributed to the thermal effects described above, which also explains the larger intensity variation in the 1545nm wavelength.
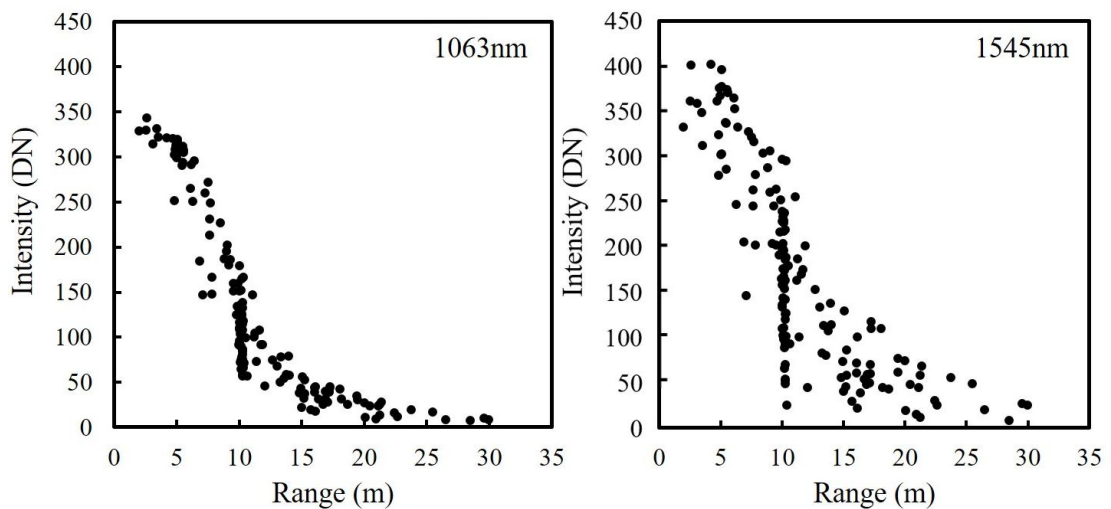
Figure 4.14. SALCA intensity response to range for both wavelengths: 1063nm (left) and 1545nm (right) for sub-panel 3. More frequent measurements were acquired at 10m.

4.8.3   Reflectance

A positive non-linear relationship between intensity and reflectance was observed. Figure 4.15 shows recorded intensity as a function of measured reflectance for one multi-reference panel measurement at two different laser case temperatures. As the laser case temperature increases, the recorded intensity for a given reflectance decreases. Once again, larger intensity variation between the laser case temperatures was seen for the 1545nm wavelength.
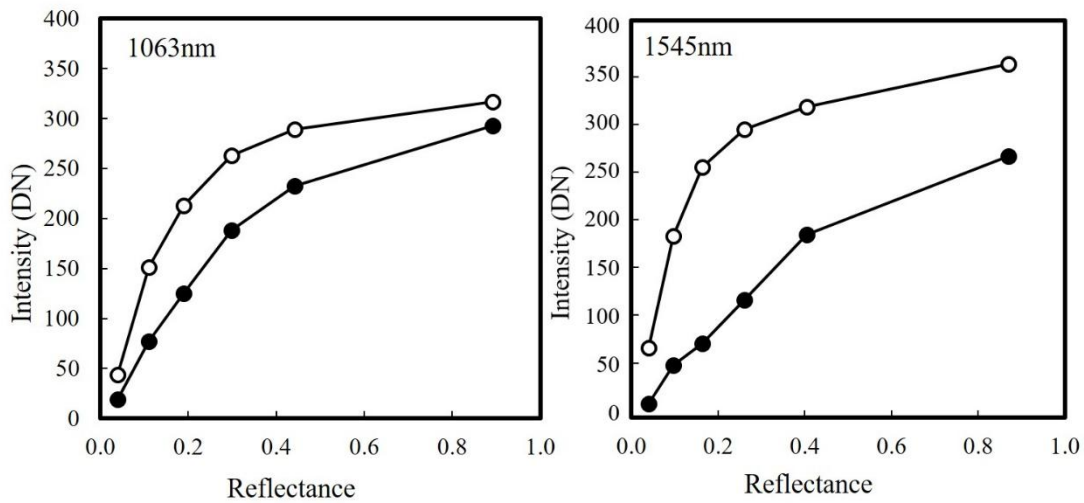
Figure 4.15 SALCA intensity reflectance response for both wavelengths: 1063nm (left) and 1545nm (right) at a range of 10m for the six sub-panels at two laser case temperatures: 21°C (open circles) and 31°C (closed circles).

The results outlined above show that a temperature dependent decrease in P_t is present, and that it is non-linear for the 1545nm wavelength and linear for 1063nm. This, coupled with the non-linear and non-monotonic variation in recorded intensity with range, and an observed non-linear response of the detector, in both wavelengths, makes empirical function fitting not a trivial task. The following section tests a neural network approach to perform the calibration to determine whether acceptable results can be obtained from a simpler alternative.

4.9   Neural networks results

This section outlines how the optimum neural network structure was determined for each wavelength and how they performed with full field scans.

4.9.1 Selecting the optimum network design

The optimisation methods outlined in Section 4.7.4 were implemented in order to select input parameters, training algorithm, and number of neurons to be used. Also the effect of adding the long range extrapolated values is discussed.

4.9.1.1 Input parameters

To identify the optimum network inputs for training, networks were developed under three scenarios of inputs: (A) intensity and range, (B) intensity, range, and laser case temperature, and (C) intensity, range, laser case temperature, and air temperature. Ten simulations were run under each scenario and the mean RMSE of the test dataset analysed (Table 4.5). Apart from the inputs, the rest of the network structure was as described in Table 4.4.

Table 4.5. Results of ten simulations under three scenarios. Mean RMSE shown for each wavelength with standard deviation.

Network inputs	1063nm Mean RMSE (SD)	1545nm Mean RMSE (SD)
A: Intensity, range	0.1011 (0.0117)	0.1269 (0.0195)
B: Intensity, range, laser case temperature	0.0797 (0.0072)	0.0767 (0.0047)
C: Intensity, range, laser case temperature, air temperature	0.0820 (0.0099)	0.0818 (0.0064)

Condition B showed the lowest average RMSE and the least variability (lowest standard deviation) indicating that these inputs generated a more stable network and the most successful generalisation. Therefore, intensity, range, and laser case temperatures were used as inputs for the networks for both wavelengths.

4.9.1.2 Training algorithm

Ten simulations were run using a Bayesian regularisation training algorithm which resulted in an average RMSE of 0.0802 (stdev = 0.0054) for the 1545nm wavelength and 0.0850 (stdev = 0.0064) for the 1063nm wavelength. These RMSE values were slightly less favourable than using the gradient descent method (Table 4.5) suggesting that the gradient descent algorithm generalised better in this case. Furthermore, the resultant frequency distributions of calibrated full field scans were very similar (Figure 4.16) indicating that the training algorithm did not have a great impact on the output. As a result, gradient descent was chosen as the training algorithm.
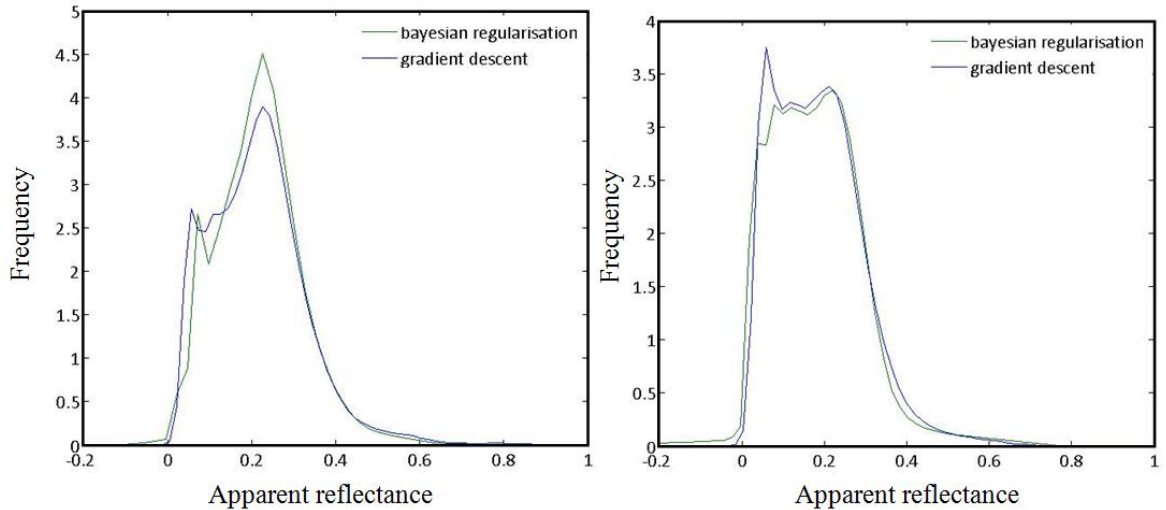
Figure 4.16. Frequency distribution (smoothed kernel density) of apparent reflectance output for a full field scan. Example of simulations run using two different training algorithms on the 1063nm wavelength (left) and the 1545nm wavelength (right).

4.9.1.3 Number of neurons

Figure 4.17 shows the RMSE of the test datasets with increasing number of neurons. These results illustrate that too few neurons in a network can lead to an unstable output, that is, the network does not have sufficient power to learn the complex patterns required. Fifteen neuron networks were chosen as the optimum value due to the stability and repeatability of the network output with multiple simulations. This suggests that despite the varying RMSE values (explained by the random division of sub-panels into the test dataset), the networks produce a consistent generalisation to a full field scan.

4.9.1.4 Extrapolating long ranges

Figure 4.18 demonstrates the inability of neural networks to extrapolate to new values outside the range of the training dataset. The images on the left show an output of the network before any longer range estimates were added to the training set. There is a clear range effect that becomes apparent after approximately 25m. The images on the right of the figure show an output of the network after longer range estimates had been manually extrapolated from the range-intensity relationship and added to the training set, in which the range effect has been removed. In addition, the field scans will be restricted to the plot radius defined in Chapter 3 in the remaining work described here.
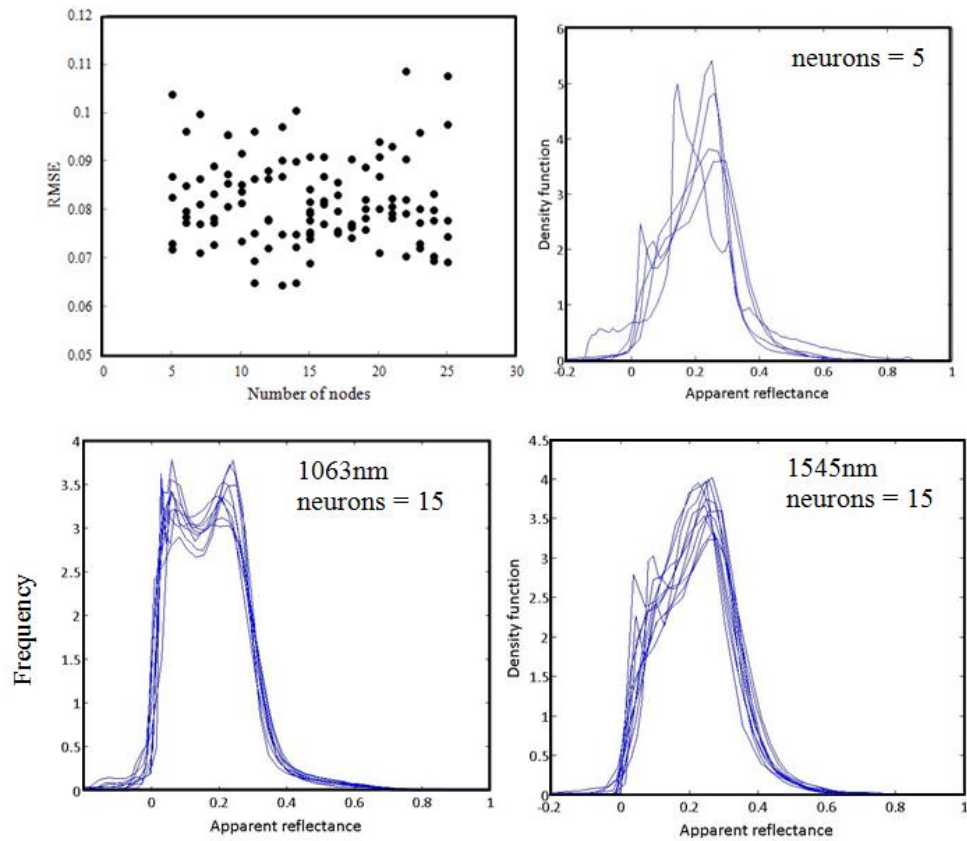
Figure 4.17. Effect of the number of neurons on RMSE of the test dataset. Top left: result of 5 simulations using different numbers of neurons (nodes) for 1063nm wavelength. Top right: impact of having too few neurons leading to an unstable network design. Bottom graphs: result of ten simulations with 15 neurons for the 1063nm (left) and 1545nm (right).
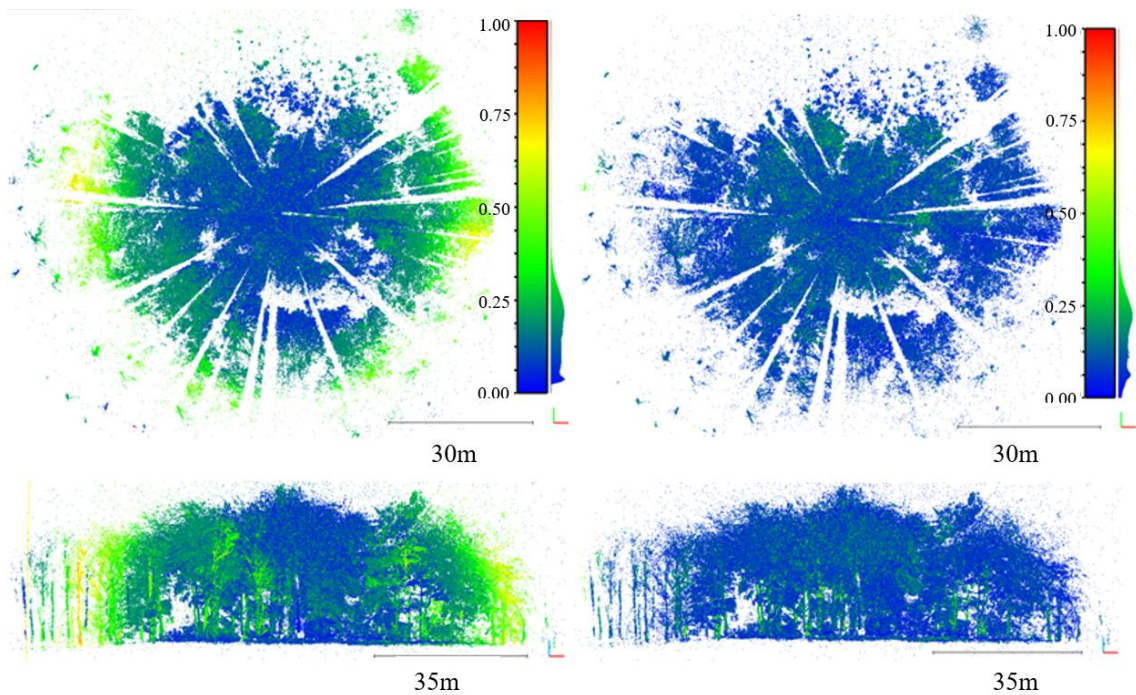
Figure 4.18. Impact of introducing long range estimates into training of the network. Top images display 3D forest point cloud from above, bottom images display a lateral view.

4.9.1.5 Final networks

The final network architecture for both wavelengths is shown in Figure 4.19. Ten simulations were run using the defined network properties and the network which resulted in the lowest RMSE for the test dataset was selected for both wavelengths. The final networks had an average error of 7.2% reflectance for the 1063nm wavelength (RMSE=0.0721) and 6.9% reflectance for the 1545nm wavelength (RMSE=0.0691).
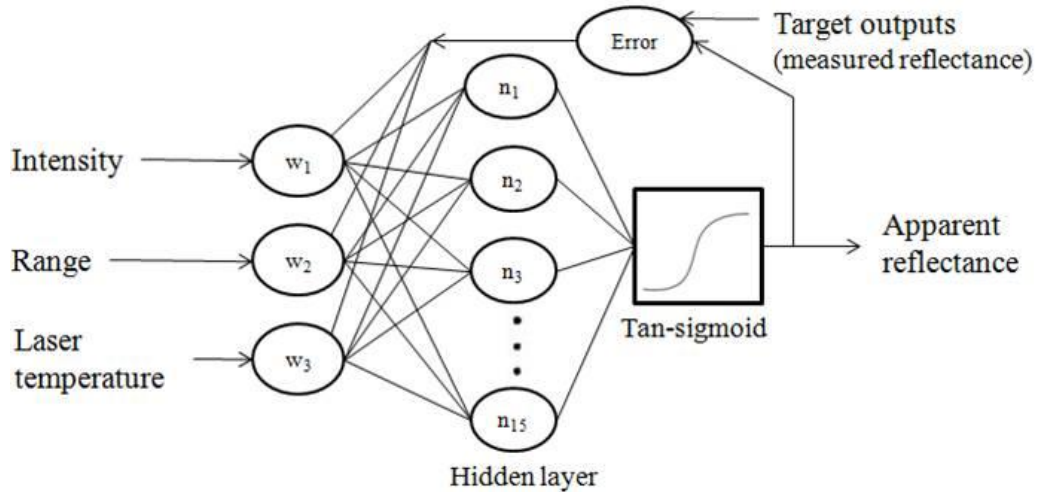
Figure 4.19. Architecture of the neural network selected for both wavelengths.

4.10   Calibrated forest plots

The final stage to assess the performance of the established network was to investigate the apparent reflectance output in the context of the forest environment, rather than just assessing the panel data. Figure 4.20 shows apparent reflectance characteristics using a scan acquired on 31st July 2014 at Plot 1 (oak plot), Delamere Forest. The top images in Figure 4.20a and b, show a section of the forest point cloud before and after calibration, where the trees display a range effect in the intensity image (nearer stems have a higher intensity than those further away), in the calibrated image they appear more uniform in reflectance. The calibrated full forest scan for both wavelengths can also be seen in Figure 4.20, along with histograms showing that the frequency distribution of apparent reflectance values are as expected (majority of the values between 0-100% reflectance).

(a)

Intensity (DN)

1063nm

Apparent reflectance (%)

(b)
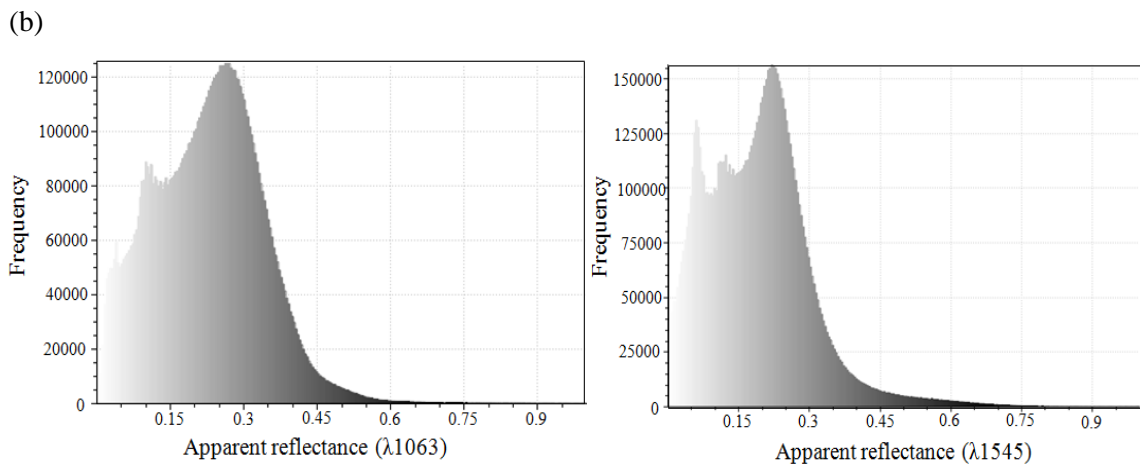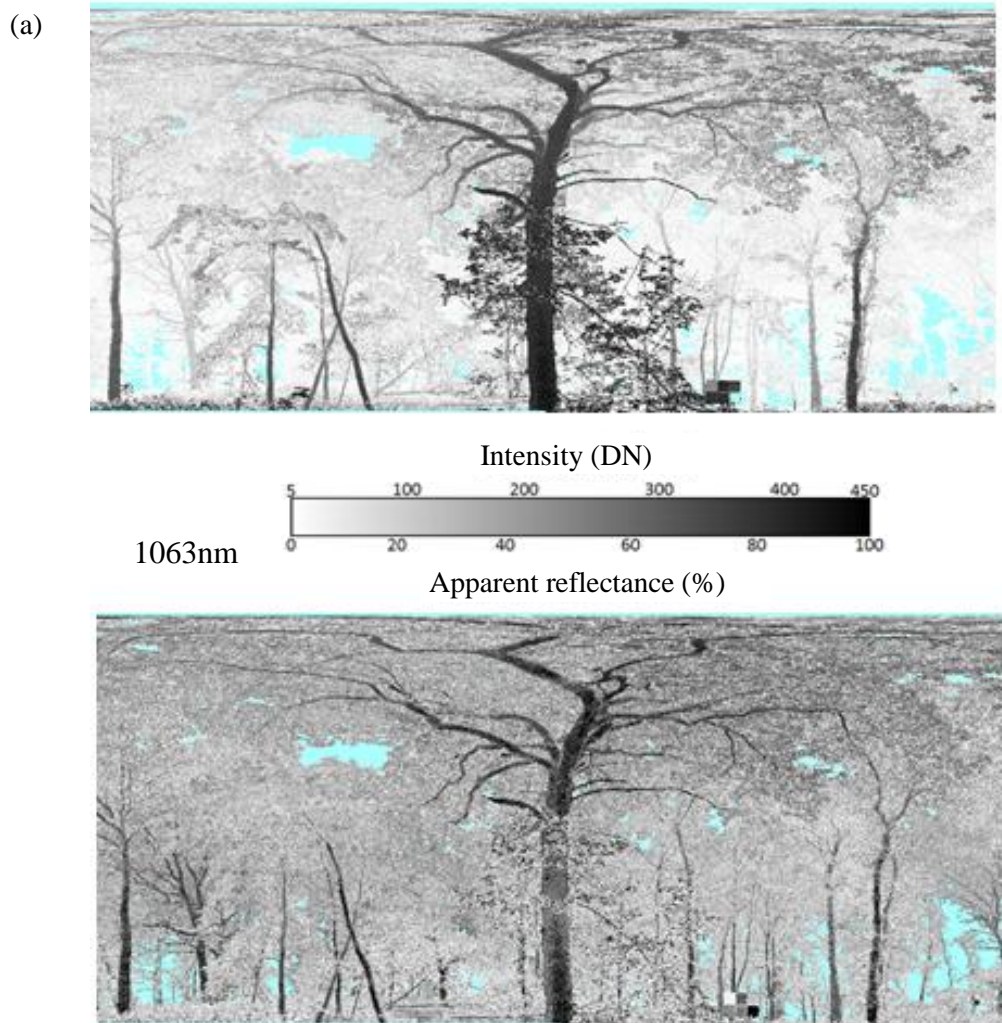
Figure 4.20. Point clouds plotting by azimuth and elevation angles before (intensity) and after (apparent reflectance) calibration for 1063nm wavelength (a) and 1545nm (c). Histograms show the frequency distribution of apparent reflectance values in both wavelengths (b). [Continued on following page].

84

(c)
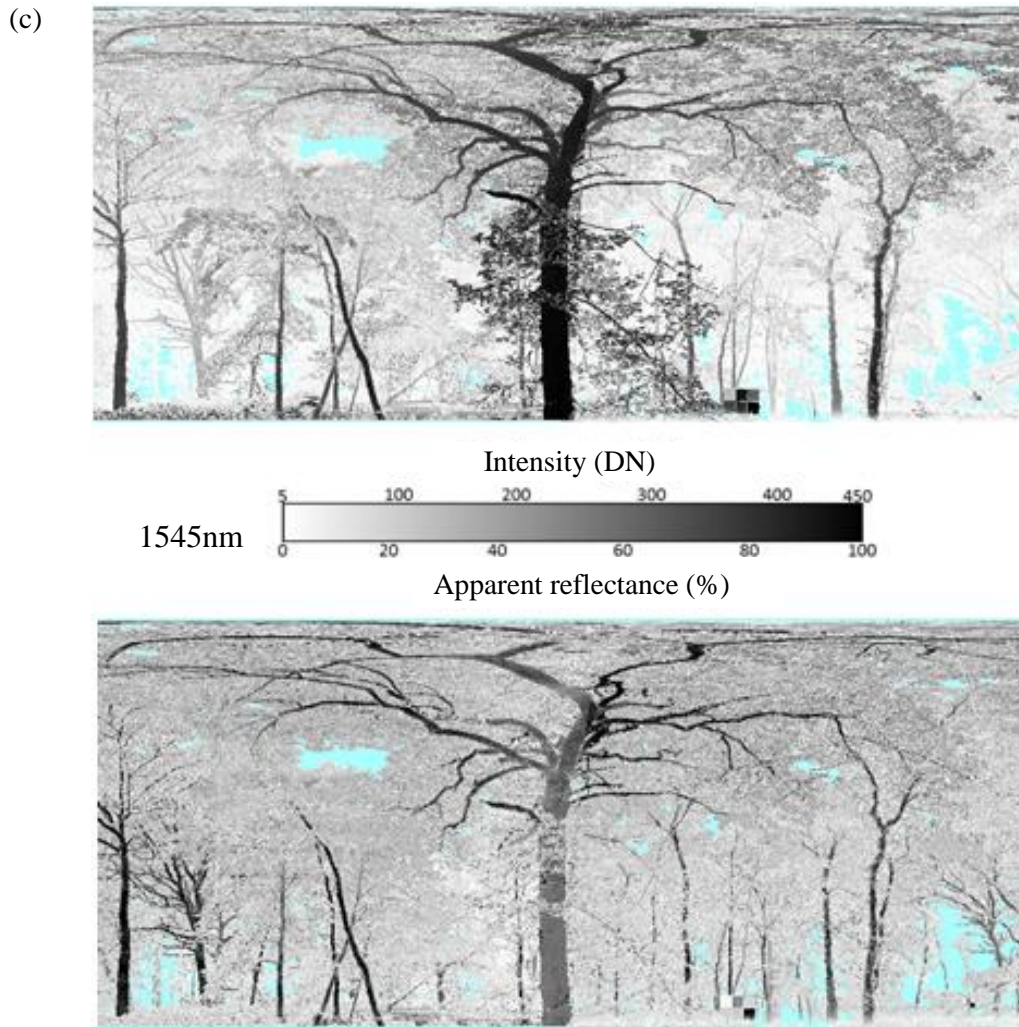
Figure 4.20. Continued.

4.10.1 Reflectance outside 0-1

A small number of the apparent reflectance values estimated from the neural network lay outside of 0 to 1 reflectance, which indicates that the network has not performed well as this is outside the possible range of reflectance values. The location and quantities of these anomalies are shown in Figure 4.21 and Table 4.6.

Visual interpretation of the forest point clouds in Figure 4.21 indicated that the unexpected reflectance estimates occur almost entirely in the leafy part of the canopy rather than stems or branches. The most obvious explanation is that the data points displayed inputs outside the range of training data. The three inputs (intensity, range, laser case temperature) for

these subsets were plotted and compared to the training inputs (Figure 4.10) and the results are discussed below.
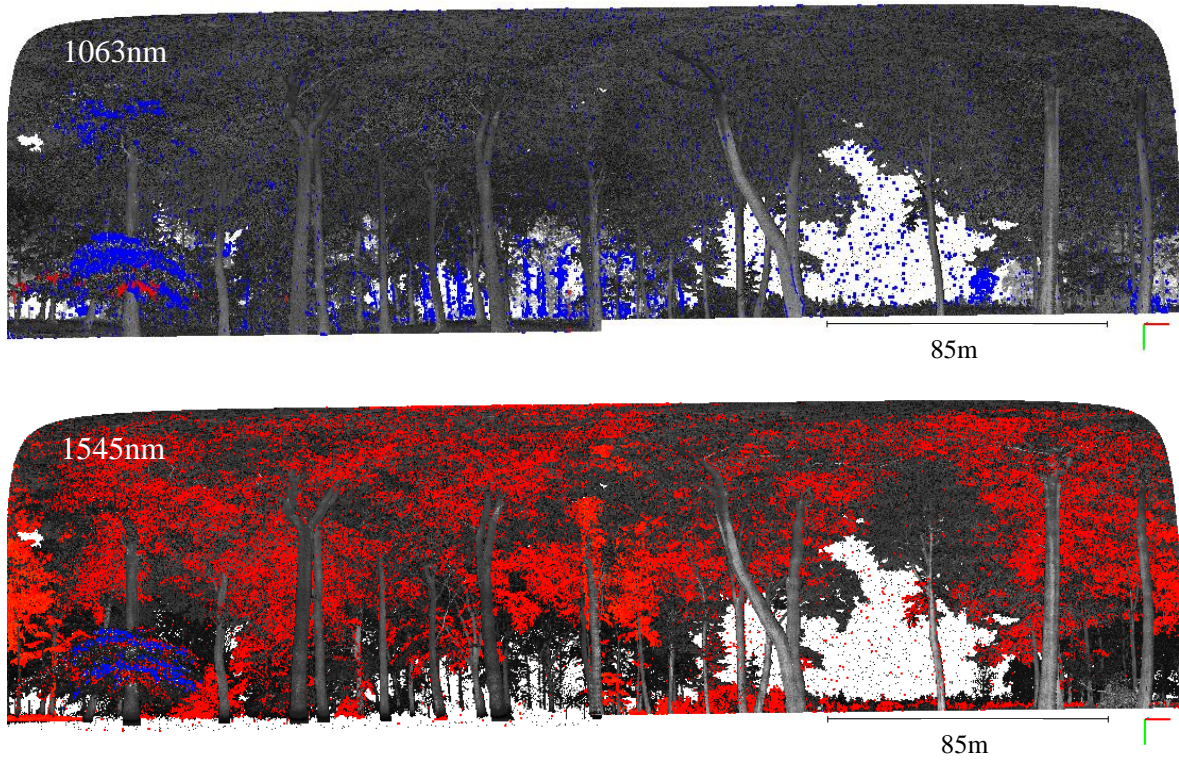
Figure 4.21. Location of returns with estimated reflectance values below 0% (shown in red) and above 100% (shown in blue) for both wavelengths: 1063nm top and 1545nm bottom image. Note the point size is increased for the highlighted points for clarity. The table describes the proportion of these occurrences in the full point cloud.

Table 4.6. The proportion of returns calibrated to outside 0-100% for both wavelengths

Wavelength	Number of returns with estimated **reflectance <0** (as a % of the full scan)	Number of returns with estimated **reflectance >1** (as a % of the full scan)
1063nm	327 (<0.01%)	12140 (0.13%)
1545nm	147655 (1.53%)	873 (0.09%)

1063nm wavelength: For the returns with an apparent reflectance less than zero the intensities were within the range of the training data. However, the returns were at very close range (between 0.8 and 4.5m) and very low laser case temperatures (19.2-20.5°C) where there was limited training data. For the returns with an apparent reflectance value greater than 100% the intensities were very low and high (<30DN and >340DN), close and far range (<10m and >42m), and low laser temperatures (19.3-20.8°C).

1545nm wavelength: The returns with an apparent reflectance less than zero had very low intensities (96% <10DN) which is only just above the noise threshold, whereas those with an apparent reflectance greater than 100% had very high intensities (>500DN) and at close range (>7m).

These results indicate that the neural network is not generalising well to inputs beyond the range (or where there are limited data) of the training dataset, as expected. However, the number of returns affected is less than 0.14% for the 1063nm wavelength and 1.62% of the full forest scan. It is expected that the proportion of affected returns in the 1545nm wavelength is higher because this wavelength displays more variation with temperature.

4.10.2 Stability of reflectance estimates

The results above indicate that a generally successful neural network has been determined for each wavelength considering the radiometric complexities requiring correction. However, in order to assess the reliability of the network two calibrated forest scans which were acquired on consecutive days in leaf-off conditions were compared. Figure 4.22 shows that the neural network produces a stable output in both wavelengths. These results increase confidence in the network and mean that changes that are seen between scans are more likely to be the result of ecological changes in the forest rather than variances in the calibrated output.
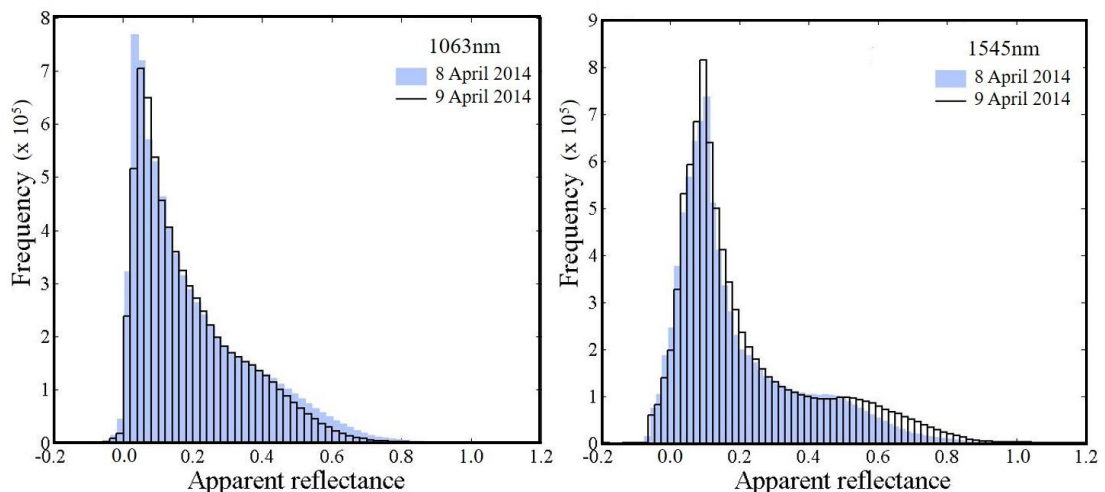
Figure 4.22. Frequency distribution of two calibrated scans acquired on consecutive days (8th-9th April) in Plot 1 for the 1063nm wavelength (left) and the 1545nm wavelength (right). Very similar distributions indicate a similar output and therefore a stable network.

4.11   Conclusion

This work has demonstrated the potential of neural networks for providing a radiometric calibration of raw intensities from a novel TLS sensor to realistic values of apparent reflectance, successfully accounting for the complexities of TLS intensity response. The main limitation to this approach is that neural networks do not extrapolate very well outside the range of training inputs, therefore this hinders the performance of the network if the training dataset does not span the full intensity, range, and temperature variation of the full field scans, as demonstrated in this chapter. The final networks had an average reflectance error of 7.2% and 6.9% for the 1063nm and 1545nm wavelengths respectively. To improve these results, and increase the networks accuracy to new data, more data should be included in the training stage of the neural network development, particularly around the limits of the current dataset (close and far ranges, reflectance between 45% and 80%, and high and low laser case temperatures).

The neural networks developed in this chapter will be applied to all the forest scans, acquired at both Alice Holt and Delamere Forest, to provide estimates of apparent reflectance. These results will then form the basis of analyses in the next chapter to investigate whether returns resulting from leaf material can be separated from those resulting from woody material based on spectral properties. This, as well as other spatial and temporal forest properties will be the focus of subsequent chapters.

CHAPTER 5

Separating foliage and wood in oak trees with dual-wavelength TLS

5.1   Introduction

The aim of this chapter is to test a range of methods for separating leaves and wood in TLS scans of oak trees, and relates to research Objective 2. The data analysed in this chapter was collected during the Alice Holt data collection campaign where a set of TLS scans was acquired in leaf-off and leaf-on conditions along with direct destructive sampling, and spectral measurements, of three oak trees, referred to as tree 01 (large oak), tree 02 (medium oak) and tree 03 (small oak). The chapter has four principle sections (Figure 5.1) and will commence by examining the interactions between dual-wavelength full-waveform laser pulses and a broad-leaved deciduous oak woodland. The individual trees of interest will then be extracted from the full scan and the returns examined using corresponding leaf-on and leaf-off scans. The measured leaf and wood reflectance is considered and the results of the destructive field measurements presented. Next, current methods of separating leaf and wood material in TLS are discussed before implementing three approaches: (1) number of returns based approach based on subtracting leaf-off returns from leaf-on returns, (2) applying a simple threshold on apparent reflectance values for the 1545nm wavelength, and (3) applying a threshold on a ratio of apparent reflectance between the wavelengths.
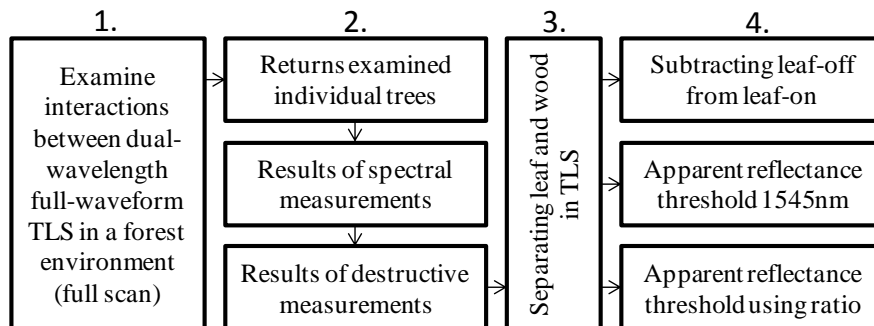
Figure 5.1: Overview of Chapter 5.

5.2 Description of full-waveform dual-waveform TLS data in a forest environment

This section provides a description of the full-waveform dual-wavelength data recorded by the SALCA instrument. The raw data files were processed according to the method outlined in section 4.3.4 in order to decompose the full-waveform into a series of discrete echoes, representing hits on vegetation, for both wavelengths. Geometry was attached to each return, and returns resulting from ringing were removed. This processing chain resulted in two data files: one containing returns from the 1063nm wavelength, and the other containing returns from the 1545nm wavelength (expressed as $\lambda 1063$ and $\lambda 1545$ hereafter). Each dataset was calibrated to apparent reflectance using the neural networks developed in Chapter 4. The datasets examined in this section were acquired on 14th July 2014 (full-leaf conditions) at Alice Holt forest for Tree 01 (the largest oak tree) from the South scanning position, using low resolution (0.24° in azimuth and 0.06° in zenith). The main characteristics of the returns for both wavelengths in a forest environment are now discussed.

A total of 2,467,200 pulses are emitted from each laser during a low resolution full hemisphere scan. Around three million returns were recorded from each laser: 3,030,304 ($\lambda 1063$) and 2,994,333 ($\lambda 1545$). The ability to record data along the entire length of each pulse allows multiple partial hits along each beam to be extracted and therefore the number of returns may exceed the number of pulses emitted, as in this case. Although the lasers follow the same optical path and therefore sample the environment with the same geometry, a marginal difference in the number of returns from each laser can occur. There are numerous reasons for this, including: the return signal not high enough to exceed the noise threshold (due to reflectance of target at particular wavelength, for instance), invalid returns (such as noise or ringing) in one of the lasers which has not been removed during processing, or the difference in output power of the lasers. For this dataset, the 1063nm wavelength had 1.0% more recorded returns than the 1545nm wavelength.

5.2.1 Range distribution

The frequency distribution of range of all returns is shown in Figure 5.2. As expected, the distribution is very similar between wavelengths and decreases with range. A large frequency peak is present at close range (between approximately 3m and 8m) where the majority of returns occur; this is caused by understorey and low branches in close

proximity to the scanner. There is a further peak between 15m and 20m which represents the canopy. There are very few returns beyond 40m up to 60m, the maximum range set during data acquisition. This can be explained by three factors: the laser beams exiting the top of the canopy, vegetation blocking the laser beams from reaching further into the forest (occlusion), and low intensity returns that are 'lost' in noise. In general, the frequency distribution of range will be influenced by vertical vegetation structure (ground, understorey and canopy layers), lateral vegetation characteristics (tree spacing and density of plant material in each layer), and sensor and processing specifications (signal to noise ratio, maximum range of lasers).
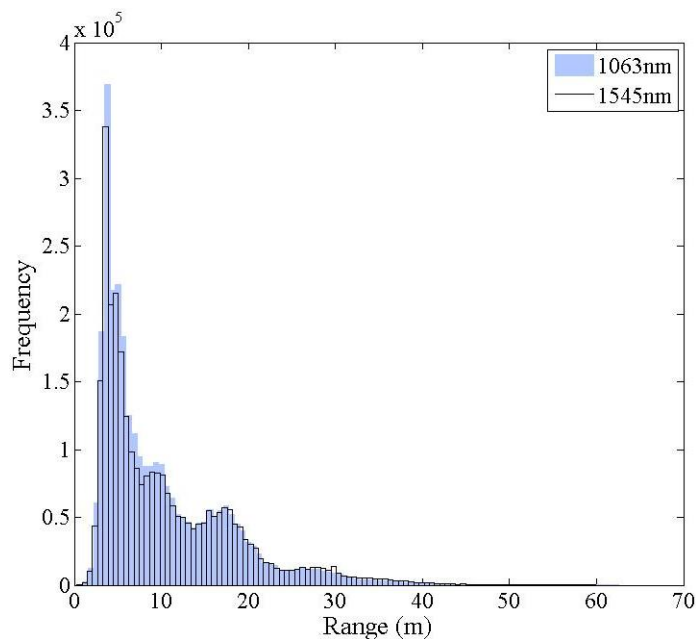
Figure 5.2. Frequency distribution of range in metres for both wavelengths.

5.2.2 Multiple return analysis

The proportion and spatial distribution of multiple returns in the forest plot are illustrated in Figure 5.3. The large tree visible in the centre right of the top images is Tree 01 viewed from the South. Around 75% of returns in the dataset are generated from the first interaction between each laser beam and an object in the forest. If the object only partially occupied the footprint of the beam the remaining energy not intercepted continues on through the stand, to either exit the forest (around 55% of laser beams in this dataset) or hit a second object (around 20% of laser beams). This can occur multiple times for each laser pulse in a forest environment, with a maximum of seven ($\lambda 1063$) and eight ($\lambda 1545$) returns recorded, which occurred in around 0.1% of laser beams for this dataset.
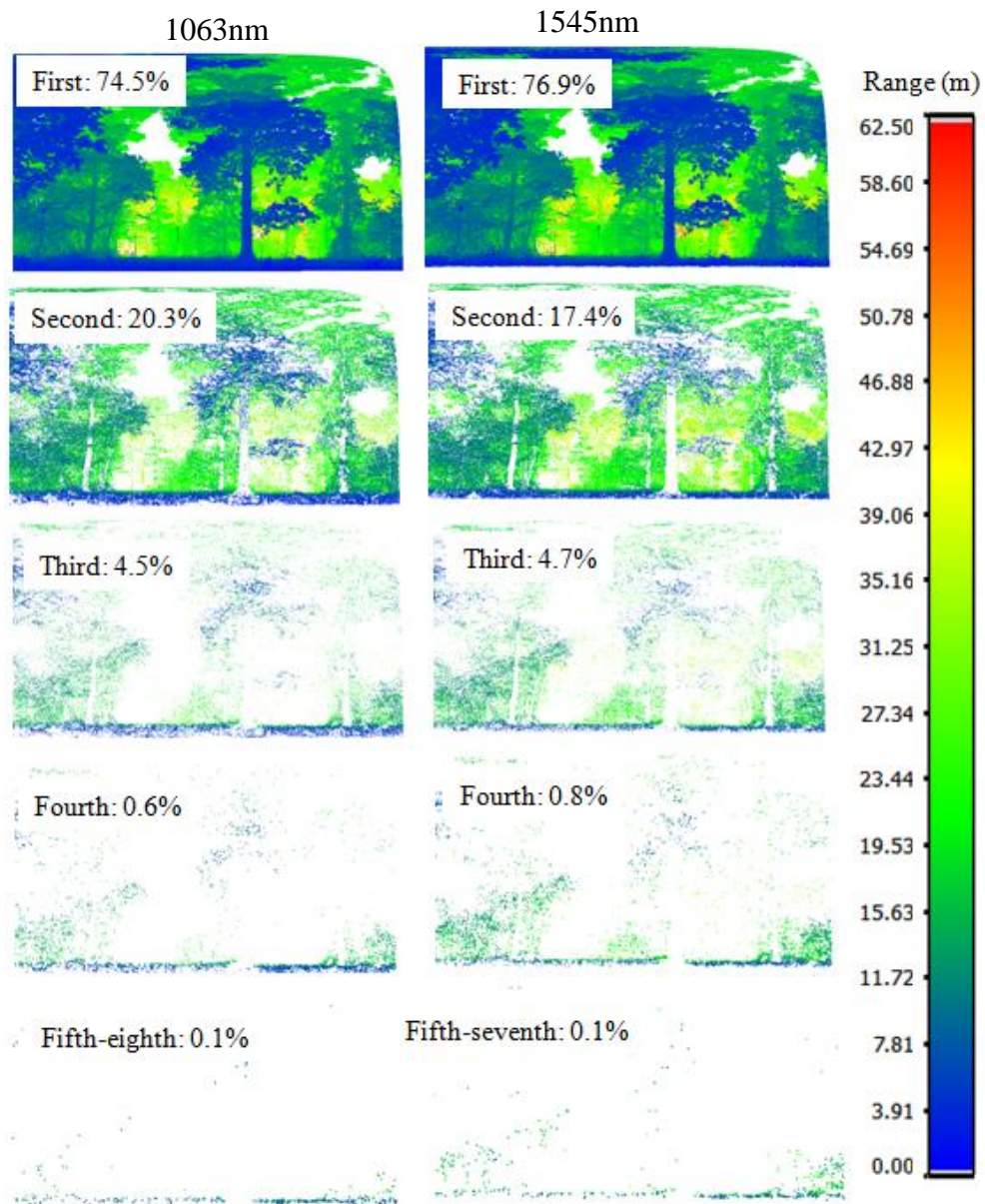
Figure 5.3: Distribution and proportion of return order in both wavelengths. The returns are plotted in 2D by azimuth and elevation angles and coloured by range according to the colourbar on the right. The points in the last 4 plots have been enlarged for clarity. Fifth, sixth, seventh (and eighth for 1545nm wavelength) returns have been plotted together due to very low frequency.

Multiple returns (two or more partial hits) occur mainly in areas of 'soft' targets and along the edges of 'hard' targets. Soft targets such as leafy material in tree canopy or ground vegetation (grass in this case) are collections of many small scattering elements that are heterogeneous in reflectivity, spatial orientation, and distribution. Hard targets such as trunks and branches are generally larger than the footprint, continuous, and opaque (Clawges *et al.,* 2007). These results suggest that commercial TLS sensors which are

deployed in first return mode in a forest would omit around 25% of recordable information.

5.2.3   Intensity distribution

Figure 5.4 shows the frequency distribution of all intensities in both wavelengths. The large frequency peaks at very low intensities result from low reflectance targets at the particular wavelength, targets at very long range, or partial hits (where only a portion of the laser footprint samples the surface). There is a peak in the number of returns with an intensity value between 300 and 400DN (λ1063) and between 400 and 500DN (λ1545). This is likely to be the result of forest targets in close proximity to the instrument. It is not possible to attach reflectance properties of forest targets to intensity at this stage until it has been corrected to apparent reflectance for the reasons outlined in Chapter 4. For example, a dark target at very close range could exhibit the same intensity as a very bright target at long range. The frequency peak at higher DN in the 1545nm wavelength could be due to this laser having a higher output power and therefore more photons per pulse are available to be reflected from targets, received by the detector, and digitised to intensity; or that objects have a higher reflectance in 1545nm (or both).
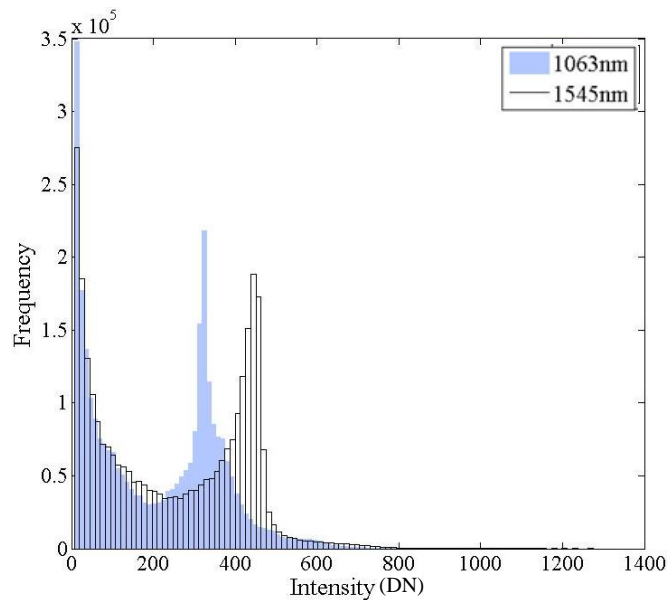
Figure 5.4. Frequency distribution of raw intensity for both wavelengths including all returns.

Very few returns occur over 400DN (λ1063) and 500DN (λ1545) with the maximum intensity recorded as 1123.2 (λ1063) and 1274.8 (λ1545). To provide some context, during the experimental calibration work described in Chapter 4, intensity values over 500DN

only occurred at very close range (<5.5m) from the brightest sub-panel (89% reflectance in λ1063 and 87% in λ1545). In the dataset explored here, 2.9% and 3.3% of returns have an intensity over 500DN in each wavelength, occurring exclusively on targets at near-ranges (<8m for λ1063 and <10m for λ1545). Although there are unlikely to be any natural targets in the forest with a reflectance as high as the brightest calibration sub-panel, the panel and reflective targets (used to merge scans together) were present in this scan and so may account for some of these high DN values. However, the exceptionally high DN values were surprising, and will be discussed further in the following section.

5.2.4 Waveform peak widths

For each return, the width of the peak is recorded. That is, the number of range bins that the digital number remains over the noise threshold for each return. This information can provide further information on the return which may relate to target properties such as roughness (Jutzi & Stilla, 2005). The frequency distribution of peak width is shown in Figure 5.5. The majority of returns had a width of 1 to 5 range bins (98.97%: λ1063, and 97.97%: λ1545), with around half (59.1%: λ1063, and 51.08%: λ1545) exhibiting a width of 3. Returns with a recorded width of 1 had a very low intensity, typically just over the noise threshold, which could relate to very dark or distant targets or partial hits.
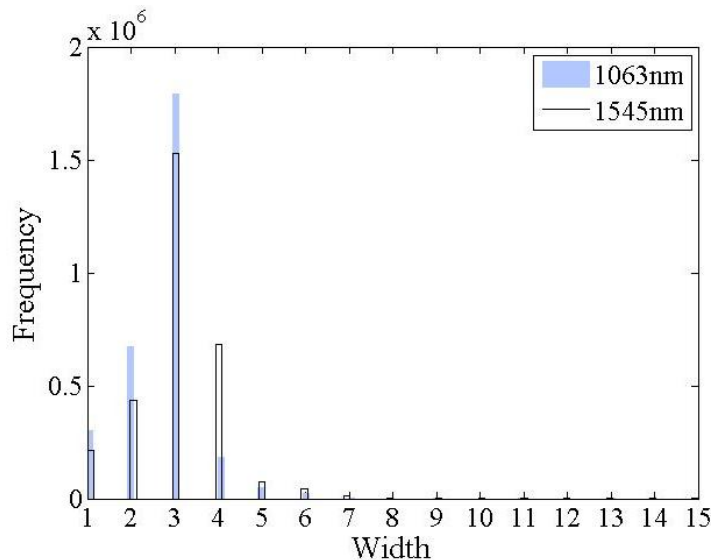
Figure 5.5. Frequency distribution of peak widths for both wavelengths.

Widths were recorded up to 14 (λ1063) and 15 (λ1545) range bins. In order to better understand the characteristics of the width parameter and the very wide peaks, the raw full waveforms for returns with different widths were examined. Examples of waveforms with

different widths are shown in Figure 5.6. This shows that some returns with a large width number actually contain 'hidden peaks': peaks that are hidden through close proximity to each other which generate overlapping echoes (Adams *et al*. 2012). Visual analysis of the spatial distribution of these large width returns determined that they occur in areas containing soft targets. An examination of the raw waveforms in this manner also confirmed that the two laser beams were well aligned, as the signal from both wavelengths were very closely matched, as illustrated in Figure 5.6e.
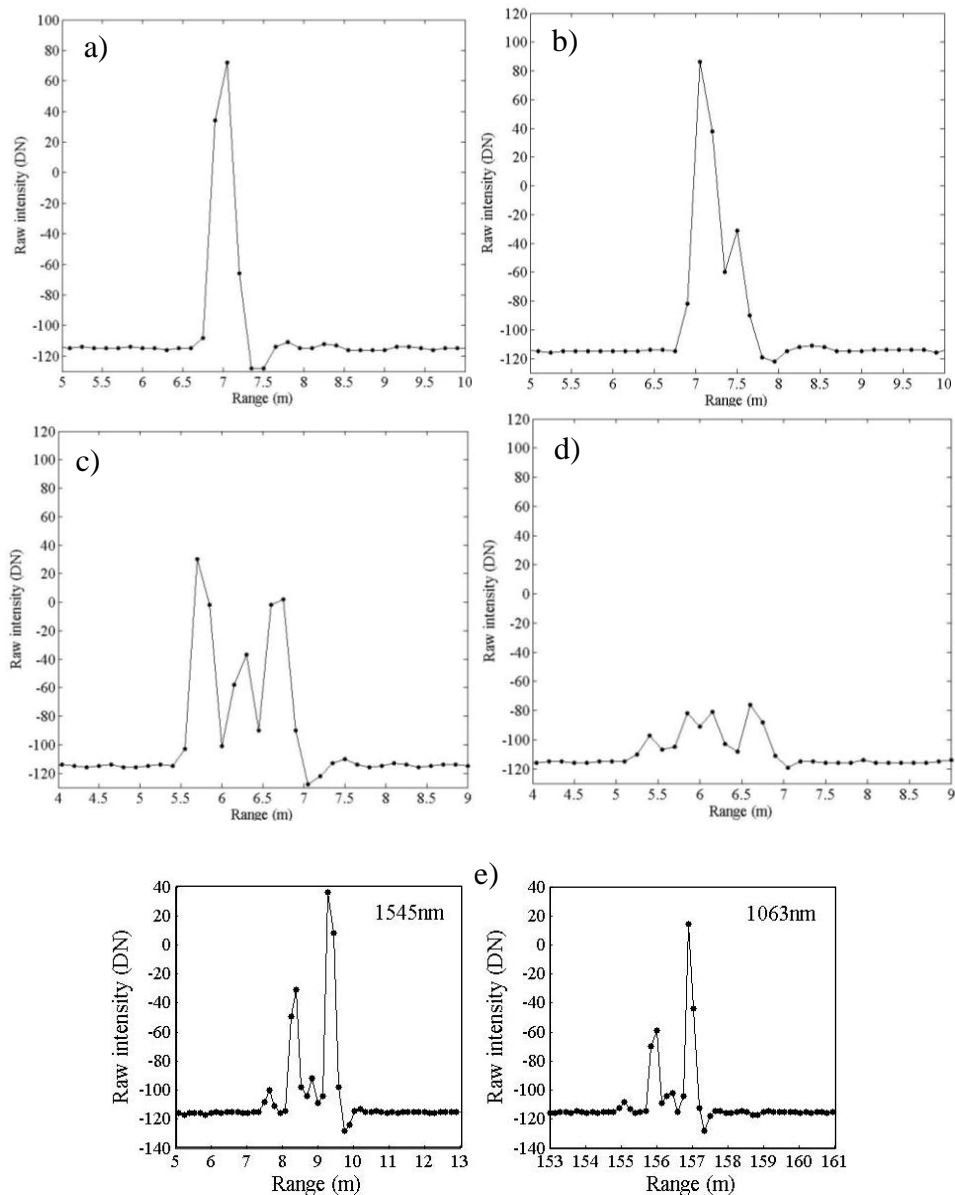
Figure 5.6. Raw waveforms for returns with widths of a) 4, b) 6, c) 10, and d) 12. Plot e) shows a corresponding waveform for both wavelengths. Graphs plotted using raw intensity (recorded between -127 and 127) and range. Black circles represent intensity recorded at each range bin.

Hidden peaks occur when objects are very close together (such as leaves in a tree canopy), partial hits occur, and the signal does not fall beneath the noise threshold and therefore the processing algorithm treats it as a single return and continues to sum the current intensities. These very wide peaks correlated to some of the very high intensity values noted in Figure 5.4. In order to establish the proportion of returns with large widths that contain hidden peaks, twenty raw waveforms for each width number of 4 or more were examined. Table 5.1 shows that all the sampled returns with a width of 4 contained a single peak (Figure 5.6a). The majority of sampled returns with a width of 5 also showed a single peak, however a double peak occurred in the majority of returns with a width of 6 or 7 (Figure 5.6b), and a triple peak in a width of 8 or more (Figure 5.6c). When these returns were left unchanged and the dataset was input to the neural network for calibration, the high intensity value generated an incorrect, very high apparent reflectance estimate. However, if the information from the hidden peaks was discarded, as in Chauve *et al*. (2009) who only kept one peak when hidden peaks were detected, structural information would be lost. Therefore, based on the results in Table 5.1 a new protocol was adopted.

Table 5.1. Number of returns with 1 peak, 2 peaks, 3 peaks or 4 peaks (n=20 waveforms examined per width)

Width	1 peak	2 peaks	3 peaks	4 peaks
4	**20**	0	0	0
5	**12**	8	0	0
6	5	**15**	0	0
7	0	**17**	3	0
8	0	8	**12**	0
9	0	4	**15**	1
10+	0	1	**14**	5

The returns which had a recorded width of 5 or less were not changed. When a width of 6 or 7 occurred, a double peak was assumed and the return split into two separate returns and attributed half the intensity value each, the rest of the return attributes were unaltered. In a similar manner, a width of 8 or more was assumed to be a triple return and the information split into 3 separate returns where the intensity divided by 3. This return splitting 'fix' was applied to all the tree point clouds and then the datasets were re-calibrated to apparent reflectance.

It should be noted that this is a basic method to correct for hidden peaks. In future work this should be looked at in more detail, for instance by amending the initial processing algorithm so that overlapping echoes are detected at an early stage and split into the appropriate number of returns. This would combine the current processing protocol with a signal processing peak detection algorithm but is outside the scope of this research since it only affected a very small amount (<3%) of all recorded returns.

5.2.5 Apparent reflectance

The full scans were calibrated to apparent reflectance for both wavelengths and the resultant distribution for the example dataset is shown in Figure 5.7. There are a number of returns which have produced an apparent reflectance of less of zero, particularly in the 1063nm wavelength and the most likely explanation for this is that the input parameters for this scan (intensity, range or temperature) were outside or near the limits of the training data used in the development of the neural network procedure, as discussed in Chapter 4 (section 4.10.1). Both wavelengths exhibit a low apparent reflectance peak between 0 and 10% (apparent reflectance of 0.1), and this is likely to be the result of partial hits. A second peak is evident around 20% in the 1063nm wavelength and at a lower apparent reflectance of between 10% and 20% in the 1545nm wavelength, which is consistent with the lower reflectance of leaves at this wavelength.
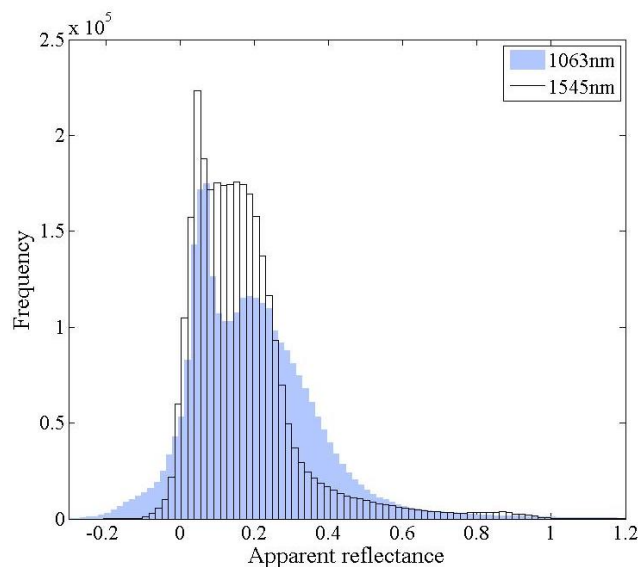
Figure 5.7. Frequency distribution of apparent reflectance for a full leaf-on scan for both wavelengths

5.3   Characterising individual oak trees

The rest of this chapter is concerned with the individual oak trees at Alice Holt. Table 5.2 shows the available SALCA scans acquired for each tree; all scans were conducted in low resolution mode. As detailed in Chapter 3, each tree was intended to be scanned from common multiple aspects in leaf-off and leaf-on conditions. However, poor weather in March 2014 presented an obstacle to collecting all required data. The leaf-off scans were attempted over several days but unfortunately were repeatedly aborted before completion due to rain, wind, and technical problems with the instrument in cold weather. As a result, there is no useable leaf-off data for Tree 02, and only two leaf-off scans for Tree 03.

Table 5.2. Summary of SALCA scans acquired for each tree showing number of scans under leaf-off and leaf-on conditions and the scanning position (S = South, NW = North West, etc).

Tree	Leaf-off 26th-27th March 2014	Leaf-on 2nd-3rd July 2014
Tree 01	3 (NE, NW, S)	3 (NE, NW, S)
Tree 02	None	3 (NW, SE, SW)
Tree 03	2 (S, N)	3 (NW, NE, S)

With the exception of computing the crown projection area of each tree for direct LAI calculation (Section 5.3.2.1), the rest of the chapter considers each tree and scanning position independently as 'single scans'. The main limitation of using a single TLS viewpoint is the occlusion effect. For instance, only half of the trunk surface can be sampled using single side-lateral location scanning and this can lead to an underestimation of canopy parameters (Zheng & Moskal, 2012). The decision was made to use single scans for this study in order to allow common methods to be implemented between the single tree data collected at Alice Holt and the forest plots at Delamere Forest, where the focus is on seasonal change from a single viewpoint. This approach also facilitates comparisons between the scans for different views of the trees. The following sections present the spectral results of the trees acquired with the ASD spectroradiometer, destructive sampling, and finally the TLS point clouds are examined.

5.3.1   Leaf and wood spectral reflectance

Comprehensive spectral reflectance measurements were acquired coincident with the tree felling, as described in Chapter 3, and a summary of the results is presented here. Figure

5.8a shows the spectral reflectance signature of the 48 leaves sampled from Tree 01. The form of this plot is of a typical spectral signature of a green leaf. At 1063nm, the top and bottom of the leaves had an average reflectance of 43.0% (std = 2.5%) and 40.2% (std = 2.3%), respectively. One of the water absorption features is observable between 1400nm and 1600nm, lowering the reflectance of both the top and bottom (to a similar reflectance) of the leaves at the SALCA wavelength of 1545nm compared with 1063nm. Measurements of the spectral reflectance of leaf tops and bottoms were taken for samples from each height stratum of each tree. In total, 48 leaves were sampled from Tree 01, 28 leaves from Tree 02, and 12 from Tree 03. The results are presented in Figure 5.8b by height. To account for the trees being different heights, the mean height for the stratum that each sample belonged was normalised by the height of the tree, to aid comparisons between trees (where 1 is the maximum height of the tree).

Based on these results, oak leaves are separable based on their reflectance at 1063nm and 1545nm. All three oak trees showed similar mean reflectance for all height strata in both wavelengths. Similar to Figure 5.8a, the underside of leaves has a tendency for a slightly lower reflectance, particularly in the 1063nm wavelength. Since the leaves from the different trees and height levels exhibit similar reflectance, it is reasonable to treat all the leaves with a single reflectance value for each wavelength, with an overall mean reflectance of 41.9% (λ1063) and 25.2% (λ1545).

Due to wet weather conditions, no woody spectral measurements were taken from Tree 03 (small oak), and therefore the work will proceed under the assumption that it had the same spectral properties as Tree 01 and Tree 02. This is a reasonable assumption due to the trees being of the same species, around the same age (0.3m height difference between Tree 02 and 03), and sharing very similar environmental conditions due to their close proximity to one another. Figure 5.9a shows the full spectral signature for different structural classes of woody material for Tree 01.
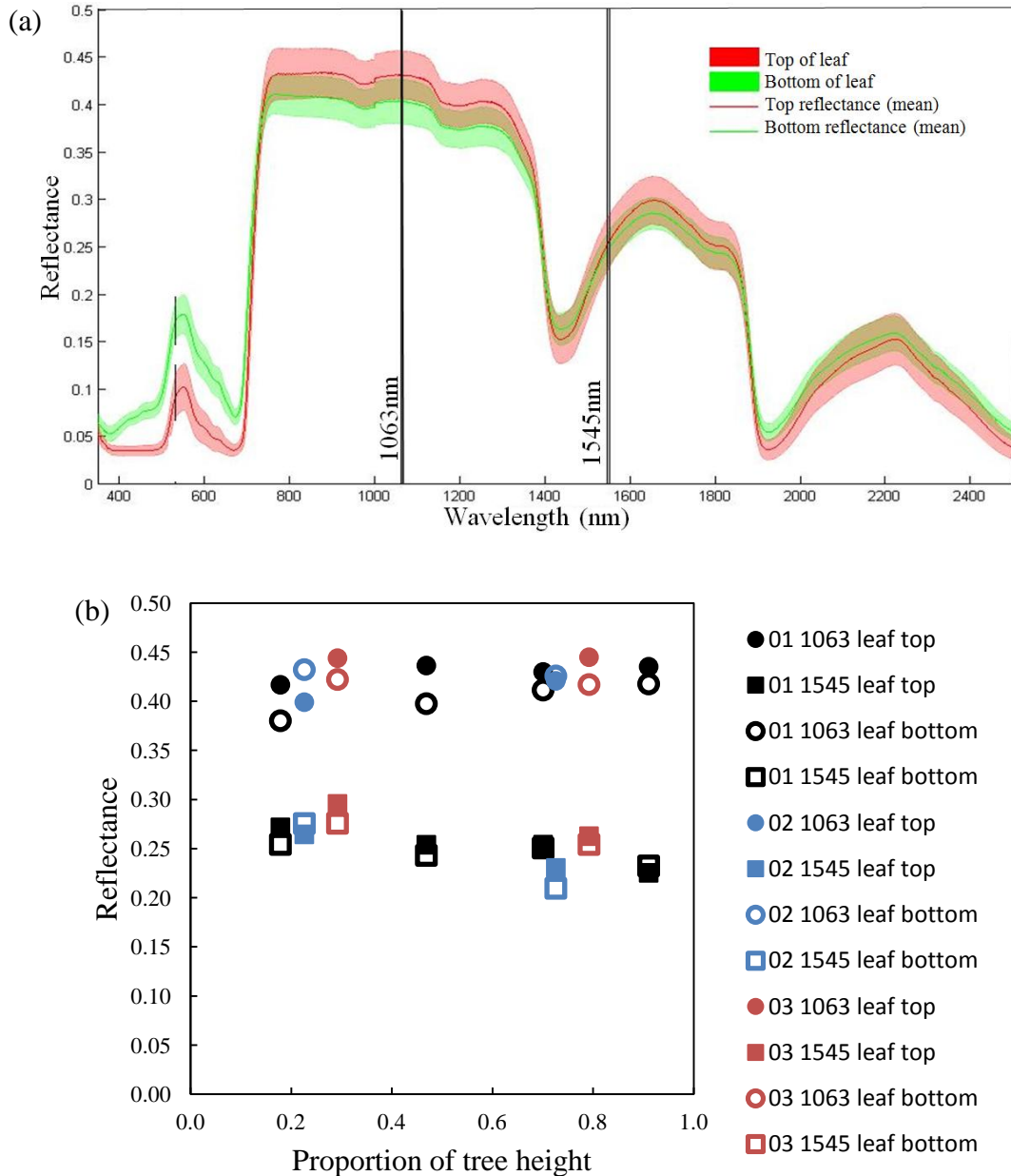
Figure 5.8. Spectral measurements of leaves. a) full spectral signature of leaf top and bottom for all sampled leaves from tree 01 (courtesy of Rachel Gaulton) shaded areas show ± 2 std, b) mean reflectance of leaf top and bottom for all trees for both wavelengths, plotted by mean height of stratum as a proportion of tree height. Circles and squares represent the 1063nm and 1545nm wavelengths, respectively. Closed symbols represent leaf top measurements and open symbols represent measurements taken on leaf bottoms. Each tree is shown in a different colour.

Excluding the twigs and shoots, the mean reflectance of woody material appeared to be similar at 1063nm and 1545nm, although the 1063nm showed higher variance. The spectral results from the twigs and shoots exhibit a larger variance and a significantly lower reflectance than the other woody categories in the 1545nm wavelength. This would suggest that these components have higher water content than the other structural elements.

This could also be explained by measurement errors caused by the fine material being smaller than the ASD contact probe footprint. As a solution, the twigs and shoots were layered into dense bunches and pressure was applied to the contact probe to achieve a satisfactory seal. Some of the variance in the measurements may also be caused by significant amounts of lichen and moss on the bark, particularly on the trunk and large branches (evident in chlorophyll absorbance at 670nm). An examination of the woody spectral results from both trees confirm that the mean reflectance was very similar in both wavelengths (Figure 5.9b).
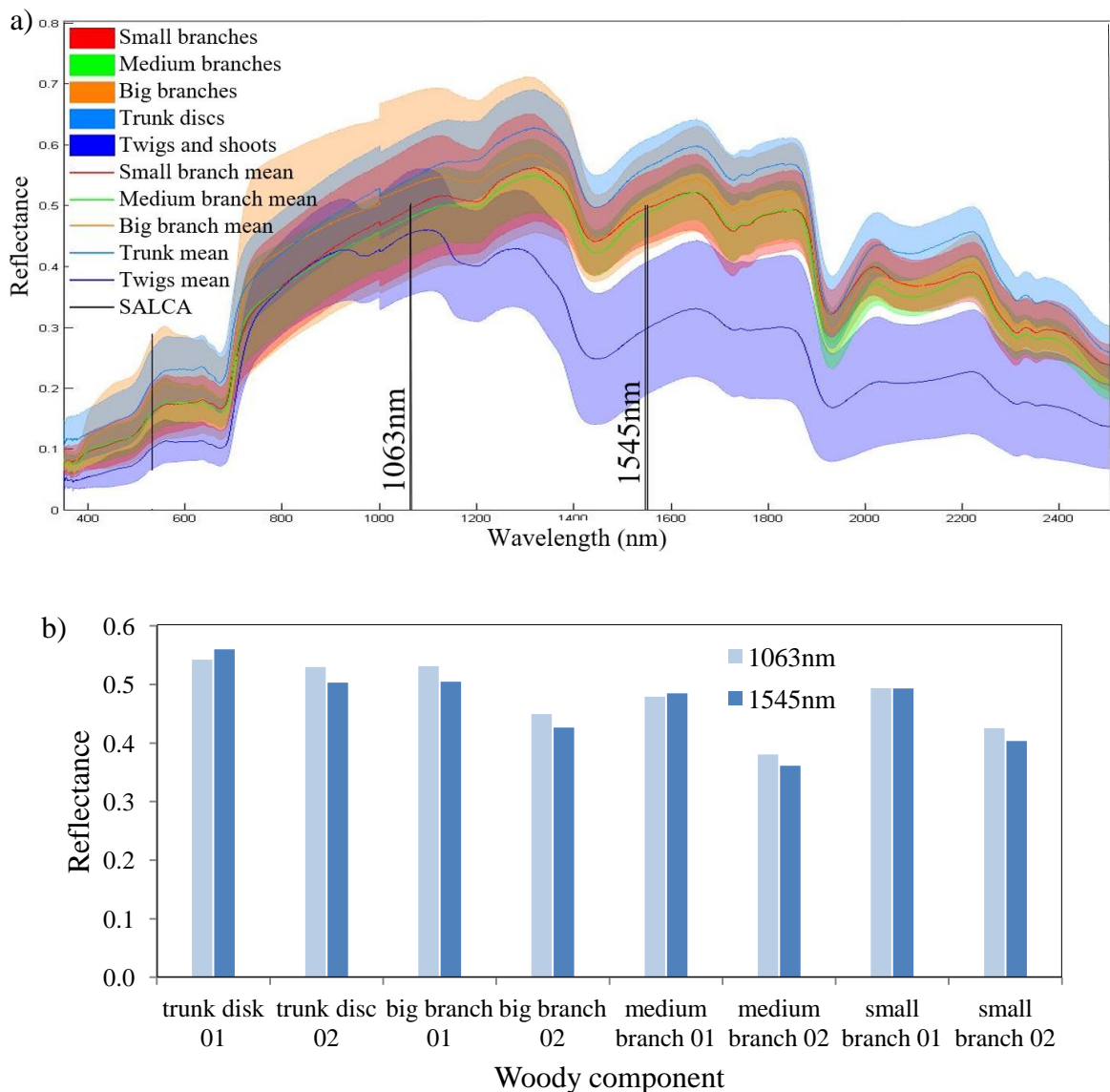
Figure 5.9. a) spectral measurements from the woody samples for tree 01 (courtesy of Rachel Gaulton) shaded areas show ± 2 std, b) mean reflectance of woody material at 1063nm and 1545nm for tree 01 and tree 02.

The spectral variance was higher for the woody components of the trees compared with the leaves (Figure 5.10). The results suggest that spectral separability based on a ratio of reflectance for the two wavelengths may be successful. This is due to wood and leaves exhibiting a similar reflectance in the 1063nm wavelength and leaves showing a lower reflectance in the 1545nm wavelength.
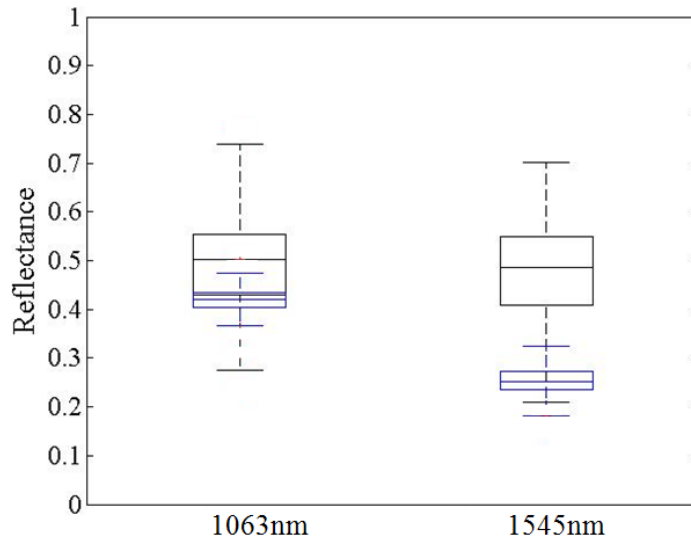
Figure 5.10. Box plots displaying spectral results for all woody samples (black) and all leaf samples (blue) for all trees. On each box, central mark is the median, the edges of the box are the 25th and 75th percentiles, and the whiskers extend to the most extreme data points.

5.3.2 Destructive sampling

The three individual oak trees were felled after the leaf-on TLS scans had been acquired. Each of the trees were manually defoliated and direct detailed measurements taken of the foliage and woody structures, following the protocol described in Chapter 3. This section presents the results from the destructive field campaign. One of the outputs of the tree defoliation was to achieve a direct measure of leaf area index (LAI), and in order to scale the leaf area over the appropriate unit of ground, the first stage was to calculate the area of ground that each tree occupied, which can be done from the TLS data, as outlined below.

5.3.2.1 Scaling LAI to individual trees

In a stand of trees, each tree occupies an area determined by its crown projection which can be defined as the area of vertical projection of the outermost perimeter of the crown on the horizontal plane (Gspaltl *et al.*, 2012). This can be thought of as the trees' silhouette if viewed from nadir. The crown projection area, which is closely related to the

photosynthetic capacity of a tree (Lowman & Rinker, 2004), is an important parameter to characterise for a number of reasons including tree biomass, stand productivity, habitat structure, canopy growth dynamics, competitive interactions between the crowns, and even the aesthetic value of a stand (Fleck *et al.,* 2011; Pretzsch, 2014). To facilitate the computation of single tree leaf area index (LAI), it is necessary to know the crown projection area with which to scale the calculated total leaf area.

Manual methods include deriving an estimate of crown projection area from more easily measurable features such as trunk diameter, height, and/or crown length (Uzoh & Ritchie, 1996; Gill *et al.*, 2000). Measuring crown projection area directly involves measuring the directions and distance of maximum crown extensions (usually at 8 points at set angles) and calculating the coordinates to act as a vertex of a polygon and then calculating its area (Fleck *et al.*, 2011; Miranda-Fuentes *et al.*, 2015).

TLS is capable of measuring canopy projection area in a more efficient manner than manual measurements, and with higher accuracy. This is usually carried out by projecting the tree canopy point cloud in 2D and fitting a shape to its perimeter. The most common methods of shape fitting are to use a convex hull algorithm (Miranda-Fuentes *et al.*, 2015; Gspaltl *et al.* 2012; Hauglin *et al.*, 2014; Wei-heng *et al.*, 2014; Fleck *et al.*, 2011), assume a circular projection and compute a radius from the maximum crown diameter and a centre point (Wang *et al.*, 2008; Moorthy *et al.*, 2011), or interactively fit an ellipse (Srinivasan *et al.*, 2015).

To limit the effects of occlusion from a single scan position, the leaf-on SALCA scans of the tree trees were combined into a single point cloud. This was done using tie points visible in each scan to merge the point clouds into a common coordinate system. The merged point clouds were projected onto a horizontal plane using the x- and y- coordinates and a circle was fitted as this best characterised the 2D shape of the oak canopy (Figure 5.11). The area of each circle represents the crown projection area, and by adding height axis information (min=0, max=height of tree) a cylinder can be used to describe the three-dimensional space occupied by each tree (illustrated in Figure 5.11).
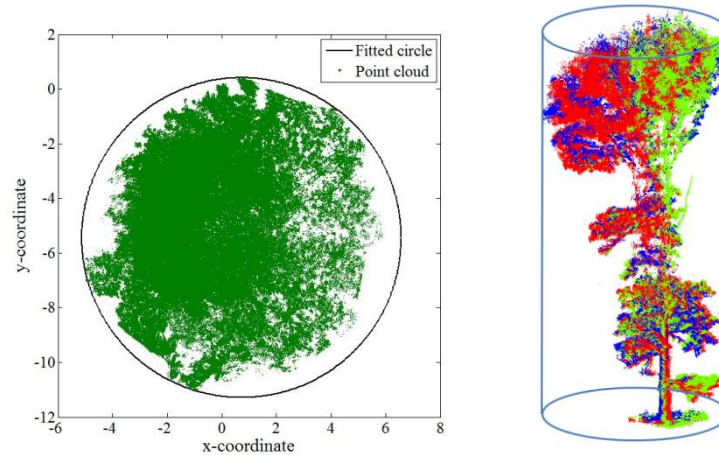
Figure 5.11: Defining the crown projection area for each tree.

5.3.2.2 Destructive sampling results

The results of the destructive sampling experiment are presented in this section. Accompanying measurements of bark, wood (biomass and density), and leaf properties (nitrogen content) were also measured but are not presented as it is outside the scope of this research. Table 5.3 shows the height and diameter at breast height (DBH) based on manual measurements, and crown projection area of each tree calculated from the TLS point cloud as described above.

Table 5.3. Tree diameter at breast height (DBH), height, and crown projected area for the three trees.

Tree	DBH (cm)	Height (m)	Crown projection area (m^2)
01	41.9	22.4	107.48
02	33.4	19.9	61.69
03	27.0	19.6	56.19

Table 5.4 shows the results of the destructive leaf measurements. As detailed in the methods, each tree was completely defoliated, dried and weighed ('all leaves'), and scaled by the specific leaf area of 100 randomly sampled leaves for each height stratum of each tree. The final tree LAI was calculated by dividing the scaled leaf area by the crown projection area. The medium oak (Tree 02) had the largest total LAI of 3.47, followed by the large oak (Tree 01) with 3.15, and then the small oak (Tree 03) having the lowest LAI of 2.73. These values are realistic for the forest type (Kozlowski *et al.*, 1991).

Figure 5.12 illustrates the vertical distribution of LAI for each tree. Of particular interest is the high LAI in the top section of the canopy. This is where light availability is at its

highest therefore more leaf production and higher photosynthetic activity is expected (Marek *et al*., 1989).

Table 5.4. Direct leaf measurements. DM = dry mass.

Tree	Stratum H_{min} (m)	Stratum H_{max} (m)	Specific Leaf Area $(m^2\ kg^{-1})$	Leaf Mass Area $(g\ m^{-2})$	Dry Mass (kg)	Leaf Area (m^2)	Leaf Area Index	Total LAI
			Area (100 sample)/ DM (100 sample)	DM (100 sample)/area (100 sample)	All leaves	DM (all leaves) * SLA (100 sample)	Leaf area/ crown proj area	
01	0.0	8.0	17.34	57.67	3.51	60.91	0.57	
01	8.0	13.0	13.44	74.40	1.71	22.96	0.21	3.15
01	13.0	18.4	12.78	78.26	3.83	48.95	0.46	
01	18.4	22.4	10.44	95.77	19.70	205.67	1.91	
02	0.0	9.0	16.85	59.34	2.70	45.50	0.74	3.47
02	9.0	19.9	11.46	87.26	14.73	168.80	2.74	
03	0.0	11.5	17.06	58.62	1.07	18.28	0.33	2.73
03	11.5	19.6	11.51	86.92	11.75	135.19	2.41	
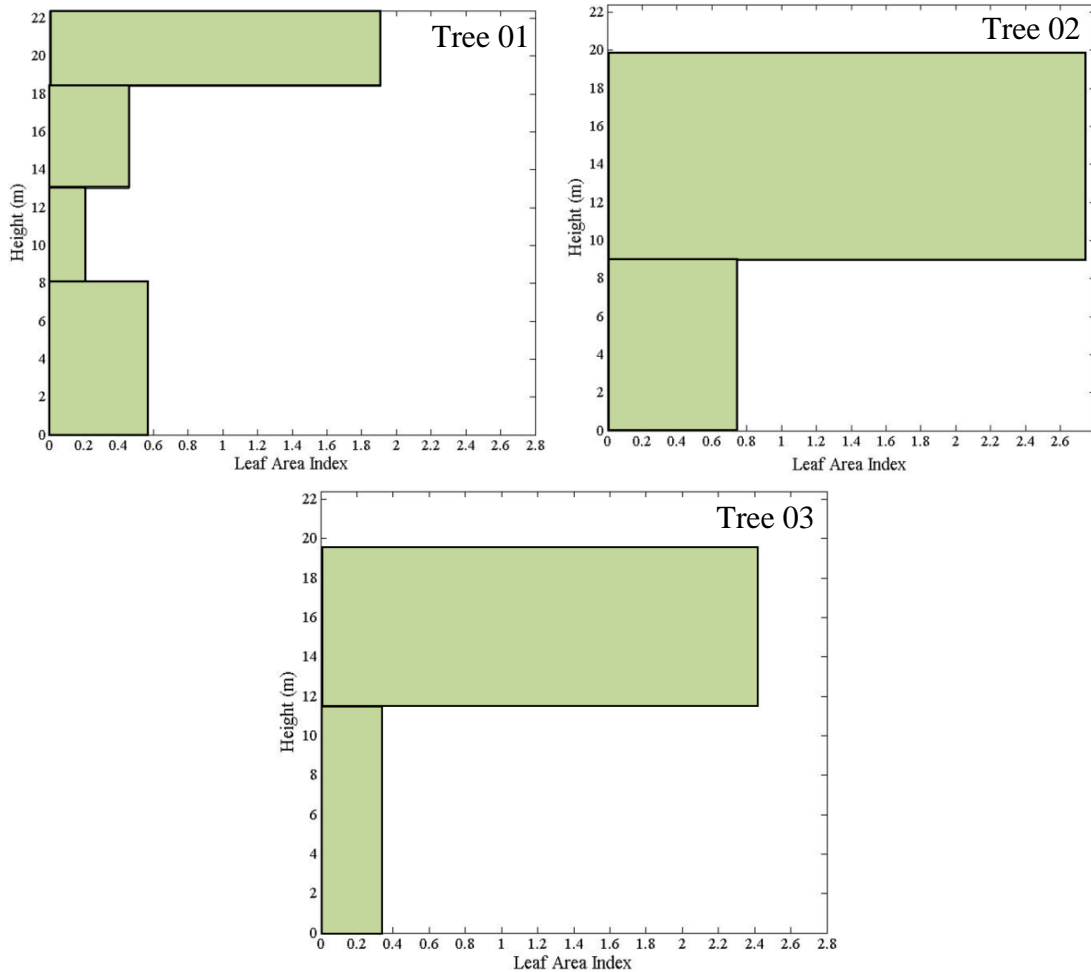
Figure 5.12. Vertical profiles of direct LAI by height, for the three oak trees.

5.4   TLS data analysis for individual trees

Returns corresponding to the individual trees were manually delineated from the full forest point cloud, using CloudCompare$^©$ 3D mapping software (Open Source software available to download from http://www.danielgm.net/cc/). The tree of interest in each scan was visually identified in the point cloud, and then gradually segmented by rotating the scene in 3D and removing all points from adjacent crowns or trunks. Oak has characteristically well-defined crowns which made this segmentation process relatively simple. This was repeated for all three trees for both wavelengths for the leaf-off and leaf-on scans. Since Tree 01 was the only tree with multiple corresponding leaf-off and leaf-on TLS scans, this tree was the subject of analysis for this section, before the same approaches are applied to the remaining scans of the other two trees at the end of this chapter.

Figure 5.13 shows the frequency-height profiles of the leaf-off and leaf-on scans from different views of Tree 01 next to a point cloud of the tree from the South scanning position. The height parameter was calculated by correcting the z-coordinate for the offset (0.3m) between the ground and the optical centre of the instrument. As expected, the profiles look very similar between the two wavelengths for all scanning positions. The profiles contain frequencies below zero; this is because the SALCA instrument scans down to -6° in elevation. The difference in the magnitude and location of the frequency peaks between the scanning positions of the tree is controlled by the structural elements of the tree that protrude in a certain direction. For instance, the first peak, occurring at around 2m, corresponds to the low branch observable in the point cloud image. The frequency peak is significantly higher from the North East scanning position as the branch protrudes in this orientation.

In general, the frequency peaks are larger in the leaf-on scans due to the presence of leaves. However, at the very top of the tree (>17m) the leaf-off scans show a higher frequency of returns and a higher recordable height. This is caused by occlusion in the middle and lower parts of the tree, preventing beams from reaching the upper canopy (Takeda *et al*., 2008).
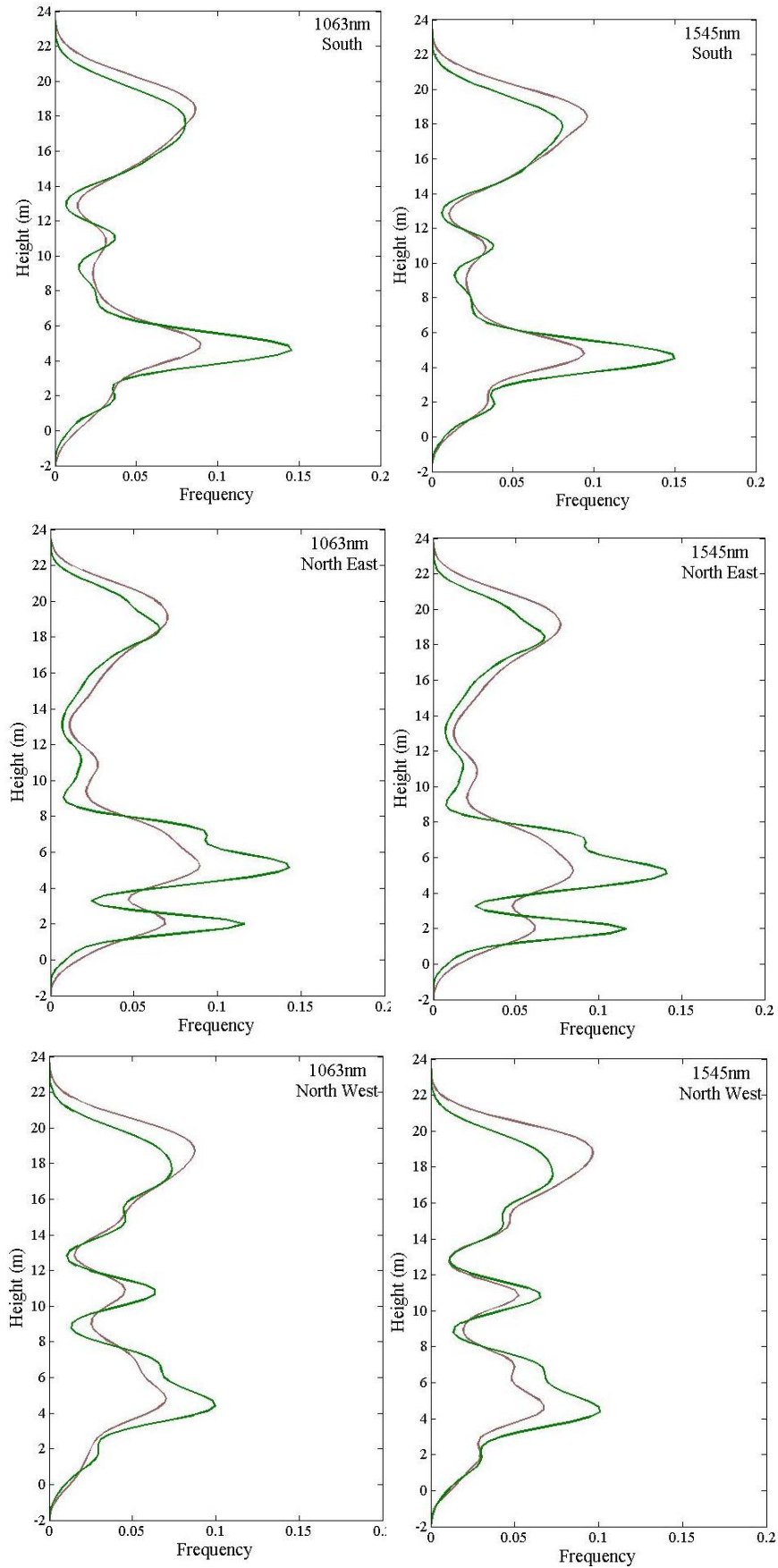
Figure 5.13. TLS height profiles of Tree 01 for the three scanning positions for both wavelengths showing all returns. Green line = leaf-on, brown = leaf-off.

Table 5.5 summarises the number of returns recorded for each scanning position for Tree 01. The leaf-on point clouds increased by a similar proportion for the South and North East viewpoint, with a slightly lower increase from the North West, where there was a larger amount of trunk and branches visible from this view.

Table 5.5. Summary of number of returns for tree 01 for each scanning position for both wavelengths

TLS view	1063nm			1545nm		
	Leaf-off	Leaf-on	% increase	Leaf-off	Leaf-on	% increase
S	217985	369400	69.46	240348	367316	52.83
NE	176744	296591	67.81	189363	297877	57.30
NW	218469	309732	41.77	245907	309421	25.83

An example of a leaf-off and leaf-on calibrated point cloud for both wavelengths is shown in Figure 5.14 from the South scanning position, and the frequency distribution of apparent reflectance output for the three scanning positions is shown in Figure 5.15. The branches and trunks appear brighter than the leaves in the 1545nm wavelength consistent with the fact that the middle-infrared wavelength is in the band of water absorption of vegetation. In 1063nm wavelength there is a clear peak in leaf-off at lower reflectance, which could be partial hits, and also material at higher reflectance. For leaf-on there is a matching peak with lower reflectance (partial hits) and then a second clear peak around 35% reflectance which is full hits on leaves. In the 1545nm wavelength for the leaf-off scans there is a large peak at low reflectance (partial hits) and then a second peak around 50-60% reflectance which is full hits on woody material. For the leaf-on scans again there are two clear peaks, one at 5% reflectance (partial hits) and one at 20% reflectance (full hits on leaves).

The measured spectral data indicated that the oak leaves have a measured reflectance around 42% (λ1063) and 25% (λ1545). This means that the average apparent reflectance of the peak representing leaves is lower, 35% (λ1063) and 20% (λ1545) than the mean reflectance measured with the ASD instrument. This was also noted in Béland *et al.* (2014) and Balduzzi *et al.* (2011) and can be explained by the presence of partial hits and non-Lambertain scattering of the foliage. Rather than the assumed Lambertain scattering, leaves may scatter light anisotropically and therefore there will be a decrease in the intensity of the return signal as the angle between the laser pulse and the leaf normal

increases. The amount of decrease will depend upon the specular reflectance characteristics of the foliage (Béland *et al.,* 2011; Balduzzi *et al.,* 2011).
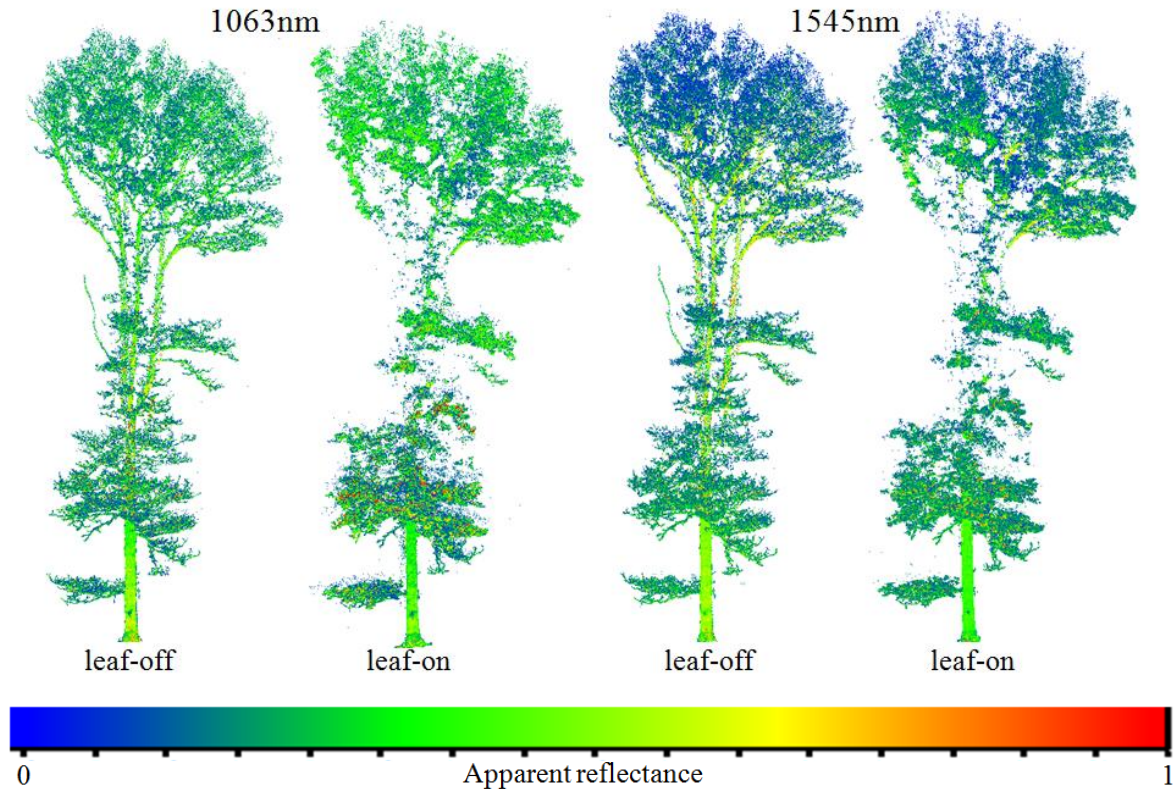
Figure 5.14. Point clouds of Tree 01 symbolised by apparent reflectance as shown in the colourbar.

Figure 5.16 shows the frequency distribution of the leaf-off and leaf-on scans from the South scanning position, to allow the location of the peaks between the wavelengths to be compared. The location of the first peak corresponding to partial hits occurs in the same position for both seasons at both wavelengths. The peak representing leaves is at a lower apparent reflectance for the 1545nm than the 1063nm wavelength, although there is substantial overlap. There is a clear peak around 50% in the leaf-off 1545nm wavelength with some corresponding returns in this reflectance area in the leaf-on scan. However, the peak corresponding to full hits on wood in the 1063nm wavelength is not so distinct.
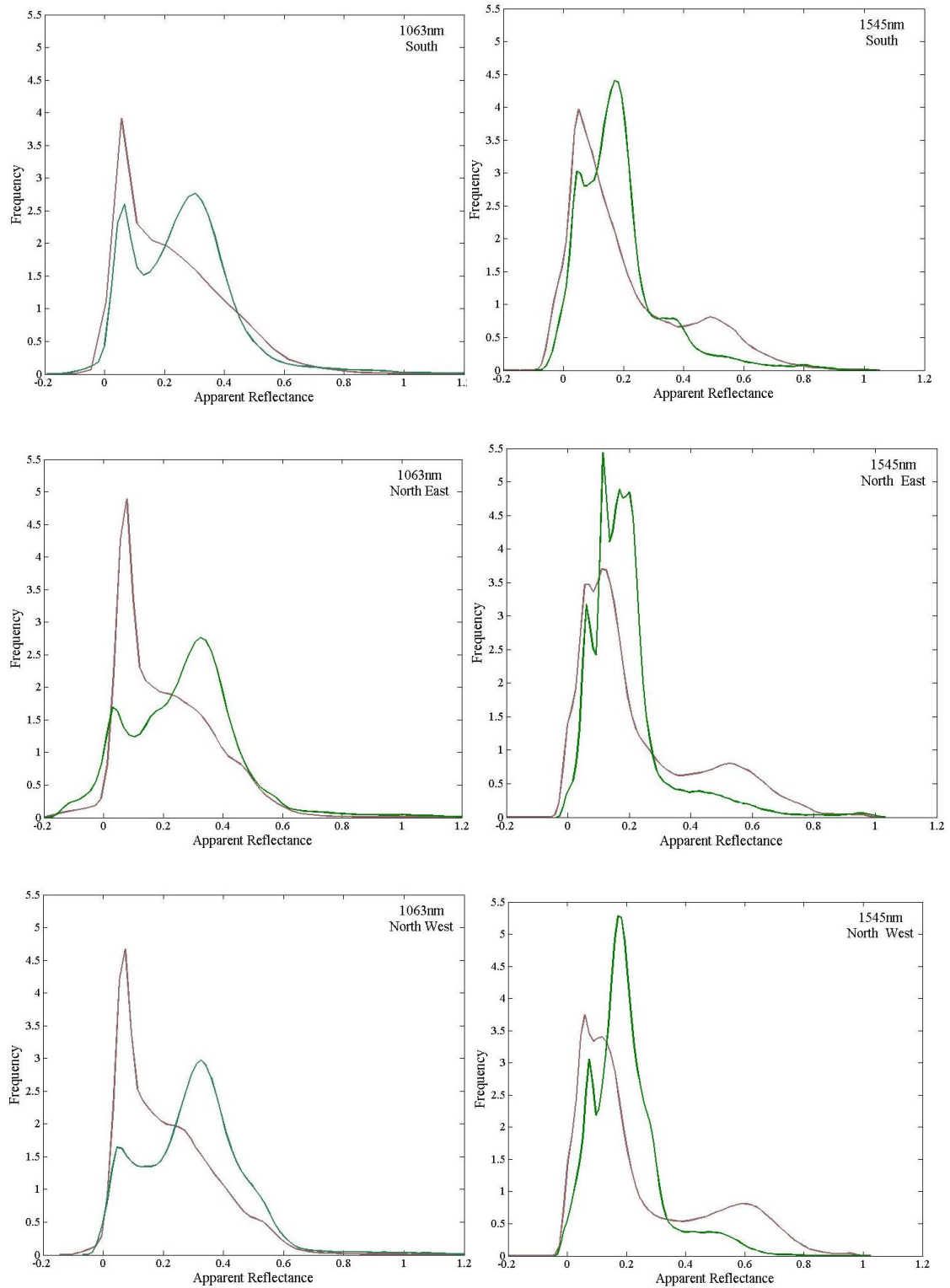
Figure 5.15. Frequency distribution of leaf-off and leaf-on apparent reflectance for three scanning positions in both wavelengths, showing all returns.
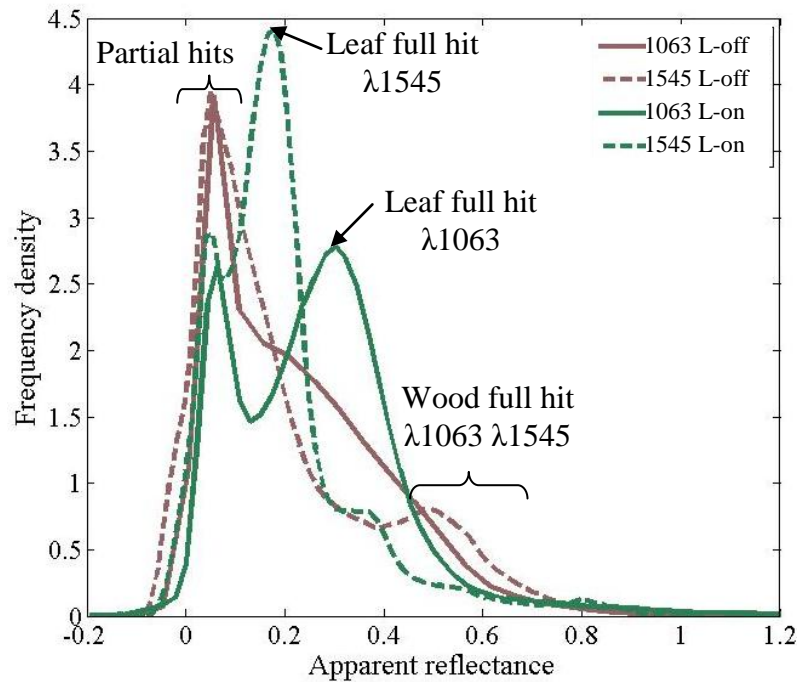
Figure 5.16. Frequency distribution of leaf-off (L-off) and leaf-on (L-on) apparent reflectance for the South scanning position for both wavelengths. Annotated to show reflectance features for both wavelengths.

5.5   Separating leaf and wood for individual oak trees

The ability to separate forest returns into foliage and wood components is important due to their different ecological functions, as outlined in previous chapters. For TLS studies, this is vital to achieving quantitative metrics for trees and forests, in order to derive accurate information relating to phenology, carbon allocation, and quantification of biomass, and for assessing structural components of vegetation. Leaf-off and leaf-on TLS scans can help with understanding the interactions between lasers pulses and forest canopy material. The destructive measurements acquired in this experiment provide an opportunity for validating the leaf and wood separation. This section discusses and implements current and new methods to achieve foliage and wood separation from TLS data.

5.5.1   Introduction to leaf and wood separation using TLS

The ability to distinguish between returns resulting from foliage and wood has been noted as a limitation of several TLS forest studies, and more generally, is still an unsolved problem for indirect measurements. One method of achieving this separation has been to apply a manually determined threshold based on the intensity of the reflected signal. However, this relies on there being a significant difference in reflectivity between the wood and foliage material at the wavelength of the TLS instrument, such as the water

absorption window of radiation near 1550nm (Béland *et al*., 2011), or in the green wavelength (Clawges *et al*., 2007). This method has been tested for broadleaved (Béland *et al*., 2011) and coniferous (Seielstad *et al*., 2011) species on a tree level, sometimes requiring a different threshold for each tree (Yanez *et al*., 2008). Another method is to perform scans in both leaf-off and leaf-on conditions and subtract the leaf-off returns (Clawges *et al.,* 2007). However, this method is only applicable to deciduous forests and relies on multiple scans several months apart, and even then, is not a true representation of the true foliage component due to the assumption of a random distribution of woody tissue with respect to the position of leaves (Piayda *et al*., 2015). Leaf, wood separation is sometimes performed after inserting a merged point cloud into a voxel grid, a 3D space composed of adjacent cubic cells of specific size and coordinates (Hosoi & Omasa, 2006; 2007). Furthermore, the studies mentioned above all used small experimental trees.

Béland *et al*. (2011) compared leaf-off and leaf-on scans from two position either side of a tree using a first return Optech ILIS-3D TLS at 1545nm wavelength, first normalising the TLS return intensities to 20m range using linear fitting (ignoring near and far range), then identifying an intensity threshold by analysis of normalised intensity histograms for leaf-off and leaf-on scans. To compensate for parts of branches not visible to the TLS in the leaf-on scans (occluded by leaves) the bin values for the leaf-off histograms were multiplied by a correction factor (between 0 and 1). Once separated into leaves and wood, the data was then voxelised to complete the analysis. This study highlighted the effect of partial hits (e.g. around the edge of tree trunk). Béland *et al.* (2014) extended this approach by using a multiple return TLS Riegl VZ-400 at 1550nm wavelength to scan ten blue oak trees (mean height 9.5m). Histograms of normalised intensities were analysed to distinguish between multiple and single returns from leaf-off and leaf-on scans and categorise the returns into leaf, wood, and noise.

The next sections implement three methods for separating leaf and woody returns from TLS scans. First, based on the number of returns in corresponding leaf-off and leaf-on scans, secondly, applying an apparent reflectance threshold to the 1545nm wavelength, and finally, introducing a new method using both wavelengths to generate an apparent reflectance ratio.

5.5.2 Leaf and wood based on number of returns

Clawges *et al*. (2007) used a Leica HDS 3000 TLS with a wavelength 532nm (green) to scan individual larch trees (between 2m and 4m in height) from four positions in leaf-off and leaf-on. The total leaf-off returns for every 1m vertical section was subtracted from the corresponding data in leaf-on. The number of 'leafy' laser returns calculated using this method was significantly correlated with manual-based estimates of leaf area ($R^2 = 0.822$; Clawges *et al*., 2007). Following the approach by Clawges *et al*. (2007), 'leafy' returns were calculated for each scanning position of Tree 01 based on the four height strata defined during the direct measurements. As a corresponding leaf-off and leaf-on scan was also available for Tree 03 (South), this was also included for additional data points. The number of 'leafy' laser returns was then plotted against the one-sided area of collected leaves for each of the strata (Figure 5.17). The data shown here is using the 1063nm wavelength, the 1545nm wavelength showed a very similar response.

With the exception of the top vertical sections of both trees, there was a positive relationship between the number of 'leafy' laser returns and the measured one-sided area of leaves. However, the form of the relationship is not the expected logarithmic increase in attenuation and reflection of light with increased concentration of leaf area, as described by the Beer-Lambert Law, and demonstrated in Clawges *et al*. (2007). These results could be explained by the lack of sufficient data points or differences between the studies, Clawges *et al*. (2007) used young coniferous larch individuals, merged scans, and a first return scanning mode.
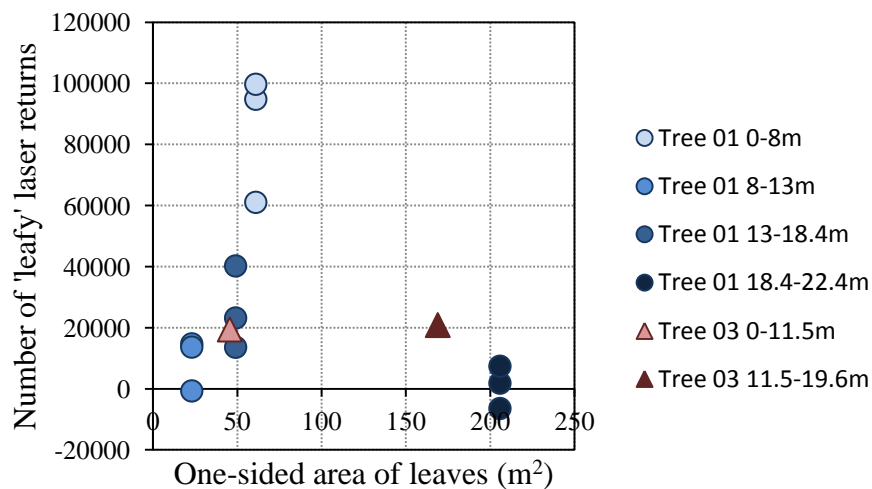
Figure 5.17. Number of 'leafy' laser returns (λ1063nm) vs. one-sided area of collected leaves, for the height strata.

The top vertical sections of the trees showed a very difference response, with a very low (and in one case negative) number of 'leafy' returns compared with the collected one-sided area of leaves, which exhibited the largest leaf areas of all strata. These points can be seen on Figure 5.17 as dark blue circles (Tree 01) and dark red triangle (Tree 03). This exemplifies the impact of occlusion, caused by the lower canopy and the position of the instrument, as discussed earlier. This suggests that an accurate TLS LAI estimation for these strata may not be possible unless occlusion is accounted for.

5.5.3   Leaf and wood separation using a threshold on a single channel

This section classifies each return in the point cloud to 'leaf' or 'wood' based on the spectral response of these targets in the middle-infrared region of the electromagnetic spectrum (the 1545nm wavelength) where the reflectance difference has been shown to be significant. In order to define an appropriate threshold for the two classes, the apparent reflectance histograms for leaf-off and leaf-on SALCA scans were examined (Figure 5.18). As expected, multiple returns occur at lower apparent reflectance values, and it is observable that many partial hits on wood fall within the same reflectance range as full hits on leaves. These are not distinguishable solely using apparent reflectance and will be incorrectly classified as leaf material.
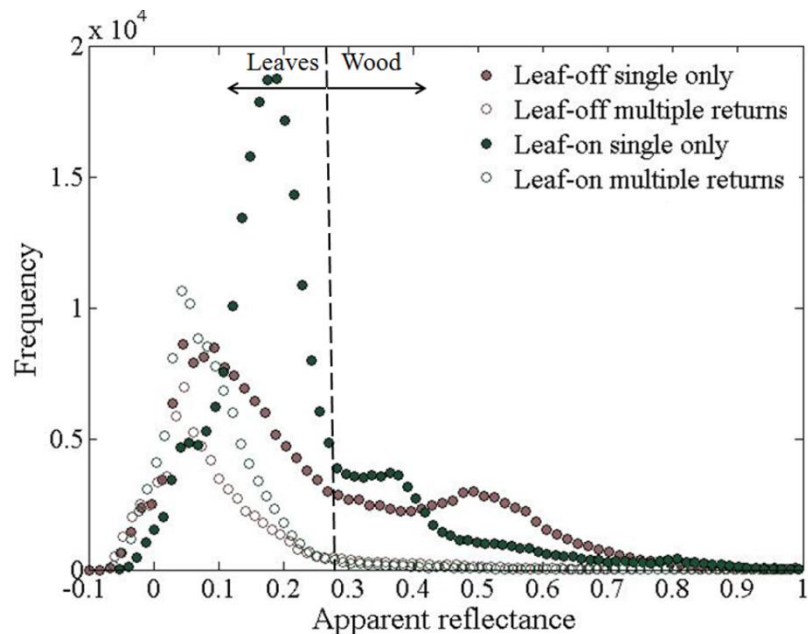
Figure 5.18. Frequency distribution of leaf-off and leaf-on scans for tree 01 South (1545nm wavelength). Threshold of 29% illustrated. The NE and NW scanning positions displayed similar distribution but are not added to graph for clarity.

Between 29% and 41% apparent reflectance, there are some leaf returns that will be incorrectly categorised as wood (where the frequency of laser pulses exceeds the leaf-off). Béland *et al.* (2014) also applied a lower threshold of half the measured leaf reflectance, and discarded everything below this as 'noise', meaning that pulse returns that occupied less than half of the footprint were not included in the analysis. This approach was not adopted for this research as it meant that too many valid returns were also discarded which would lower the structural resolution of the point clouds.

Based on the histograms, a threshold of 0.29 (29% reflectance) was adopted to separate foliage and wood in the 1545nm wavelength. Figure 5.19 shows the leaf-on and leaf-off point clouds for tree 01 from all scanning positions after the classification was applied. The green points in the top images show the points categorised as 'leaf' (with an apparent reflectance less than or equal to 0.29), and the brown points are those categorised as 'wood' (apparent reflectance of over 0.29). Visual examination of the results in the 3D point clouds suggest that this approach was very successful for all three scanning positions: the trunk and branches appear in brown and the rest are green. However, as previously discussed, partial hits on woody material generate an apparent reflectance within the region of leaf reflectance and therefore are misclassified as such. This is evident around the edges of the trunk and branches (shown in inset in Figure 5.19). This is also illustrated in the bottom images in Figure 5.19 which show the result of the same method applied to the leaf-off scans, where the points classified as 'leaf' are displayed in blue. As expected, the fine branches and edges of larger branches have been miss-classified as leaf, leading to large misclassification errors (70.0%, 67.3%, 64.1% for the South, North East, and North West scanning positions respectively). Furthermore, the ASD measurements suggested that fine branches exhibit a lower reflectance than the trunk and larger branches, which may also contribute to the misclassification error (Figure 5.9a).

To investigate whether the leaf-on classification could be improved, the returns corresponding to woody partial hits were extracted from the point clouds to determine whether there were any measurable characteristics of these that could be used to distinguish them automatically from leaf returns. To this end, the apparent reflectance (λ1063 and λ1545), normalised and simple ratios (a description of how the ratios were computed can be found in the following section), and peak width of the extracted woody

partial hits were examined. The results determined that the woody partial hits did not show any features that would make them distinguishable from leaf returns.
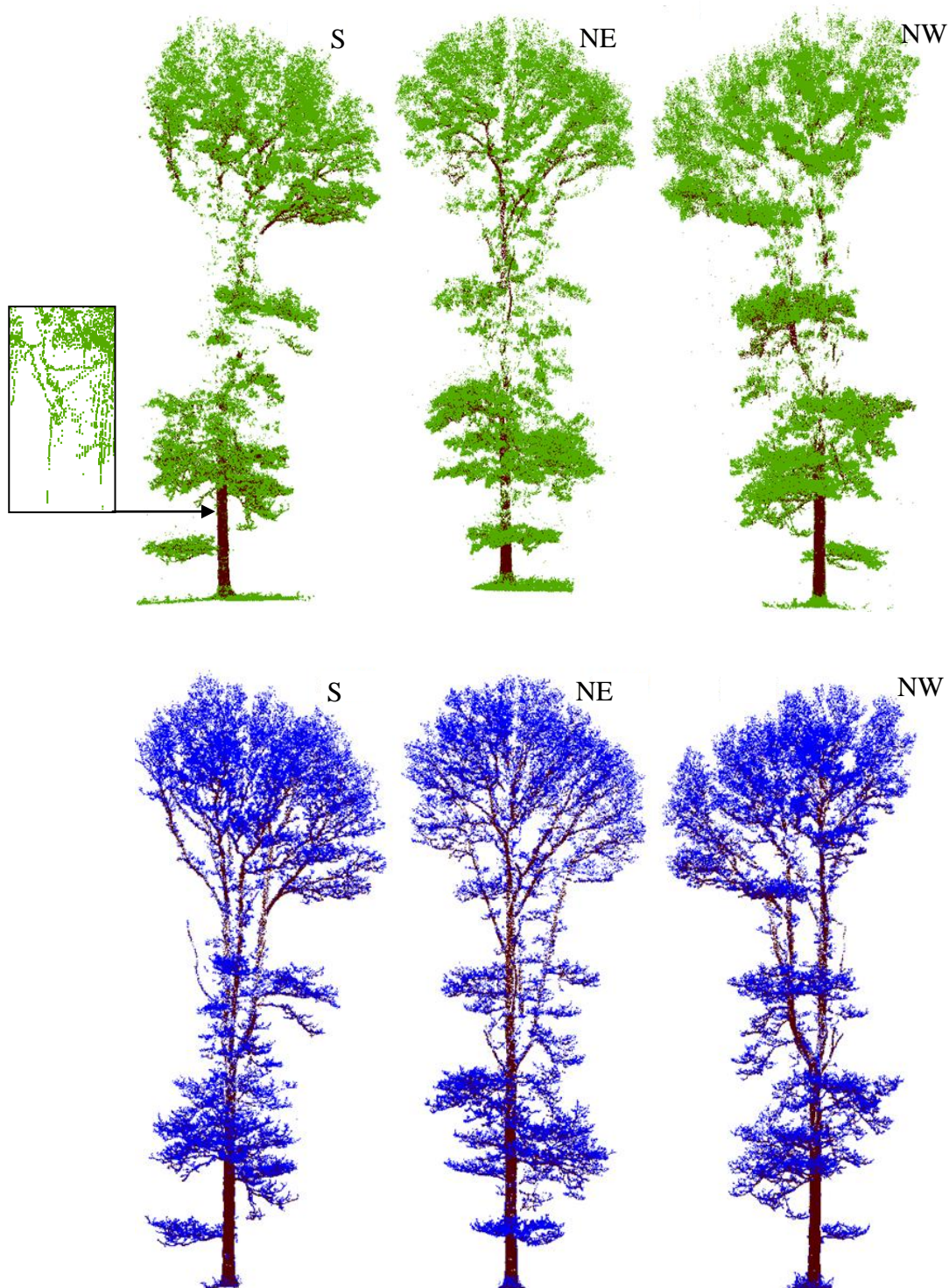
Figure 5.19: Point clouds for Tree 01 classified into 'leaf' or 'wood' using 29% apparent reflectance threshold in the 1545nm wavelength, for all three scanning positions. Top images show leaf-on where green points have been allocated to 'leaf' category and brown points allocated to 'wood'. Bottom images shows the same procedure for leaf-off, with the 'leaf' points symbolised in blue which represent the miss-classification error.

5.5.4 Using a ratio for leaf wood separation

The last section demonstrated how recorded intensity calibrated to apparent reflectance can be used for classifying a TLS point cloud into target classes. However, the approach did not account for the portion of the laser pulse hitting the target, causing numerous woody partial hits to be incorrectly categorised as leaves. This source of error can potential be addressed with dual-wavelength lidar. As described in Chapter 4, and suggested by Gaulton *et al.* (2013) and Danson *et al.* (2014), taking a ratio of the apparent reflectance values for each return may address some of the limitations of the previous approaches by generating a measure solely dependent on the reflectance of the target and independent of amount of material in the laser footprint and beam incidence angle. The ratio is calculated as a Normalised Difference Index (NDI) where ρ is the reflectance:

$$NDI = \frac{(\rho 1063 - \rho 1545)}{(\rho 1063 + \rho 1545)} \tag{5.1}$$

Taking a ratio in this manner should therefore be sensitive to moisture content and allow a threshold to be applied to classify the point clouds as 'leaf' or 'wood'. Up to this point, the TLS data has been examined as two independent datasets, one for each wavelength. In order to calculate these ratio values, it was first necessary to match each return between the wavelengths, implemented in this research as follows. For each corresponding laser pulse, the difference in range between the two lasers was calculated. Pairings were only kept which had similar range values, threshold of 0.12m (less than a range bin) was adopted after experimentation on multiple waveforms. Once the returns had been matched for all scans, the NDI was computed according to Equation 5.1. The resultant frequency histograms for the leaf-on and leaf-on scans for the three scanning positions for Tree 01 are shown in Figure 5.20.

All of the histograms show a similar form, with the frequency peak for the leaf-off scans occurring at a lower ratio than the leaf-on. This is due to a lower 1545nm apparent reflectance for leaf returns compared with the corresponding 1063nm return and therefore a lower denominator resulting in a higher ratio for leaf-on datasets. However, the histograms show that there is substantial overlap between the leaf-off and leaf-off ratios. In a similar manner as the threshold on a single channel (Figure 5.18a), this suggests that a ratio threshold will also generate misclassification errors associated with leaves that are categorised as wood, and wood that is categorised as leaf. If this threshold was decreased

then the amount of leaf classified as wood would decrease but the amount of wood as leaf would increase, if the threshold was increased then the opposite would occur.
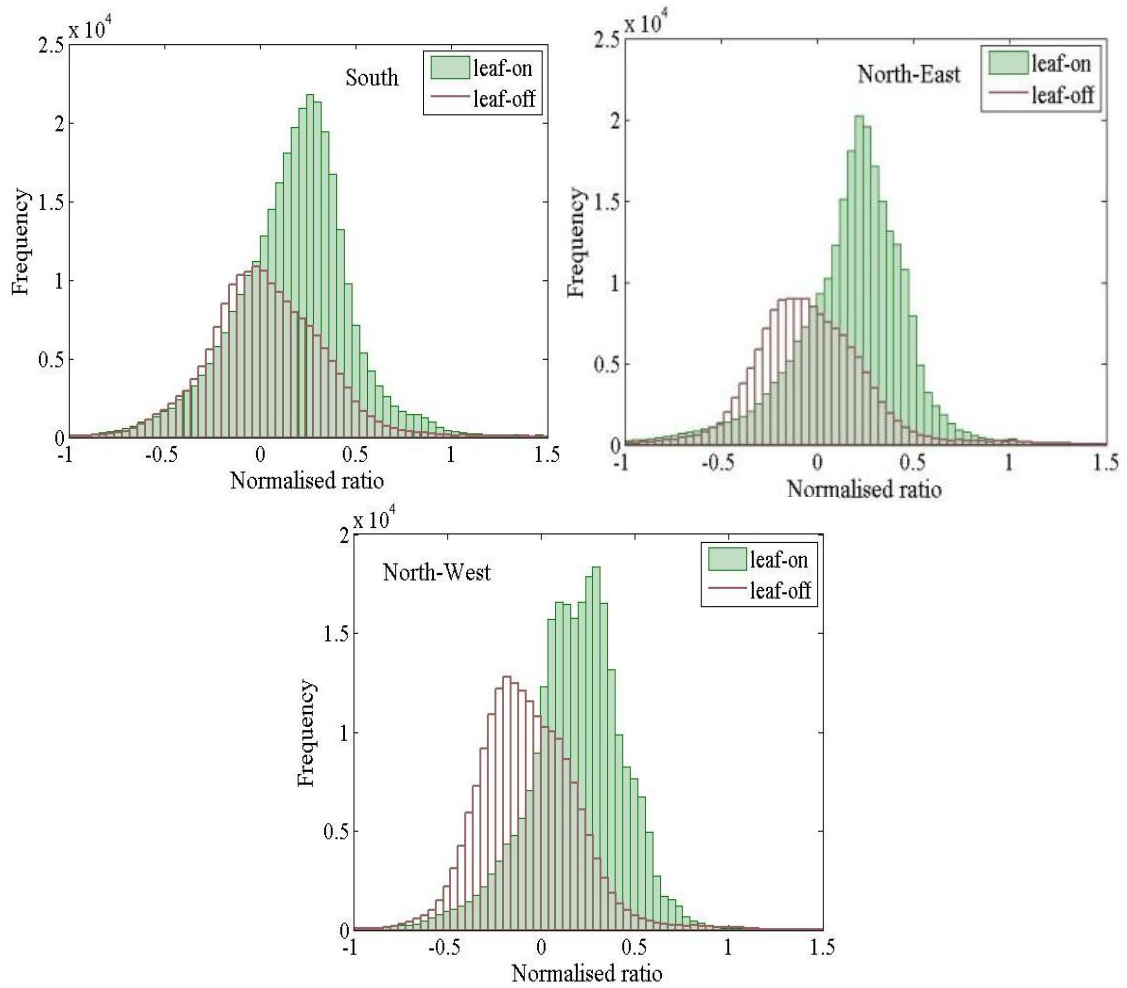
Figure 5.20. The SALCA Normalised Ratio Index (NDI) frequency histograms for leaf-off and leaf-on scans for the three scanning positions for Tree 01.

Figure 5.21 shows the result of applying the NDI threshold of 0.1 to leaf-on (top images) and leaf-off (bottom images) for tree 01 for all scanning positions. The leaf-on results suggest that overall the classification is successful, however some returns from the trunk have been incorrectly categorised as leaves (highlighted in the inset). However, the leaf-off scans exhibit a lower misclassification error compared to the earlier approach (38.6%, 28.4%, 24.9% in the South, North East, and North West scanning positions). The majority of the misclassification error occurs in fine branches which could be explained by the results from the ASD reflectance measurements.
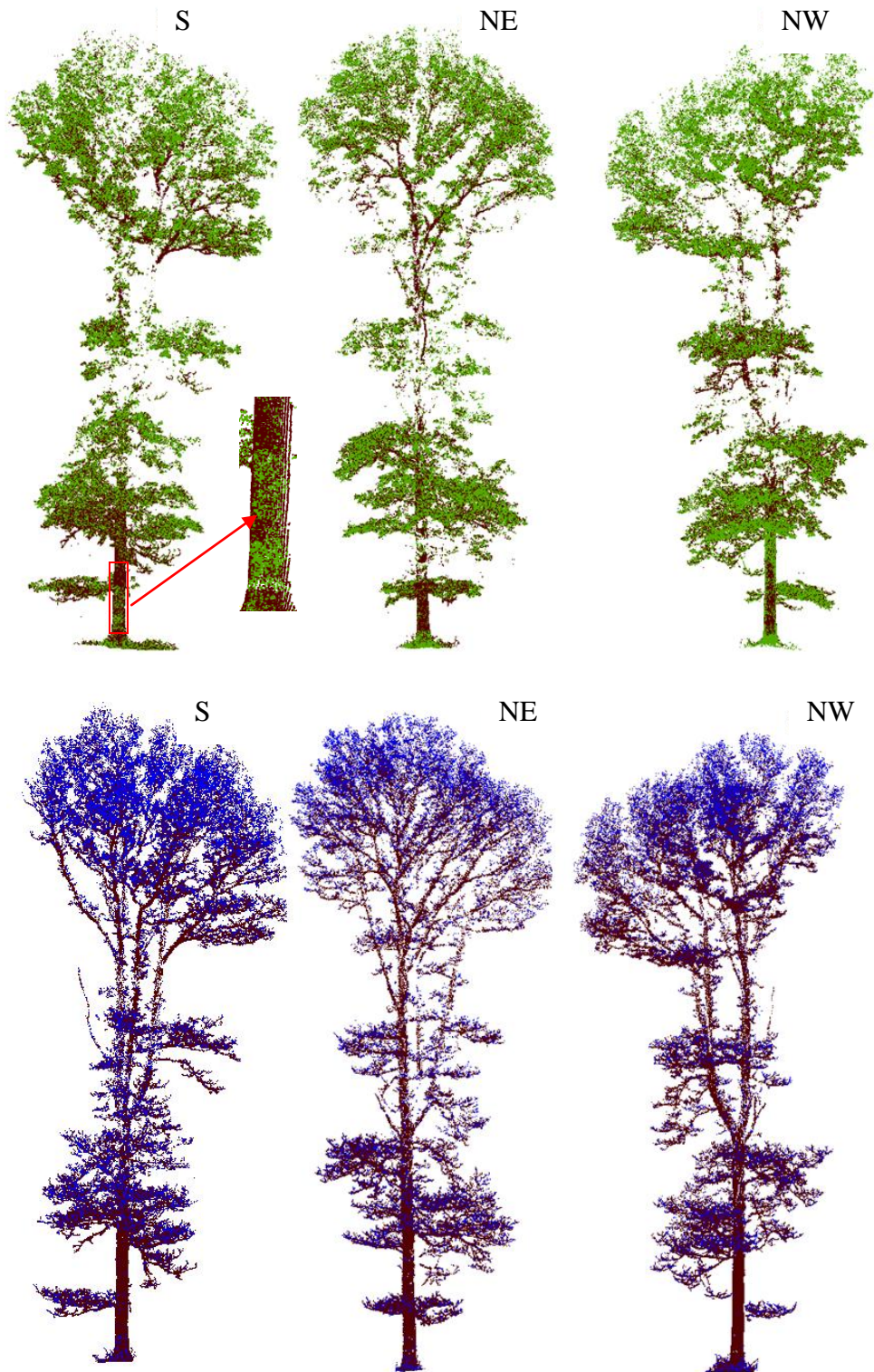
Figure 5.21. Point clouds for Tree 01 classified into 'leaf' or 'wood' using a NDI threshold of 0.1, for all three scanning positions. Top images show leaf-on where green points have been allocated to 'leaf' category and brown points allocated to 'wood'. Bottom images shows the same procedure for leaf-off, with the 'leaf' points symbolised in blue which represent the miss-classification error.

To investigate the misclassification of the tree trunk in more detail, returns that were classified as leaves and wood, based on the ratio alone, were manually extracted from the tree trunk. These represent full hits (edge of the trunk avoided) on woody material. Figure 5.22 shows the extracted returns as a function of the apparent reflectance at both wavelengths. The figure suggests that the wood apparent reflectance in the 1063nm wavelength is highly variable (ranging from 20% to 70%), whereas the apparent reflectance in the 1545nm wavelength is relatively stable at approximately 35-40%. Therefore, when a NDI ratio of 0.1 was applied, a number of woody returns were miss-classified (blue points in Figure 5.22). According to the ASD measurements, the trunk has a reflectance of around 55% for the 1063nm wavelength and 56% in the 1545nm wavelength. The lower trunk of interest here was at very close range to the scanner (range 5 to 6m) therefore a possible explanation for the misclassification is that the calibration did not perform well at this close range in the 1063nm wavelength.
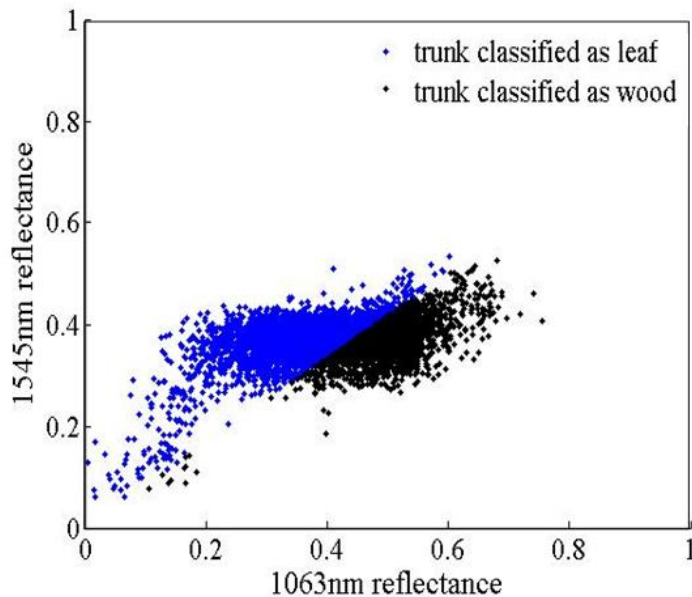
Figure 5.22. Extracted trunk returns plotted by wavelength and reflectance. Blue points represent returns incorrectly classified as leaves, and black returns represent returns correctly classified as wood, when a NDI threshold of 0.1 was applied.

5.6 Leaf and wood separation on Tree 02 and Tree 03

Figure 5.23 and Figure 5.24 show the results of applying the same leaf-wood separation methods discussed above. The top three point clouds in both Figures present the results of using a single wavelength to perform the segmentation, and the bottom point clouds

present the results of applying a threshold to the NDI. In both Figures, the returns classified to leaf are shown in green, and those to wood in brown. It is observable from these images that there appears to be a range effect present. This is the case for all trees except Tree 03 NW. To investigate whether the performance of the calibration of these scans, the laser temperatures recorded during data acquisition were compared with the laser temperatures used to build the neural networks in Chapter 4. The leaf-on scans for these datasets were collected in summer where air temperatures were very high. The three trees were scanned in multiple positions consecutively over a single scanning day, starting with Tree 01, followed by Tree 02, and then to Tree 03. As a consequence of high ambient air temperatures, little wind, and prolonged instrument activity, the laser temperatures recorded for Tree 02 and Tree 03 (except Tree 03 NW) fell outside of the neural network training data (Figure 4.11; Table 5.6). Figures 5.23 and 5.24 also show that the number of returns are reduced in the NDI point clouds. This means that many returns were discarded during the calculation of the ratios (Section 5.5.4).

Table 5.6. Laser case temperature ranges for the tree scans. The scans shaded in orange are those where the temperature ranges are outside the neural network training data (see Figure 4.11).

Tree	Condition	Scan position	Temp min °C	Temp max °C
01	Leaf-off	S	22.8	24.4
01	Leaf-off	NE	25.5	25.9
01	Leaf-off	NW	25.6	26.2
01	Leaf-on	S	21.5	28
01	Leaf-on	NE	28.6	30.5
01	Leaf-on	NW	32.5	34.5
02	Leaf-on	NW	34.6	36.2
02	Leaf-on	SE	32.25	35.65
02	Leaf-on	SW	33.95	34.4
03	Leaf-off	S	24	24.5
03	Leaf-off	N	23.6	25.2
03	Leaf-on	NW	32.35	32.6
03	Leaf-on	NE	37	38.5
03	Leaf-on	S	35.8	36.4
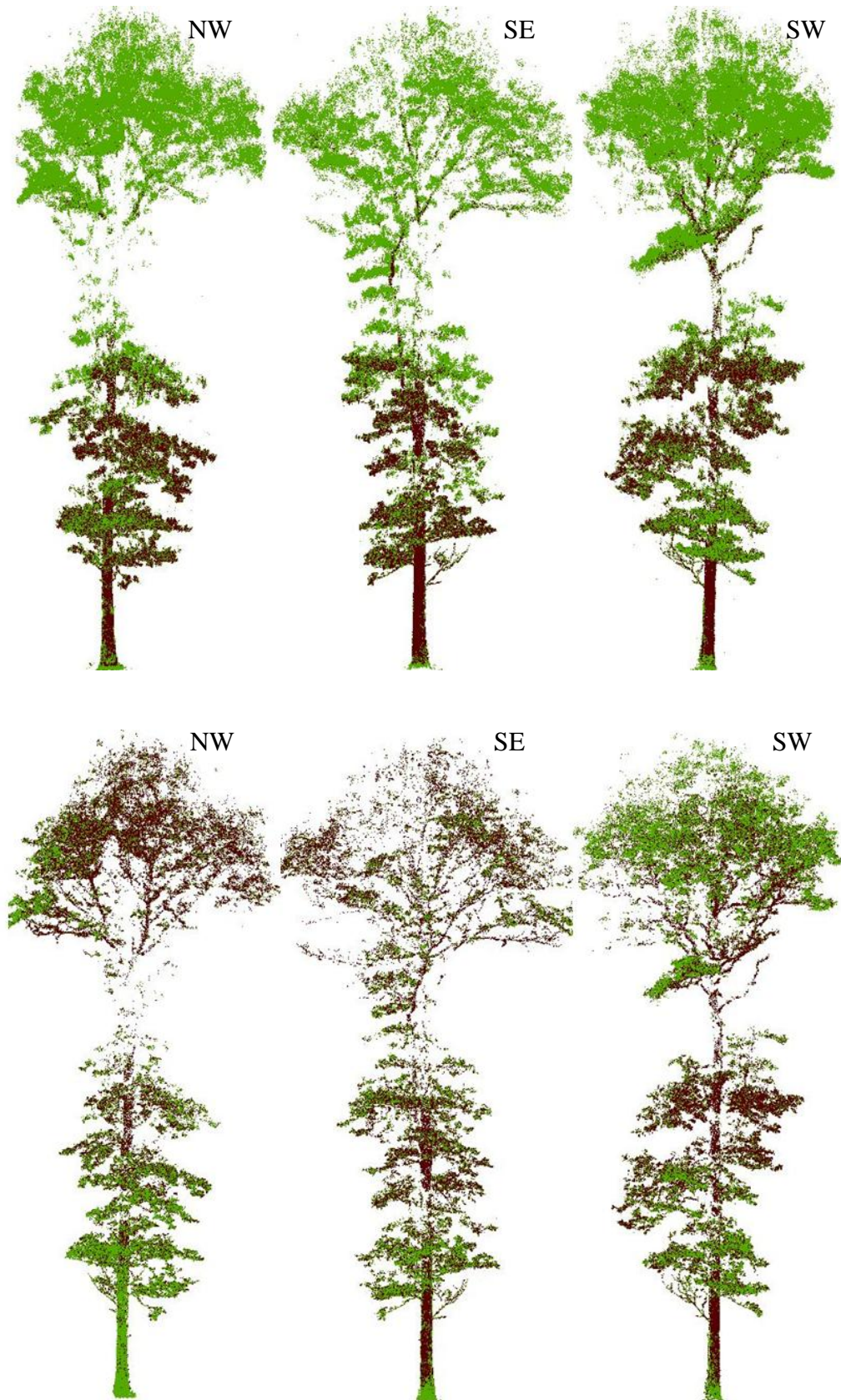
Figure 5.23. Point clouds for Tree 02 classified into 'leaf' or 'wood' using a 1545nm threshold of 0.29 (top) NDI threshold of 0.1 (bottom), for all three scanning positions. Images show leaf-on where green points have been allocated to 'leaf' category and brown points allocated to 'wood'.

Figure 5.24. Point clouds for Tree 03 classified into 'leaf' or 'wood' using a 1545nm threshold of 0.29 (top) NDI threshold of 0.1 (bottom), for all three scanning positions. Images show leaf-on where green points have been allocated to 'leaf' category and brown points allocated to 'wood'.

Figure 5.25 shows the result of the same methods applied to the two leaf-off scans for Tree 03. The two point clouds on the left are classified by single wavelength, and those on the right by NDI threshold, where returns classified as 'leaf' are displayed in blue. In a similar manner to the misclassifications seen in Tree 01, using the NDI produced lower misclassification errors (27.75% and 24.88%), compared to using the 1545nm wavelength alone (58.44% and 55.53%).
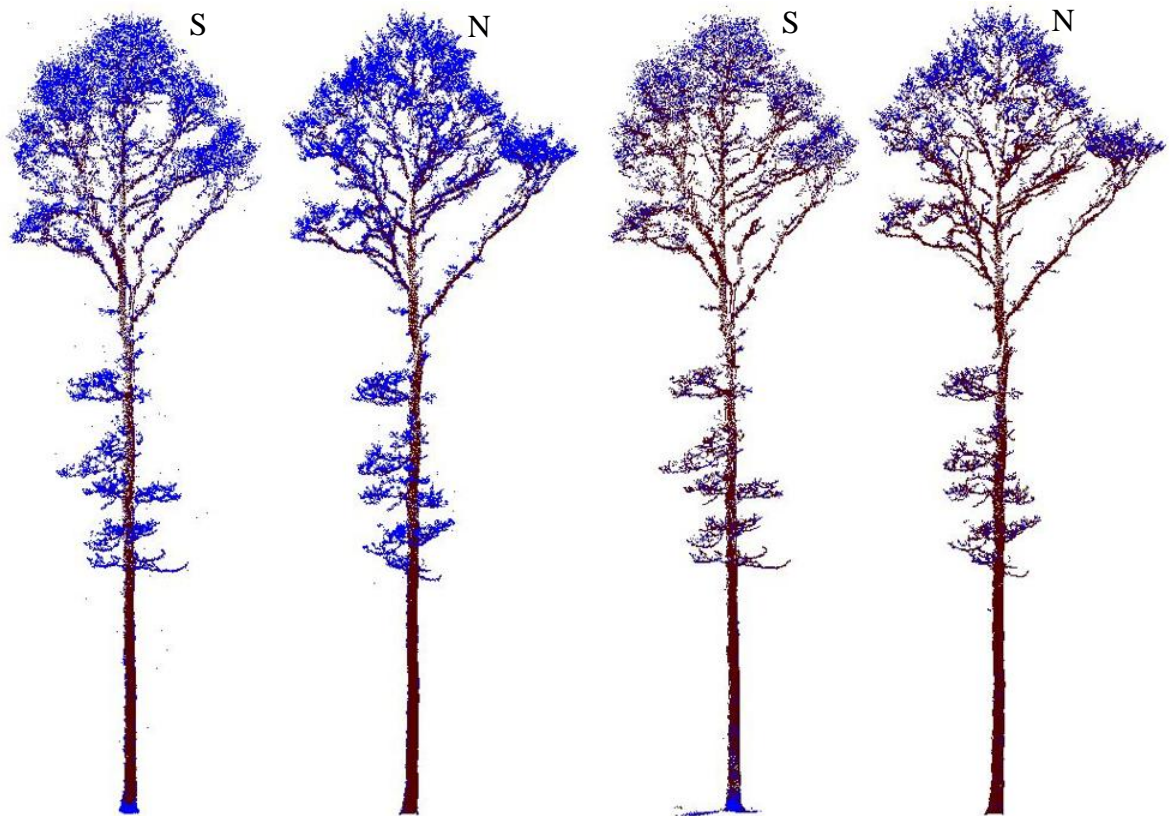
Figure 5.25. Point clouds for Tree 03 classified into 'leaf' or 'wood' using a threshold on 1545nm wavelength of 0.29 (left two images) and an NDI threshold of 0.1 (right two images), for all three scanning positions. Images show leaf-off where blue points have been allocated to 'leaf' category and brown points allocated to 'wood'.

5.7   Conclusion

This chapter used direct measurements and multiple-location TLS to investigate the characterisation of three individual oak trees. The data collection campaign was affected by adverse weather which prevented a full set of corresponding leaf-off and leaf-on scans from being acquired. Unfortunately, this is a well-documented limitation of TLS,

particularly in experimental instruments such as SALCA that have a longer scan time making them more susceptible to poor measurement conditions.

The upper part of a woody canopy often becomes a blind region in TLS measurements, a situation opposite to that in airborne laser scanning (Hosoi & Omasa, 2007). This occlusion in TLS scans proved to be a limiting factor, preventing sampling of the upper canopy. This was illustrated by the fact there were more returns in the upper canopy from the leaf-off scans than the leaf-on scans. Although this does not hinder the ability to separate leafy and woody material, it does mean that the amount of material in this region (and therefore LAI) will be underestimated. One way to overcome this limitation is to merge multiple scans and include scanning positions from higher elevations. Recent studies have combined airborne and ground-based scanners to eliminate the blind regions of each lidar (Hosoi & Omasa, 2007; Hosoi *et al.*, 2010). However, merging scans can introduce errors from overlapping coverage of laser returns and imperfect registration (Clawges *et al.,* 2007). The focus of this research was to observe and quantify change from a single viewpoint and therefore using a merged point cloud on the individual trees would have prevented common methods being applied between the field sites.

Three approaches were utilised to investigate the separation of leafy and woody material using the SALCA point clouds. Comparing the number of leaf-off and leaf-on returns by height stratum showed a positive relationship between number of 'leafy' returns and one-sided area of collected leaves, except for the upper canopy which was heavily affected by occlusion. The second method demonstrated that a separation of leaf and woody material could be achieved by applying a threshold on the 1545nm wavelength, however partial hits on wood were also included. The final method utilised the dual-wavelength capacity of SALCA by applying a threshold on a ratio of the apparent reflectance of both wavelengths. A reasonable output was generated although a certain amount of miss-classification was obvious from the leaf-on scans and calculated to be between 24% and 38% when applied to the leaf-off scans. The importance of having a robust apparent reflectance calibration has been highlighted in this chapter with the poor leaf and wood separation results seen in Tree 02 and Tree 03 where calibration inputs were outside of the range of the neural network training data. It is clear that further work is required to improve the robustness of the calibration procedure to better account for the temperature-dependent effects on recorded intensity.

CHAPTER 6

Tree leaf area index calculation and validation

6.1   Introduction

The aim of this chapter is to develop a method for estimating LAI at the tree scale from dual-wavelength TLS. Results were validated using direct destructive measurements collected at Alice Holt forest, discussed in Chapter 5. This provides a means to assess the leaf and wood separation developed in the previous chapter, and contributes to Objective 2 of this research.

6.2   Background

As described in Chapter 5, a cylindrical volume was fitted to the merged tree point cloud (with radius R, centre [cx cy], and height H) to calculate the crown projected area. The cylinder can be split into multiple vertical layers (L), each layer defined by the minimum (h_{min}) and maximum (h_{max}) height of the strata used for the direct measurements (Figure 6.1).
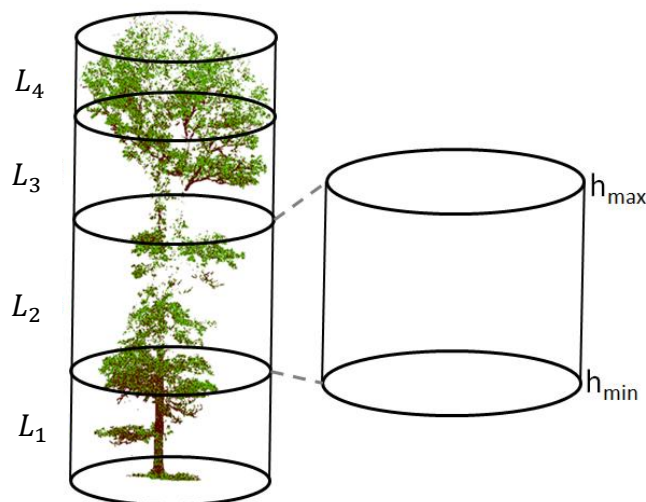
Figure 6.1. Graphical representation of Tree 01 point cloud encased in cylindrical volume with four vertical layers (L$_{1-4}$), each defined by a minimum (h$_{min}$) and maximum height (h$_{max}$).

126

The cylinder and cylindrical layers for each tree define the 3D space over which the direct LAI measurements are valid. These defined volumes therefore provide the basis for the LAI estimations from TLS. There are three prominent approaches for estimating LAI using point cloud data generated from a laser scanner (Chapter 2.7.2): hinge angle inversion, regression method of Jupp *et al.* (2009), and applying the principles of the Beer-Lambert Law. The first two approaches are based on a full canopy cover and are therefore not applicable to a single isolated tree which is of interest here. As a result, LAI was estimated based on the principles outlined in the Beer-Lambert Law which states that light transmittance through a solution depends upon the extinction coefficient, absorber concentration, and path length. Table 6.1 outlines the adaption of this approach to a single tree canopy.

Table 6.1. Adaption of the Beer-Lambert Law to estimate LAI for a single tree canopy from TLS

Parameter in Beer-Lambert Law	Parameter for single tree
Solution	*Tree point cloud*
	Based on the assumption that the light intercepting elements are randomly distributed. Figure 6.1 illustrates that leaves within the cylinder are clumped around branches rather than randomly distributed within the cylinder. The Clumping Index (Ω) was used to account for the deviation from random and translating effective LAI to true LAI.
Absorbance	*Gap Fraction*
	Based on the assumption that gap fraction is equivalent to transmittance.
Extinction coefficient	*Foliage orientation*
	Defined as the fraction of foliage area projected onto a perpendicular plane (G-function; Ross, 1981). A spherical leaf angle distribution is assumed where G is approximated to 0.5 (Martens *et al.*, 1993).
Concentration of solution	*Leaf Area Density*
	Based on the assumption of isotropic canopy radiation.
Path length through solution	*Path length through cylinder*
	The path length through the canopy is no longer a function of $\cos(\theta)$ as per a full cover canopy. For a cylinder, the path length is related to azimuth and zenith view angles in relation to the location and geometry of the cylinder. Normalised path lengths are used to scale gap fraction by the longest path length for each volume of interest.

6.3   Methods

A method for estimating LAI for a single tree was developed based on adaption of the Beer-Lambert Law (Table 6.1), and is outlined in this section.

6.3.1   Datasets and approach

An overview of the datasets and approaches utilised for the validation analysis are shown in Figure 6.2. Estimates of PAI were generated using all the returns from the 1545nm wavelength and those matched between the wavelengths during the NDI calculations. The 1545nm wavelength was chosen due to its ability to penetrate further into the canopy than the 1063nm wavelength. Due to the inclusion of woody material in the PAI approach, no spectral information is utilised and purely a binary presence or absence of material is considered. PAI was estimated by cylindrical layer, and for each dataset at the tree level (one tree cylinder) and by summing the PAI calculated for each layer.
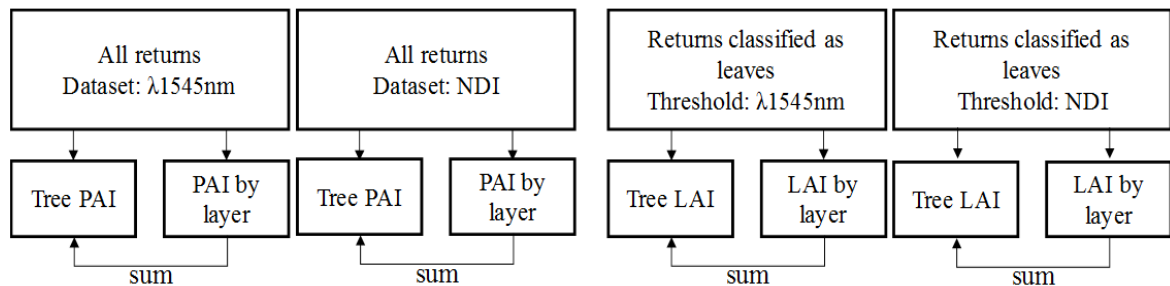
Figure 6.2. Overview of methods to calculate PAI and LAI

Estimates of LAI were generated using the returns classified as leaves and the thresholding methods outlined in Chapter 5: using the λ1545nm data, and using the NDI. Assuming that all the leaves have a similar apparent reflectance, the amount of leaf material for each measured returns can be accounted for using the calibrated apparent reflectance values in relation to the reflectance of a full hit on a leaf. LAI was estimated by cylindrical layer, and for each dataset at the tree level (one tree cylinder) and by summing the LAI calculated for each layer.

Due to the calibration issues for Tree 02 and Tree 03, the analysis in this chapter was applied only to Tree 01 where a reasonable leaf and wood separation had been achieved (Chapter 5). The leaf-on datasets for the three scanning positions (South, North-East and North-West) were analysed independently. The following section describes the basis for

128

PAI and LAI estimation calculation based on a modified Beer-Lambert Law approach, before the methods for calculating path length and Clumping Index are described.

6.3.2 Calculating PAI

Gap fraction $Pgap$ was calculated using all returns from each tree point cloud, for the entire tree and for each cylindrical layer (L):

$$Pgap = 1 - \frac{\sum w}{\bar{M}} \tag{6.1}$$

$$Pgap_L = 1 - \frac{\sum w_L}{\bar{M}_L} \tag{6.2}$$

where w is a weighting which sums to one for each laser beam, to allow for vertically resolved PAI from multiple return systems (Calders *et al*., 2015). $\bar{M}$ is the sum of available path lengths for the tree or the cylindrical layer $\bar{M}_L$ of interest. w is calculated as follows:

$$w = 1/n_s .\bar{S} \tag{6.3}$$

Where n_s is the number of total returns for the transmitted laser pulse and $\bar{S}$ is the normalised path length through the cylinder (or cylindrical layer) for that beam. This is based on two assumptions: an equal distribution of energy is intercepted at each return, and that the entire footprint is intercepted (i.e. a single return is assumed to be a full hit). $\bar{M}$ and $\bar{M}_L$ can be calculated for the following scenarios:

For λ1545 dataset

$$\bar{M} = \bar{S}_{total} \tag{6.4}$$

$$\bar{M}_L = \bar{S}_{total(L)} - \bar{S}_{occluded} \tag{6.5}$$

For NDI dataset

$$\bar{M} = \bar{S}_{total} - \bar{S}_{ratio} \tag{6.6}$$

$$\bar{M}_L = \bar{S}_{total(L)} - \bar{S}_{occluded(L)} - \bar{S}_{ratio(L)} \tag{6.7}$$

Where $\bar{S}_{total}$ is the total path lengths for all the laser beams that pass through the cylinder or cylindrical layer, $\bar{S}_{occluded}$ is the total path lengths for the beams that were occluded before reaching the target layer, and $\bar{S}_{ratio}$ is the total path lengths for the beams where

returns occurred in either wavelength dataset but they were not matched during the NDI calculations. The bar above the variables indicates that they are normalised path lengths, where a value of one is the maximum path length for each volume of interest. Plant area index is then calculated for the tree PAI and by layer PAI_L as follows:

$$PAI = \frac{-2 \ln (Pgap)}{\Omega} \tag{6.8}$$

$$PAI_L = \frac{-2 \ln (Pgap_L)}{\Omega_L} \tag{6.9}$$

$$PAI = \sum PAI_L \tag{6.10}$$

where Ω is the clumping index for the tree and by layer (Ω_L).

6.3.3 Calculating LAI

Foliage gap fraction $Pgap$ was calculated using the returns classified as leaves, for the entire tree and for each cylindrical layer (L):

$$Pgap = 1 - \frac{\sum i}{\overline{M}} \tag{6.11}$$

$$Pgap_L = 1 - \frac{\sum i_L}{\overline{M}_L} \tag{6.12}$$

where i is a weighted leaf reflectance to account for the amount of material in the beam footprint:

$$if \ \sum \rho \geq \rho_{leaf}, \quad i = \frac{\rho}{\sum \rho}.\overline{S} \tag{6.13}$$

$$if \ \sum \rho < \rho_{leaf}, \quad i = \frac{\rho}{\rho_{leaf}}.\overline{S} \tag{6.14}$$

where ρ is the apparent reflectance of a return at $\lambda 1545nm$ and ρ_{leaf} is the apparent reflectance of a full hit on a leaf at $\lambda 1545nm$, and $\overline{S}$ is the normalised path length for that beam. $\overline{M}$ is the sum of available path lengths for the tree or the cylindrical layer $\overline{M}_L$ of interest, and can be calculated for the following scenarios:

For λ1545 threshold

$$\bar{M} = \bar{S}_{total} - \bar{S}_{wood} \tag{6.15}$$

$$\bar{M}_L = \bar{S}_{total(L)} - \bar{S}_{occluded(L)} - \bar{S}_{wood(L)} \tag{6.16}$$

For NDI threshold

$$\bar{M} = \bar{S}_{total} - \bar{S}_{ratio} - \bar{S}_{wood} \tag{6.17}$$

$$\bar{M}_L = \bar{S}_{total(L)} - \bar{S}_{occluded(L)} - \bar{S}_{ratio(L)} - \bar{S}_{wood(L)} \tag{6.18}$$

Where $\bar{S}_{total}$ is the total path lengths for all the laser beams that pass through the cylinder or cylindrical layer, $\bar{S}_{occluded}$ is the total path lengths for the beams that were occluded before reaching the target layer, and $\bar{S}_{ratio}$ is the total path lengths for the beams where returns occurred in either wavelength dataset but were not matched during the NDI calculations. $\bar{S}_{wood}$ is the total path lengths for the returns classified as woody material. The bar above the variables indicates that they are normalised path lengths, where a value of one is the maximum path length for each volume of interest. Leaf area index is then calculated for the tree LAI and by layer LAI_L as follows:

$$LAI = \frac{-2 \ln (Pgap)}{\Omega} \tag{6.19}$$

$$LAI_L = \frac{-2 \ln (Pgap_L)}{\Omega_L} \tag{6.20}$$

$$LAI = \sum LAI_L \tag{6.21}$$

where Ω is the clumping index for the tree and by layer Ω_L.

6.3.4   Calculating path length, $\bar{S}$

A set of Cartesian coordinates (x,y,z) were generated to simulate all the laser beams that are emitted in a full scan, at maximum recorded range (60m). The beams that made contact with the cylinder were extracted, based on the geometry of each shot and the outer bounds of the cylinder (Figure 6.3).
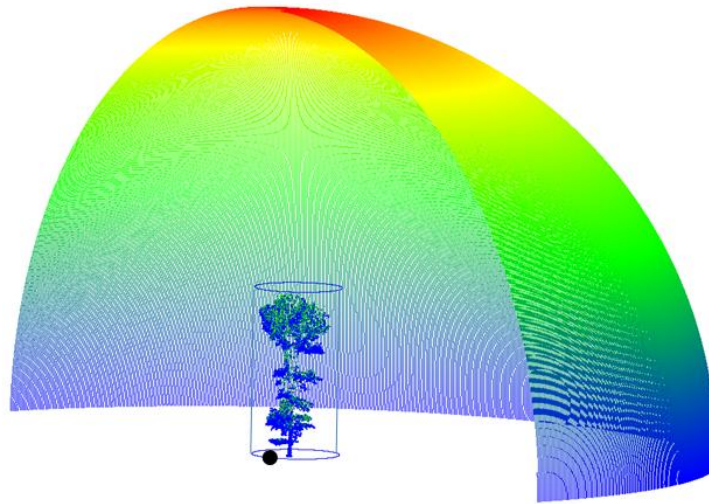
Figure 6.3. Graphical representation of simulated beams (dome of points symbolised by zenith angle) that pass through the cylinder containing the tree point cloud, the black circle shows the location of the SALCA instrument.

For each selected beam, the path length S through the cylinder was calculated using the following protocol, which is illustrated in Figure 6.4. Each laser beam can be defined as a straight line that passes through the origin (0,0,0: SALCA position) and the x,y,z coordinate of the simulated point. On the horizontal plane, the straight line can be described in the form $y = mx$, where $m = y/x$. Similarly, each cylinder's cross-sectional circle is defined by its centre point (cx, cy) and radius (R) in the form $(x-cx)^2+(y-cy)^2 = R^2$. The intersection points of the circle and the lines were calculated which returned two points: the point where the beam enters the cylinder (x_1, y_1) and the point where the beam exits the cylinder (x_2, y_2). The distance between the origin and the first intersection point (a) and the distance between the intersection points (b) were then computed for each laser path. Distance b represents the horizontal distance that each beam travelled through the cylinder. The vertical distances were then calculated between the origin and the first intersection point (c) and between the two intersection points (d), using the elevation angle (θ). When the beam exits the top of the cylinder (c + d > height of cylinder (H)), length d was re-calculated as H-c. The path length (S) was then computed for each laser beam. Each path length was then normalised by the maximum path length to become a weighting between 0 and 1, to give $\bar{S}$.
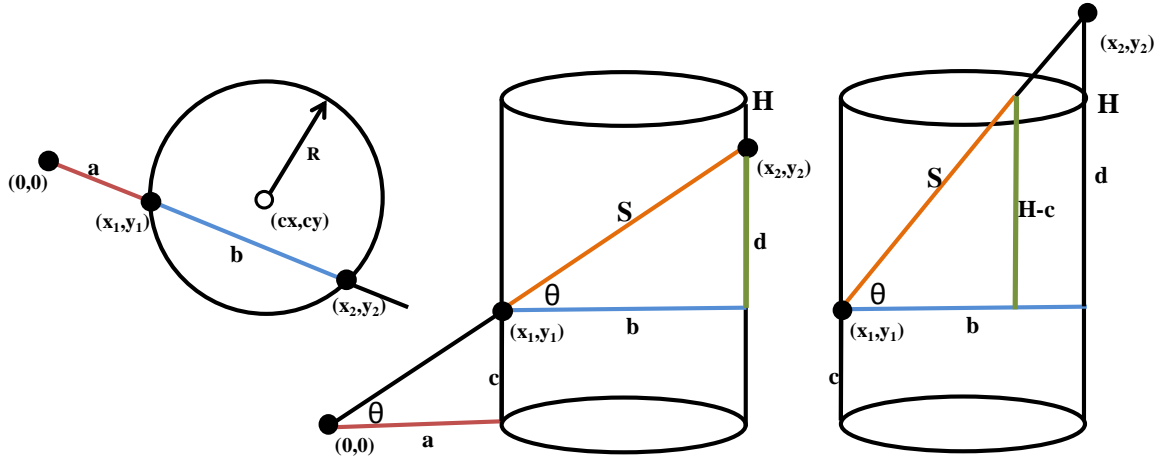
Figure 6.4. Calculating path length through a cylinder for each laser beam

The above calculations compute the normalised path lengths for the entire cylinder, used when estimating the gap fraction for the tree as a whole. When estimating gap fraction by layer, the above method was adjusted to calculate the path lengths for each cylindrical layer independently. Furthermore, in the case that the origin was located within the cylinder, the protocol was adjusted accordingly.

6.3.5   Calculating clumping index, Ω

Accounting for clumping is not a trivial task, several methods have been developed to attempt to deal with this complex problem but there is no current consensus on a solution. For this research, a 3D point pattern analysis approach was adopted. This method was chosen due to the incorporated of a volume parameter, which would allow the cylindrical volumes to be represented within the analysis.

The clumping index was calculated directly from the point clouds for each layer Ω_L, and for the entire cylinder Ω, following a nearest neighbour distance analysis. The approach was adapted for 3D point clouds generated from laser scanning systems by Ramirez (2011), and involves calculating the average Euclidean distance for each point to its closest neighbour ($\overline{NND}$):

$$\overline{NND} = \frac{\sum NND}{n} \tag{6.22}$$

where NND is the nearest neighbour distance for all points and n is the number of points. The average nearest neighbour distance for a random arrangement of points ($\overline{NND_R}$) within the same volume (McGrew & Monroe, 2003) is also computed:

$$\overline{NND_R} = \frac{1}{2\sqrt{Density}} \qquad (6.23)$$

where *Density* is equal to the number of points divided by the volume. Then the clumping index is calculated by comparing the two outputs:

$$\Omega = \frac{\overline{NND}}{\overline{NND_R}} \qquad (6.24)$$

The resultant clumping index would equal one or zero if the point cloud had a perfectly random or clustered spatial arrangement, respectively. As the method was developed for estimation of clumping index by zenith and azimuth interval for a full plot, it was amended to the cylindrical volume approach adopted in this research.

An illustration of the approach applied to estimating Ω_L is shown in Figure 6.5. The tree point cloud is divided into the four vertical layers to reflect the direct measurements (cylinder on right) and can be compared to the same number of points located randomly inside the same volumes (cylinder on left). Clustering analysis was carried out using all the returns (for PAI) and the leaf returns (for LAI), for each scanning position and cylinder independently.
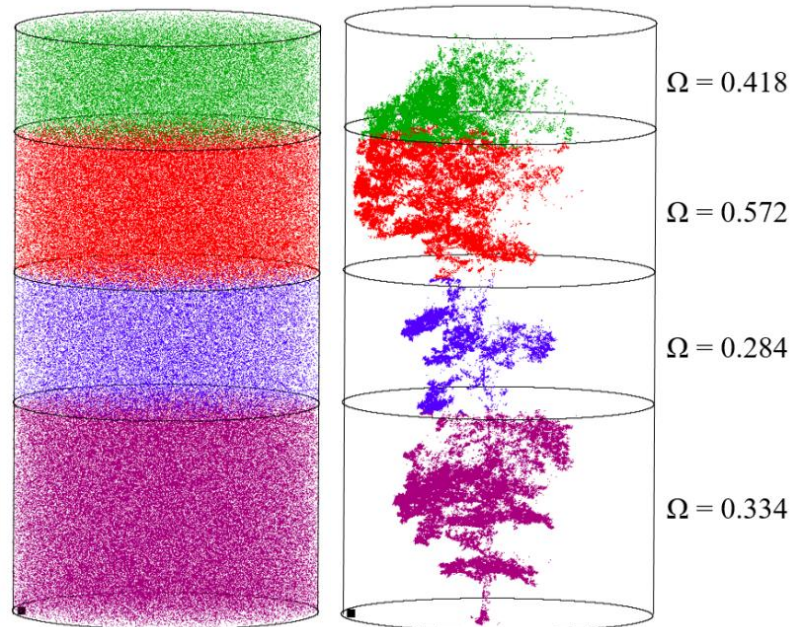
Figure 6.5. Graphical illustration of clumping index estimation by cylindrical layer. Left image shows randomly located points within the layers, and right image shows the tree point cloud. Using the nearest neighbour analysis generates the clumping indexes to the right. The Ω values shown are for the South scanning position for Tree 01 for leaf-only returns. The black square (bottom left of both cylinders) shows the position of the TLS.

6.4   Results and discussion

Figure 6.6 shows the relationship between the estimated PAI derived from TLS and the direct measurements of LAI, for Tree 01. The values are shown by vertical strata (L1-L4) for the two datasets (λ1545nm and NDI) and for the three scanning positions (South, North-East, North-West). The total tree PAI values are also shown in each graph by the two methods used for calculation; using a single cylinder (closed circles) and summing the four layers (open circles).

For the four strata, both datasets showed a similar pattern. An overestimation of LAI from TLS was observed for the bottom three layers (L1, L2, L3). This was due to the inclusion of woody material in the calculations. The highest vertical layer (L4) shows a significant underestimation of LAI using TLS. Despite the methods that were in place to acount for occlusion, these results suggest that the top of the tree canopy was not sampled sufficiently to allow an accurate estimation of LAI.

Figure 6.6 shows that summing the layers generates a PAI closer to the measured value, due to the fact that this method deals with some of the effects of occlusion. However, due to the underestimation of layer 4 seen in all of the datasets, an accurate tree PAI estimation has not been produced.
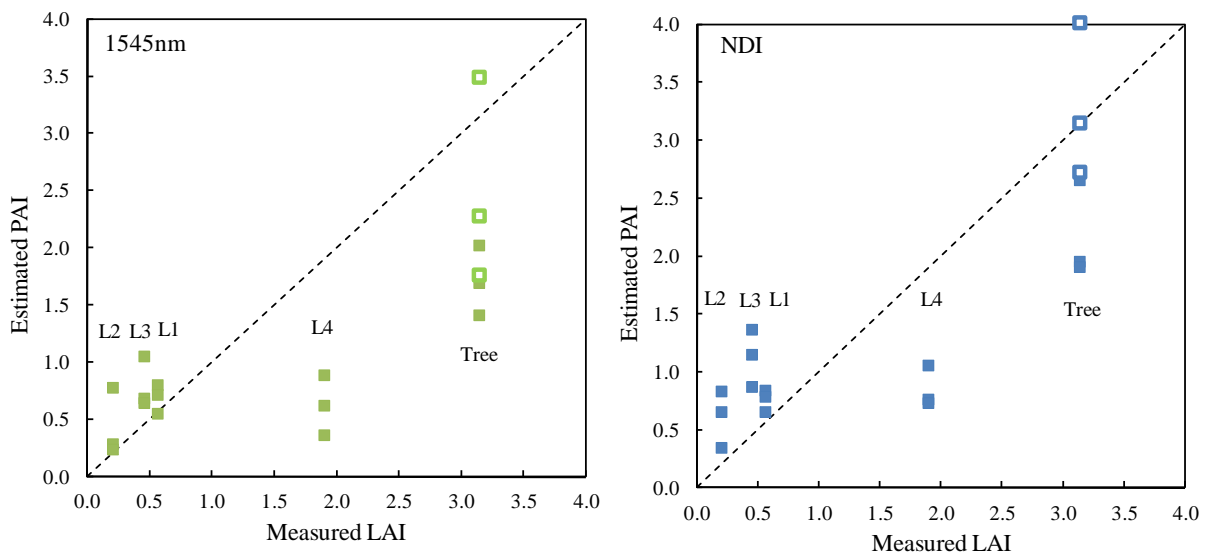
Figure 6.6. Relationship between estimated PAI from TLS and measured LAI for the four vertical layers (L1-L4) and total tree for Tree 01 for datasets 1545nm (left) and NDI (right). Solid squares indicate single cylinder for the layer/tree and empty squares indicate summing of layers.

Figure 6.7 shows the estimated LAI values for Tree 01 and by tree layer (L1-L4) and for the three scanning positions (South, North-East, North-West). Two thresholding methods have been used to determine the returns resulting from leaves, based on the ρ1545nm and the NDI. Compared with Figure 6.6, using the leaf component of the point cloud and accounting for the amount of material in the footprint has generated estimates of LAI of a similar magnitude to the direct measureements, for layers 1 to 3. The underestimation of LAI for the toppmost layer, and the tree scale estimates is still evident. However, from removing the 'woody' returns and accounting for partial hits, the variance between estimates from the different scanning positions has decreased.
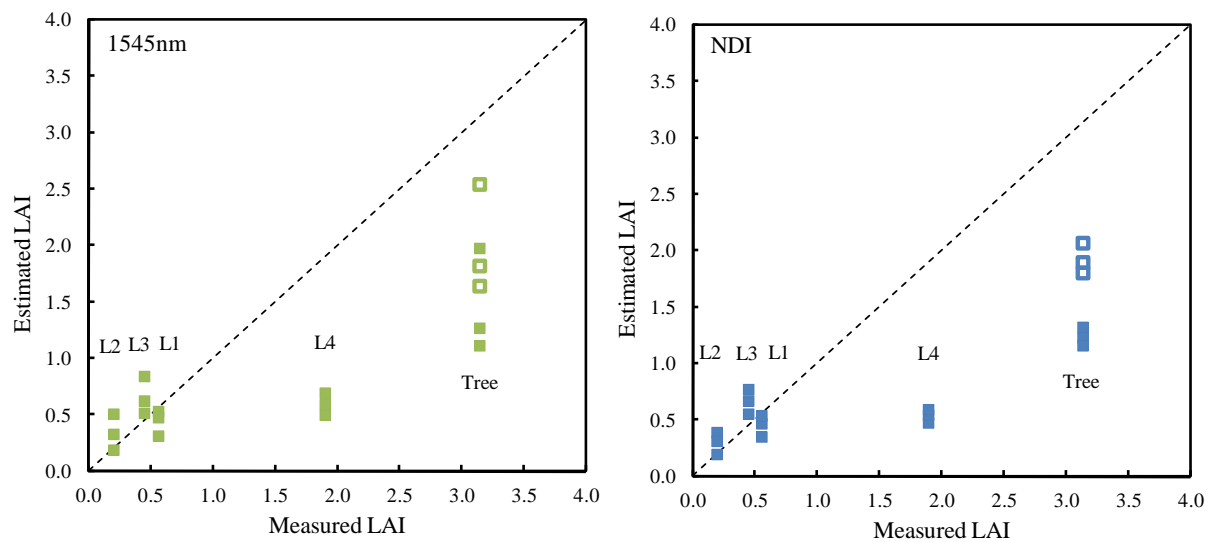
Figure 6.7. Relationship between estimated LAI from TLS and measured LAI for the four vertical layers and total tree for Tree 01.

Although the results outlined above suggest that this approach has potential for calculating LAI for a single tree from dual-wavelength TLS, it is clear that further research is required into this experimental approach, particularly in the areas acknowledged in Table 6.2. This chapter also highlights the challenges that exist when attempting to validate the performance of a leaf-wood classification for a real tree (as opposed to a virtual tree construction). In this research, an attempt to validate the 'leaf' component has been made via the parameter of LAI. As there is no standard method for estimating LAI for individual trees, uncertainties will be introduced from both the leaf-wood separation procedure and the LAI calculations, and the two sources of error cannot easily be uncoupled.

Table 6.2. Discussion of factors relating to the approach that require further attention.

Factor	Discussion
Field protocol	To ensure an accurate validation of the TLS-derived LAI with the direct LAI, further consideration should be given to the assignment of height strata. For instance, during the direct measurements, the tree was divided into height strata based on the measured position along the trunk. Therefore, the leaves were assigned to a height strata bases on the height position of their branch. In contrast, for the tree TLS point cloud, each return in the point cloud was assigned to a height strata based on the z-value that it was located (e.g. Figure 6.5). This is most important for the upper layers where the majority of leaf material is present. A possible solution would be to combine the upper two layers. This may improve accuracy as L3 is currently over-estimated, and L4 underestimated (Figure 6.6 and 6.7).
Beer-Lambert Law	This approach is based on a number of assumptions, as outlined in Table 6.1. Further investigation is required to ensure that the modified Beers-Lambert Law approach is valid for the scenario present in this chapter.
Validation	The results in Figure 6.7 suggest that TLS-derived LAI has a higher accuracy at low LAI. However, in order to characterise the relationship (and therefore assess the accuracy) of the measured and estimated parameters, a more extensive dataset may be required which includes a full range of LAI values. Once the reflectance calibration has been improved for the remaining two trees for which validation data is available, a larger dataset will be available.
Occlusion	The LAI for the upper layer of the canopy is currently underestimated (Figure 6.6 and 6.7). This may be partly due to differences into assigning the leaf returns to height strata (as discussed above), but further consideration should be given to occlusion in the tree canopy, to ensure that this significant factor is accounted for in the calculations.
Clumping	The Clumping Index is used as a correcting factor in the calculations to convert effective LAI to true LAI, and its value has a substantive impact on the results. Correcting for clumping is a complex problem in TLS and investigation of alternative methods to derive the Clumping Index could be sought and compared to those generated here.
Leaf-wood separation	Future consideration should also be given to improving the leaf-wood separation for Tree 01 which may improve the LAI calculations. This includes improving the reflectance calibration and further investigation into defining the spectral-based threshold applied to perform the classification into the two components.

6.5   Conclusion

In order to fulfil the aim of this chapter and contribute to research Objective 2, a method for estimating LAI on the tree scale using dual-wavelength TLS has been developed. This was carried out by considering the tree point cloud as a set of 3D points encased in a cylindrical volume. PAI and LAI were estimated based on the principles outlined in the Beer-Lambert Law. The approach outlined above also attempted to account for observations discussed in previous chapters:

- Effect of occlusion (Chapter 2, Chapter 5) – splitting the cylinder into multiple vertical layers allowed for the beams to be identified that should pass through the target layer but were blocked by lower vegetation.
- Returns not included in the NDI point clouds (Chapter 5) – the returns were identified which were present in either wavelength point cloud but not matched during the NDI process.
- Overestimation of LAI due to inclusion of woody material (Chapter 2) – returns classified as wood were removed from the point cloud so that true LAI could be computed. Furthermore, the beams blocked by woody material were accounted for during the LAI calculations as a further measure for correcting for occlusion.
- Overestimation of LAI due to the inclusion of partial hits (Chapter 2) - Using a foliage only point clouds allows the apparent reflectance for each return to be scaled by the reflectance of a full hit on a leaf, therefore accounting for the amount of material in the footprint.

The novelty in the approach described in this chapter lays in the utilisation of single scan, large single tree, leaf-only TLS point clouds, but more work is required to ensure the validity and application of approach. The following chapter examines the separation of woody and leafy material on plot scale and generation of plot PAI and LAI, for the five test plots surveyed at Delamere Forest.

CHAPTER 7

Spatial characteristics of foliage distribution at plot scale

7.1   Introduction

This chapter contributes to Objective 3 of this research: to examine the spatial and temporal characteristics of foliage in a range of UK forest types, using data acquired during the Delamere multi-temporal field campaign. A leaf-off and leaf-on scan was selected for each plot to assess the spectral separability of leafy and woody material across the different species. To fulfil the objective, the spatial distribution of foliage across the different stands was then examined.

The multi-temporal field campaign undertaken at Delamere Forest resulted in 57 datasets acquired over the five plots (Plot 1 = 18 scans, Plot 2 = 17 scans, Plot 3 = 14 scans, Plot 4 = 5 scans, Plot 5 = 2 scans) throughout a full year from April 2014 to April 2015 (Figure 7.1). On each visit, TLS scans were collected with the SALCA instrument together with coincident digital hemispherical photographs (DHP), according to the protocol outlined in Chapter 3. DHP images are not available for the last two visits to Delamere due to file corruption within the camera. Although unfortunate not to have a full set of coincident images, a comparison between TLS and DHP is still possible using the data available.

The datasets selected for examination in this chapter are highlighted in Figure 7.1. The chosen scans represent a winter (leaf-off for deciduous stands) and summer (full-leaf for deciduous stands) scenario which was used to investigate the spectral and structural characteristics of the plots. To aid comparison between plots, the dates chosen were as close together in time as possible: plot 1 and plot 2 acquired on 1st April and 31st July; plot 3 acquired on 2nd April and 31st July; plot 4 acquired on 9th April and 7th August, and; plot 5 acquired on 9th April and 2nd September. These scans are all high resolution (0.06°in both azimuth and zenith) with a maximum laser range of 60m.

Spectral data was collected from four of the plots (Plots 1-4) on a single date in full leaf (17th July 2014; Julian day 198). These were used to assess the spectral separability of materials for each of the tree species used in this campaign. No ASD spectral measurements were taken at Plot 5 as access to this part of the forest was not permitted when the equipment was available.
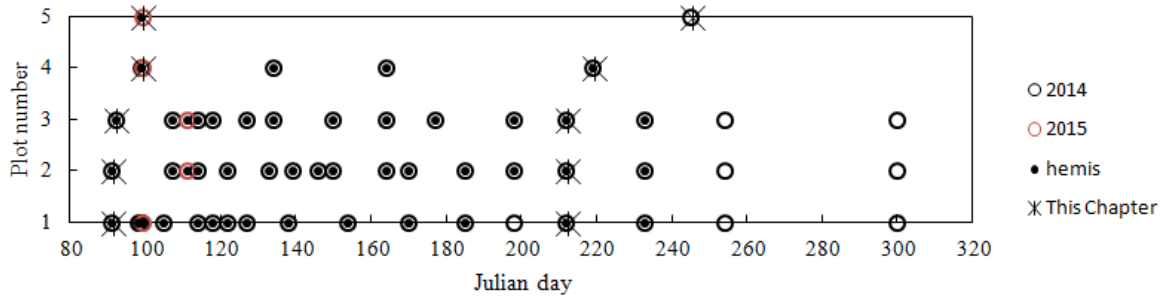
Figure 7.1. Summary of the Julian day on which each dataset was acquired. Open black circles represent dates in 2014 and open red circles are dates in 2015. Dates where coincident hemispherical photographs were acquired are shown in filled black circles, and the dates chosen for analysis in this chapter are highlighted using asterisks.

7.2   Methods

The selected hemispherical photographs were analysed to measure gap fraction and LAI according to the protocol outlined in Chapter 3. Rather than a single tree basis of Chapter 6, this chapter considers the plot scale and therefore adopts the 'hinge' and regression methods of LAI (or PAI) and FAVD (or PAVD). Both these methods allow clumping to be partly accounted for within the calculations and allow a comparison between approaches (Jupp *et al.*, 2009).

The TLS datasets were analysed in two ways, first, all returns from both wavelengths were used to obtain gap fraction using the point-based approach. Then plant area index (PAI), and profiles of plant area volume density (PAVD) were generated. Second, each leaf-on scan was classified into returns resulting from hits on leaves and those from wood in order to estimate foliage gap fraction using the apparent reflectance based-approach, leading to true LAI, and FAVD at the plot scale. The following sections outline the methods in more detail.

7.2.1   Gap fraction from all returns
Calculating gap fraction using all the returns from a scan in a point-based approach is analogous with DHP data analysis, due to the inclusion of woody material. Therefore, the

full point clouds were analysed to allow a comparison with DHP. Figure 7.2 shows the workflow for the analysis of a SALCA-derived point cloud to achieve estimates of gap fraction, PAI, and PAVD.
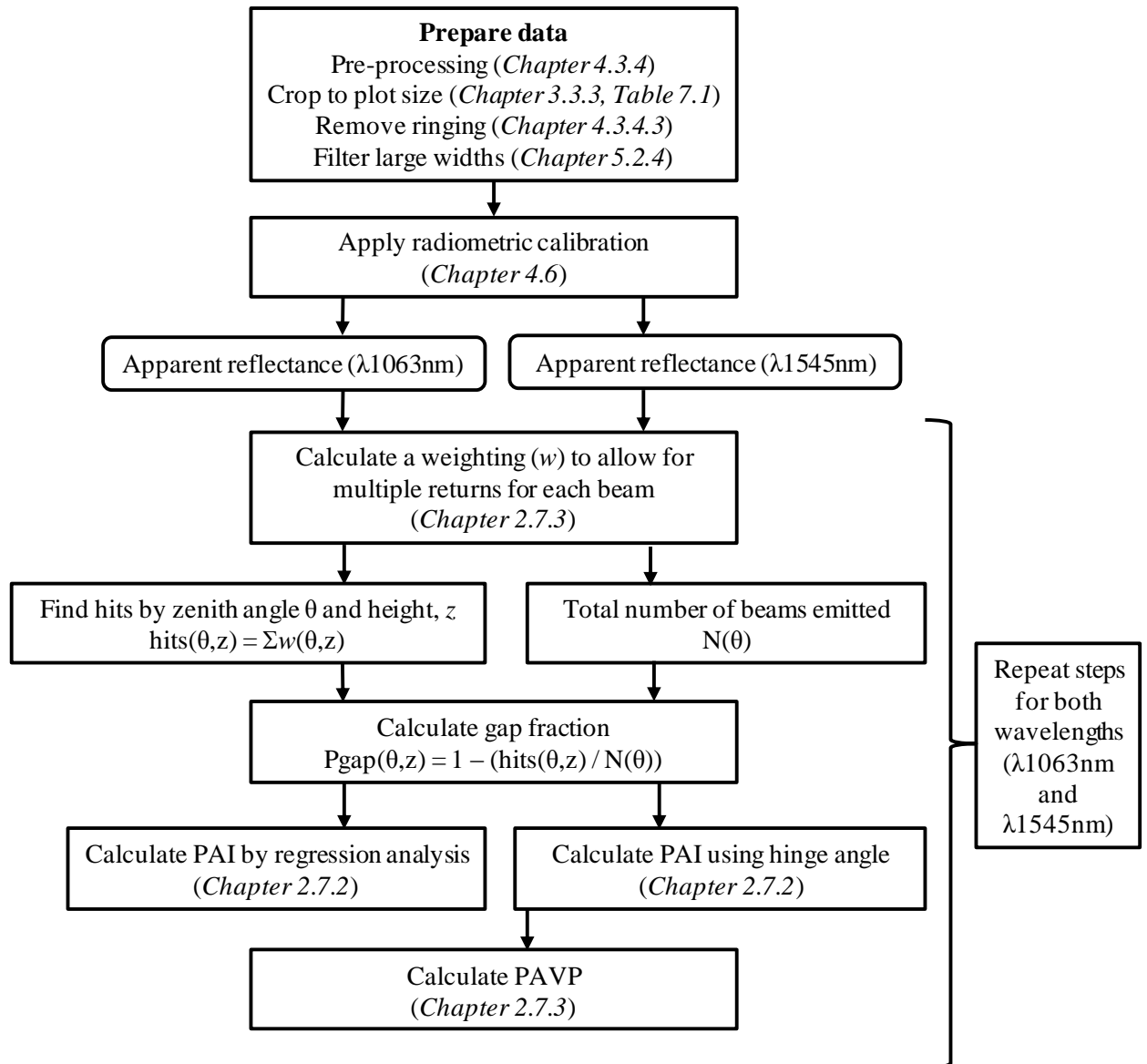
Figure 7.2. Workflow for the analysis of a SALCA point cloud to achieve estimates of PAI and PAVD.

Each TLS scan was prepared for analysis by applying pre-processing algorithms to extract discrete returns from the full-waveforms, the point cloud was cropped to the defined radial area (Chapter 3), the effect of ringing removed (Chapter 4), and the overlapping returns split into single hits (Chapter 5). The artificial neural networks developed in Chapter 4

were then applied to produce an apparent reflectance product for every return in both wavelengths. To enable a vertically resolved directional gap fraction using multiple returns, each measured 'hit' in the gap fraction calculation was scaled by the number of returns for each laser beam, to generate a weighting *w* (Calders *et al*., 2011) (Chapter 2.7.3, Equation 2.8). The weights were then summed by zenith interval for each height bin, and divided by the total number of beams emitted for that zenith interval, to generate an estimate of gap fraction. PAI was estimated using two methods: regression analysis (Jupp *et al*., 2009) and hinge angle inversion (Warren-Wilson, 1963). Finally, vertical plant profiles were derived following Jupp *et al*. (2009).

7.2.2 Gap fraction from leaf returns

Figure 7.3 shows the analysis workflow to achieve estimates of true leaf area index and foliage profile. The datasets for each scan was processed to apparent reflectance product for each wavelength and the Normalised Difference Index (NDI) was calculated for all matching returns. Following the approach in Chapter 5, leaf-off and leaf-on histograms were examined to define thresholds to separate leaf returns from woody returns based on two approaches: using a single channel (λ1545nm), and using the NDI. In a similar manner to Chapter 6, the apparent reflectance for each return was scaled by the reflectance of a full hit on a leaf to account for the amount of material in the footprint. This methodology is described in the following equations:

$$if \ \sum \rho \geq \rho_{leaf} \ \ i = \frac{\rho}{\sum \rho} \tag{7.1}$$

$$if \sum \rho < \ \rho_{leaf} \ \ i = \frac{\rho}{\rho_{leaf}} \tag{7.2}$$

where ρ is the reflectance of a hit, i is the apparent reflectance of a leaf return at λ1545nm and ρ_{leaf} is the reflectance of a full hit on a leaf, i is a parameter to account for the amount of leaf material in the beam footprint. The sum of i for each beam is equal to one for a full interception and is equal to zero for no leaf material in the footprint.

The vertically resolved directional gap fraction ($Pgap$) is then calculated as follows:
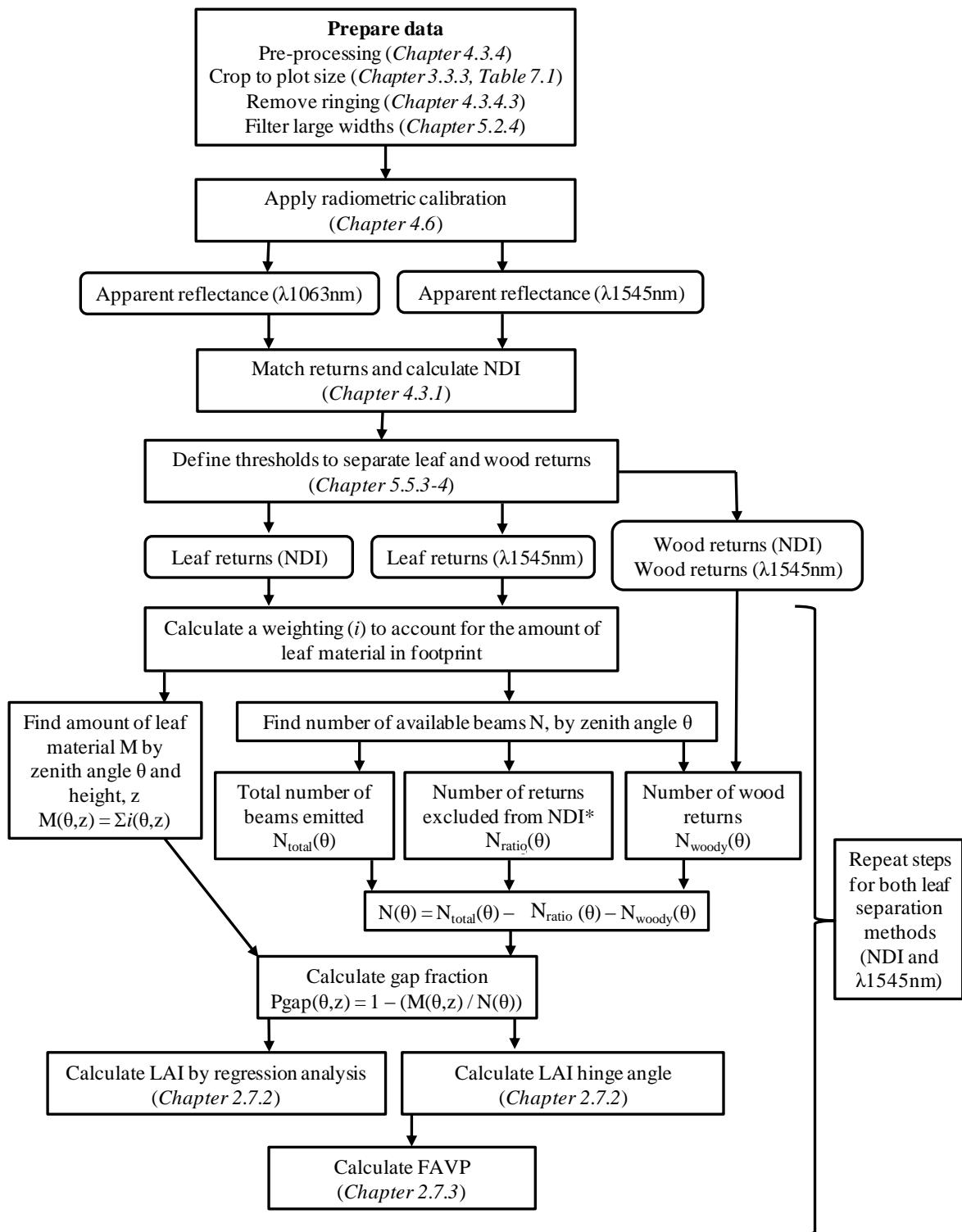
Figure 7.3. Workflow for the analysis of a SALCA point cloud to achieve estimates of LAI and FAVD. Step marked with * is not required for leaf returns on single channel

$$Pgap(\theta, z) = 1 - \frac{\sum i(\theta, z)}{N(\theta)} \tag{7.3}$$

where N is the number of available beams for the zenith angle θ and is defined as:

$$N(\theta) = N_{total}(\theta) - N_{ratio}(\theta) - N_{woody}(\theta) \tag{7.4}$$

where N_{total} is the total number of beams emitted, N_{ratio} is the number of returns that are present in either wavelength but were not matched and therefore were excluded from the NDI (not applicable for single channel method), and N_{woody} is the number of woody returns, for each zenith angle θ. As in the previous section, LAI was estimated using two methods; regression analysis (Jupp *et al.*, 2009) and hinge angle inversion (Warren-Wilson, 1963) and, vertical foliage profiles derived following Jupp *et al.* (2009). This workflow was followed for each of the thresholding methods independently.

7.3   Results and discussion

7.3.1   Plot characteristics

DHP images for the five plots in their 'winter' and 'summer' states are shown in Figure 7.4. The canopies of Plots 1-3 composed of broadleaf deciduous species, transform from open woody structures in a leaf-off state to closed canopies during summer when foliage development has reached maturity. The evergreen coniferous species which comprise Plot 4 show minimal visual changes from a summer to winter state. Green material is visible on the winter DHP of plot 5, the deciduous conifer, confirming field notes that this stand was not in an entirely 'leaf-off' state. This was caused by felling works in the area which delayed when the leaf-off scan was possible. As a result, bud-burst and leaf unfolding had already commenced in some of the individuals. However, comparison with the summer scan of the same plot confirmed that there was still a large amount of foliage development that could be assessed between the dates.
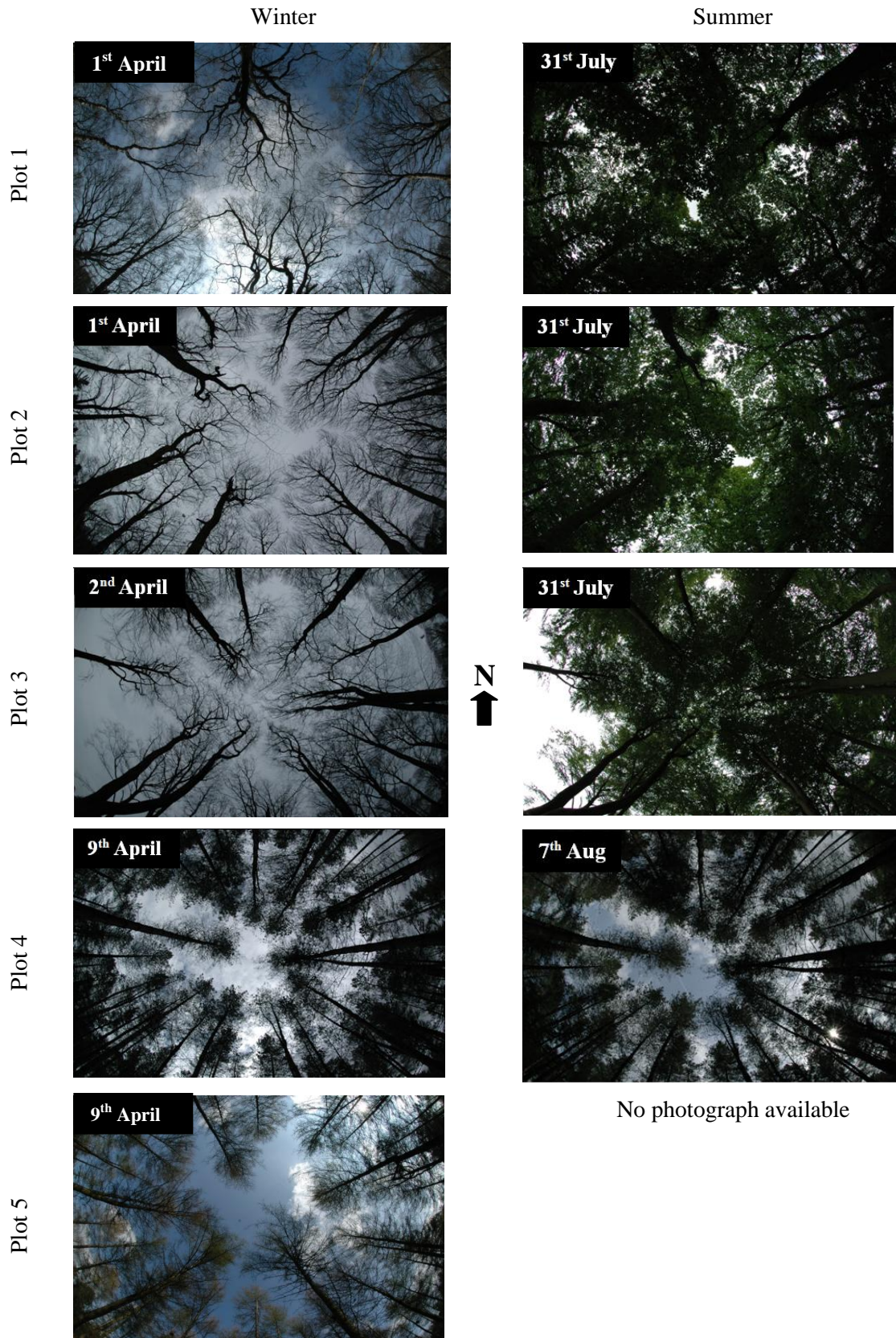
Figure 7.4. DHP images of the plots in winter and summer conditions, at the dates chosen for the analysis in this chapter.

The three-dimensional nature of TLS data allowed plot measurements to be generated which are impossible from DHP. Table 7.1 shows the height of the tallest trees (top height) and resultant plot radius for each plot, defining the area within which the TLS measurements are assumed to be valid. The height and radius measurements were calculated following the procedure in Chapter 3.3.3 from the winter TLS scans. The lowest top height occurred in Plot 5 which therefore resulted in the smallest plot radius of 36.4m in radius, compared with plot 2 which contained the tallest top height and plot radius of 44.7m.

Table 7.1. Plot top height and resultant plot radius for the five plots.

Plot	Top height (m)	Plot radius (m)
1	22	38.1
2	28	44.7
3	23	39.8
4	23	39.8
5	21	36.4

7.3.2   Leaf and wood spectral results

Spectral measurements in Plot 1 were carried out on one Oak tree located directly to the South of the plot centre. The median reflectance of ten bark samples and ten leaf samples at SALCA wavelengths are shown in Figure 7.5. According to these results, bark has a similar reflectance at both wavelengths, and leaves have a lower reflectance at 1545nm compared with 1063nm. For both wavelengths, leaf reflectance is lower than bark reflectance.

Fifteen bark ASD measurements and five leaf samples were taken at Plot 2. The results indicate that the reflectance of bark has high variance at both wavelengths but shows similar values, whereas leaf reflectance is lower at 1545nm compared to 1063nm and has lower variance. For the 1063nm wavelength, bark has a similar reflectance to leaf, whereas at 1545nm bark has a higher reflectance than leaves.

For Plot 3, spectral measurements of fifteen beech bark and ten leaf samples showed that bark has a similar reflectance at both SALCA wavelengths. The leaf measurements indicate that beech leaves have a lower reflectance at 1545nm compared to 1063nm. For

the 1063nm wavelength, bark and leaf material showed a similar reflectance, and at 1545nm bark had a higher reflectance than leaves.

Both bark and needles show a lower reflectance at 1545nm than 1063nm in Plot 4 (evergreen conifers). The measurements consist of five samples on three trees (Scots pine, Weymouth pine, Corsican pine) and five samples on a mixed bunch of same species of needles. The leaf samples showed a large amount of spectral variability, particularly at 1063nm.

As discussed in Chapters 2 and 4, it is expected that leaves and bark have a similar reflectance at 1063nm, whereas at 1545nm leaves are expected to exhibit a lower reflectance than bark due to leaf moisture content (which is the case for all four plots). The results presented here indicate that spectral response varies between species and, most notably for bark measurements, shows a high amount of spectral variability. However, these results are limited by the measurement challenges faced during spectral data collection (particularly for Plot 4; Chapter 3), the limited number of samples taken, and the instrument differences between the ASD and a laser scanner. It should also be noted that the plots contain other species besides those sampled and trees of different ages, particuarly in Plots 1 and 4 which further complicates characterising spectral response at stand level.
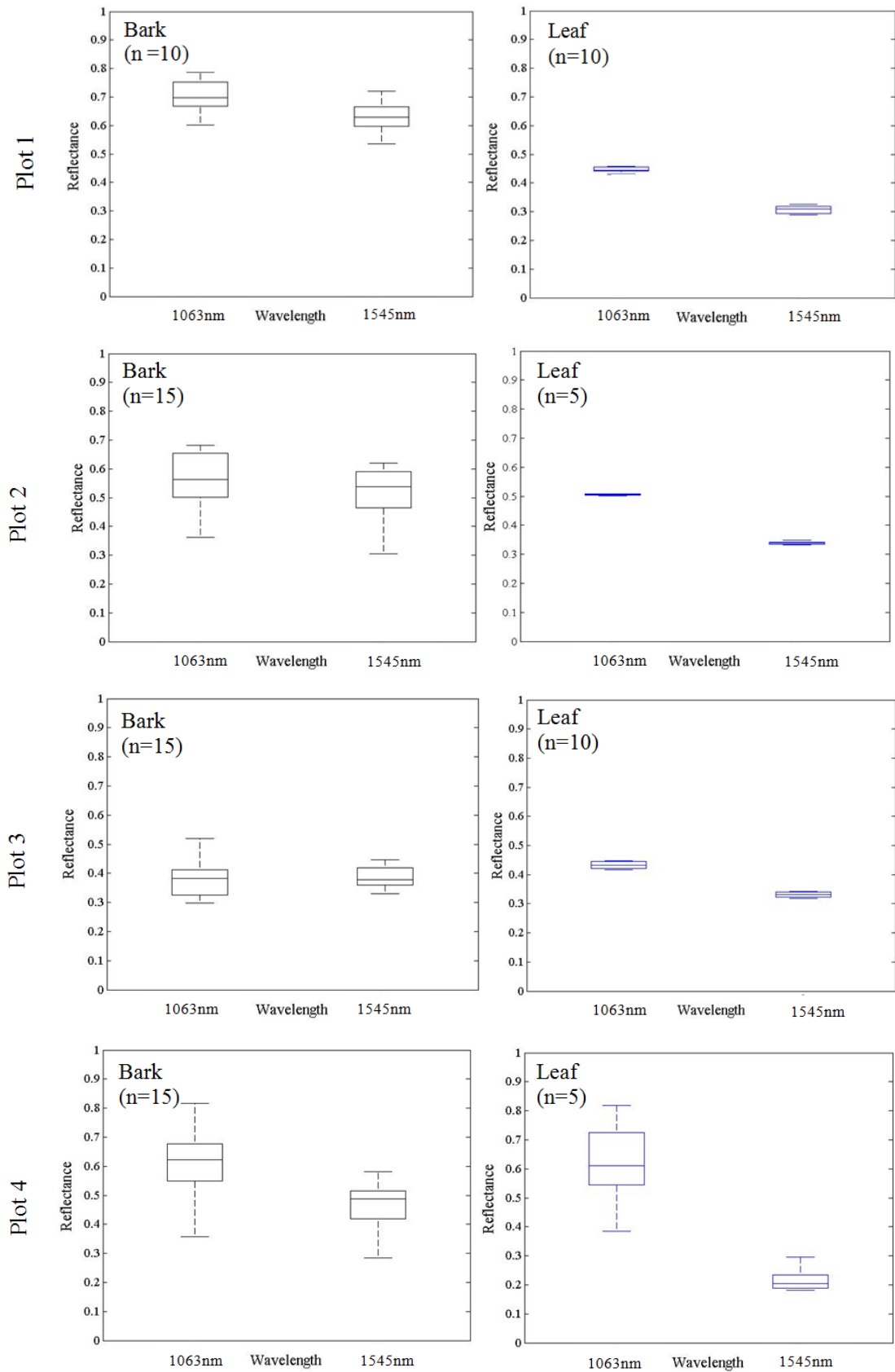
Figure 7.5. Spectral results taken with the ASD spectoradiometer for Plot 1 (top) to Plot 4 (bottom) for samples of wood (left) and leaves (right). On each box, central mark is the median, the edges of the box are the 25th and 75th percentiles, and the whiskers extend to the most extreme data points.

7.3.3   Apparent reflectance and NDI

Calibrated point clouds and the NDI products are presented in Figure 7.6a-e for the five test plots. All returns are displayed, plotted by azimuth and elevation angle and coloured according to the scale-bars displayed. Apparent reflectance values outside of the expected range of 0-1 are highlighted in purple (<0) and red (>1). These values are artefacts of the neural network calibration, as discussed in Chapter 5. This apparent reflectance product is the baseline for the separation of leaf and woody material discussed in the following sections. The point clouds for the bottom two images in Figure 7.6a-e display the results of the NDI of the paired reflectance value of each wavelength.

Generally, Figure 7.6 indicates that the neural network has corrected the raw intensity to apparent reflectance successfully. This is supported by the absence of range-effects that dominate the display of raw intensity. The tree trunks and primary branches exhibit similar values of apparent reflectance which are higher than the apparent reflectance of the foliage and fine branches, due to spectral properties and partial hits. A small proportion of low apparent reflectance values (less than zero) are apparent for some returns in both wavelengths. This occurs particularly for near-range targets in the λ1063nm (such as a low branch in Plot 2 in leaf-on, or close calibration panels in Plot 5 in leaf-off) and for far-range targets in the λ1545nm (such as in leaf-off for Plots 1-3).

The NDI images in Figure 7.6 display returns in blue which exhibit a low NDI (that is, a higher apparent reflectance at λ1545nm relative to the apparent reflectance at λ1063nm), and a high NDI in red. From a visual assessment of the NDI images, a clear separation between the foliage and woody returns is not observable. Furthermore, in some of the results, there is a clear division between lateral sides of the scan, most likely an artefact from the thermal drift in intensity; this is particularly apparent for Plots 2 and 5. The following section will examine the separation of returns into leaf and wood in more detail.

a) Plot 1
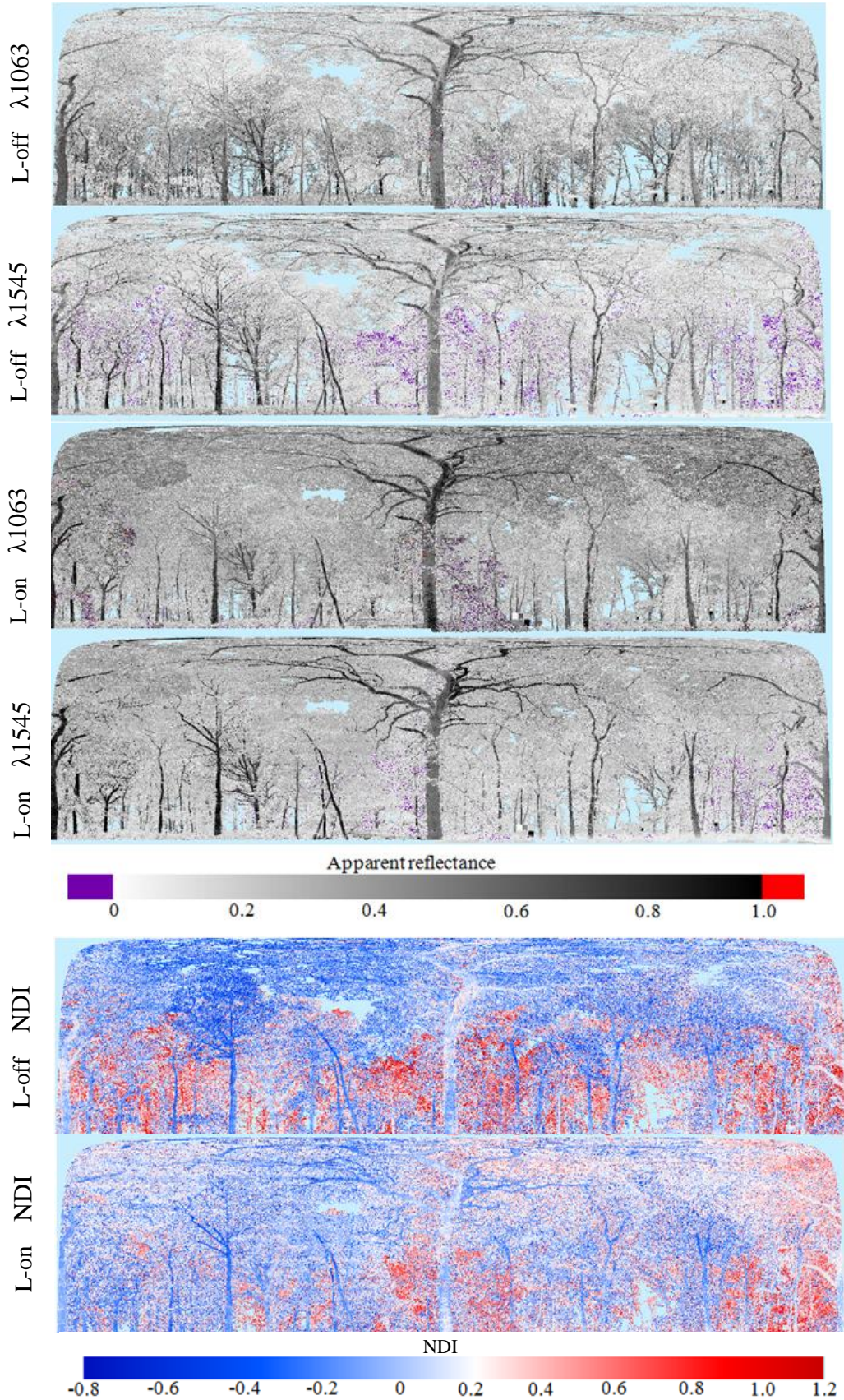
Figure 7.6. Top four images show apparent reflectance point clouds plotted by azimuth and zenith angles in winter and summer conditions for both wavelengths. Bottom two images symbolised by the NDI. For Plots 1-5 (a-e) [Figure continued over several pages]

b) Plot 2

Apparent reflectance

NDI
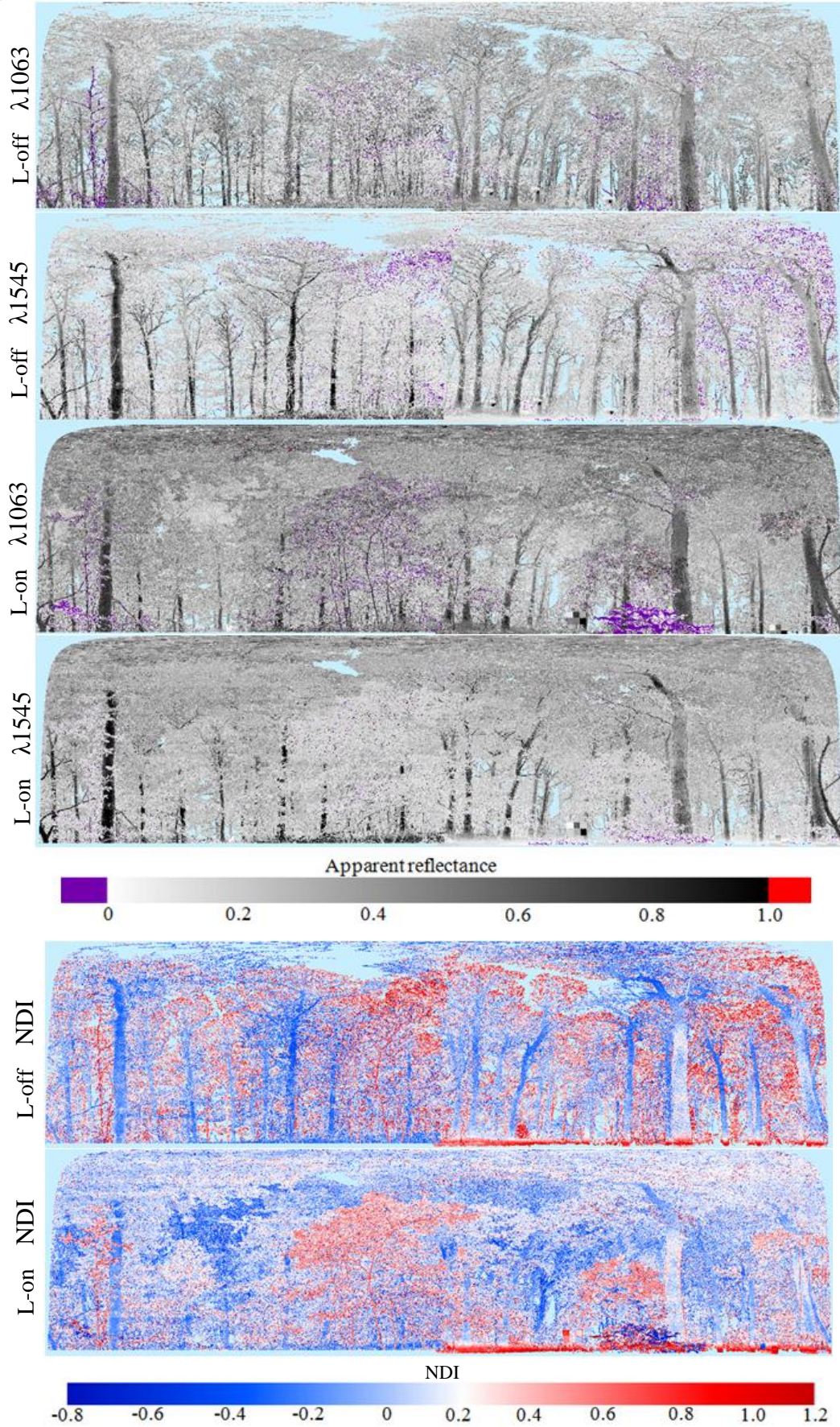
Figure 7.6 continued.

c) Plot 3
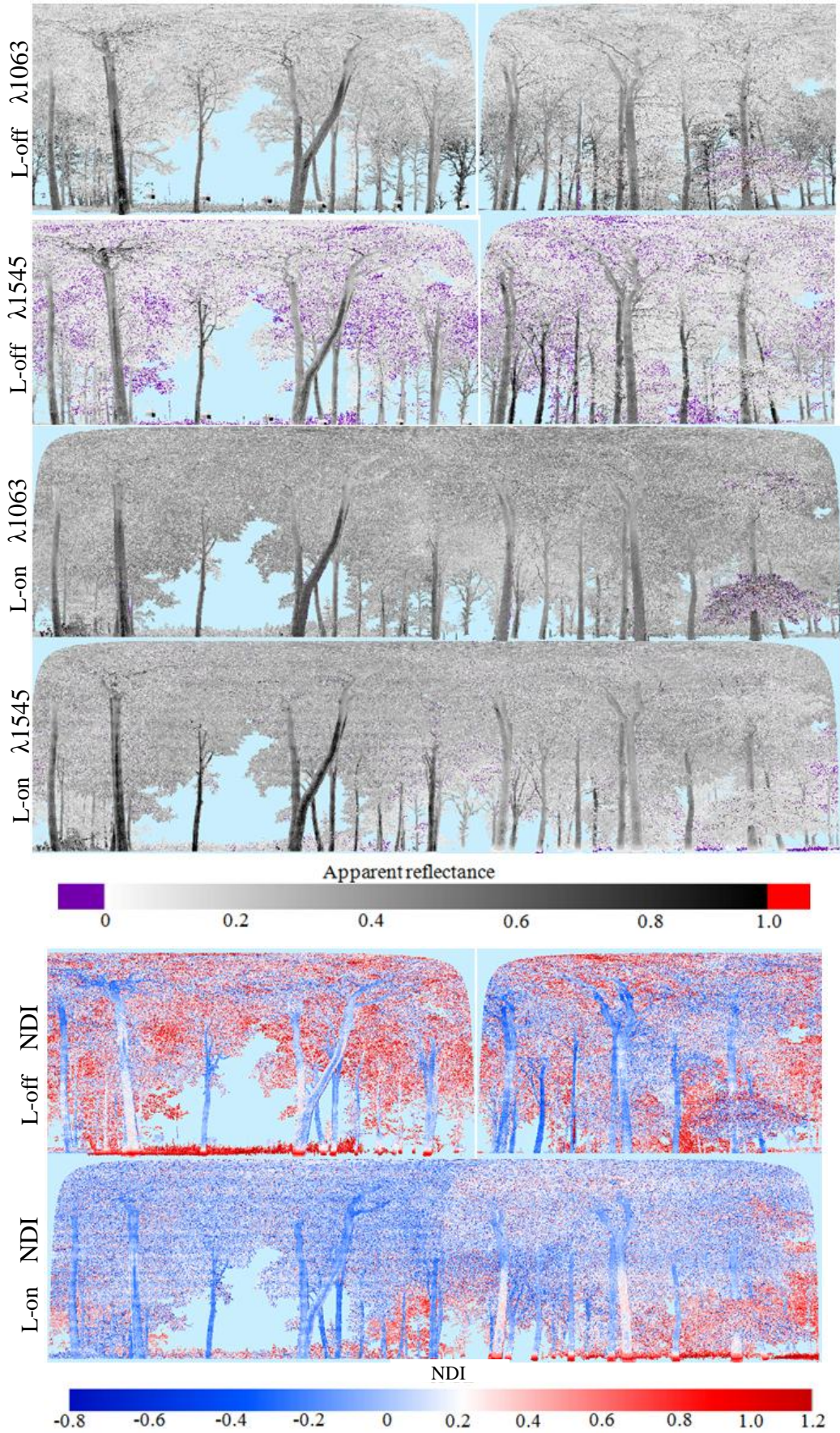
Figure 7.6 continued.

d) Plot 4
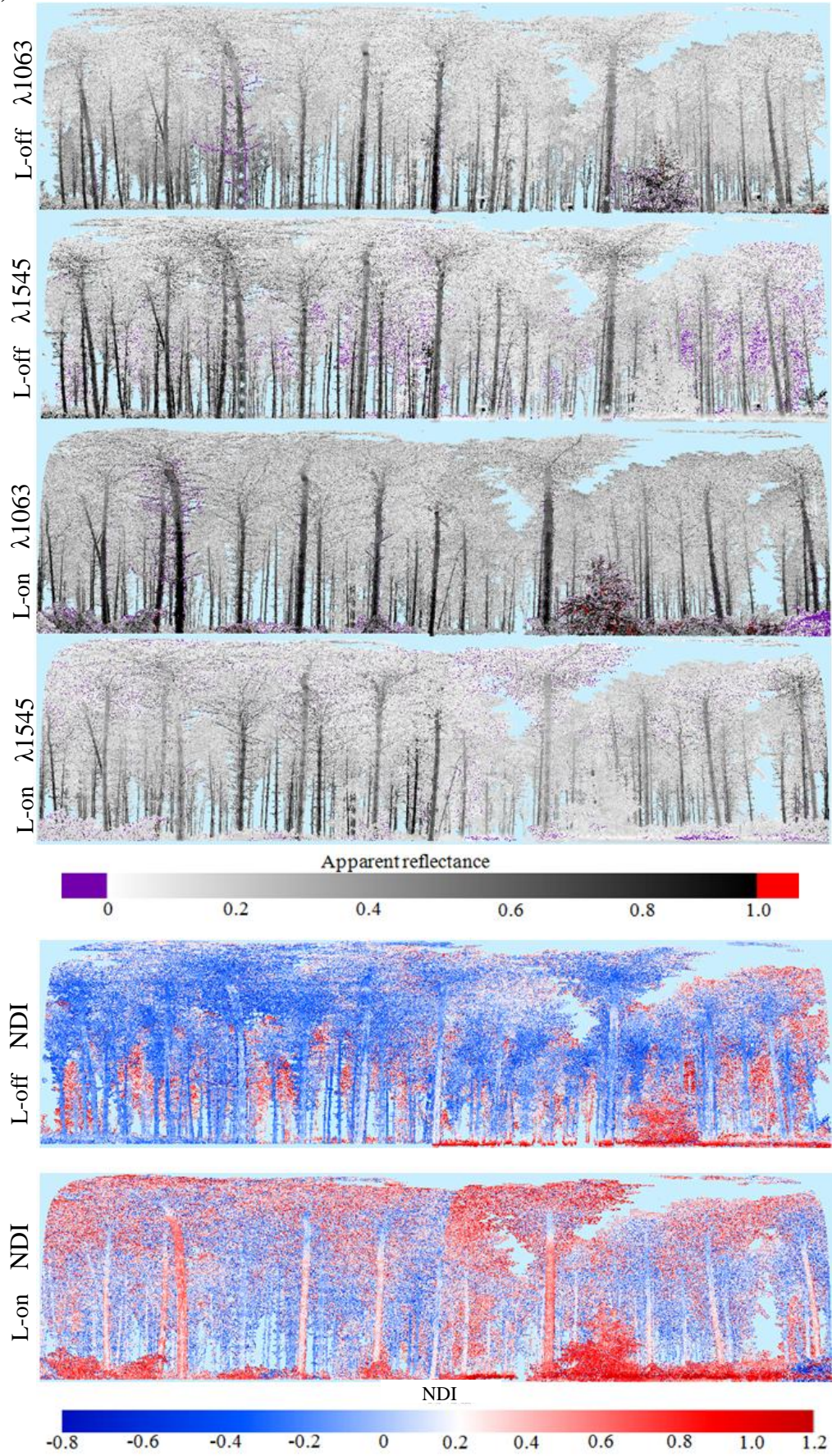
Figure 7.6 continued.

e) Plot 5

Figure 7.6 continued.

154
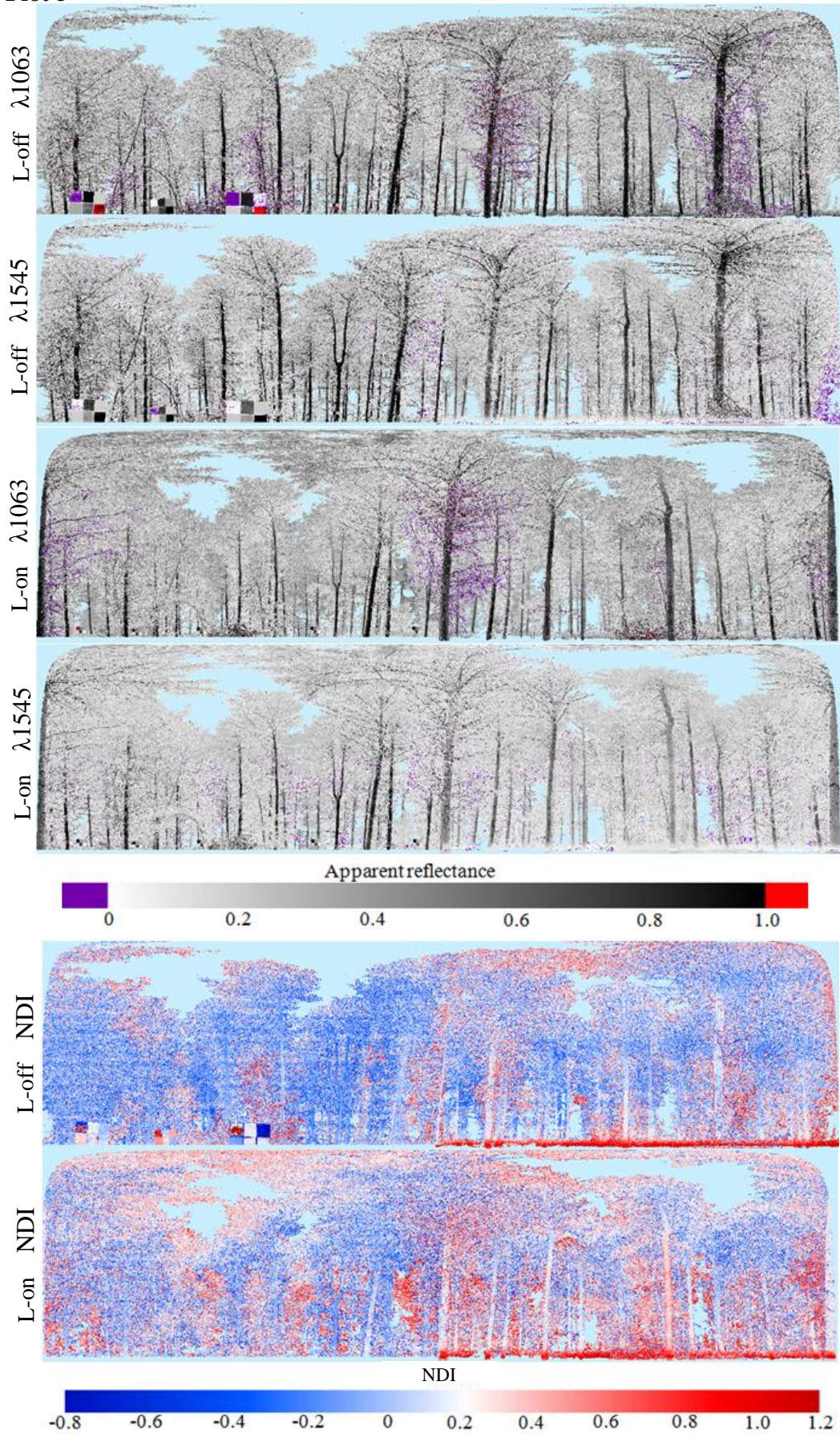
7.3.4 Separating leaf and wood returns

This section investigates the spectral separability of leaf and woody material in the five test plots at Delamere forest. The results are summarised in Figure 7.7 which show the winter and summer frequency distribution of apparent reflectance for all returns in both wavelengths, and the leaf-off and leaf-on frequency distribution of NDI, by plot. Two methods were trialled for separating the point cloud into returns resulting from foliage and returns resulting from woody material, as outlined in Chapter 5. The first was achieved by applying a simple threshold on the apparent reflectance of the 1545 wavelength, defined by the location of the leaf-on frequency peak. In a similar way, a threshold was applied using the NDI for the second method. The results of applying both approaches are illustrated for a sample of the full plot and an extracted individual tree (Figure 7.7).

Based on the leaf-off and leaf-on apparent reflectance histograms shown in Figure 7.7, the following observations may be made:

- At λ1063nm, the leaf-on scans had more returns with higher apparent reflectance values compared with the corresponding leaf-off scans for Plots 1, 2, and 3. This indicates that foliage has a higher reflectance than wood at this wavelength.
- At λ1545nm, the leaf-on scans had more returns with higher apparent reflectance values compared with the corresponding leaf-off scans for Plots 1, 2, and most notably, Plot 3. This indicates that foliage has a higher reflectance than woody material at this wavelength. However, a larger number of apparent reflectance values below zero indicates poor calibration for Plot 3 in leaf-off.
- Plot 4 and Plot 5 show a very similar distribution of apparent reflectance for leaf-off and leaf-on at both wavelengths. However, the NDI for leaf-on was higher than leaf-off.
- Plots 1, 2, 4, and 5, showed a higher NDI under leaf-on compared with leaf-off.
- Plot 3 showed a lower NDI under leaf-on conditions compared with leaf-off.
- For all histograms, there was a large overlap in apparent reflectance values between leaf-off and leaf-on datasets.

In order to define the threshold values for classification to leaf and wood, an iterative process was followed to minimise misclassification of wood to leaf (based on the leaf-off scans) and the location of the 'leafy' peak, based on the histograms shown in Figure 7.7 and approach described in Chapter 5. To assess the accuracy of each approach, the

same thresholds were applied to the leaf-off scans to generate a misclassification error for Plots 1, 2, 3, and 5. To assess Plot 4, composed of evergreen coniferous species, the same threshold value was applied to the winter and summer scan and the results compared. The chosen thresholds and misclassification errors are given in Table 7.2 and the threshold values are marked on histograms as black vertical lines.

a) **Plot 1**
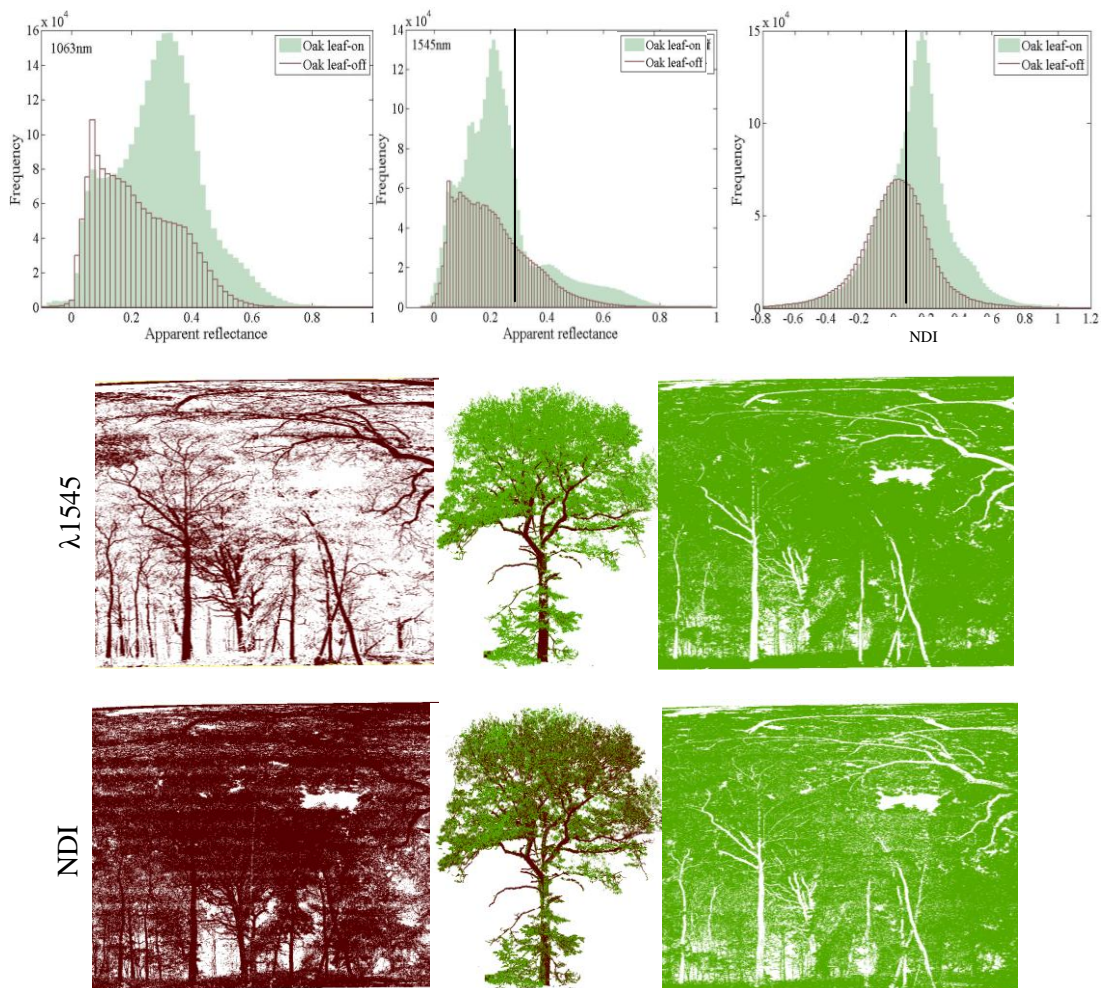
Figure 7.7. Apparent reflectance distributions and resultant leaf and wood separation for Plots 1-5 (a-e). Histograms show the frequency distribution of winter (brown) and summer (green) scans for the λ1063nm (left), λ1545nm (middle) and NDI (right). Black vertical lines show location of threshold on distribution. Point clouds show the results of thresholding the returns into wood (left) and leaf (right) for the plot scale and a selected representative individual tree, using a single wavelength (top) and the NDI (bottom). Plot 4 (d) show the winter leaf-off (left) and summer leaf-on (right) results. [Figure continued over several pages]

b) Plot 2
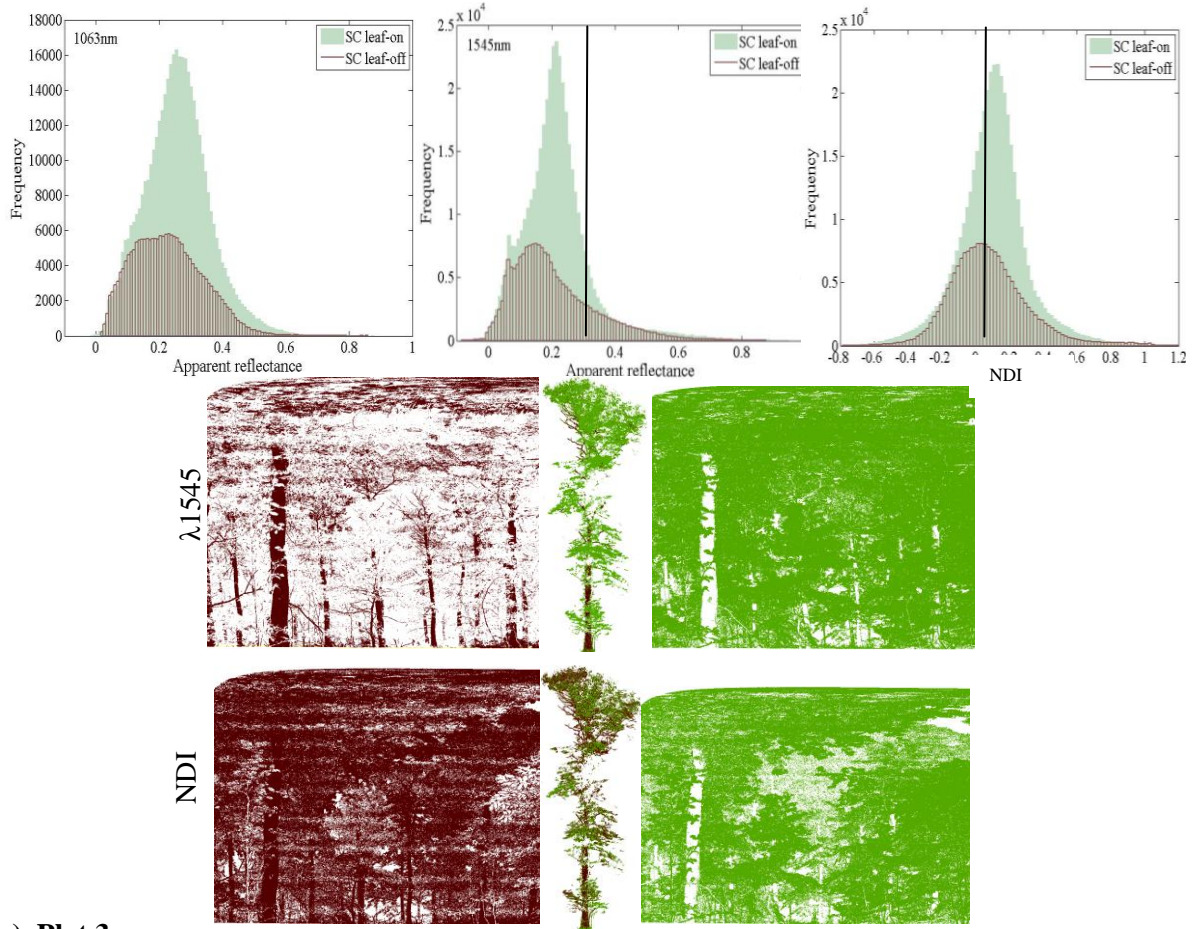
c) Plot 3
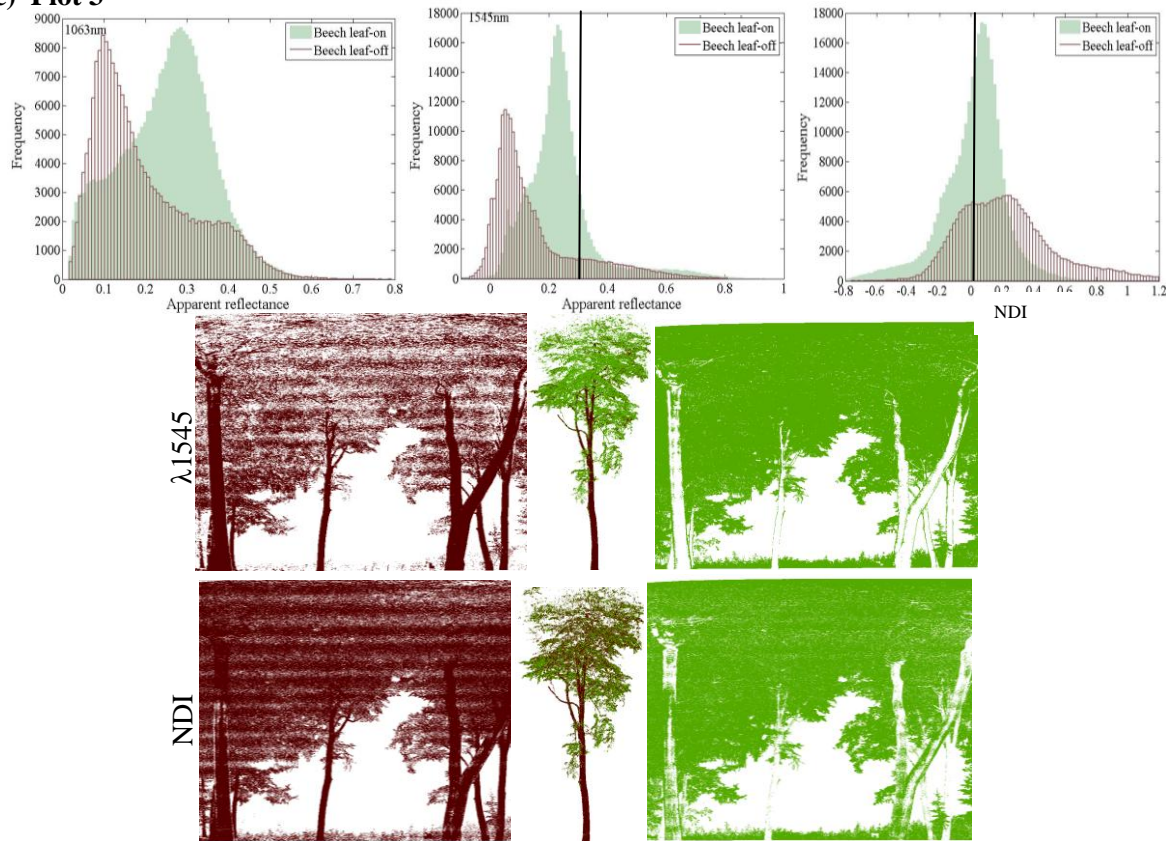
Figure 7.7 continued.

d) Plot 4

winter   summer
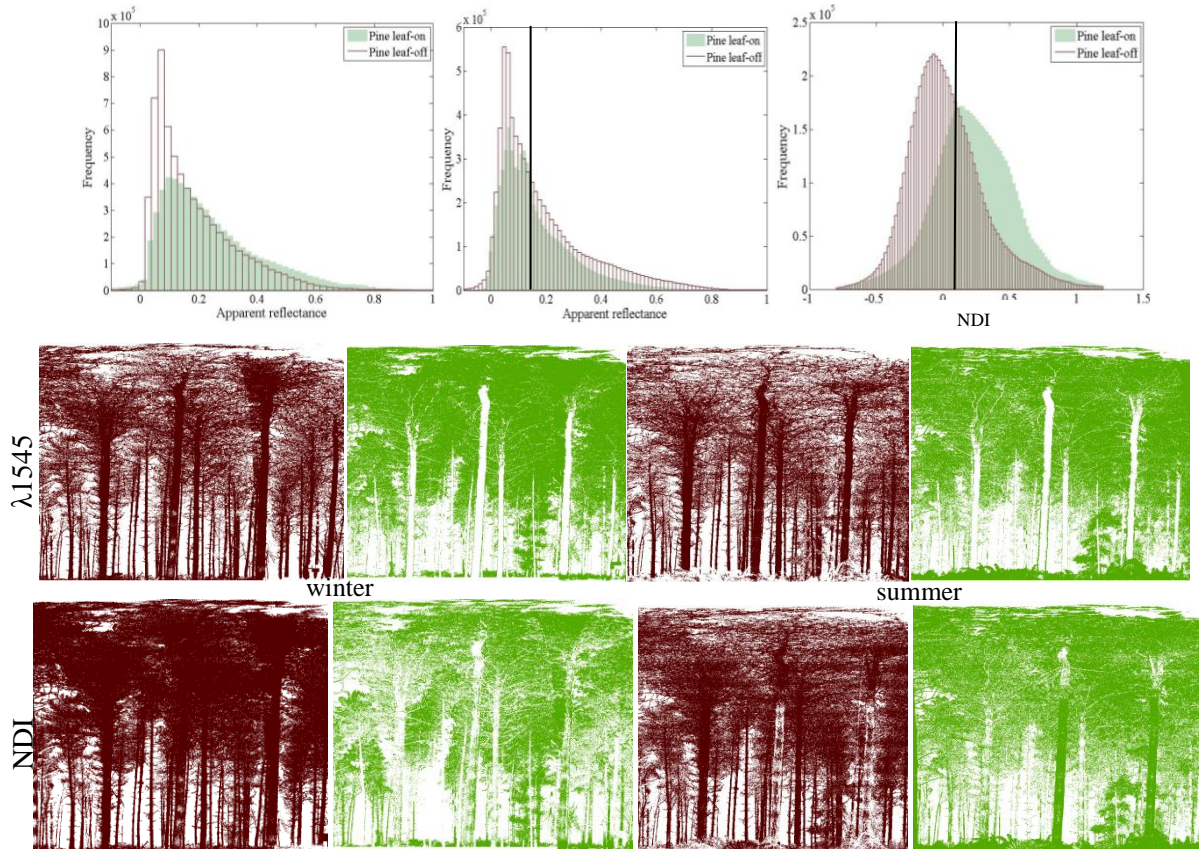
e) Plot 5
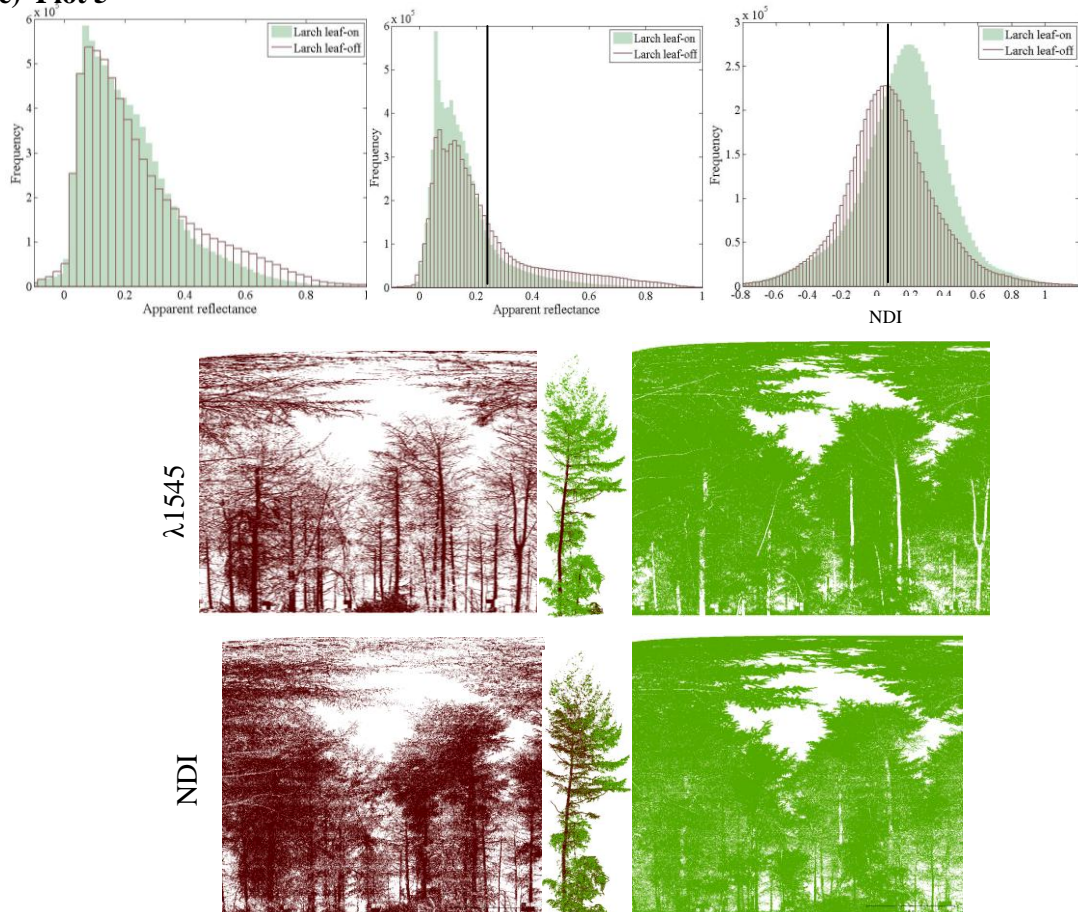
Figure 7.7 continued.

For all four deciduous plots, thresholding the NDI showed a lower misclassification error compared to using the λ1545, indicating that the NDI approach is more accurate.

Table 7.2. Separation threshold values chosen for each plot for both methods: using a single channel and NDI. The error describes the percentage of leaf-off returns classified as leaf.

	1545nm apparent reflectance		NDI	
Plot	Threshold	Error %	Threshold	Error %
1	0.29	79.80	0.10	42.57
2	0.32	82.43	0.10	44.08
3	0.28	82.01	0.03	32.15
4	0.16	-	0.17	-
5	0.22	65.90	0.09	49.17

The point cloud images in Figure 7.7 show the result of the thresholding processes. The returns illustrated in brown are those which have been categorised as woody material, and those in green represent leafy material. For Plot 4, the plot-scale result of the classification on the winter and summer scan is given.

In general, thresholding using the λ1545nm wavelength has performed well: trunks and branches have clearly been separated from the canopy, but the incorporation of partial hits around tree trunks is evident in the leaf class (particularly Plot 3), as cited in previous studies (Béland *et al.,* 2011). Thresholding using the NDI values has also picked out many of the tree trunks but many leaf hits are classified as woody material. This tendency to classify leaves as wood could also explain the smaller misclassification error when applied to the leaf-off scans. The results of Plot 4 also indicate that the repeatability of using a single thresholding value on the NDI may not be reliable (Figure 7.7e).

7.3.5 Estimating PAI for test plots

Gap fraction by zenith angle interval for the five test plots is shown in Figure 7.8. The broadleaf deciduous plots (1-3) show similar trends:

- In summer, gap fractions were lower than in winter due to canopy closure by leaf development.

- In winter, gap fractions decreased with increasing zenith angle due to the presence of trunks and branching structures at higher zenith angles. In summer, gap fraction remains relatively stable over all zenith angles as leaves fill gaps at all vertical and horizontal layers of the stand.

- In winter, gap fractions derived from TLS were lower than those derived from DHP, possibly due to the inclusion of partial hits causing an underestimation from TLS (Lovell *et al.,* 2003; Calders *et al.*, 2011).

- In summer, gap fractions derived from TLS are similar to those derived from DHP. This could be explained by the effects of partial hits being less pronounced in a closed canopy, due to more overlapping objects.

- Gap fractions derived using the λ1063nm dataset are higher than corresponding estimates at λ1545nm. This is most likely due to the 1545nm wavelength penetrating further into the canopy due to its higher output laser power.

Plot 4 shows a decrease in gap fraction with increasing zenith angle and a slightly higher gap fraction in winter than summer derived from DHP. The gap fractions derived from TLS show a very similar form between winter and summer and between the wavelengths, although slightly lower than the DHP estimates. The gap fractions are higher than those derived from the summer scans at Plots 1, 2 and 3 indicating that Plot 4 is a more open stand. Plot 5 shows a similar trend as described above but the summer and winter gap fractions are very different at high zenith angles where the gap fraction increases in summer and decreases in winter. This may be explained by foliage development directly above the scanner. There is no summer DHP image for comparison.
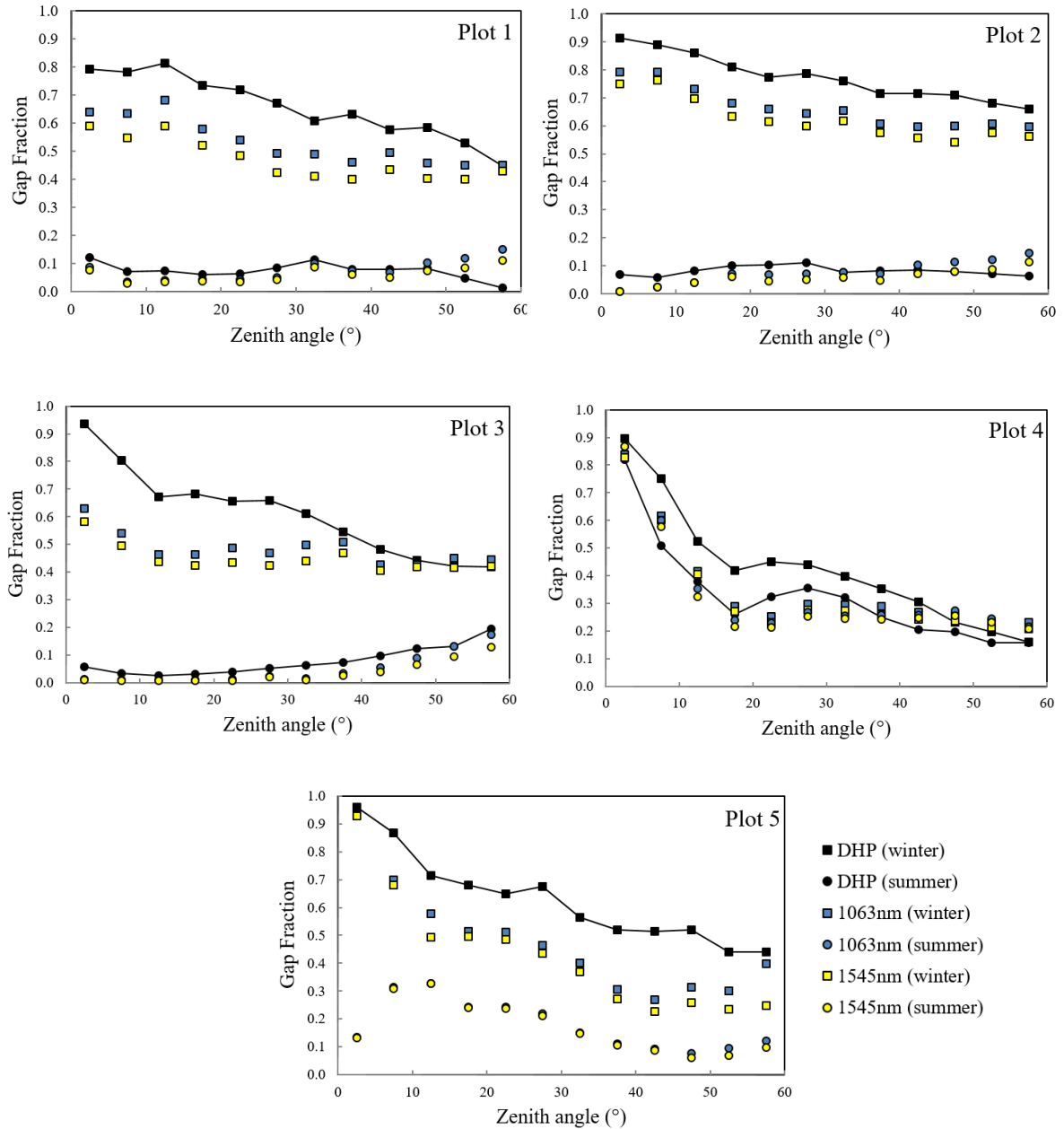
Figure 7.8. Gap fraction by zenith angle interval for the five plots. Leaf-off and leaf-on results are shown with squares and circles, respectively. Black markers and lines show estimates derived from DHP, and estimates derived from SALCA wavelengths 1063nm and 1545nm are shown as blue and yellow markers respectively.

Table 7.3 and Table 7.4 show the plant area index estimates derived from SALCA wavelengths 1063nm and 1545nm respectively. According to these results, Plot 5 had the highest PAI and Plot 4 the lowest PAI. Plot 4 showed very little change between winter and summer, as expected. Plot 5 showed the smallest increase in PAI of all the deciduous stands from leaf-off to leaf-on.

Table 7.3. Plant Area Index (PAI) estimated by the hinge and regression method (Jupp *et al*., 2009) for the winter and summer scans for the five plots, wavelength **1063nm**.

Plot	Winter		Summer	
	PAI (hinge)	PAI (regression)	PAI (hinge)	PAI (regression)
1	0.885	0.842	2.096	1.948
2	0.663	0.621	2.119	1.749
3	0.719	0.705	1.933	1.778
4	1.496	1.599	1.503	1.676
5	1.785	1.713	2.311	2.557

Table 7.4. Plant Area Index (PAI) estimated by the hinge and regression method (Jupp *et al.,* 2009) for the winter and summer scans for the five plots, wavelength **1545nm**.

Plot	Winter		Summer	
	PAI (hinge)	PAI (regression)	PAI (hinge)	PAI (regression)
1	0.929	0.882	2.434	2.282
2	0.758	0.706	2.400	2.092
3	0.953	0.919	2.253	2.060
4	1.447	1.608	1.895	1.932
5	2.289	2.146	2.557	2.580

The two SALCA wavelengths produced very similar estimates of PAI (Figure 7.9a), although the 1545nm laser tended to produce slightly higher PAI due to the increase in laser output power compared with the 1063nm laser. The two methods implemented to derive PAI (hinge and regression) from the TLS give very similar results (Figure 7.9b), although slightly higher using the hinge method, perhaps due to the impact of clumping. The close relationship between the methods support the previous work by Strahler *et al.* (2008), Jupp *et al.* (2009) and Zhao *et al.* (2011).
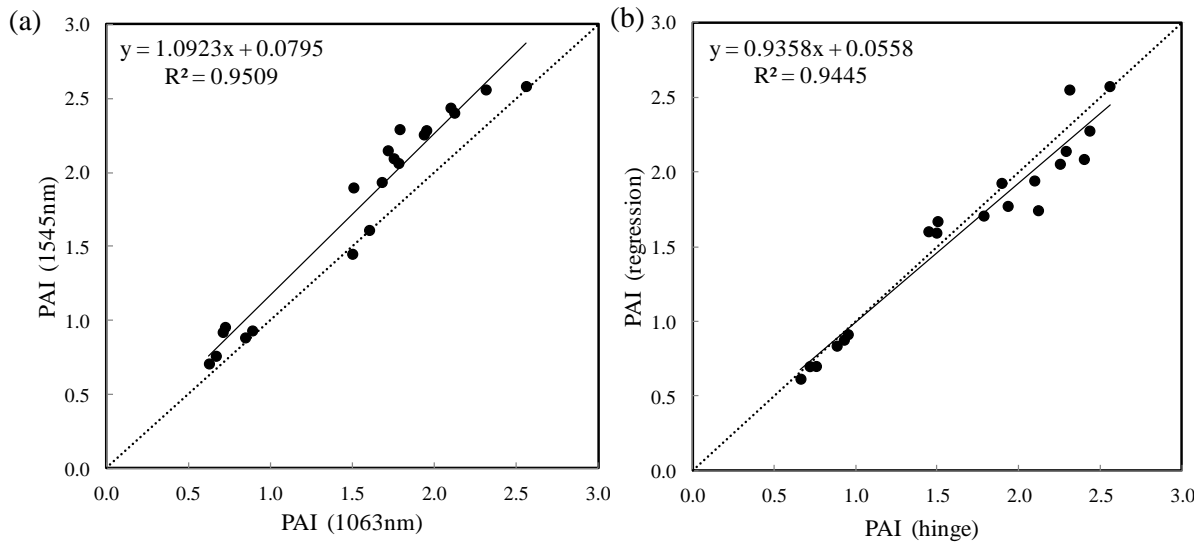
Figure 7.9. (a) Relationship between PAI estimated from the two SALCA wavelengths using both methods, and (b) Relationship between PAI estimated using the two methods: hinge angle inversion and regression (Jupp *et al*., 2009). Dotted lines are 1:1 fit and continuous lines are results of linear regression fitting.

The relationship between PAI derived from both wavelengths and *effective* PAI derived from DHP is shown in Figure 7.10a. The relationship between PAI derived from both wavelengths and *true* PAI derived from DHP is shown in Figure 7.10a. The effective PAI is combined with a clumping factor (generated by the image processing software) to obtain the true PAI. There was a higher correlation with both wavelengths and effective PAI from DHP ($R^2 = 0.6261$; 1545nm, $R^2 = 0.7358$; 1063nm) than with both wavelengths and true PAI from DHP ($R^2 = 0.5306$; 1545nm, $R^2 = 0.654$; 1063nm). This indicates that PAI derived using the hinge method from TLS is more comparable with PAI derived from DHP before clumping correction has been applied. Leaf-off TLS derived PAI (Plot 1,2,3) remain very similar to DHP derived true PAI, whereas the leaf-on PAI results are higher than those derived from TLS.

The leaf-off PAI from Plot 5 is an outlier on all graphs, where the PAI derived from both wavelengths is higher than effective and true PAI. This could be explained by structural factors as Plot 5 consisted of dense, short, woody conifers, quite different to the other plots. This illustrates the potential for the apparent reflectance approach to gap fraction could be utilised where partial hits are considered (Jupp *et al.,* 2009).

(a)

(b)
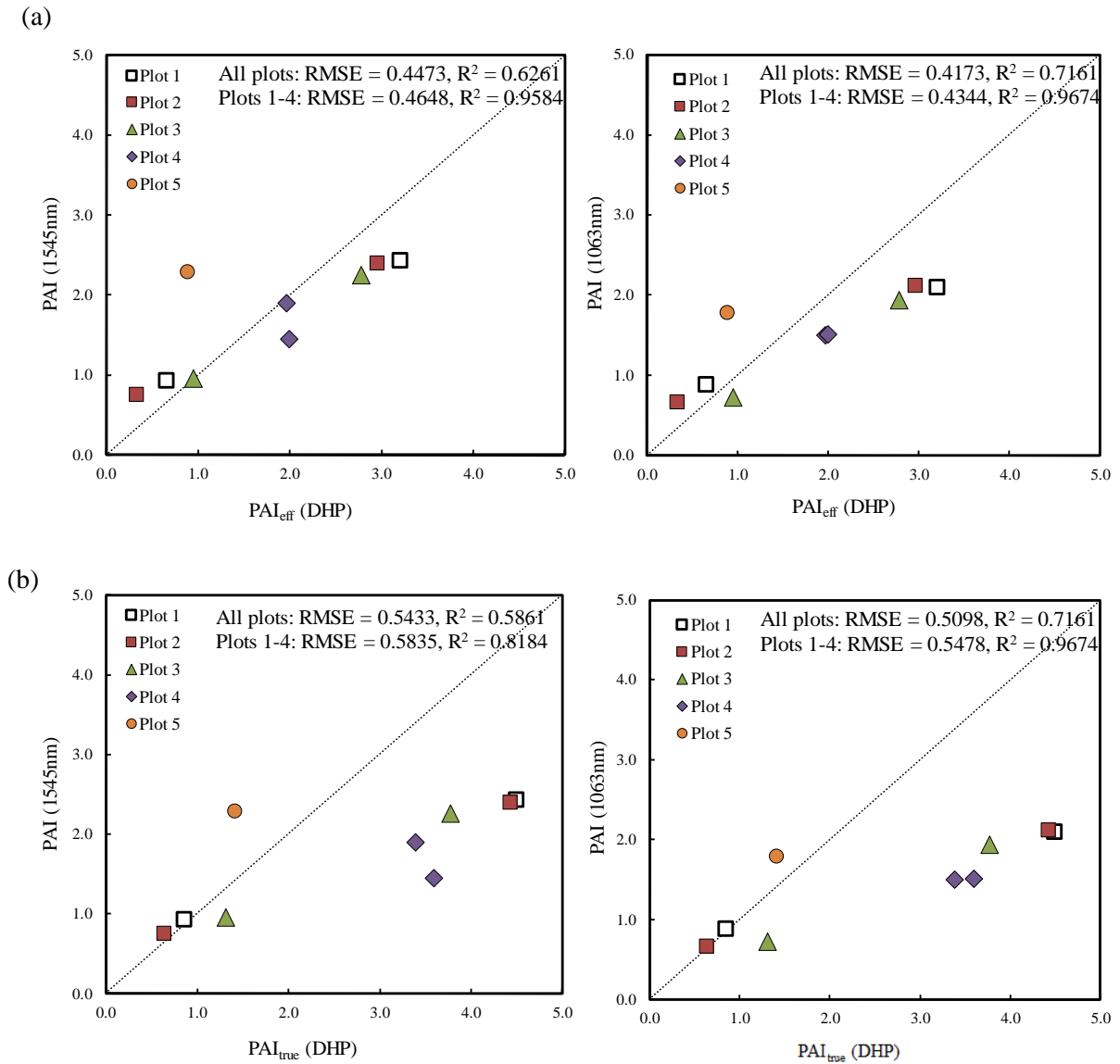
Figure 7.10. Relationship between PAI derived from the two SALCA wavelengths (1545; left, 1063; right) and (a) effective PAI (PAI_{eff}) derived from DHP, and (b) true PAI (PAI_{true}) derived from DHP.

Taking the derivative of the PAI profiles provides the PAVD as shown in Figure 7.11. It is clear from these graphs that the five plots show different characteristics in terms of the vertical distribution of material. For instance, the plant material and leaf growth is distributed fairly evenly throughout the vertical layers of Plot 2 and there is a well-defined understorey, compared with the other plots where the plant material and leaf growth is concentrated in the canopy. As before, the 1545nm laser generated more returns at higher vertical layers due to its higher output power. The distribution of plant material at Plot 4 is fairly constant throughout both scans and wavelengths, as would be expected from the evergreen conditions.
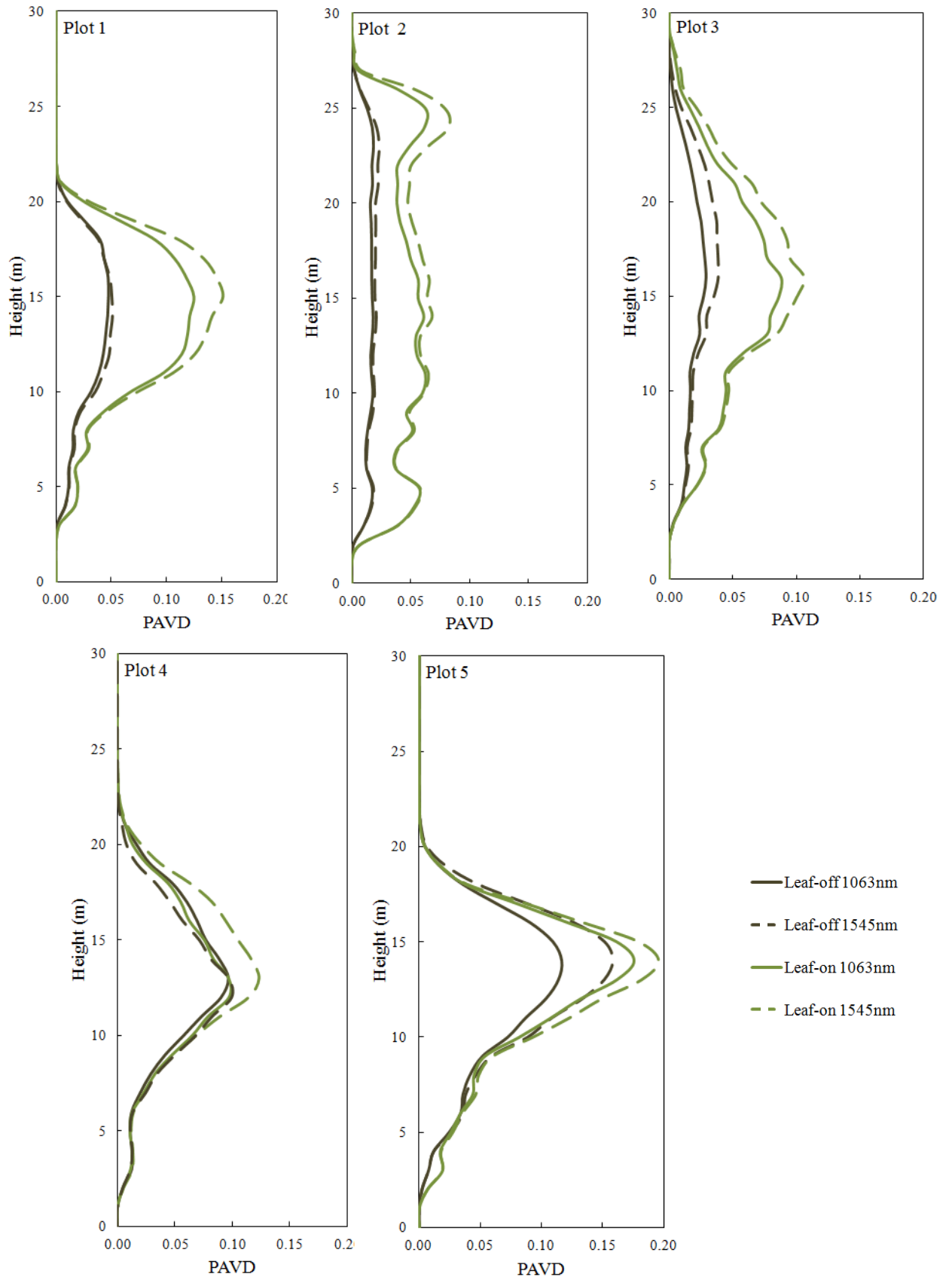
Figure 7.11. Vertical profiles of Plant Area Volume Density (PAVD) by height (z) in meters, for the five plots.
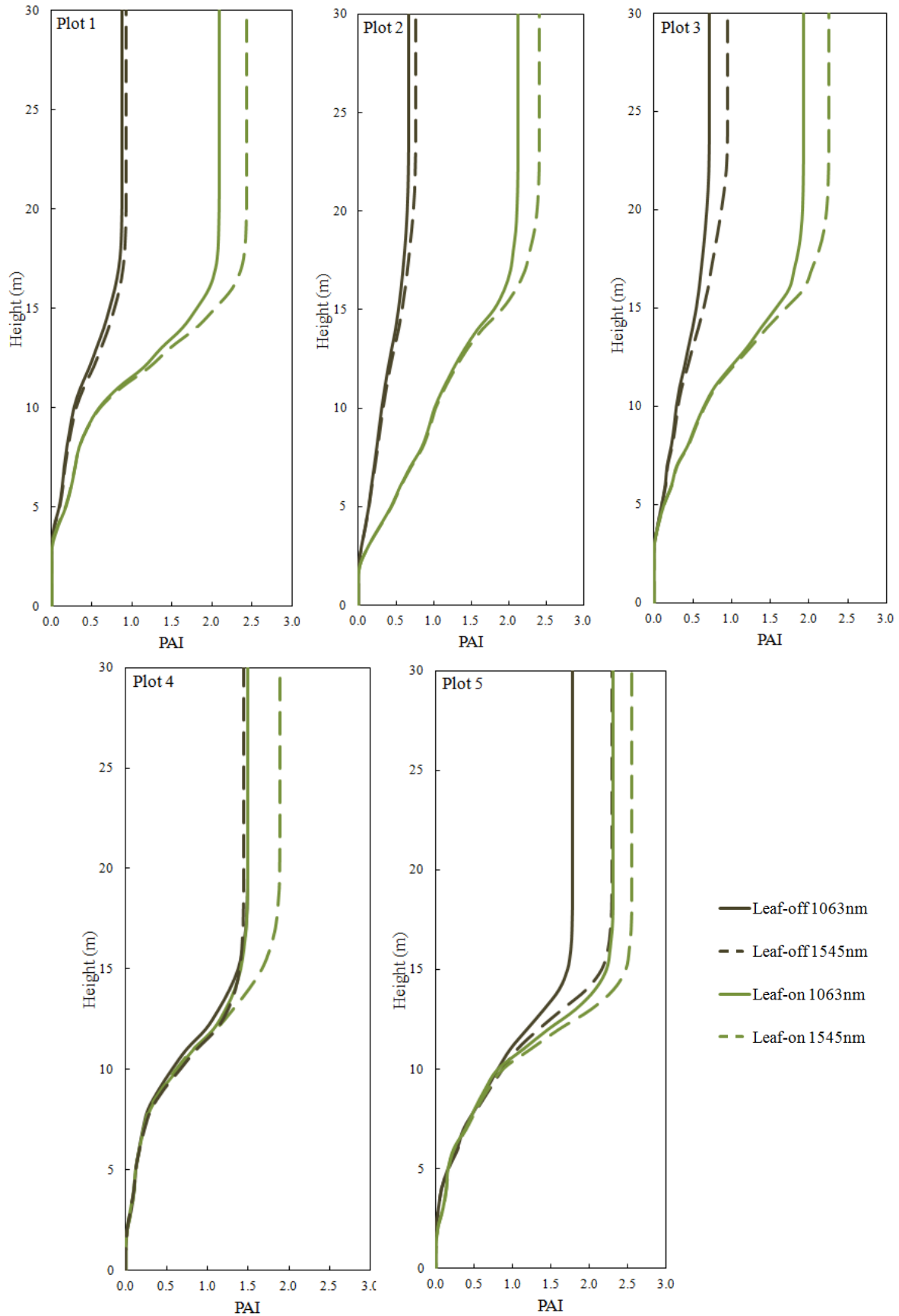
Figure 7.12. Vertical profiles of cumulative Plant Area Index (PAI) by height for the five plots.

Figure 7.12 show cumulative vertical profiles of PAI by height for the five plots. This provides a quantitative assessment of plant material growth by vertical layer of the canopy. As expected, the deciduous plots (1, 2, 3, and 5) showed an increase in plant material in the summer. Plot 4 show very similar PAI characteristics in all but the summer dataset at 1545nm which is considerably higher. As before, this is most likely due to the higher output power of that laser triggering more returns in the leafy canopy.

7.3.6   Estimating true leaf area index (LAI) for different forest stands

After the leaf-on point clouds were classified into returns resulting from leafy material using the 1545nm and NDI thresholding methods, LAI was estimated using the hinge angle and regression analysis for the five plots. The results are shown in Table 7.5 and Table 7.6. For Plot 4 the results are from applying the approaches to both the winter and summer datasets. As before, the LAI estimated from the hinge angle and regression methods showed very similar results ($R^2 = 0.92$). LAI was highest in Plot 5 and lowest in Plot 4, using both methods.

Table 7.5. Leaf Area Index (LAI) estimated by the hinge and regression method (Jupp *et al.,* 2009) for the leaf-on scans for the five plots, **1545nm thresholding** method. The two values for Plot 4 correspond to winter and summer analysis.

Plot	1545nm	
	LAI (hinge)	LAI (regression)
1	1.750	1.669
2	1.345	1.136
3	1.643	1.522
4	0.924, 1.161	1.070, 1.253
5	2.179	2.184

Table 7.6. Leaf Area Index (LAI) estimated by the hinge and regression method (Jupp *et al.,* 2009) for the leaf-on scans for the five plots, **NDI thresholding** method. The two values for Plot 4 correspond to winter and summer analysis.

Plot	NDI	
	LAI (hinge)	LAI (regression)
1	1.634	1.577
2	1.840	1.597
3	1.249	1.125
4	0.658, 0.453	0.547, 0.754
5	0.895	0.764

It is clear that, for any given forest stand, LAI will be lower than PAI, based on the fact that woody material is absent from LAI calculations. However, the relationship between PAI and LAI will differ between stands due to the structure of the vegetation components. For instance, a needle-leaf stand (such as Plot 5) will have a lower leaf to wood ratio (and therefore a smaller difference between LAI and PAI) compared with a broadleaf stand. There is little literature on this relationship; presumably because of the lack of current methods of obtaining true LAI. Figure 7.13 shows the PAI (λ1545nm) derived for each test plot with the corresponding estimates of true LAI based on leaf-classification using the two thresholding methods. The LAI for Plots 1,3,4 and 5 is larger when derived from the 1545nm classification method compared with when derived from the NDI classification, whereas Plot 2 show the opposite. The estimates from the two LAI methods are similar for Plot 1 but the other plots show a marked difference between estimates, most notably for Plot 5. LAI for Plot 4 shows an increase during summer when based on the 1545nm thresholding which is consistent with the PAI estimates, however the NDI approach shows a decrease in winter LAI. This further indicates that the NDI may not be reliable.
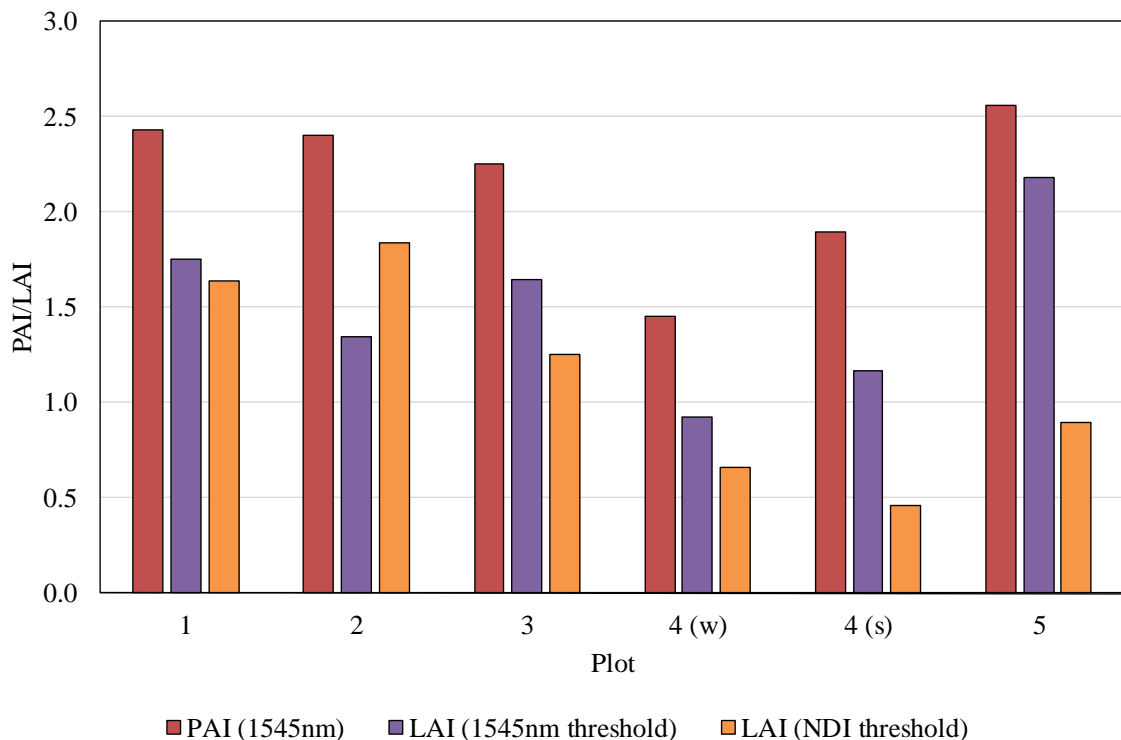
Figure 7.13. Bar chart showing summer leaf-on PAI (red bars), and leaf-on LAI based on the two thresholding methods: using the 1545nm dataset (purple bars) and the NDI (orange bars), for each plot. Two datasets were used for Plot 4; winter (w) and summer (s). PAI/LAI derived using the hinge method.

Figure 7.14 show the true LAI profiles for all five plots, using the 1545nm and NDI classification methods, shown in purple and orange respectively. The profiles for Plot 1 and Plot 3 are very similar using both thresholding methods although slightly lower LAI estimates using the NDI. Plot 2 shows an overall higher LAI using the NDI which go beyond the PAI values shown in Figure 7.10 up to a vertical height of 14m. Whereas the NDI yields a considerable lower LAI than using the 1545nm wavelength for Plot 5. It would be expected that the LAI profiles for Plot 4 would be very similar between the winter and summer scan, with a slight increase in the summer LAI due to needle expansion. This form is shown in the LAI estimated using the 1545nm method, however the opposite characteristics is shown in the LAI when the NDI method is adopted. Vertical profiles of FAVD for each plot are shown in Figure 7.15. The profiles further show the features described above and the distribution of foliage within each plot.
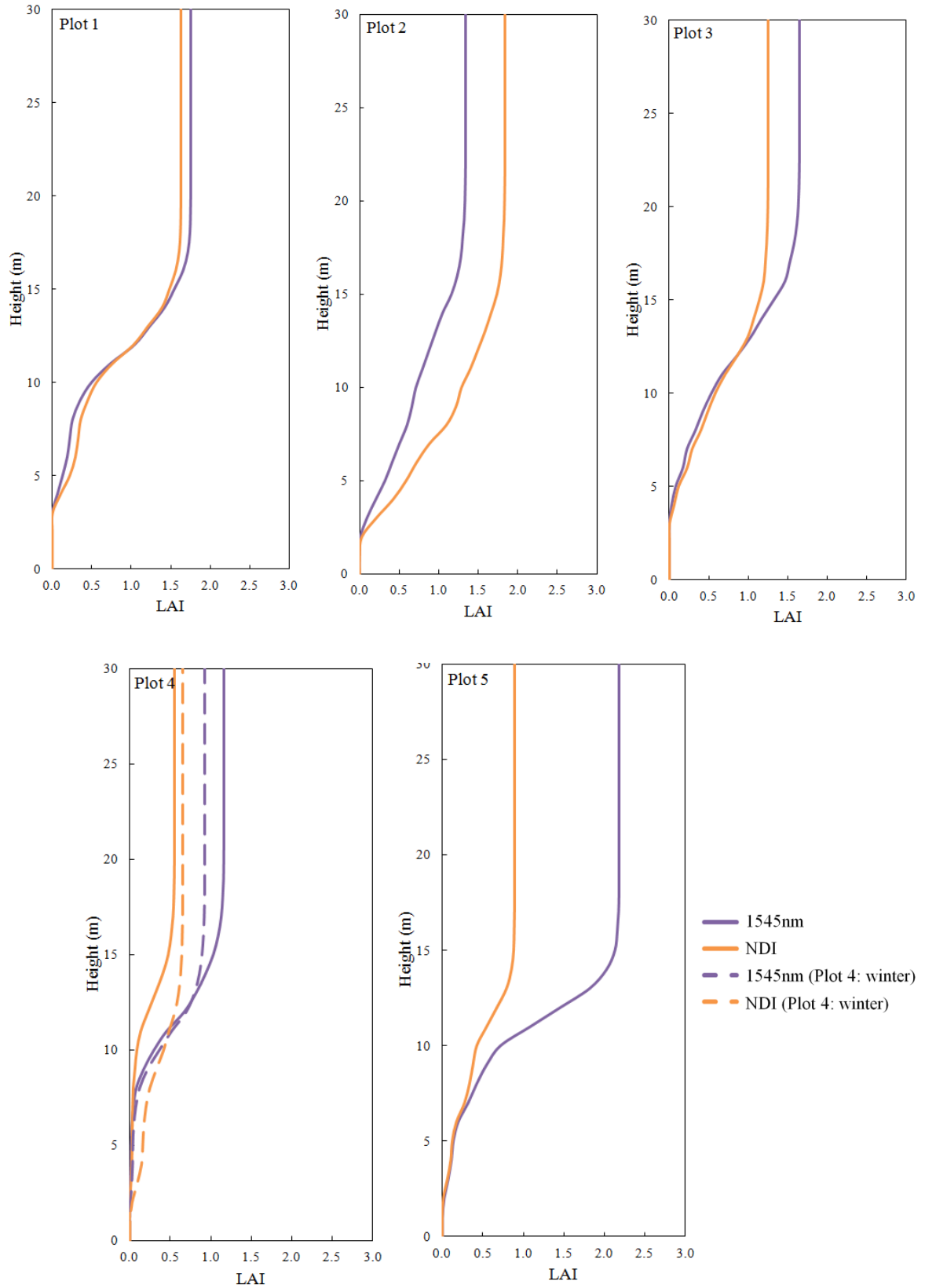
Figure 7.14. Vertical profiles of Leaf Area Index (LAI) by height (z) in meters for the five plots.
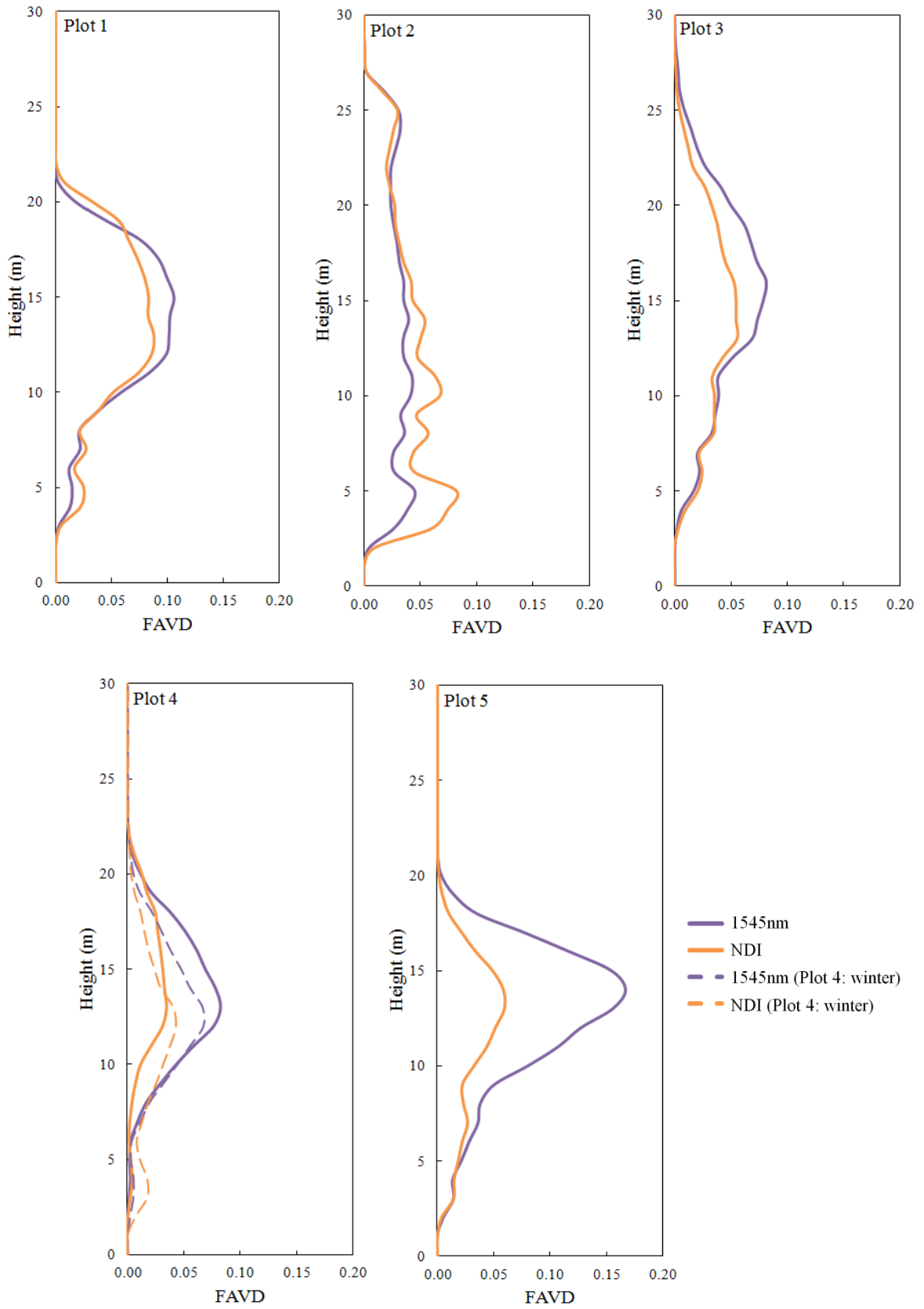
Figure 7.15. Vertical profiles of Foliage Area Volume Density (FAVD) by height (z) in meters for the five plots in leaf-on conditions.

7.4   Conclusion

This chapter has examined five test plots at Delamere forest in leaf-off and leaf-on conditions. The calibrated SALCA datasets were used to generate quantitative measures of plant material present at a given time: PAI and PAVD, and then the point cloud was classified into foliage and woody material based on the apparent reflectance values in order to derive true LAI and FAVD for the five forest plots. This approach has shown how the 3D spatial characteristics of foliage at a stand level can be assessed (Objective 3).

A key conclusion of this chapter is that applying a threshold to classify the returns into those resulting from leaves and wood is reliant on the spectral separability of these components. However, the largely overlapping leaf-on and leaf-off histograms in Figure 7.7 indicate that this is not the case. Vertical profiles of PAI and PAVD have provided a robust quantitative method for plot scale measurements in a range of forest types, and the results were similar between the wavelengths and methods. PAI from TLS had a stronger correlation with effective PAI from DHP rather than true PAI.

Using a 'leaf'-only point cloud, the first true LAI and foliage profiles were generated for all five test plots. Separation of leaves based on thresholding the 1545nm wavelength provided promising results for the leaf-on scan, however the effects of partial hits limit the use of this approach. The NDI thresholding method is reliant on the accuracy of the calibration in both wavelengths, and of matching of returns between the two lasers; as such results (particularly on Plot 4) have suggested that it is currently unreliable. The following chapter builds on the findings of this study to assess the seasonal change in plant material over a full annual cycle for the five plots surveyed in Delamere Forest.

CHAPTER 8

Seasonal dynamics of UK woodland canopies

8.1   Introduction

The aim of this chapter is to examine the seasonal dynamics of foliage growth in a variety of forest types, contributing to Objective 3. This will be achieved by examining the time-series of data collected at Delamere Forest at the five test plots. This chapter builds on the analysis undertaken in Chapter 7, as outlined in the following section.

8.2   Review of methods

In Chapter 7, the 1545nm thresholding method to separate foliage and woody material generated promising results for full leaf conditions. However, this approach is not sensitive to fine scale seasonal changes, the focus of this chapter, due to the presence of partial hits. The NDI thresholding method was reliant on a similar spectral response in 1063nm for both foliage and woody components, a difference in reflectivity in 1545nm, and an accurate reflectance calibration. However, it was clear from the comparison of leaf-on and leaf-off apparent reflectance frequency distributions, that a robust NDI threshold was not achievable for the plots. The approach may perform more successfully by applying a dynamic NDI threshold, fitted iteratively on a scan-by-scan basis, but this would decrease the automation of this approach, and dramatically increase the implementation time to beyond the scope of this research. As a result, for the work described in this chapter there was no classification of the point cloud into foliage and wood, and therefore PAI was generated as opposed to LAI, meaning that the results obtained relate to the change in plant material. One advantage of using PAI rather than LAI is that the values derived were comparable with DHP.

In Chapter 7, the hinge and regression methods for calculating PAI generated very similar results ($R^2 = 0.94$; Figure 7.9), and therefore only one method was implemented for the analysis. The hinge method was chosen following Jupp *et al.* (2009). It was also found that

the two SALCA wavelengths (1063nm and 1545nm) produced very similar results ($R^2 =$ 0.95; Figure 7.9), and therefore, the data from a single wavelength was used in this chapter. The 1063nm wavelength was chosen as it has been shown to be less affected by thermal effects compared with the 1545nm wavelength, and as a result has a more stable intensity response (Figure 4.13) which is important when analysing seasonal change detection.

The 57 Delamere TLS scans were processed according to the methodology shown in Figure 8.1, which was developed based on the findings of Chapter 7 as discussed above. Once all the scans had been processed to PAI and PAVD (Figure 8.1), the results relating to the spring leafing-out period were extracted for closer analysis. A common method of characterising the leafing out period in deciduous environments is to fit a sigmoidal 'S-curve' to a time series of PAI (or NDVI, where appropriate) (Zhang *et al*., 2003; Che *et al*., 2014; Ryu *et al*., 2014; Calders *et al*., 2015). The curvature change rate of the fitted function can be used to determine the leaf-out date (also known as 'start-of-season') which initiates a rapid growth period, and a full-leaf date, where the PAI becomes stable. The sigmoid function can be described as:

$$y(t) = \frac{U - L}{1 + e^{-k(t-t_m)}} + L \tag{8.1}$$

where $y(t)$ is the estimated PAI at time (t), t is the Julian day, U and L are the upper and lower asymptotes, k is the growth rate (slope), and t_m is the inflection point at which the growth rate reaches its maximum. The lower asymptote corresponds to the PAI in leaf-off conditions (Calders *et al*., 2015). This was carried out on the spring PAI data for each plot using optimisation of parameters of the sigmoid function.

8.3   Results and discussion

This section presents the results for all five test plots. First, the results of the multi-temporal PAI and PAVD estimates derived from TLS are examined, followed by a comparison to PAI estimates derived from DHP. Finally, the results for the spring green-up period are analysed and discussed.

Prepare data
Pre-processing (*Chapter 4.3.4*)
Crop to plot size (*Chapter 3.3.3, Table 7.1*)
Remove ringing (*Chapter 4.3.4.3*)
Filter large widths (*Chapter 5.2.4*)

Apply radiometric calibration
(*Chapter 4.6*)

Apparent reflectance (λ1063nm)

Calculate a weighting (*w*) to allow for
multiple returns for each beam
(*Chapter 2.7.3*)

Find hits by zenith angle θ and height, *z*
$hits(\theta,z) = \Sigma w(\theta,z)$

Find total number of beams emitted
$N(\theta)$

Calculate gap fraction
$Pgap(\theta,z) = 1 - (hits(\theta,z) / N(\theta))$

Calculate PAI using hinge angle
(*Chapter 2.7.2*)

Calculate PAVP
(*Chapter 2.7.3*)

Figure 8.1. Workflow for the analysis of a SALCA point cloud to achieve estimates of PAI and PAVD.

Following processing to apparent reflectance it was clear that the reflectance calibration had not performed well for a small number of the scans. Further investigation found this occurred where laser case temperatures were unusually high (mostly affecting the summer scans), and therefore out of the range of training data used in the development of the neural network approach (Chapter 4). Although the apparent reflectance values were not used in the point-based gap fraction approach implemented here, the high laser case temperatures affect the resultant PAI estimates for the following reason. As noted in Chapter 4, a negative relationship exists between laser case temperature and recorded intensity (Figure 4.13). An implication of this is as laser case temperature increases, the number of returns

for a given scene decreases as low intensity returns that would previously be recorded fall below the noise threshold. This relationship therefore affects the number of 'hits' (representing plant material) used to estimate PAI. As a result, the scans which exhibited high laser case temperatures were excluded from analysis. Predominantly this occurred in the summer months where a stable PAI is expected; therefore the removed estimates should not affect the general interpretation of the results. Cleaning of scans, resulting in removal of datasets from analysis, is not uncommon in TLS analysis (e.g. Griebel *et al*., 2015).

8.3.1   Seasonal variation in stand PAI

Figure 8.2 shows the time-series of PAI generated from TLS, for the five test plots. Plots 1-3 (Figure 8.2 a-c) show the results for the broadleaf deciduous stands, where the temporal PAI form show a similar trend, summarised in the following observations.

Spring (April, May) is characterised by an increase in PAI as new material emerges from dormant buds and unfolds and expands to form leaves throughout the canopy. This signals the start of the growing season as the new material becomes photosynthetically-active. The PAI for Plot 1 (oak) showed a linear increase from 0.89 to 2.36 between Julian days 91-127. A linear increase is also evident for Plot 2 (sweet chestnut) during this period where the PAI increased from 0.66 to 1.39 between Julian days 91-139, before displaying a sharp increase in PAI to Julian day 150. This could be attributed to a rapid increase in plant material during the second half of May. In Plot 3 (beech) (Figure 8.2c), there was minimal change in plant material until the end of April, where a rapid increase in PAI can be observed from 0.87 to 1.95 (Julian days 118-134). Quantifying spring growth has high ecological value as it drives the physiological activity of the canopy, this will be examined in more detail later in the chapter.

Summer (June, July, and August) is characterised by a state of maturity in the canopy when leaves are fully expanded and the forest is at maximum productivity. A plateau of PAI is evident in the three broadleaf deciduous plots at approximately: 3.3 (Plot 1), 2.8 (Plot 2), and 2.0 (Plot 3). According to the results, Plot 1 reaches a stable PAI from early May to mid-June, and then increases again to reach a higher PAI throughout July and most of August; indicating a second growth period at the end of June. Plot 2 shows a similar form where PAI is stable through June and into July, before an increase in PAI is evident in August. In Plot 3 PAI was relatively stable from mid-May to mid-September.

(a) Plot 1
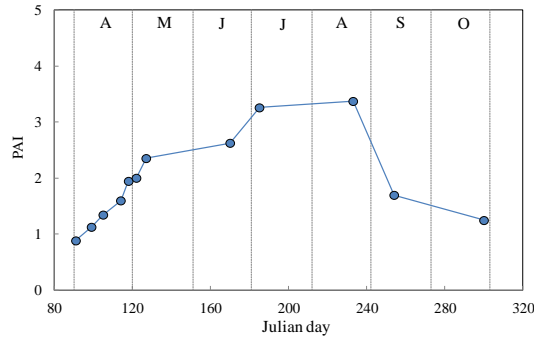
(b) Plot 2
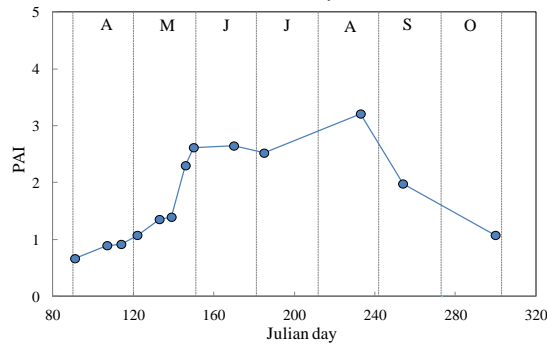
(c) Plot 3
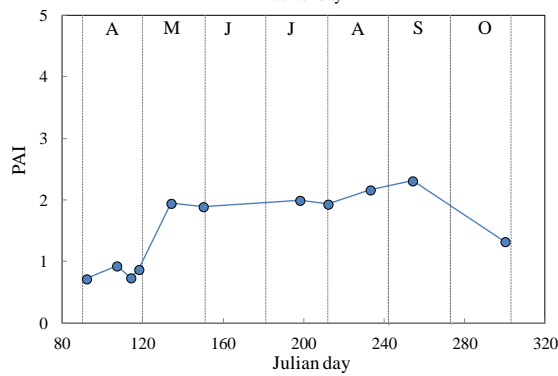
(d) Plot 4
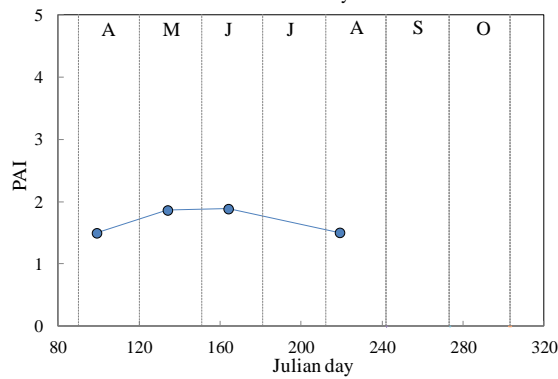
(e) Plot 5
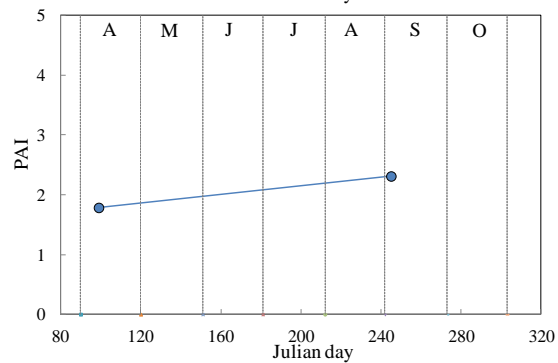
Figure 8.2. Time-series of PAI derived from TLS for the five test plots at Delamere Forest, from April (A) to October (O).

177

The increase in summer PAI observed in Plot 1 and 2 indicates a second growth period. Some woodland species, such as oak, have a second flush of leaves (lammas growth) around July/August (Thomas, 2011).

Autumn (September, October) in the broadleaf deciduous stands is characterised by senescence and abscission, when changing environmental conditions drive a decrease in photosynthetic capacity. This is evident in all three plots. Plot 1 and Plot 2 display a decreasing PAI throughout September and October to values of 1.25 (Plot 1) and 1.07 (Plot 2), and Plot 3 from mid-September to a PAI value of 1.33. These values of PAI are higher than those observed at start of scanning in April, indicating that the plot has not yet reached its leaf-off state. This is confirmed by the presence of foliage evident on DHP images and recorded in field notes for these dates.

Plot 4, comprised of needle-leaf evergreen species, showed a relatively stable PAI over the four scans, as expected. However, slightly higher values of PAI were observed in May and June compared with April and August, with a total increase in PAI of approximately 0.4. The two measurements acquired in Plot 5, the needle-leaf deciduous stand, show an increase in PAI from 1.79 (9th April) to 2.31 (2nd September). The relatively small increase in PAI for this stand can be attributed to three factors: the stand was not in a completely leaf-off state in April, the second measurement was acquired in September when PAI may have already started to decrease, and that Japanese larch trees have a notably 'woody' composition (therefore an expected higher wood to leaf ratio).

8.3.2 Vertical structure of plant material

Vertical profiles of PAVD and PAI are shown in Figure 8.3 for the five test plots. PAI is displayed as a cumulative value; the derivative of which is the PAVD at a 1m height resolution. A comparison of the results derived for Plot 1 and Plot 2 exemplify the significance of vertically resolved parameters. The minimum and maximum PAI values for these two plots was similar (0.85-3.37: Plot 1 and 0.66-3.21: Plot 2) yet the vertical distribution of the plant material is very differently. These structural differences have important implications for radiation interception, growth, and habitat characteristics, but would be overlooked if PAI alone was examined. For Plots 1, 3, 4 and 5, the vertical distribution of canopy material could be described by a Gaussian distribution curve (although Plot 4 shows a negative skewness), showing maximum leaf area at an intermediate position within the crown which gradually decreases upward and downward

through the canopy (Kozlowski *et al.*, 1991). The vertical distribution of plant material at Plot 2 is more stable with height, with no single well-defined crown. This could be attributed to the presence of many juvenile trees in the understorey, altering the height distribution.

Plot 1 shows a gradual filling out of the canopy over the year. In leaf-off conditions (pale red line; Julian day 91), the woody canopy is well-defined but PAVD is relatively constant with height between 11 to 18m. Development of foliage during spring and summer has driven an increase in PAVD throughout the canopy but with a notable bias to the upper canopy; during maximum recorded PAI (Julian days 185 and 233), the peak PAVD value is located at 17m. This is an oak-dominated plot and the high volume of leaf area at the top of the canopy is supported by the findings during the destructive campaign at Alice Holt on the oak trees outlined in Chapter 5. Interestingly, the results show that during autumn when PAI begins to decrease (Julian days 254 and 300) more leaf material is lost from the upper canopy relative to the lower canopy. This could be explained by the leaves at the top of the canopy being more exposed to wind so that breaks in the abscission layer cause earlier leaf-fall, compared to the more sheltered lower canopy.

Leaf-off conditions in Plot 2 (Julian day 91) is characterised by a relatively constant volume of woody material with height. As foliage develops throughout spring and summer, several peaks in leaf area emerge; most notable at around 4m and 24m in height, caused by development of the understorey and upper canopy, respectively. Two clusters of PAVD and PAI profiles can be observed, with a gap between Julian days 139 and 146. This indicates that a surge in foliage growth occurred between these dates. In a similar manner to Plot 1, the autumn scans (Julian days 254 and 300) show that PAI decreased more rapidly from the upper canopy compared with the lower canopy and understorey.

Plot 3 also exhibits two distinct clusters of PAI and PAVD profiles, separated by Julian days 127 and 134 (earlier than Plot 2). Compared to a relatively constant distribution of woody material with height in leaf-off conditions, the summer scans (Julian days 134-254) show a distinct canopy centred at 16m. This beech stand had sparse ground vegetation and no understorey which is characteristic of this species. Therefore, the lower peaks in leaf material are due to lower branches. The decreasing leaf area in autumn is present at Julian day 300. At Julian day 254, when PAI at Plot 1 and Plot 2 is decreasing rapidly, the highest PAI is observed in Plot 3.

Plot 4 and Plot 5 display similar characteristics between winter and summer scans. Plot 4 shows an increase in leaf area during the two summer scans (Julian days 134 and 164) from 12m in height to the top of the stand, with no change in PAI in the lower layers. This indicates that the needle-leaves have increased leaf area to take advantage of higher summer solar radiation at the top of the canopy. The two winter scans in Plot 4 (Julian days 99 and 219) show very stable profiles. Plot 5 also shows minimal increase in PAI in lower canopy layers, but canopy foliage development mirroring the normal distribution of the winter scan. The lack of change in the winter to summer profiles for Plot 5 can be attributed to the woody nature of the Japanese larch needle-leaf species and the fact that this plot was not in a true leaf-off state at Julian day 99.
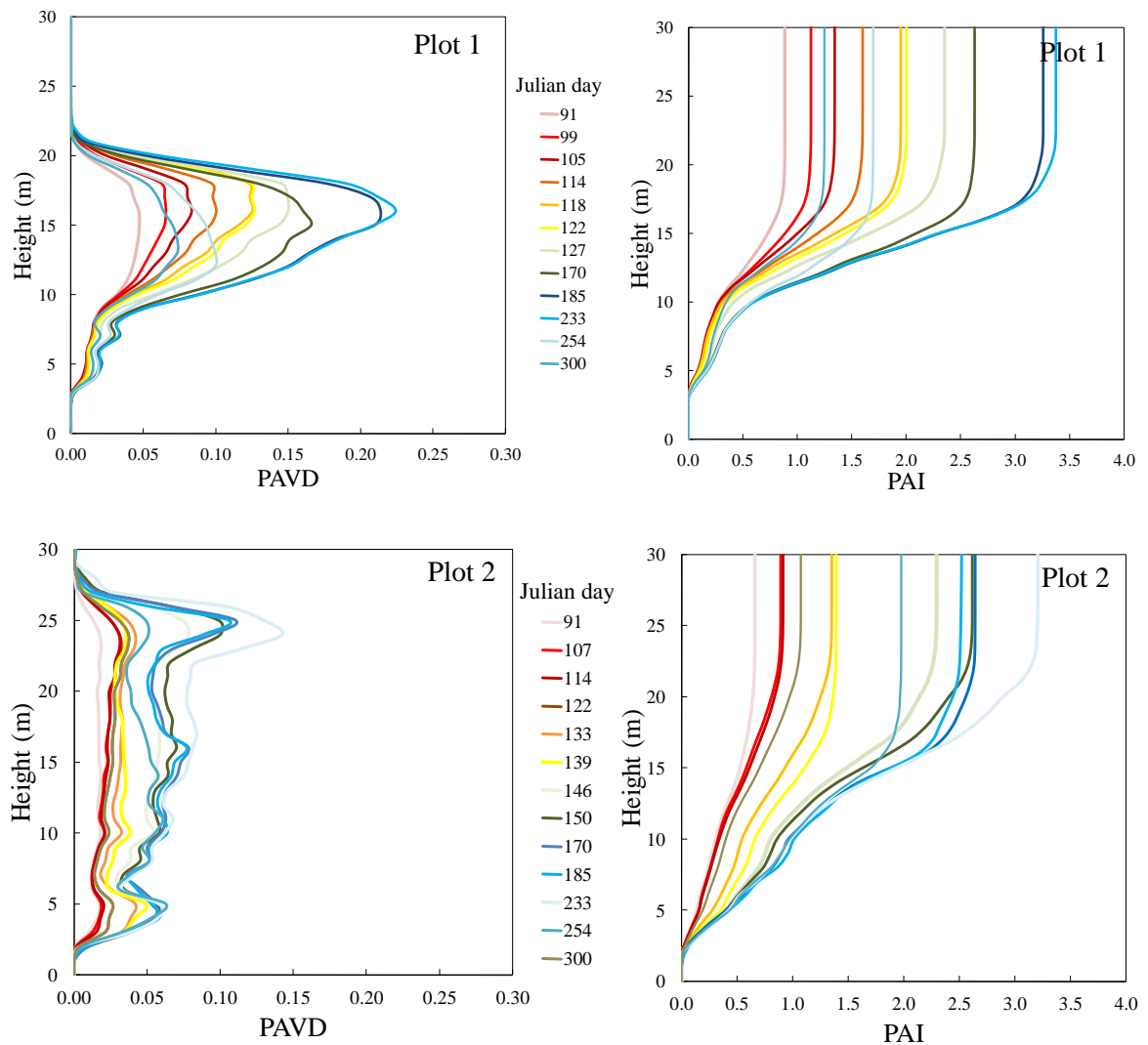
Figure 8.3. Time-series of PAI vertical cumulative profiles (left) and PAVD (right).
[Continued on following page]
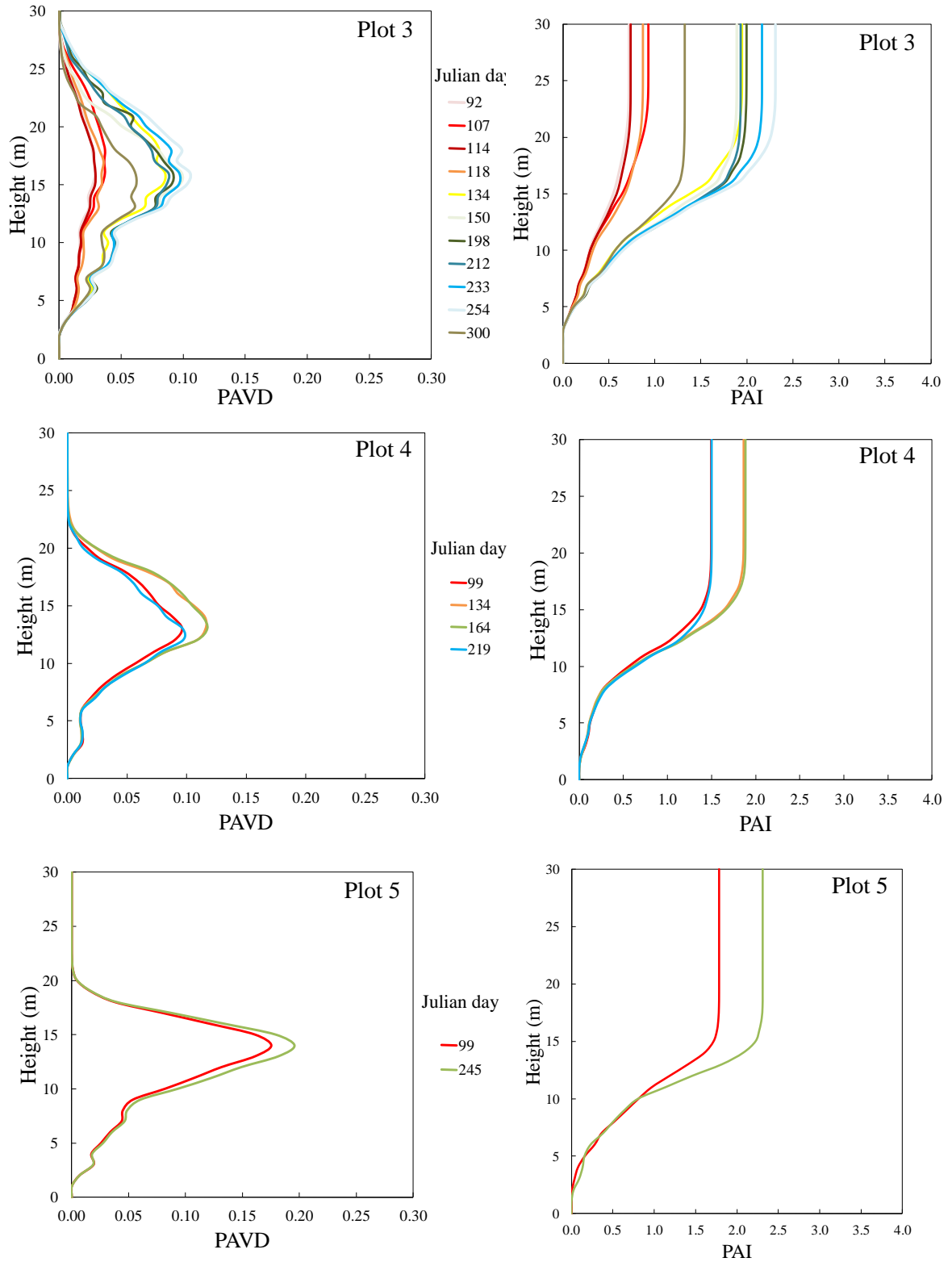
Figure 8.3. Continued.

8.3.3 Comparison of TLS and DHP

The time-series of PAI generated from TLS is compared with corresponding estimates derived from DHP in Figure 8.4 and Figure 8.5. Plot 5 is excluded from Figure 8.4 as there was only one measurement with TLS and DHP (Figure 7.10). The results show that there was good agreement between PAI derived from TLS and effective PAI derived from DHP ($R^2 = 0.74$, RMSE = 0.50; Figure 8.5a), and between PAI (TLS) and true PAI (DHP) ($R^2 = 0.70$, RMSE = 1.25; Figure 8.5b). Underestimation of TLS compared with DHP for higher PAI values was observable from both graphs, but most notable with true PAI (Figure 8.4 and Figure 8.5). Figure 8.4 shows that the PAI time-series in spring exhibited very similar values between the methods. Between Julian days 150 to 235, the PAI (DHP) continued to increase and then fall throughout this summer period, whereas the PAI (TLS) remained relatively constant. The PAI (DHP) estimates for Plot 4 showed some variation throughout the year, but the trend of increase and decrease in PAI is not reflected in the PAI derived from TLS.

The local variance in the temporal profiles of PAI, such as spring DHP in Plot 2 (between Julian days 115 and 135) or spring TLS in Plot 3 (within the first four measurements), can most likely be attributed to methodological or instrument issues. In DHP, these mainly relate to the selection of a classification threshold as it is heavily dependent on subjectivity and illumination conditions within and between the images (Jonckheere *et al.,* 2004; Calders *et al.*, 2011). For SALCA, the variability most likely is generated from the thermal effects explained at the beginning of the results section (Section 8.3).

8.3.3 Quantifying spring green-up using TLS

Figure 8.6 shows profiles of PAVD by height for the leafing-out period in the three multi-temporal deciduous plots. The profiles allow the spatial and temporal characteristics of spring growth to be observed and compared between the plots. Figure 8.7 and Table 8.1 show the results of sigmoid function fitting for the three broadleaf deciduous plots. The lower asymptote ('L'; Table 8.1) provides an estimate of the leaf-off PAI from the fitted models: 0.641 (Plot 2), 0.710 (Plot 3) and 0.788 (Plot 1), while the upper asymptote ('U') shows the full-leaf PAI: 1.911 (Plot 3), 2.652 (Plot 2) and 2.652 (Plot 1). Plot 2 had the largest increase in leaf area, and Plot 3 the smallest. The date that maximum growth occurred (t_m) was earliest in Plot 1, followed by Plot 3, and Plot 2 was the latest. The growth rate was similar for Plot 1 and Plot 2, whereas Plot 3 showed more rapid leaf

growth and expansion. These results support previous observations, however, to better constrain the parameter estimation the inclusion of more data points would be advantageous, particularly for Plot 3.
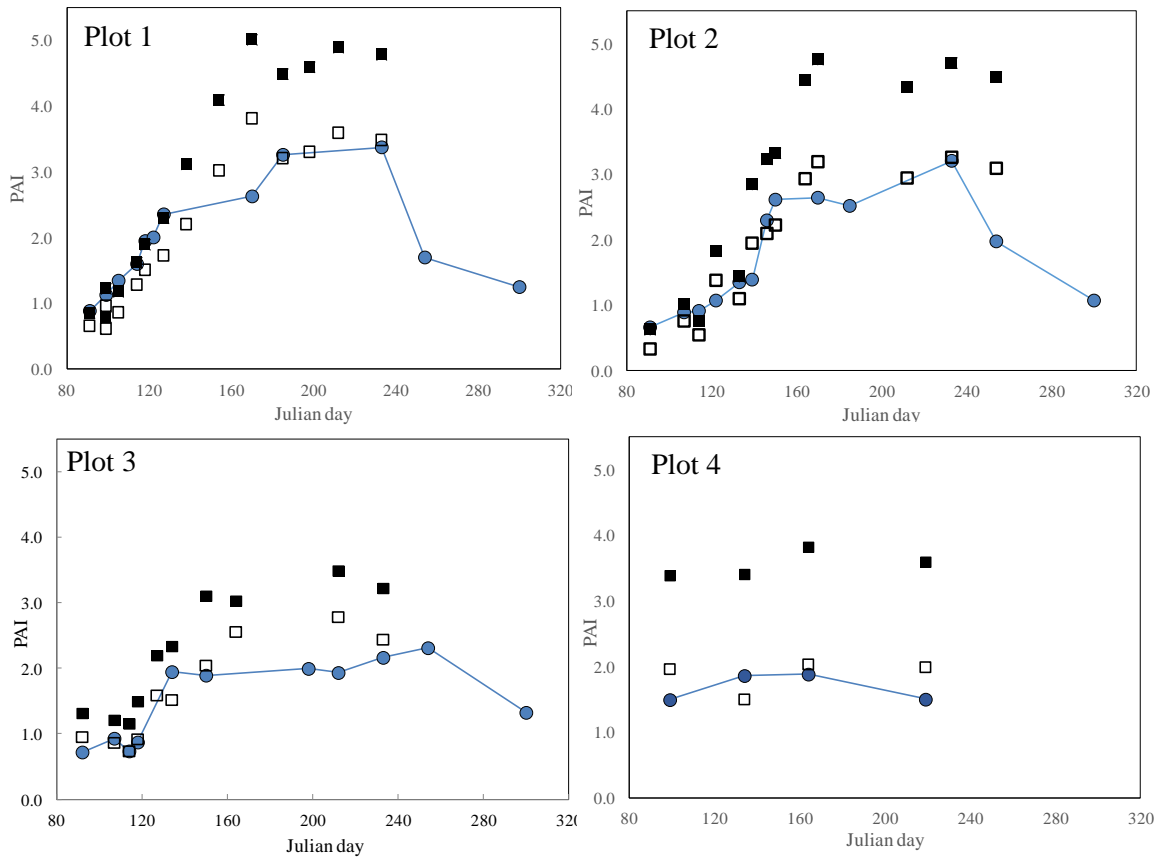
Figure 8.4. Time series of PAI derived from TLS (blue marker and line), effective PAI from DHP (open squares) and true PAI from DHP (black squares) for Plots 1-4.
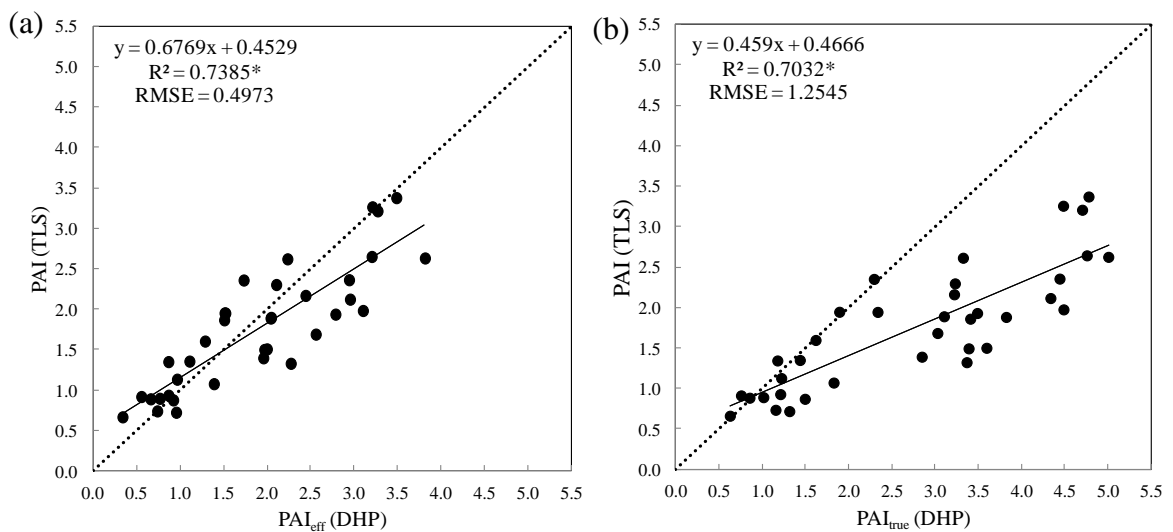
Figure 8.5. Relationship between PAI derived from TLS (using the 1063nm wavelength) and (a) effective PAI derived from DHP, (b) true PAI derived from DHP, for all the measurements in the five plots. * = significant (P ≤ 0.05).
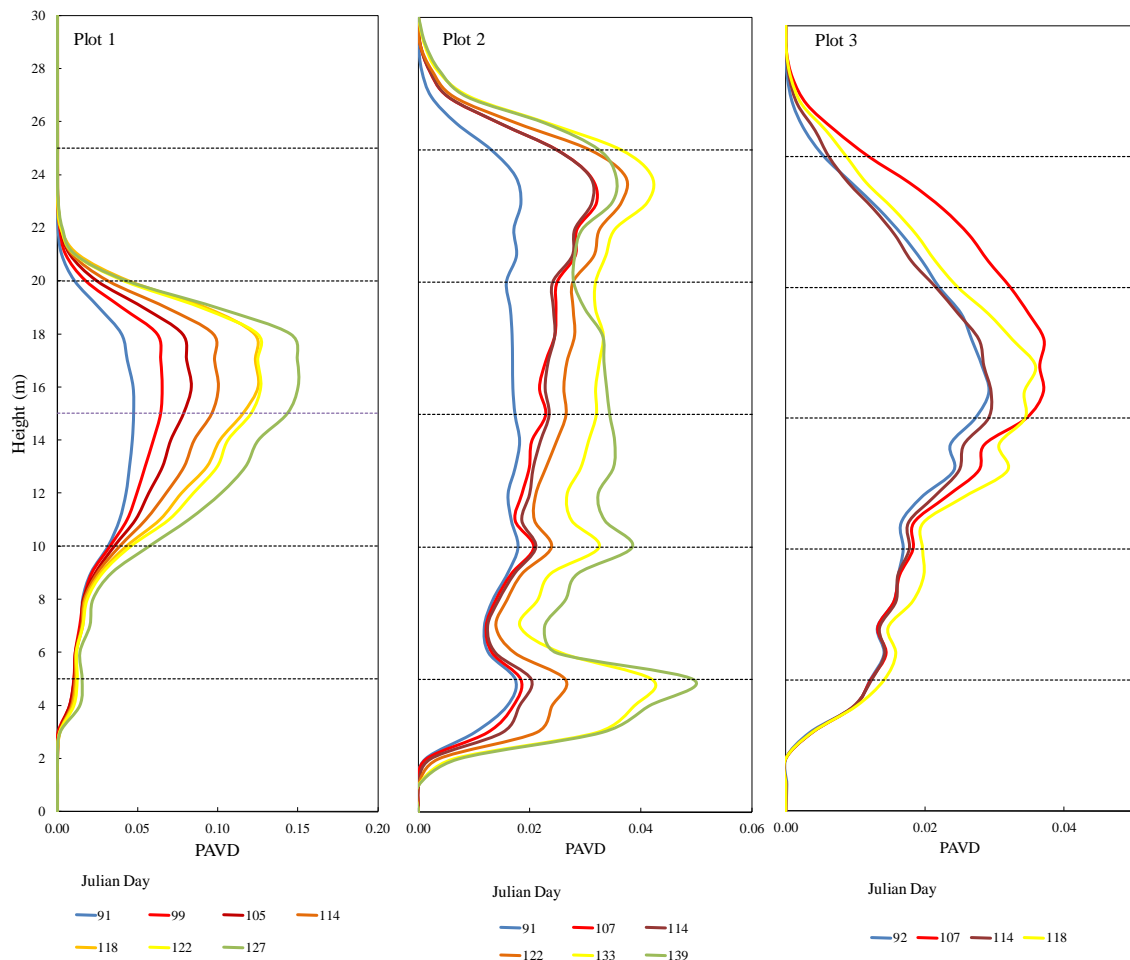
Figure 8.6. Vertical profiles of PAVD for the leafing-out period in the three multi-temporal deciduous plots, coloured by Julian day as shown in the legends.

The PAI value highlighted with a circle in Plot 3 (Figure 8.7) has a higher magnitude than expected respective to its neighbouring points. The sudden increase and decrease in PAI indicated is highly unlikely to be the result of leaf area change. Further investigation into the metadata for this scan revealed that it showed considerably lower laser case temperatures (a maximum recorded value of 22.7°) compared to the scans conducted on the dates either-side (maximum recorded values of 26.0° and 29.2°). Therefore, this PAI has a higher magnitude due to the higher intensity response that meant that more returns were recorded overall. The result of this can be observed in Figure 8.6 (red line) where the laser is able to penetrate further into the canopy.
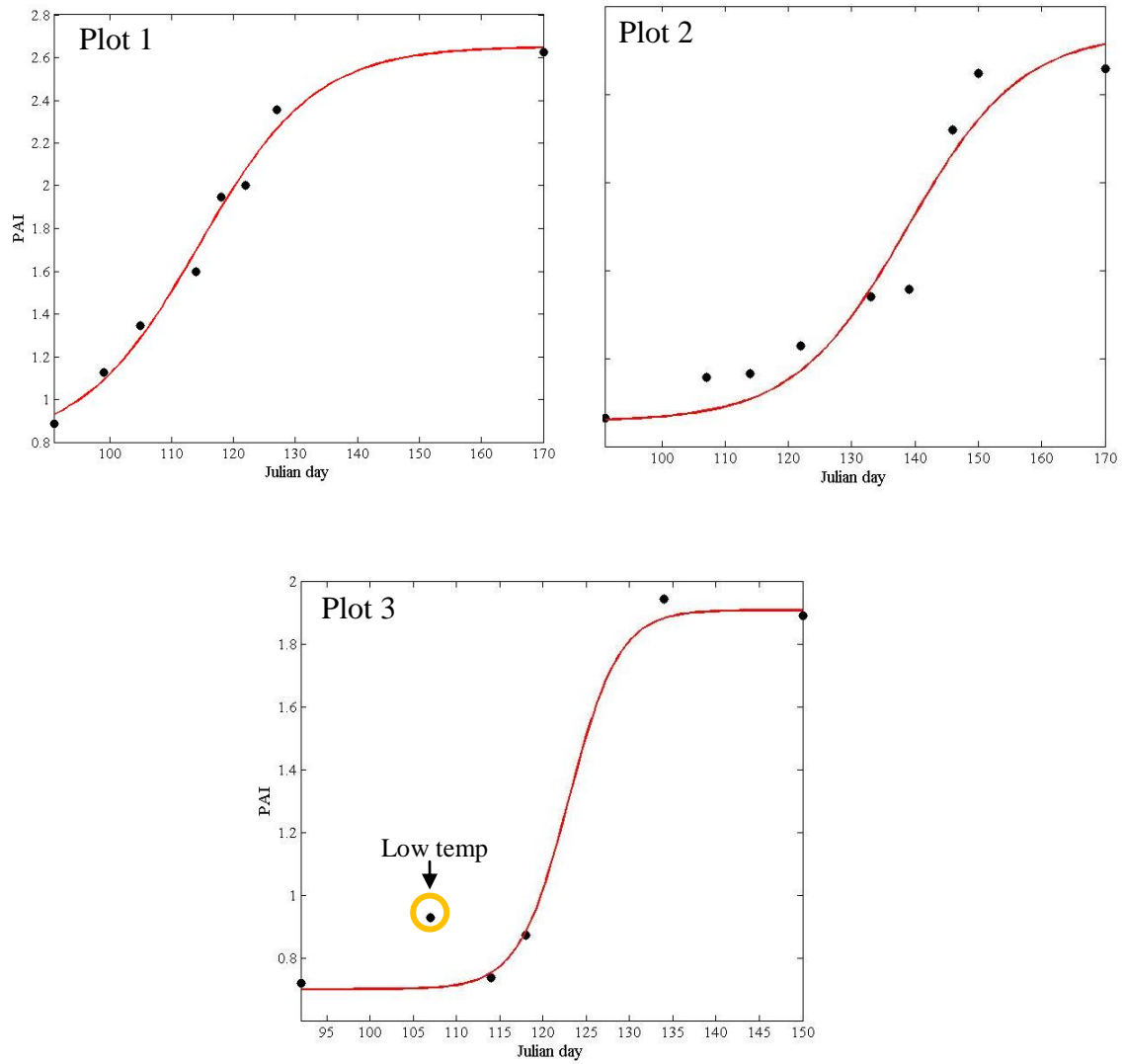
Figure 8.7. Results of sigmoid function fitting for Plot 1, 2, and 3. Black markers are TLS derived PAI estimates by Julian day, and red lines show the models.

Table 8.1. Model parameters from Equation 8.1 for Plot 1, 2 and 3.

Plot	L	U	t_m	k	RMSE
1	0.788	2.652	114.424	0.046	0.065
2	0.641	2.849	138.869	0.049	0.187
3	0.710	1.911	124.355	0.094	0.115

As shown in Calders *et al*. (2015), the sigmoid fitting shown above can be applied to a time-series of PAI for multiple vertical layers of the canopy (by summing the PAVD by

height). These approaches allow temporally and vertically resolved comparison and quantification of leaf area change within and between plots and could form the basis of an approach to monitor the phenology of woodland stands using TLS.

8.4   Conclusions

The aim of this chapter was to examine the spatial and temporal characteristics of foliage in a range of UK forest types. This has been achieved in three main ways: (i) by assessing seasonal change in PAI profiles for five different forest stands (broadleaf deciduous, evergreen conifers, and needle-leaf deciduous stands), (ii) examining how plant area is distributed vertically throughout each canopy and how this changes with time, and (iii) quantifying the 4D spring growth in the three deciduous canopies.

PAI values derived from TLS showed good agreement with those derived from DHP, most notably with the effective PAI. In general, the seasonal trends measured using both methods were similar, particularly during the leafing out period. In the summer months, the TLS showed a tendency to generate slightly lower PAI values compared to the DHP. The results have illustrated the increased ecological information derivable from 3D measurements with TLS. For instance, two stands exhibiting very similar PAI values can have entirely different vertical structure.

The results presented in this chapter have captured the seasonal dynamics of foliage growth in different forest types. However, the inability to reliably separate the point cloud into leaves and wood has resulted in PAI estimates from a single wavelength of the SALCA instrument, as presented in this chapter. This has meant that the full capacity of the dual-wavelength functionality has unfortunately not been utilised. Although considerable research activity has been focussed on the data processing and calibration of the SALCA instrument as outlined in this thesis, there are still issues to be addressed. For instance, although the radiometric response to temperature has been investigated in depth, the effect that it has on the magnitude of returns recorded and the consequent implications for 'point-based' analysis, requires further investigation. A discussion of these factors and other key issues arising from the research are presented in the next chapter.

CHAPTER 9

Discussion and conclusions

9.1 Introduction

The overall aim of this research was to improve characterisation of the seasonal dynamics of UK woodland vegetation structure using dual-wavelength terrestrial laser scanning. A multi-temporal monitoring experiment was conducted with the SALCA instrument to facilitate the quantification of foliage dynamics in a range of UK forest types. Validation of the results was provided by destructive measurements for the individual tree scale and comparison with measurements from DHP at the plot scale. The results from each research activity have been discussed throughout Chapters 4 to 8 and therefore the aim of this chapter is to provide a summary of the key findings and discuss the implications within the scope of the research objectives defined in Chapter 2. This is followed by a discussion of the future prospects for leaf-wood separation using TLS and quantifying forest structure with lidar. The thesis conclusions are presented at the end of this chapter.

9.2 Assessment of Objective 1

Objective 1, to produce an apparent reflectance product for the SALCA instrument, was achieved by developing a novel radiometric calibration procedure. This was the first demonstration of the application of neural networks to convert TLS intensity into values of apparent reflectance (Schofield *et al*., 2016). The first stage to implementing such an approach involved characterising the recorded intensity response to measurable parameters, which resulted in 868 measurements of intensity, range, reflectance, and laser case temperature for seven external reference targets. The generation of an apparent reflectance product is considered the highest level of intensity processing, as defined by Kashani *et al*. (2015), and has only been achieved for a few TLS instruments.

The ability to generate apparent reflectance from a laser scanning system is essential for inferring information on target properties and therefore increasing the ecological value of such data. The results presented in this thesis have shown that radiometric calibration of TLS data can be achieved using neural networks allowing an apparent reflectance product for the SALCA instrument, therefore satisfying Objective 1. The novel approach presented in this research can be benchmarked against other existing methods and comparisons made with results from other instruments in the future.

The main limitation of this approach to calibration was the inability of the neural networks to accurately extrapolate beyond the range of training data for which they had been trained, a known disadvantage of neural networks (Demuth & Beale, 2002). This was evident in some of the results presented; such as the apparent reflectance product for Tree 02 and Tree 03 at the end of Chapter 5, and the presence of apparent reflectance values of less than zero percent in the calibrated plots in Chapter 7. To address this limitation and improve the performance of the networks, the range of input training data should be extended, in range, reflectance, and laser temperature.

Research Question 1.1: What are the radiometric characteristics of the SALCA instrument?

This research has provided the first description of the radiometric characteristics of a unique dual-wavelength TLS. A key outcome was realising the effect of internal variations in temperature and laser output power on intensity response. A negative relationship was observed between laser temperature and recorded intensity from the SALCA instrument. The temperature-dependent decrease in intensity had a stronger effect for the λ1545nm and a stronger correlation (R^2 values between 0.78-0.92) than for the λ1063nm. The dependence of laser power on temperature is well known, and yet this is the first time that this dependency in a TLS instrument has been described.

A non-linear and non-monotonic variation in recorded intensity with range was observed; showing a near-range effect up until 8m when the inverse square range function became dominant. This form was similar to those described in Kaasalainen *et al.* (2011), Höfle (2014), Koenig *et al.* (2013), and Ramirez *et al*. (2013) for a range of other instruments. A positive non-linear relationship was found between intensity and reflectance. It is expected that intensity values increase with surface reflectance because a surface with higher

reflectivity will return more energy from the pulse. However, the non-linear response of the SALCA detector has not been reported for other TLS.

Research Question 1.2: What is the accuracy of the apparent reflectance product?

A neural network was built using optimised parameters for each wavelength independently, trained using the collected reflectance panel data, and then simulated with new data. The selected neural networks which showed the most accurate results had an average error of 7.2% reflectance for the 1063nm wavelength and 6.9% reflectance for the 1545nm wavelength. These results are comparable with calibration fitting of the DWEL instrument of 8.1% (1064nm laser) and 6.4% (1548nm laser) (Li *et al.,* 2015a).

Validation of the neural network outputs have been achieved using data extracted from calibration panels. It is very difficult to validate comprehensively for tree components, due to the high magnitude of spectral variability observed in the foliage and woody material, and ensuring that the target being validated is in fact the exact target that was imaged (due to moss or lichen on bark, for instance). The accuracy of the neural networks could be determined more comprehensively using natural targets found in forests, and also perhaps in a laboratory environment.

9.3   Assessment of Objective 2

Objective 2, to assess whether dual-wavelength lidar can be used to separate leaf and wood returns, was investigated on a tree and plot scale. Two methods for leaf-wood separation were investigated in this research which involved: (i) applying a threshold to the apparent reflectance of the 1545nm wavelength, and (ii) matching the returns from each wavelengths and taking a normalised ratio (NDI) of the apparent reflectance value, before applying a threshold. The threshold value was defined based on the frequency distributions of leaf-off and leaf-on scans, which then classified each return to one of two classes to represent leaf and wood material. There were three methods implemented to assess the performance of the leaf-wood separation achieved by each of the two method. First, a visual inspection of the classified point clouds to judge whether the returns making up the trunks and branches appeared to be classified to 'wood', and the leaf material as the other class. Second, the same procedures applied to the leaf-on scans were applied to the leaf-off conditions and the percentage of the point cloud misclassified to the leaf category was

recorded. Finally, for the individual trees at Alice Holt, the direct LAI measurements provided a validation dataset for the LAI values derived from the TLS using the returns classified as 'leaf'. This procedure allowed the assessment of whether dual-wavelength lidar can be used to separate leaf and wood returns, therefore satisfying Objective 2.

Research Question 2.1: Can leaf and wood separation be achieved on a tree and plot scale with dual-wavelength TLS?

Table 9.1 summarises the tree and plot scale misclassification errors generated by using the two thresholding methods for leaf-wood separation. The misclassification error was consistently lower when the classifications were applied on the tree scale (Chapter 5) compared to the plot scale (Chapter 7). This can be attributed to the fact that there is a larger mix of biological materials present in a plot scene, compared to an isolated individual tree. Therefore, a larger amount of spectral variability and external factors would be introduced that would affect the apparent reflectance values. For all cases the errors are lower using the NDI compared to a single wavelength suggesting that a dual-wavelength approach outperformed using a single wavelength. However, it should be noted that error was assessed in one direction (i.e. the percentage of wood classified as leaf). Unless the exact amount of leaf is known, such as in a virtual model (e.g. Tao *et al.*, 2015), quantifying the error of leaf classified as wood poses significant challenges.

Table 9.1. Summary of misclassification errors on the tree and plot scales using the two leaf thresholding methods. Values are given in percent. Tree scale results relate to the three scanning positions of Tree 01 (Chapter 5), and plot scale results are for the deciduous Plots 1, 2, 3, and 5 at full-leaf (Chapter 7).

Threshold method	Tree scale	Plot scale
λ1545nm	70.0, 67.3, 64.1	79.8, 82.4, 82.0, 65.9
NDI	38.6, 28.4, 24.9	42.6, 44.1, 32.2, 49.2

Previous leaf-wood separation research, using a single wavelength, have been carried out on small isolated individual trees (Béland *et al.*, 2011; Hosoi & Omasa, 2009). In these studies, although visual inspection of the resultant classification has been undertaken, a quantitative measure of the success of the classification was not. Furthermore, the findings

from this research indicate that extrapolating classification methods from the tree to the plot scale presents some challenges to constrain accuracy at the plot scale.

Research Question 2.2: How does leaf-wood separation vary for different UK woodland species?

The test plots surveyed at Delamere forest included five stands of differing, but common, UK woodland species. As before, the NDI showed the lowest misclassification errors for all of the plots compared with the single wavelength approach. According to the NDI results, the lowest error (32%) was achieved in Plot 3, the beech stand, which was the most homogeneous plot: single species, no ground vegetation, and trees of similar age. The largest error (49%) was found in Plot 5, the Japanese Larch stand, and the poor results here can be attributed to the fact that buds and needles are visible in the 'leaf-off' scan. Plot 1 and Plot 2 contained misclassification errors of 42% and 44%. Plot 1 was a mixed plot, dominated by oak trees but comprising sweet chestnut and silver birch individuals, as well as a varied ground vegetation layer. Although Plot 2 was mostly sweet chestnut species, apart from some conifers around the edge of one side, many juvenile individuals were present here, in close proximity of the scanner. These variables would have increased the spectral variability of the plots and therefore increased the variability in the NDI.

Based purely on the misclassification errors discussed above, it may be concluded that the NDI method (using both wavelengths), provided a more accurate method for leaf-wood separation than that based on a single wavelength (the 1545nm method). However, visual inspection of the classified point clouds, apparent reflectance distributions, and the stability of the resultant classification and LAI values, as described in earlier chapters, have indicated that there are still some significant challenges to be addressed in applying this method. The performance of using a single threshold for leaf wood separation is relatively easy to explain by the incorporation of partial hits as cited in previous studies (Béland *et al*., 2014). However, the performance of the NDI is more complicated, and could be due to a number of reasons, a discussion of which is addressed in a later section. As shown in this research, once a leaf-only product has been achieved, the apparent reflectance of each return can be used to account for partial beam interception (Chapter 6 and Chapter 7). This should help to improve accuracy of LAI measurements for TLS.

9.4 Assessment of Objective 3

Objective 3, to examine the spatial and temporal characteristics of foliage in a range of UK forest types, was addressed by comparing 57 measurements of PAVD and PAI profiles collected over a full annual seasonal cycle for the five Delamere test plots. The research presented in Chapter 7 and Chapter 8 provides the first PAI and PAVD values from the SALCA instrument. Using these repeat measurements, the spatial and temporal growth dynamics was examined, allowing Objective 3 to be fulfilled.

Research Question 3.1: Does the spatial distribution of foliage vary between stands?

Profiles of PAVD have enabled dynamics within the forest structure to be vertically resolved (such as in Griebel *et al*., 2015; Calders *et al*., 2015). A comparison of the PAVD profiles derived for the five test plots (Chapter 7 and Chapter 8) exemplify the significance of these vertically resolved parameters. The results show that the spatial distribution of plant material (and foliage when comparing a leaf-off and leaf-on condition) can vary between stands. Although in the majority of cases the bulk of the material was held in the canopy, differences in understorey and height strata of each plot could be determined. 2D methods of PAI estimation, such as DHP as shown in this study, or optical satellite-based observations, cannot differentiate between these vertical layers. The ability to describe vertical canopy structure is essential for many ecosystem studies due to its effect on net primary productivity, sub-canopy radiation, temperature and moisture environment, and as a result, habitat characterisation (Landsberg & Sands, 2011).

Research Question 3.2: Are there differences in the temporal characteristics of foliage growth between stands?

The results in this research have illustrated how PAI is variable through time, even in an evergreen stand. This illustrates the need for high temporal resolution of PAI dynamics for critical estimation of key biochemical and physical processes such as CO_2 fluxes, and water and light interception (Breda, 2003). The forest growth, measurable through comparing PAI values of repeat measurements, therefore gives insight into the magnitude of these processes over time. The results have shown that there are differences in the temporal characteristics of foliage growth between stands. These differences are observable both in timing and magnitude between the plots, and have been measured through PAI derived by both TLS and DHP. The PAI estimates have shown good

agreement between the methods although a tendency for higher summer estimates from DHP which is supported by the gap fraction calculations in Chapter 7. As both of these methods are indirect approaches, there is no 'ground-truth' for validation. However, the techniques deployed in both methods are well established and while it cannot be concluded that one method is more accurate than the other, the results provide a useful comparison as discussed.

9.5 Further consideration of the separation of leaf and wood using TLS

The aspects affecting the NDI values, and leaf-wood separation more generally, can be summarised as ecological, instrumental and processing factors. These factors are considered in light of the findings of this research together with future research needs in this area that are required.

9.5.1 Ecological

The surface reflectance of an object at a particular wavelength is a function of the complex physiochemical characteristics of the material itself, combined with other factors such as surface humidity and micro-roughness (Pesci & Teza, 2008). ASD data and apparent reflectance values obtained in this research indicated that for some species there is no clear spectral separation between leaf and bark material. The results also indicate that there is a large amount of spectral variability in tree species, particularly in bark material, and that this varies between species. Gathering representative spectral information at a plot scale is a very difficult task because of the inherent heterogeneity between and within plant species such as age, stage of growth (e.g. first and second flush of leaves can differ (Thomas, 2011)), health, site characteristics, and external factors (e.g. moisture). Further research into the spectral variability of certain species, particularly bark which is under-represented in the literature, would be beneficial.

9.5.2 Instrumental

The principle behind the NDI is that the middle-infrared laser, 1545nm, is sensitive to internal water content, whereas the near-infrared laser, 1063nm, is not. However, at 1063nm, there is still a slight sensitivity to water content which has the potential to introduce noise into the calculated ratios (Gaulton *et al*., 2013). The configuration of the SALCA instrument could potentially be simulated within a ray tracing model (such as Librat; Lewis, 1999). This would allow the effect of footprint size, sequential scanning,

and beam divergence, on the NDI to be investigated for a range of vegetation targets. More generally, the choice of wavelengths and design of the instrument (ensuring perfectly aligned beams, for instance) is key for future multi-spectral instruments. However, issues of eye-safety, cost, and availability, mean that ideal wavelengths are not always possible.

9.5.3 Processing

Deriving reliable and accurate NDI calculations relies on a calibration of intensity to apparent reflectance. The results in this research suggest that the limitations of neural network approach described earlier had limited the application of the NDI for some scans (Chapter 7.3.3), emphasising the reliance of this approach on a successful and robust calibration. Furthermore, the calculation of NDI values in itself has the potential to introduce noise. For instance, when a ratio is taken of two very small values, a relative change in either value makes a considerable change to the result. Therefore, an alternative processing method which incorporates the apparent reflectance from both wavelengths could be investigated in the future.

9.5.4 New approaches

The separation of leaf and wood material in lidar data, and other indirect approaches, remains a key goal of improving measurements of vegetated environments. The leaf-wood separation methods implemented in this research are based purely on spectral information. To address some of the challenges discussed above, other approaches could be considered to improve the classifications. These methods include classifying point clouds based on their 3D geometrical properties. Brodu & Lague (2012) developed a procedure for examining point clouds at a given location and scale, and identifying lines, planes, and volumes to classify natural scenes. For vegetation, this corresponds to stems, leaves, and 3D vegetation, respectively. Combining this information from multiple scales meant that signatures could be developed to identify categories of objects in a given scene, with accuracy of upwards of 97.5%. In very recent work, this method has been combined with apparent reflectance to provide a classification to leaf and wood for the DWEL instrument (Li *et al.*, 2015b). Similarly, newly published research by Tao *et al.* (2015) also uses geometrical features for classification. In this approach, tree point clouds were sliced into horizontal layers and within each segment, circle (and circle-like) features were identified as wood, and line segments as leaves. This achieved misclassification errors of 10.7% on a 'virtual' tree, and 13.4-16.9% on real individual trees.

A further way to improve classification would be to incorporate information on the pulse shape. For instance, Yang *et al*. (2013) classified trunk/branch or foliage by thresholding the relative width of the return waveforms, and Fieber *et al*. (2013) classified an orchard according to pulse width and a backscattering coefficient. Utilising pulse shape was considered for the SALCA instrument as part of this research, but a preliminary investigation indicated that extracting further information on pulse width may be limited by the pulse length to sampling ratio of the instrument. However, this could be examined further (although the issue of 'hidden peaks' will need to be resolved in the waveform processing; Chapter 5.2.4).

9.6   Future of quantifying forest structure with lidar

Lidar is a relatively new but rapidly developing technology. Airborne laser scanning first emerged for topographic and urban mapping in the 1970s (Baltsavias, 1999), and the demand for lidar point data sets accelerated rapidly with commercial airborne lidar systems widely available in the 1990s, and a further nine years before the first TLS was built (Heritage & Large, 2009). Since then, the variety of commercial TLS systems available has rapidly expanded leading to a wide variety of applications, such as forestry. More recently, the desire to have access to the raw data and tailored instrument characteristics have driven the development of custom-designed instruments such as SALCA, DWEL, HSL, MWCL, and VEGNET (Chapter 2.7.4). These instruments have only been operational in the last few years and are beginning to demonstrate their potential for their individual purposes. This trend in developing custom instruments coupled with the emergence of new commercial systems, is bound to see further use of the geometric and radiometric information from lidar, and find new ways to quantify and characterise vegetation. The experimental research presented in this thesis is important in investigating the information content of data from TLS systems in order to inform future instrument design and application areas.

The application of TLS for measuring vegetation seasonal dynamics has been clearly demonstrated as seen in the LAI, foliage profiles, and spring phenology quantification in this thesis. But for these plot-based measurements to be most useful, methods to extrapolate the estimates to broader scales, landscape or even regional, are required (Newnham *et al*., 2015). With the current and future availability of lidar on other

platforms; airborne and spacebourne, this link can be addressed directly. Exciting laser scanning advancements in drone technology (Riegl VUX-SYS, RIEGL, Horn, Austria), airborne (Optech Titan, OPTECH, Henrietta, USA), and spacebourne (GEDI; NASA, 2015) are already creating new opportunities in this area.

However, there are a number of current challenges that remain unresolved within the lidar community. These include factors such as occlusion, clumping, dealing with complex radiometric properties, and separation of vegetation materials, as seen in this thesis. More generally, factors such as cost-effectiveness, time, expertise, volume of datasets, and practicalities of using lidar, still pose a considerable problem. Furthermore, the acceptance and utilisation of TLS at an operational level, by ecologists and foresters in particular, also remains a challenge, for the reasons outlined above, as does the propagation of research activity to commercial implementation.

9.7   Conclusions

Vegetation seasonal dynamics over time, or phenology, is considered one of the most responsive aspects of nature to global warming, and forests themselves are also sensitive indicators of climate change through phenology. This motivates a requirement to quantitatively measure vegetation change. The complexity of dynamic heterogeneous forest environments poses measurement challenges. However, TLS systems provide an opportunity to sample these forest structures and build accurate 3D scenes which can be quantitatively analysed. One of the current limitations of the characterisation of tree and stand structures from TLS is the inability to distinguish between woody material and photosynthetically-active foliage. This is of importance due to the different ecological role each component plays. To address this concern, a custom designed dual-wavelength TLS has been developed known as SALCA. The research in this thesis has presented the use of the SALCA instrument for leaf-wood separation and the characterisation of foliage dynamics at the tree and plot scale. Based on the results obtained, a series of key conclusions may be drawn.

- Neural networks can provide an alternative radiometric calibration of raw intensities recorded from a TLS to realistic values of apparent reflectance, successfully accounting for the complexities of TLS intensity response.

- Increase in laser temperature leads to lower laser outputs and lower recorded intensities. This has been shown to be significant for the SALCA instrument, particularly for the middle-infrared wavelength. It may also be important with other TLS, especially for the increasing number of custom-designed dual/multi-wavelength systems where accurate intensities will be key to quantitative analysis of the data.

- Foliage spatial and temporal dynamics differ between species. Plant area index and PAVD profiles have shown that temporally and vertically resolved plot measurements can allow quantitative analysis of vegetation. Furthermore, PAI values derived from SALCA and DHP have shown good agreement.

- Based on misclassification errors, a dual-wavelength approach to leaf-wood separation performed better than using a single channel, on the tree and plot scale. However, visual inspection of the classified point cloud suggested that the dual-wavelength approach was not always reliable and requires further investigation.

- Dual/multi-wavelength lidar has the potential to aid separation of leaf and wood material in a point cloud, but there are significant ecological (e.g. spectral separability and variability within and between vegetation targets), instrumental (e.g. choice of wavelength), and processing limiting factors (e.g. having a robust calibration).

The original contributions to knowledge of this research can be summarised in four key points: (i) the research provided the first systematic analysis of the radiometric characteristics of a unique dual-wavelength TLS, (ii) the research developed a novel approach to radiometric calibration using neural networks, (iii) the research provided the first study aimed at separating leaf and wood returns using a dual-wavelength TLS and quantitatively comparing the results to using a single wavelength in a variety of species and scales, and (iv) the research presented the first foliage profiles from dual-wavelength LIDAR.

Future research priorities to extend and complement this research include improving the reflectance calibration for the SALCA instrument along with the development of a more comprehensive accuracy assessment, and the investigation of other methods for leaf-wood separation such as the incorporation of geometrical information.

The overall aim of this research project has been to improve characterisation of the seasonal dynamics of UK woodland vegetation structure using dual-wavelength full-waveform terrestrial laser scanning. This research has made a significant contribution to this area by developing and applying new methods and a novel instrument to address some of the current challenges.

References

Abdi, H., Valentin, V., and Edelman, B. (1999). *Neural Networks*. Thousand Oaks, CA: Sage.

Adams, T., Beets, P. and Parrish, C. (2012). Extracting more data from LiDAR in forested areas by analysing waveform shape. *Remote Sensing, 4*, 682-702.

Ahl, D. E., Gower, S. T., Burrows, S. N., Shabanov, N. V., Myneni, R. B. and Knyazikhin, Y. (2006). Monitoring spring canopy phenology of a deciduous broadleaf forest using MODIS. *Remote Sensing of Environment, 104*(1), 88-95.

Ahrends, H. E., Bruegger, R., Stoeckli, R., Schenk, J., Michna, P., Jeanneret, F., Wanner, H. and Eugster, W. (2008). Quantitative phenological observations of a mixed beech forest in northern Switzerland with digital photography. *Journal of Geophysical Research-Biogeosciences, 113*(G4), 1-11.

Ahrends, H. E., Etzold, S., Kutsch, W. L., Stoeckli, R., Bruegger, R., Jeanneret, F., Wanner, H., Buchmann, N. and Eugster, W. (2009). Tree phenology and carbon dioxide fluxes: use of digital photography at for process-based interpretation the ecosystem scale. *Climate Research, 39*(3), 261-274.

Arora, R., Rowland, L. J. and Tanino, K. (2003). Induction and release of bud dormancy in woody perennials: A science comes of age. *HortScience, 38*(5), 911-921.

Asner, G. P. (2009). Tropical forest carbon assessment: integrating satellite and airborne mapping approaches. *Environmental Research Letters, 4*(3), 1-11.

Baker, D. J., Richards, G., Grainger, A., Gonzalez, P., Brown, S., DeFries, R., Held, A., Kellndorfer, J., Ndunda, P., Ojima, D., Skrovseth, P., Souza, C. and Stolle, F. (2010). Achieving forest carbon information with higher certainty: A five-part plan. *Environmental Science & Policy, 13*(3), 249-260.

Balduzzi, M. A. F., Van der Zande, D., Stuckens, J., Verstraeten, W. W. and Coppin, P. (2011). The properties of terrestrial laser system intensity for measuring leaf geometries: A case study with conference pear trees (*Pyrus Communis*). *Sensors, 11*(2), 1657-1681.

Baltsavias, E.P. (1999). Airborne laser scanning: existing systems and firms and other resources. *Journal of Photogrammetry and Remote Sensing, 54*, 164-198.

Baret, F. (2004). *A simple method to calibrate hemispherical photographs* [Online]. http://www.avignon.inra.fr/valeri/fic_htm/methodology/main.php [Last accessed September 2014].

Béland, M., Baldocchi, D. D., Widlowski, J., Fournier, R. A. and Verstraete, M. M. (2014). On seeing the wood from the leaves and the role of voxel size in determining leaf area distribution of forests with terrestrial LiDAR. *Agricultural and Forest Meteorology, 184*(0), 82-97.

Béland, M., Widlowski, J., Fournier, R. A., Côté, J. and Verstraete, M. M. (2011). Estimating leaf area distribution in savanna trees from terrestrial LiDAR measurements. *Agricultural and Forest Meteorology, 151*, 1252–1266.

Bonan, G. (2002). *Ecological Climatology*. Cambridge: Cambridge University Press.

Bowyer, P. and Danson, F. M. (2004). Sensitivity of spectral reflectance to variation in live fuel moisture content at leaf and canopy level. *Remote Sensing of Environment, 92*(3), 297-308.

Breda, N. J. J. (2003). Ground-based measurements of leaf area index: a review of methods, instruments and current controversies. *Journal of Experimental Botany, 54*(392), 2403-2417.

Broadmeadow, M. and Matthews, R. (2003). Forests, carbon and climate change: the UK contribution. Information Note 48. Forestry Commission, Edinburgh.

Brodu, N. and Lague, D. (2012). 3D terrestrial lidar data classification of complex natural scenes using a multi-scale dimensionality criterion: Applications in geomorphology. *ISPRS Journal of Photogrammetry and Remote Sensing*, *68*, 121-134.

Cadule, P., Friedlingstein, P., Bopp, L., Sitch, S., Jones, C. D., Ciais, P., Piao, S. L. and Peylin, P. (2010). Benchmarking coupled climate-carbon models against long-term atmospheric CO_2 measurements. *Global Biogeochemical Cycles*, *24*(2) GB2016.

Calders, K., Schenkels, T., Bartholomeus, H., Armston, J., Verbesselt, J. and Herold, M. (2015). Monitoring spring phenology with high temporal resolution terrestrial LiDAR measurements. *Agricultural and Forest Meteorology, 203*, 158-168.

Calders, K., Verbesselt, J. and Bartholomeus, H. H., M. (2011). 'Applying terrestrial LiDAR to derive gap fraction distribution time series during bud break'. Paper presented at SilviLaser 2011, Hobart, Australia, 16-19 October 2011.

Campbell, J. B. (2002). *Introduction to Remote Sensing* (3rd ed.). New York: Taylor & Francis.

Campioli, M., Gielen, B., Granier, A., Verstraeten, A., Neirynck, J. and Janssens, A. (2010). Carbon allocation to biomas production of leaves, fruits and woody organs at seasonal and annual scale in a deciduous and evergreen temperate forest. *Biogeosciences Discussions, 7*, 7575-7606.

Cannell, M.G.R. and Milne, R. (1995) Carbon pools and sequestration in forest ecosystems in Britain. In: *Carbon Sequestration in Vegetation and Soils*. Report to the Global Atmosphere Division of the Department of the Environment, Institute of Terrestrial Ecology, Penicuik, Edinburgh.

Cannell, M.G.R., Palutikof, J.P. and Sparks, T.H. (1999). *Indicators of Climate Change in the UK*. Department for Environment, Transport and the Regions (DETR), 1999.

Cannell, M.G.R., Palutikof, J.P. and Sparks, T.H. (2003). *Indicators of Climate Change in the UK.* Department for Environment, Transport and the Regions (DETR), update 2003.

Carter, G. A. (1993). Responses of leaf spectral reflectance to plant stress. American *Journal of Botany, 80*(3), 239-243.

Chauve, A., Vega, C., Durrieu, S., Bretar, F., Allouis, T., Pierrot Deseilligny, M. and Puech, W. (2009). Advanced full-waveform lidar data echo detection: Assessing quality of derived terrain and tree height models in an alpine coniferous forest. *International Journal of Remote Sensing, 30*(19), 5211-5228.

Che, M., Chen, B., Innes, J. L., Wang, G., Dou, X., Zhou, T., Zhang, H., Yan, J., Xu, G. and Zhao, H. (2014). Spatial and temporal variations in the end date of the vegetation growing season throughout the Qinghai-Tibetan Plateau from 1982 to 2011. *Agricultural and Forest Meteorology, 189*, 81-90.

Chen, J. M. and Cihlar, J. (1995). Quantifying the effect of canopy architecture on optical measurements of leaf area index using two gap size analysis methods, *IEEE Transactions on Geoscience and Remote Sensing, 33*(3), 777-787.

Chianucci, F. and Cutini, A. (2012). Digital hemispherical photography for estimating forest canopy properties: current controversies and opportunities. *Journal of Biogeosciences and Forestry, 5,* 290-295.

Clark, D. B., Mercado, L. M., Sitch, S., Jones, C. D., Gedney, N., Best, M. J. and Cox, P. M. (2011). The Joint UK Land Environment Simulator (JULES), model description – Part 2: Carbon fluxes and vegetation dynamics. *Geoscience Model Development, 4*(3), 701-722.

Clawges, R., Vierling, L., Calhoon, M., & Toomey, M. (2007). Use of a ground-based scanning lidar for estimation of biophysical properties of western larch (Larix occidentalis). *International Journal of Remote Sensing, 28*(19), 4331-4344.

Cleland, E. E., Chuine, I., Menzel, A., Mooney, H. A. and Schwartz, M. D. (2007). Shifting plant phenology in response to global change. *Trends in Ecology & Evolution, 22*(7), 357-365.

Climate Change Act, 2008. (c27). London: The Stationery Office.

Cutini, A., Matteucci, G. and Mugnozza, G. S. (1998). Estimation of leaf area index with the Li-Cor LAI 2000 in deciduous forests. *Forest Ecology and Management, 105*(1-3), 55-65.

Danson, F. M., Gaulton, R., Armitage, R. P., Disney, M., Gunawan, O., Lewis, P, Pearson, G. and Ramirez, A. F. (2014). Developing a dual-wavelength full-waveform terrestrial laser scanner to characterize forest canopy structure. *Agricultural and Forest Meteorology, 198-199*, 7-14.

Danson, F. M., Hetherington, D., Morsdorf, F., Koetz, B. and Allgöwer, B. (2007). Forest canopy gap fraction from terrestrial laser scanning. *IEEE Geoscience and Remote Sensing Letters, 4*(1), 157-160.

Demuth, H. and Beale, M. (2002). *Neural Network Toolbox for Use with MATLAB.* The Mathworks, Inc., Natick, MA.

Denny, E. G., Gerst, K. L., Miller-Rushing, A. J., Tierney, G. L., Crimmins, T. M., Enquist, C. A. F Guertin, P., Rosemartin, A.H., Schwartz, M.D., Thomas, K.A. and Weltzin, J. F. (2014). Standardized phenology monitoring methods to track plant and animal activity for science and resource management applications. *International Journal of Biometeorology, 58*, 591-601.

Douglas, E. S., J. Martel, Z. Li, G. Howe, K. Hewawasam, R. A. Marshall, C. L. Schaaf, T. A. Cook, G. J. Newham, A. Strahler, and S. Chakrabarti. (2015). Finding leaves in the forest: The Dual-Wavelength Echidna Lidar. *IEEE Geoscience and Remote Sensing Letters, 12*(4), 776-780.

Drake, J. B., Knox, R. G., Dubayah, R. O., Clark, D. B., Condit, R., Blair, B. J. and Hofton, M. (2003). Above-ground biomass estimation in closed canopy Neotropical forests using lidar remote sensing: factors affecting the generality of relationships. *Global Ecology & Biogeography, 12*, 147-159.

Fieber, K. D., Davenport, I. J., Ferryman, J. M., Gurney, R. J., Walker, J. P. and Hacker, J. M. (2013). Analysis of full-waveform LiDAR data for classification of an orange orchard scene. *ISPRS Journal of Photogrammetry and Remote Sensing, 82,* 63-82.

Finotti, R., Freitas, S. R., Cerqueira, R. and Vieira, M. V. (2003). A method to determine the minimum number of litter traps in litterfall studies. *Biotropica, 35*(3), 419-421.

Fleck, S., Molder, I., Jacob, M., Gebauer, T., Jungkunst, H. F. and Leuschner, C. (2011). Comparison of conventional eight-point crown projections with LiDAR-based virtual crown projections in a temperate old-growth forest. *Annals of Forest Science, 68*(7), 1173-1185.

Forest Research (2013). *Oak budburst model* [Online]. Available at: http://www.forestry.gov.uk/fr/INFD-5ZZM2D [Last accessed December 2013].

Forestry Statistics (2013). *Forestry Statistics 2013 and Forestry Facts & Figures* [Online]. http://www.forestry.gov.uk/forestry/infd-9b8cf9 [Last accessed October 2014]. Edinburgh: Forestry Commission.

Franklin, O., Johansson, J., Dewar, R. C., Dieckmann, U., McMurtrie, R. E., Brannstorm, A. and Dybzinski, R. (2012). Modeling carbon allocation in trees: a search for principles. *Tree Physiology, 32*(6), 648-666.

Gaulton, R., Danson, F. M., Ramirez, F. A. and Gunawan, O. (2013). The potential of dual-wavelength laser scanning for estimating vegetation moisture content. *Remote Sensing of Environment, 132*(0), 32-39.

Gibbs, H. K., Brown, S., Niles, J. O. and Foley, J. A. (2007). Monitoring and estimating tropical forest carbon stocks: making REDD a reality. *Environmental Research Letters, 2*(4), 1-13.

Gill, S. J., Biging, G. S. and Murphy, E. C. (2000). Modeling conifer tree crown radius and estimating canopy cover. *Forest Ecology and Management, 126*(3), 405-416.

Givnish, T. J. (2002). Adaptive significance of evergreen vs. deciduous leaves: solving the triple paradox. *Silva Fennica, 36*(3), 703-743.

Goel, N. S. (1988) Models of vegetation canopy reflectance and their use in estimation of biophysical parameters from reflectance data. *Remote Sensing Reviews 4,* 1-212

Gower, S. T. and Norman, J. M. (1991). Rapid estimation of leaf area index in conifer and broadleaf plantations. *Ecology, 72*(5), 1896-1900.

Griebel, A., Bennett, L. T., Culvenor, D. S., Newnham, G. J. and Arndt, S. K. (2015). Reliability and limitations of a novel terrestrial laser scanner for daily monitoring of forest canopy dynamics. *Remote Sensing of Environment, 166*, 205-213.

Gspaltl, M., Sterba, H. and O'Hara, K. L. (2012). The relationship between available area efficiency and area exploitation index in an even-aged coast redwood (*Sequoia sempervirens*) stand. *Forestry, 85*(5), 567-577.

Guyot, G. (1990). *Optical properties of vegetation canopies: Applications of Remote Sensing in Agriculture*. London: Butterworths.

Hackenberg, J., Wassenberg, M., Spieker, H. and Sun, D. (2015). Non-destructive method for biomass prediction combining TLS derived tree volume and wood density. *Forests, 6(*4), 1274-1300.

Haggerty, B. P. and Mazer, S. J. (2008). *The Phenology Handbook*. UCSB Phenology Stewardship Program. University of California.

Hakala, T., Nevalainen, O., Kaasalainen, S. and Makipaa, R. (2015). Technical note: Multi-spectral lidar time series of pine canopy chlorophyll content. *Biogeosciences, 12*, 1629-1634.

Hakala, T., Suomalainen, J., Kaasalainen, S. and Chen, Y. (2012). Full waveform hyperspectral LiDAR for terrestrial laser scanning. *Optics Express, 20*(7), 7119-7127.

Hancock, S., Armston, J., Li, Z., Gaulton, R., Lewis, P., Disney, M., Danson, F. M., Strahler, A., Schaaf, C., Anderson, K. and Gaston, K. J. (2015). Waveform lidar over vegetation: An evaluation of inversion methods for estimating return energy. *Remote Sensing of Environment, 164,* 208-224.

Hänninen, H. (1990). Modelling bud dormancy release in trees from cool and temperate regions. *Acta Forestalia Fennica, 213*, 1–47.

Hauglin, M., Gobakken, T., Astrup, R., Ene, L. and Naesset, E. (2014). Estimating single-tree crown biomass of Norway spruce by airborne laser scanning: A comparison of methods with and without the use of terrestrial laser scanning to obtain the ground reference data. *Forests, 5*, 364-403.

Henning, J. G. and Radtke, P. J. (2006). Ground-based laser imaging for assessing three-dimensional forest canopy structure. *Photogrammetric Engineering & Remote Sensing, 72*(12), 1349–1358.

Heritage, G. L. and Large, A. R.G. (2009). *Laser Scanning for the Environmental Sciences*. Oxford: Wiley-Blackwell.

Hertel, C., Leuchner, M., Roetzer, T. and Menzel, A. (2012). Assessing stand structure of beech and spruce from measured spectral radiation properties and modeled leaf biomass parameters. *Agricultural and Forest Meteorology, 165*, 82-91.

Höfle, B. (2014). Radiometric correction of terrestrial lidar point cloud data for individual maize plant detection. *IEEE Geoscience and Remote Sensing Letters, 11*(1), 94-98.

Höfle, B. and Pfeifer, N. (2007). Correction of laser scanning intensity data: Data and model-driven approaches. *ISPRS Journal of Photogrammetry and Remote Sensing, 62*(6), 415-433.

Holopainen, M., Vastaranta, M. and Hyyppä, J. (2014) Outlook for the Next Generation's Precision Forestry in Finland. *Forests, 5*(7), 1682-1694.

Hopkinson, C. and Chasmer, I. E. (2007). Using discrete laser pulse return intensity to model canopy transmittance. *The Photogrammetric Journal of Finland, 20*(2), 16-26.

Hosoi, F. and Omasa, K. (2006). Voxel-based 3-D modeling of individual trees for estimating leaf area density using high-resolution portable scanning lidar. *IEEE Transactions on Geoscience and Remote Sensing, 44*(12), 3610-3618.

Hosoi, F. and Omasa, K. (2007). Factors contributing to accuracy in the estimation of the woody canopy leaf area density profile using 3D portable lidar imaging. *Journal of Experimental Botany, 58*(12), 3463-3473.

Hosoi, F. and Omasa, K. (2009). Detecting seasonal change of broad-leaved woody canopy leaf area density profile using 3D portable LIDAR imaging. *Functional Plant Biology, 36*, 998-1005.

Hosoi, F. and Omasa, K. (2012). Estimation of vertical plant area density profiles in a rice canopy at different growth stages by high-resolution portable scanning lidar with a lightweight mirror. *ISPRS Journal of Photogrammetry and Remote Sensing, 74*, 11-19.

Hosoi, F., Nakai, Y. and Omasa, K. (2010). Estimation and Error Analysis of Woody Canopy Leaf Area Density Profiles Using 3-D Airborne and Ground-Based Scanning Lidar Remote-Sensing Techniques. *Geoscience and Remote Sensing, IEEE Transactions on, 48*(5), 2215-2223.

Houghton, R. A. (2005). Aboveground forest biomass and the global carbon balance. *Global Change Biology,* 11, 945–958.

Houghton, R. A., Hall, F. and Goetz, S. J. (2009). Importance of biomass in the global carbon cycle. *Journal of Geophysical Research, 114*, 1-13.

Ide, R. and Oguma, H. (2010). Use of digital cameras for phenological observations. *Ecological Informatics, 5*(5), 339-347.

IPCC (2007). *Contribution of Working Group I to the Fourth Assessment Report of the Intergovernmental Panel on Climate Change*. Solomon, S., Qin, D., Manning, M., Chen, Z., Marquis, M, Averyt, K. B., Tignor, M. and Miller, H. L. (eds.). Cambridge: Cambridge University Press.

IPCC (2013). *Working Group I Contribution to the IPCC Fifth Assessment Report Climate Change 2013: The Physical Science Basis*. Stocker, T., Dahe, Q., Plattner, G. Cambridge: Cambridge University Press.

IPCC (2014). Climate Change 2014: Synthesis Report. *Contribution of Working Groups I, II and III to the Fifth Assessment Report of the Intergovernmental Panel on Climate Change*. Pachauri, R. K. and Meyer, L. A. (eds.). Cambridge: Cambridge University Press.

Jarvis, P. G. and Leverenz, J. W. (1983). Productivity of temperate, deciduous and evergreen forests. In: Lange, O. L., Nobel, P. S., Osmond, C. B., and Ziegler, H. (eds.). *Physiological Plant Ecology*. New York: Springer-Verlag, pp. 233-280.

Jensen, J. R. (2006). *Remote Sensing of the Environment: An Earth Resource Perspective* (2nd ed.). London: Prentice Hall.

Ji, L., Wylie, B. K., Nossov, D. R., Peterson, B., Waldrop, M. P., McFarland, J. W., Rover, J. and Hollingsworth, T. N. (2012). Estimating aboveground biomass in interior Alaska with Landsat data and field measurements. *International Journal of Applied Earth Observation and Geoinformation, 18*, 451-461.

Jonckheere, I., Fleck, S., Nackaerts, K., Muys, B., Coppin, P., Weiss, M. and Baret, F. (2004). Review of methods for in situ leaf area index determination Part I. Theories, sensors and hemispherical photography. *Agricultural and Forest Meteorology, 121*, 19-35.

Jupp, D. L. B., Culvenor, D. S., Lovell, J. L., Newnham, G. J., Strahler, A. H. and Woodcock, C. E. (2009). Estimating forest LAI profiles and structural parameters using a ground-based laser called 'Echidna'. *Tree Physiology*, 29(2), 171-181.

Jutzi, B. and Stilla, U. (2005). Measuring and processing the waveform of laser pulses. *Optical 3-D Measurement Techniques VII, 1*, 194-203.

Kaasalainen, S., Jaakkola, A., Kaasalainen, M., Krooks, A. and Kukko, A. (2011). Analysis of incidence angle and distance effects on terrestrial laser scanner intensity: Search for correction methods. *Remote Sensing, 3*, 2207-2221.

Kaasalainen, S., Krooks, A., Kukko, A. and Kaartinen, H. (2009). Radiometric calibration of terrestrial laser scanners with external reference targets. *Remote Sensing, 1*(3), 144-158.

Kaasalainen, S., Kukko, A., Lindroos, T., Litkey, P., Kaartinen, H., Hyyppae, J. and Ahokas, E. (2008). Brightness measurements and calibration with airborne and

terrestrial laser scanners. *Ieee Transactions on Geoscience and Remote Sensing, 46*(2), 528-534.

Kashani, A. G., Olsen, M. J., Parrish, C. E. and Wilson, N. (2015). A review of lidar radiometric processing: From ad hoc intensity correction to rigorous radiometric calibration. *Sensors, 15*(11), 28099-28128.

Kirchhof, M., Jutzi, B. and Stilla, U. (2008). Iterative processing of laser scanning data by full waveform analysis. *ISPRS Journal of Photogrammetry and Remote Sensing, 63*(1), 99-114.

Koch, E., Bruns, E., Chmielewski, F. M., Defila, C., Lipa, W. and Menze, A. (2007) *Guidelines for plant phenological observations* [Online]. Available at: http://www.omm.urv.cat/documentation.html [Last accessed December 2014].

Koenig, K., Höfle, B., Müller, L., Hämmerle, M., Jarmer, T., Siegmann, B. and Lilienthal, H. (2013). 'Radiometric correction of terrestrial lidar data for mapping of harvest residues density'. Paper presented at the ISPRS Annals of the Photogrammetry, Remote Sensing and Spatial Information Sciences, Volume II-5/W2, 2013 ISPRS Workshop Laser Scanning 2013, 11 – 13 November 2013, Antalya, Turkey.

Kozlowski, T. T., Kramer, P. J. and Pallardy, S. G. (1991). *The Physiological Ecology of Woody Plants*. Diego, CA: Academic Press.

Landsberg, J. J. and Sands, P. J. (2011). *Physiological Ecology of Forest Production: Principles, Processes and Modelling*. Oxford, UK: Elsevier.

Lang, G.A., Early, J.D., Martin, G.C. and Darnell, R.L. (1987) Endo-, para-, and eco-dormancy: physiological terminology and classification for dormancy research. *HortScience, 22*, 371–377.

Leblanc, S. G., Chen, J. M., Fernandes, R., Deering, D. W. and Conley, A. (2005). Methodology comparison for canopy structure parameters extraction from digital hemispherical photography in boreal forests. *Agricultural and Forest Meteorology, 129*(3–4), 187-207.

Lefsky, M. A., Cohen, W. B., Parker, G. G. and Harding, D. J. (2002). Lidar Remote Sensing for Ecosystem Studies. *BioScience, 52*(1), 19-30.

Lewis, P. (1999). Three-dimensional plant modelling for remote sensing simulation studies using the botanical plant modelling system. *Agronomie - Agriculture and Environment, 19*, 185-210.

Li, C. and Strahler, A. H. (1985). Geometric-optical modelling of a conifer forest canopy. *IEEE Transactions on Geoscience and Remote Sensing, 23*, 705-721.

Li, C. and Strahler, A. H. (1992). Geometric-optical bidirectional reflectance modelling of the discrete crown vegetation canopy: Effect of crown shape and mutual shadowing. *IEEE Transactions on Geoscience and Remote Sensing, 30*, 276-292.

Li, Z., Strahler, A., Jupp, D., Schaaf, C., Howe, G., Hewawasam, K., Chakrabarti, S., Cook, T., Paynter, I., and Saenz, E. (2015a). 'Calibration of a full-waveform, dual-wavelength terrestrial laser scanner.' Paper presented at SilviLaser 2015, Le Grande Motte, France, 28-30 September, 2015.

Li, Z., Strahler, A., Schaaf, C., Jupp, D., Howe, G., Hewawasam, K., Chakrabarti, S., Cook, T., Paynter, I., Saenz, E., Yang, X. and Yao, T. (2015b). 'Improving canopy vertical structure measurements with dual-wavelength laser scanning'. Paper presented at AGU, San Francisco, 14-18 December 2015.

Liang, L., Schwartz, M. D. and Fei, S. (2011). 'Examining spring phenology of forest understory using digital photography'. Paper presented at the Proceedings of the 17th Central Hardwood Forest Conference, Carbondale, Illinois, 5-8 March 2011.

Lichti, D.D., Gordon, S.J. and Stewart, M.P. (2002). Ground-based laser scanners: operation, systems and applications. *Geomatica, 56*(1), 21-33.

Lim, K. P., Treitz, P., Wulder, M. A. and St-Onge, B. A. (2003). LiDAR remote sensing of forest structure. *Progress in Physical Geography, 27*(1), 88-106.

Litton, C. M., Raich, J. W. and Ryan, M. G. (2007). Carbon allocation in forest ecosystems. *Global Change Biology, 13*(10), 2089-2109.

Lovell, J. L., Jupp, D. L. B., Culvenor, D. S. and Coops, N. C. (2003). Using airborne and ground-based ranging lidar to measure canopy structure in Australian forests. *Canadian Journal of Remote Sensing, 29*(5), 607-622.

Lowman, M. D. and Rinkerm H. R. (eds) (2004). *Forest Canopies*. Oxford, UK: Elsevier.

Mallet, C. and Bretar, F. (2009). Full-waveform topographic lidar: State-of-the-art. *ISPRS Journal of Photogrammetry and Remote Sensing, 64*(1), 1-16.

Malthus, T. J., Suarez-Minguez, J., Woodhouse, I. H. and Shaw, D. T. (2002). *Review of remote sensing in commercial forestry*. Edinburgh: Forestry Commission.

Marek, M., Masarovicova, E., Kratochvilova, I., Elias, P. and Janous, D. (1989). Stand microclimate and physiological activity of tree leaves in an oak-hornbeam forest. *Trees, 3*(4), 234-240.

Martens, S. N., Ustin, S. L. and Rousseau, R. A. (1993). Estimation of tree canopy leaf area index by gap fraction analysis. *Forest Ecology and Management, 61*(1–2), 91-108.

McGrew, J. C. and Monroe, C.B. (2003). *An Introduction to Statistical Problem Solving in Geography* (2nd ed). New York: McGraw Hill.

MEA, (2005). *Ecosystems and Human Well-being: Synthesis*. Washington, DC: Island Press.

Menzel, A., Sparks, T. H., Estrella, N., Koch, E., Aasa, A., Ahas, R. and Zust, A. (2006). European phenological response to climate change matches the warming pattern. *Global Change Biology, 12*(10), 1969-1976.

Migliavacca, M., Sonnentag, O., Keenan, T. F., Cescatti, A., O'Keefe, J. and Richardson, A. D. (2012). On the uncertainty of phenological responses to climate change, and implications for a terrestrial biosphere model. *Biogeosciences, 9*(6), 2063-2083.

Miller-Rushing, R. B. and Primack, A. J. (2008). Global warming and flowering times in Thoreau's Concord: A community perspective. *Ecology, 89*, 332-341.

Miranda-Fuentes, A., Llorens, J., Gamarra-Diezma, J. L., Gil-Ribes, J. A. and Gil, E. (2015). Towards an optimised method of olive tree crown volume measurement. *Sensors, 15*(2), 3671-3687.

Mizunuma, T., Wilkinson, M., L. Eaton, E., Mencuccini, M., I. L. Morison, J., Grace, J. and Ostle, N. (2013). The relationship between carbon dioxide uptake and canopy colour from two camera systems in a deciduous forest in southern England. *Functional Ecology, 27*(1), 196-207.

Monsi, M. and Saeki, T. (1953). Uber den Lichtfaktor in den Pflanzengesellschaften und seine Bedeutung für die Stoffproduktion. *Japanese Journal of Botany* 14, 22–55. English translation, On the factor of light in plant communities and its importance for matter production, published in *Annals of Botany* (2005) 95, 549-567.

Moorthy, I., Miller, J. R., Jimenez Berni, J. A., Zarco-Tejada, P., Hu, B. and Chen, J. (2011). Field characterization of olive (*Olea europaea L.*) tree crown architecture using terrestrial laser scanning data. *Agricultural and Forest Meteorology, 151*(2), 204-214.

Morin, X., Lechowicz, M.J., Auspurger, C., Ókeefe, J., Viner, D. and Chuine, I. (2009). Leaf phenology in 22 North American tree species during the 21st century. *Global Change Biology* 15:961–975.

Morison, J. (2012) *Understanding the Carbon and GHG balance of UK Forests* [Online]. Available at: www.forestry.gov.uk/pdf/FCRP018.pdf/$FILE/FCRP018.pdf [Last accessed October 2014]. Edinburgh: Forestry Commission.

Morris, D., Boyd, D., Crowe, J., Johnson, C. and Smith, K. (2013). Exploring the potential for automatic extraction of vegetation phenological metrics from traffic webcams. *Remote Sensing, 5*(5), 2200.

Morsdorf, F., Kötz, B., Meier, E., Itten, K. I. and Allgöwer, B. (2006). Estimation of LAI and fractional cover from small footprint airborne laser scanning data based on gap fraction. *Remote Sensing of Environment, 104*, 50-61.

Nahar, K. (2012). Artificial neural network. *Compusoft, International Journal of Advanced Computer Technology*, 1(2), 25-27.

Naito, H., Rahimzadeh-Bajgiran, P., Shimizu, Y., Hosoi, F. and Omasa, K. (2012). Summer-season Differences in NDVI and iTVDI among Vegetation Cover Types in Lake Mashu, Hokkaido, Japan Using Landsat TM Data. *Environment Control in Biology, 50*(2, Sp. Iss. SI), 163-171.

NASA (2015) [Online]. Available at: http://science.nasa.gov/missions/gedi/ [Last accessed October 2015].

Neal, R. M. (1996). *Bayesian Learning for Neural Networks*. UK: Springer.

Newnham, R. M., Sparks, T. H., Skjoth, C. A., Head, K., Adams-Groom, B. and Smith, M. (2013). Pollen season and climate: Is the timing of birch pollen release in the UK approaching its limit? *International Journal of Biometeorology, 57*(3), 391-400.

Okubo, H. (2000). Growth Cycle and Dormancy in Plants. In Viemont, J. D. and Crabbe, J. (eds.), *Dormancy in Plants from Whole Plant Behavior to Cellular Control* (pp. 1-22). Wallingford, UK: CABI. pp. 1-22.

Packham, J. R., Harding, D. J. L., Hilton, G. M. and Stuttard, R. A. (1992). *Functional Ecology of Woodlands and Forests*. London: Chapman & Hall.

Pareja, T. F., Pablos, A. G. and Oliva, J. (2013). 'Terrestrial Laser Scanner (TLS) Equipment Calibration'. Paper presented at the Proceedings of the 5th Manufacturing Engineering Society International Conference, Zaragoza, June 2013.

Peñuelas, J. and Filella, I. (2001). Responses to a warming world. *Science, 294*, 793-794.

Pesci, A. and Teza, G. (2008). Effects of surface irregularities on intensity data from laser scanning: an experimental approach. *Annals of Geophysics, 51*(5-6), 839-848.

Pfeifer, N. and Briese, C. (2007). 'Laser Scanning - Principles and Applications'. Paper presented at III International Scientific Conference, Geo-Sibir, Nowosibirsk, 25-27 April 2007.

Pfeifer, N., Höfle, B., Briese, C., Rutzinger, M., and Haring, A. (2008). Analysis of the backscattered energy in terrestrial laser scanning data. *The International Archives of Photogrammetry, Remote Sensing and Spatial Information Science, 37*, 1045-1052.

Piayda, A., Dubbert, M., Werner, C., Correia, A., Pereira, J. S. and Cuntz, M. (2015). Influence of woody tissue and leaf clumping on vertically resolved leaf area index and angular gap probability estimates. *Forest Ecology and Management, 340*, 103-113.

Pitman, A. J., de Noblet-Ducoudré, N., Cruz, F. T., Davin, E. L., Bonan, G.B., Brovkin, V., Claussen, M., Delire, C., Ganzeveld, L., Gayler, V., van den Hurk, B. J. J. M., Lawrence, P. J., van der Molen, M. K., Müller, C., Reick, C. H., Seneviratne, S. I., Strengers, B. J. and Voldoire, A. (2009). Uncertainties in climate responses to past land cover change: First results from the LUCID intercomparison study. *Geophysical Research Letters 36,* L14814.

Polgar, C. A. and Primack, R. B. (2011). Leaf-out phenology of temperate woody plants: from trees to ecosystems. *New Phytologist, 191*(4), 926-941.

Portillo-Quintero, C., Sanchez-Azofeifa, A. and Culvenor, D. (2014). Using VEGNET in-situ monitoring LiDAR (IML) to capture dynamics of plant area index, Structure and phenology in Aspen Parkland Forests in Alberta, Canada. *Forests, 5*(5), 1053-1068.

Pretzsch, H. (1997). Analysis and modeling of spatial stand structures. Methodological considerations based on mixed beech-larch stands in Lower Saxony. *Forest Ecology and Management, 97*(3), 237-253.

Pretzsch, H. (2014). Canopy space filling and tree crown morphology in mixed-species stands compared with monocultures. *Forest Ecology and Management, 327*, 251-264.

Ramirez, F. A., Armitage, R. P. and Danson, F. M. (2013). Testing the application of terrestrial laser scanning to measure forest canopy gap fraction. *Remote Sensing, 5*(6), 3037-3056.

Ramirez, F.A. (2011). *Terrestrial laser scanning measurements to characterise temporal changes in forest canopies*. Ph.D. Thesis. University of Salford, UK.

Raumonen, P., Kaasalainen, M., Akerblom, M., Kaasalainen, S., Kaartinen, H., Vastaranta, M., Holopainen, M., Disney, M. and Lewis, P. (2013). Fast automatic precision tree models from terrestrial laser scanner data. *Remote Sensing, 5*(2), 491-520.

Ray, D., Morison, J. I. L., and Broadmeadow, M. (2010). *Climate Change: Impacts and Adaption in England's Woodlands*. Edinburgh: Forestry Commission.

Read, D.J., Freer-Smith, P.H., Morison, J.I.L., Hanley, N., West, C.C. and Snowdon, P. (eds) (2009) Combating climate change – a role for UK forests. An assessment of the potential of the UK's trees and woodlands to mitigate and adapt to climate change. The Stationery Office, Edinburgh.222 pp.

Read, H. J. and Frater, M. (1999). *Woodland Habitats*. London: Routledge.

Rees, W. G. (1990). *Principles of Remote Sensing*. Cambridge: Cambridge University Press.

Richardson, A. D., Anderson, R., Arain, M. A., Barr, A., Bohrer, G., Chen, G., Chen, J., Ciais, P., Davis, K., Desai, A., Dietze, M., Dragoni, D., Garrity, S. R., Gough, C. M., Grant, R., Hollinger, D. Y., Margolis, H. A., McCaughey, H., Migliavacca, M., Monson, R. K., Munger, J. W., Poulter, B., Raczka, B. M., Ricciuto, D. M., Sahoo, A. K., Schaefer, K., Tian, H., Vargas, R., Verbeeck, H., Xiao, J. and Xue, Y. (2012). Terrestrial biosphere models need better representation of vegetation phenology: results from the North American Carbon Program Site Synthesis. *Global Change Biology, 18*, 566-584.

Richardson, A. D., Braswell, B. H., Hollinger, D. Y., Jenkins, J. P. and Ollinger, S. V. (2009). Near-surface remote sensing of spatial and temporal variation in canopy phenology. *Ecological Applications, 19*(6), 1417-1428.

Richardson, A. D., Keenana, T. F., Migliavaccab, M., Ryua, C., Sonnentag, O. and Toomeya, M. (2013). Climate change, phenology, and phenological control of

vegetation feedbacks to the climate system. *Agricultural and Forest Meteorology, 169*, 156–173.

Richardson, D. M., Rundel, P. W. and Jackson, S. T. (2007). Human impacts in pine forests: past present and future. *Annual Review of Ecology, Evolution and Systematics, 38*, 275-297.

Ross, J. (1981). *The Radiation Regime and Architecture of Plant Stands*. Dr W. Junk Publishers. The Hague, 391.

Ryu, Y., Lee, G., Jeon, S., Song, Y. and Kimm, H. (2014). Monitoring multi-layer canopy spring phenology of temperate deciduous and evergreen forests using low-cost spectral sensors. *Remote Sensing of Environment, 149*, 227-238.

Schofield, L. A., Danson, F. M., Entwistle, N. S., Gaulton, R. and Hancock, S. (2016). Radiometric calibration of a dual-wavelength terrestrial laser scanner using neural networks. *Remote Sensing Letters, 7*(4), 299-308.

Schwalm, C. R., Williams, C. A., Schaefer, K., Anderson, R., Arain, M. A., Baker, I., Barr, A., Black, T. A., Chen, G., Chen, J. M., Ciais, P., Davis, K. J., Desai, A., Dietze, M., Dragoni, D., Fischer, M. L., Flanagan, L. B., Grant, R., Gu, L., Hollinger, D., Izaurralde, R. C., Kucharik, C., Lafleur, P., Law, B. E., Li, L., Li, Z., Liu, S., Lokupitiya, E., Luo, Y., Ma, S., Margolis, H., Matamala, R., McCaughey, H., Monson, R. K., Oechel, W. C., Peng, C., Poulter, B., Price, D. T., Riciutto, D. M., Riley, W., Sahoo, A. K., Sprintsin, M., Sun, J., Tian, H., Tonitto, C., Verbeeck, H., and Verma, S. B. (2010) A model data intercomparison of CO_2 exchange across North America: Results from the North American Carbon Program site synthesis. *Journal of Geophysical Research, 115*, G00H05.

Schwartz, M. D., Reed, B. C. and White, M. A. (2002). Assessing satellite-derived start-of-season (sos) measures in the conterminous USA. *International Journal of Climatology, 22*(14), 1793-1805.

Seeley, S.D. (1996). Modelling climatic regulation of bud dormancy. In: Lang, G. A. (ed.). *Plant dormancy: Physiology, biochemistry and molecular biology*. Wallingford, U.K: CAB International. pp. 361-376.

Seidel, D., Fleck, S. and Leuschner, C. (2012). Analyzing forest canopies with ground-based laser scanning: A comparison with hemispherical photography. *Agricultural and Forest Meteorology, 154-155*, 1-8.

Seielstad, C., Stonesifer, C., Rowell, E. and Queen, L. (2011). Deriving fuel mass by size class in douglas-fir (Pseudotsuga menziesii) using terrestrial laser scanning. *Remote Sensing, 3*(8), 1691-1709.

Slevin, D., Tett, S. F. B. and Williams, M. (2015). Multi-site evaluation of the JULES land surface model using global and local data. *Geoscience Model Development, 8*, 295–316.

Solberg, A., Svein, S., Weydahl, D. J. and Astrup, R. A. (2009). *Leaf area index estimation using ENVISAT ASAR and Radarsat-2*. Note No. SAMBA/30/09, Norwegian Computing Center, NR.

Sonnentag, O., Hufkens, K., Teshera-Sterne, C., Young, A. M., Friedl, M. A., Braswell, B. H. and Richardson, A. D. (2012). Digital repeat photography for phenological research in forest ecosystems. *Agricultural and Forest Meteorology, 152*, 159-177.

Sparks, T. H. and Menzel, A. (2002). Observed changes in seasons: An overview. *International Journal of Climatology, 22*(14), 1715-1725.

Sparks, T.H. and Gill, R. (2002). Climate change and the seasonality of woodland flora and fauna. In: Climate Change: Impacts on UK Forests. MSJ Broadmeadow (ed.). Forestry Commission Bulletin 125. Edinburgh: Forestry Commission. Pp. 69-82.

Srinivasan, S., Popescu, S., Eriksson, M., Sheridan, R. D. and Ku, N. W. (2015). Terrestrial laser scanning as an effective tool to retrieve tree level height, crown width, and stem diameter. *Remote Sensing, 7*(2), 1877-1896.

Strahler, A. H., Jupp, D. L. B., Woodcock, C. E., Schaaf, C. B., Yao, T., Zhao, F. and Boykin-Morris, W. (2008). Retrieval of forest structural parameters using a ground-based lidar instrument (Echidna (R)). *Canadian Journal of Remote Sensing, 34*, S426-S440.

Street, H.E. and Opik, H. (1984). *The Physiology of Flowering Plants* (3rd ed.). London: Edward Arnold Ltd.

Takeda, T., Oguma, H,m Sano, T., Yone, Y. and Fujinuma, Y. (2008). Estimating the plant area density of a Japanese larch plantation using a ground-based laser scanner. *Agricultural and Forest Meteorology, 143*(3), 428-438.

Tao, S., Guo, Q., Xu, S., Su, Y., Li, Y. and Wu, F. (2015). A geometric method for wood-leaf separation using terrestrial and simulated lidar data. *Photogrammetric Engineering and Remote Sensing, 91*(10), 767-776.

Tarrasenko, L. (1998). *A guide to neural computing applications*. London: Arnold.

Thomas, P. (2011). *Trees: Their Natural History*. Cambridge: Cambridge University Press.

UKCP09 (2009). UK Climate Projections 2009 [Online]. Available at: http://ukclimateprojections.defra.gov.uk/ [Last accessed March 2015].

Uzoh, F. C. C. and Ritchie, M. W. (1996). *Crown area equations for 13 species of trees and shrubs in Northern California and Southwestern Oregon*. United States Department of Agriculture. Research paper PSW-RP-227. Albany, CA.

Vaccari, S., van Leeuwen, M., Calders, K., Coops, N. C. and Herold, M. (2013). Bias in lidar-based canopy gap fraction estimates. *Remote Sensing Letters, 4*(4), 391-399.

Vain, A., Yu, X., Kaasalainen, S. and Hyyppa, J. (2010). Correcting airborne laser scanning intensity data for automatic gain control effect. *IEEE Geoscience and Remote Sensing Letters*, 7(3), 511-514.

Wagner, W., Hyyppä, J., Ullrich, A., Lehner, H., Briese, C. and Kaasalainen, S. (2008). 'Radiometric calibration of full-waveform small-footprint airborne laser scanners'. Paper presented at the he International Archives of the Photogrammetry, Remote Sensing and Spatial Information Sciences. Vol. XXXVII. Beijing 2008.

Wagner, W., Roncat, A., Melzer, T. and Ullrich, A. (2007). Waveform analysis techniques in airborne laser scanning. *International Archives of Photogrammetry and Remote Sensing, XXXVI*, 413-418.

Wagner, W., Ullrich, A., Ducic, V., Melzer, T. and Studnicka, A. (2006). Gaussian decomposition and calibration of a novel small-footprint full-waveform digitising airborne laser scanner. *Journal of Photogrammetry and Remote Sensing*, 60, 100-112.

Walter, J. N., Fournier, R. A., Soudani, K. and Meyer, E. (2003). Integrating clumping effects in forest canopy structure: an assessment through hemispherical photographs. *Canadian Journal of Remote Sensing, 29*(3), 388-410.

Wang, Q. and Li, P. (2013). Canopy vertical heterogeneity plays a critical role in reflectance simulation. *Agricultural and Forest Meteorology, 169*, 111-121.

Wang, Y. S., Miller, D. R., Welles, J. M. and Heisler, G. M. (1992). Spatial variability of canopy foliage in an oak forest estimated with fisheye sensors. *Forest Science, 38*(4), 854-865.

Wang, Y., Weinacker, H. and Koch, B. (2008). A lidar point cloud based procedure for vertical canopy structure analysis and 3D single tree modelling in forests. *Sensors, 8*(6), 3938-3951.

Wareing, P.F. and Phillips, I.D.J. (1981). *Growth and differentiation in plants* (3rd ed.). Exeter: Pergamon Press.

Warren-Wilson, J. (1959). Analysis of the spatial distribution of foliage by two-dimensional point quadrats. *New Phytologist, 58*(1), 92-99.

Warren-Wilson, J. (1960). Inclined point quadrats. *New Phytologist, 59*(1), 1-8.

Warren-Wilson, J. (1963). Estimation of foliage denseness and foliage angle by inclined point quadrats. *Australian Journal of Botany, 11*, 95-105.

Watson, D. J. (1947). Comparative physiological studies in the growth of field crops. I: Variation in net assimilation rate and leaf area between species and varieties, and within and between years. *Annals of Botany, 11*, 41-76.

Watt, P. J. and Donoghue, D. N. M. (2005). Measuring forest structure with terrestrial laser scanning. *International Journal of Remote Sensing, 26*(7), 1437-1446.

Webb, W.L., Lauenroth, W.K., Szarek, S.R. and Kinerson, R.S., 1983. Primary production and abiotic controls in forests, grasslands, and desert ecosystems in the United States. *Ecology, 64*: 134-151.

Wehr, A. and Lohr, U. (1999). Airborne laser scanning - an introduction and overview. International Society for Photogrammetry and Remote Sensing. *Journal of Photogrammetry and Remote Sensing, 54*(2-3), 68-82.

Wei-heng, X. U., Zhong-ke, F., Zhi-feng, S. U., Hui, X. U., You-quan, J. I. and Ou, D. E. N. (2014). An automatic extraction algorithm for individual tree crown projection area and volume based on 3D point cloud data. *Spectroscopy and Spectral Analysis, 34*(2), 465-471.

Weiss, M., Baret, F., Smith, G. J., Jonckheered, I. and Coppind, P. (2004). Review of methods for in situ leaf area index (LAI) determination Part II. Estimation of LAI, errors and sampling. *Agricultural and Forest Meteorology, 121*, 37–53.

Welford, D. and Mooradian, A. (1982). Output power and temperature dependence of the linewidth of single-frequency CW (GaAI) as diode lasers. *Applied Physics Letters, 40*(10): 865-867.

Welles, J. M. and Cohen, S. (1996) Canopy structure measurement by gap fraction analysis using commercial instrumentation. *Journal of Experimental Botany*, 47, 1335-1342.

White, M. A. and Nemani, R. R. (2003). Canopy duration has little influence on nnual carbon storage in the deciduous broad leaf forest. *Global Change Biology, 9*, 967-972.

Wilson, J. B. (2011). Cover plus: ways of measuring plant canopies and the terems used for them. *Journal of Vegetation Science, 22*(2), 197-206.

Wolpert, D. H. (1996). The lack of a priori distinctions between learning algorithms. *Neural Computation, 8*(7), 1341-1390.

Woodman, J. N. (1971). Variation of net photosynthesis within the crown of a lrage forest-grown conifer. *Photosynthetica, 5*, 50-54.

Wulder, M. A. (1998). Optical remote sensing techiques for the assessment of forest inventory and biophysical parameters. *Progress in Physical Geography, 22*(4), 449-476.

Yanez, L., Homolova, L., Malenovky, Z. and Schaepman, M. E. (2008). International Archives of Photogrammetry, Remote Sensing and Spatial Information Sciences ISPRS, Beijing, China, 3-11 July 2008 p45-50.

Yang, X.Y., A.H. Strahler, C.B. Schaaf, D.L.B. Jupp, T. Yao, F. Zhao, Z.S. Wang, D.S. Culvenor, G.J. Newnham, J.L. Lovell, R. Dubayah, C.E. Woodcock, and W. Ni-Meister. (2013). Three- dimensional forest reconstruction and structural parameter retrievals using a terrestrial full-waveform Lidar instrument (Echidna (R)), *Remote Sensing of Environment, 135*, 36–51.

Zhang, X., Friedl, M. A., Schaaf, C. B., Strahler, A. H., Hodges, J. C. F., Gao, F., Reed, B. and Huete, A. (2003). Monitoring vegetation phenology using MODIS. *Remote Sensing of Environment, 84*, 471–475.

Zhang, Y., Chen, J. M., and Miller, J. R. (2005). Determining digital hemispherical photograph exposure for leaf area index estimation. *Agricultural and Forest Meteorology, 133*(1–4), 166-181.

Zhao, F., Strahler, A. H., Schaaf, C. L., Yao, T., Yang, X., Wang, Z., Schull, M. A., Roman, M. O., Woodcock, C. E. and Olofsson, P. (2012). Measuring gap fraction, element clumping index and LAI in Sierra Forest stands using a full-waveform ground-based lidar. *Remote Sensing of Environment, 125*, 73-79.

Zhao, F., Yang, X., Schull, M. A., Roman-Colon, M. O., Yao, T., Wang, Z., Zhange, Q., Jupp, D. I., Lovell, J. L. and Culvenor, D. S. (2011). Measuring effective leaf area index, foliage profile, and stand height in New England forest stands using a full-waveform ground-based lidar. *Remote Sensing of Environment, 115*(11), 2954-2964.

Zhao, F., Yang, X., Schull, M.A., Román-Colón, M.O., Yao, T., Wang, Z., Zhang, Q., Jupp, D.L., Lovell, J.L. and Culvenor, D.S. (2011). Measuring effective leaf area index, foliage profile: and stand height in New England forest stands using a full-waveform ground-based lidar. *Remote Sensing of Environment, 115*, 2954–2964

Zheng, G. and Moskal, L. M. (2012). Computational-geometry-based retrieval of effective leaf area index using terrestrial laser scanning. *IEEE Transactions Geoscience and Remote Sensing, 50*(10), 3958-3969.

APPENDIX

SALCA code

Overview

This appendix contains Matlab code developed to process data from the SALCA instrument. The following functions are included:

- *salca_cuba*: To read raw SALCA binary files and extract waveform information to text files.
- *geom_cuba*: Calculates Cartesian coordinates (x,y,z) and zenith and azimuth angles.
- *Ringing*: Cleans point cloud by removing returns generated by ringing.
- *match_returns*: Searches (by range) for corresponding returns from both wavelengths and calculates the NDI ratios.
- *sim_nn*: To calculate intensity to apparent reflectance by using an artificial neural network.

salca_cuba.m

```matlab
function [pulse15 pulse10] = salca_cuba(path, basename, start, stop);


% input data:
    % path: Path to folder storing scanning mode data (ending in \).
    Enter as a String contained in single quotes '
    % basename: Name of folder containing the data. Enter as a String
    contained in single quotes '
    % start: Number of first azimuth file to read (commonly 0)
    % stop: Number of last azimuth file to read (3050, for full scan)

pulse15 = zeros(12000000, 6);        % preallocation output matrix
listPtr15 = 1;                       % pointer to last free position

pulse10 = zeros(12000000, 6);        % preallocation output matrix
listPtr10 = 1;                       % pointer to last free position

azimuths = (stop - start) + 1;       % number of azimuth positions

output_rows = azimuths * 3200;       % number of rows

threshold = 17;    % define noise threshold for identifying valid returns
backsig = 11.3;    % average of background signal (-115.7 + 127)

range1545 = [0.15:0.15:60]'; % range intervals (60m range)
range1063 = [0:0.15:64.95]'; % range intervals (60m range)

% range1545 = [0.15:0.15:106.05]';  % use for 105m range
% range1063 = [0:0.15:109.95]';     % use for 105m range

%% import binary files one azimuth at a time

for azindex = start : stop
    ident = num2str(azindex);

    str = sprintf('%s',path,basename,'_',ident,'.bin');

fid = fopen(str, 'r');
data = fread(fid, [1400,3200],'*int8');   % use for 60m range
% data = fread(fid, [1700,3200],'*int8'); % use for 105m max range
fclose(fid);
data = double(data);

% split wavelengths by row number
data1545split = data(1:400,:);       % row400 = 60m
data1063split = data(967:end,:);     % row967 = 145.05m

% data1545split = data(1:707,:); % use for 105m range
% data1063split = data(967:end,:); % use for 105m range

%% 1545nm data

 for j = 1:3200;
    zenindex = j;
```

```matlab
        data1545 = [range1545 data1545split(:,j)+127-threshold];

% For no returns: If no data above threshold in ranges 1.5m-60m then skip
column
if data1545(10:400,2) <= 0;
  zenindex = zenindex + 1;
  continue;
end

% For no outgoing pulse in first 2 range bins: If no data above threshold
at first or second range (0.15m or 0.3m) for first pulse then make
0.15m=1
if data1545(1:2,2) <= 0;
 data1545(1,2) = 1;
end;

idx = find(data1545(:,2) < 1); % remove data below threshold
data1545(idx,:) = [];

%% Search for returns

m = data1545; % [range intensity]
m = [m(:,1), m(:,2), (m(:,1).*m(:,2))]; % a third column is added: range
* intensity
return_no = -1; % return_no is initalised to -1, so the first return will
be coded as zero.

z = zeros([1,7]); % create a pre-allocated matrix
                  % Column_1= return number
                  % Column_2= intensity sum
                  % Column_3= width
                  % Column_4= weightR/intensity sum (REMOVED AT END OF
                  % CODE)
                  % Column_5= estimated range
                  % Column_6= Zenith index (1-3200)
                  % Column_7= Azimuth index (0-3050)

width = 1;  % initial values
sum_int = m(1, 2);
weightR = m(1, 3);
separation = 0.15;

for i = 1:size(m,1)

    if i < size(m,1);

        p = m(i+1,1) - m(i,1); %test value
        if abs(m(i+1,1) - m(i,1) - separation) < eps(m(i+1,1)) % the
range is <= 0.15

            width = width + 1;
            sum_int = sum_int + m(i+1, 2);
            weightR = weightR + m(i+1, 3);

        else % the range is > 0.15

            return_no = return_no + 1;
```

```matlab
            if return_no > 0

                z = [z; return_no (sum_int+((threshold-backsig)*width))
width weightR/sum_int ((weightR/sum_int) - z(2,4)) azindex zenindex];
                width = 1;
                sum_int = m(i+1, 2);
                weightR = m(i+1, 3);

            else % this is to make sure that estR = 0 when return_no = 0

                estR = 0;
                z = [z; return_no (sum_int+((threshold-backsig)*width))
width weightR/sum_int estR azindex zenindex];
                width = 1;
                sum_int = m(i+1, 2);
                weightR = m(i+1, 3);

            end

        end

    else % the last row of the input matrix is reached

        if return_no < 0

            estR = 0;
            return_no = return_no + 1;
            z = [z; return_no (sum_int+((threshold-backsig)*width)) width
weightR/sum_int estR azindex zenindex];

        else

            return_no = return_no + 1;
            z = [z; return_no (sum_int+((threshold-backsig)*width)) width
weightR/sum_int ((weightR/sum_int) - z(2,4)) azindex zenindex];

        end

    end

end

z = z(2:size(z,1),:); % remove the first row of the output matrix '[0 0 0
0 0 0]'
idx=find(z(:,1)==0); % remove records for outgoing pulse
z(idx,:)=[];
z(:,4)=[]; % remove column 4 (weightR/intensity sum)

pulse15(listPtr15:listPtr15 + (size(z,1)-1),:) = z;   % store new item
listPtr15 = listPtr15 + (size(z,1));        % increment position pointer

 end

 %% 1063nm wavelength

 for j = 1:3200;
```

219

```matlab
    zenindex = j;
    data1063 = [range1063 data1063split(:,j)+127-threshold];

if data1063(26:434,2) <= 0;
  zenindex = zenindex + 1;
  continue;
end

idx = find(data1063(:,2) <1 );
data1063(idx,:) = [];

%% search for returns

m = data1063; % [range intensity]
m = [m(:,1), m(:,2), (m(:,1).*m(:,2))]; % a third column is added: range
* intensity
return_no = -1; % return_no is initalised to -1, so the first return will
be coded as zero.

z = zeros([1,7]);   % create a pre-allocated matrix
                    % Column_4= weightR/intensity sum (REMOVED AT END OF
CODE)

width = 1;
sum_int = m(1, 2);
weightR = m(1, 3);
separation = 0.15;

for i=1:size(m,1)

    if i < size(m,1);

        p = m(i+1,1) - m(i,1); %test value
        if abs(m(i+1,1) - m(i,1) - separation) < eps(m(i+1,1)) % the
range is <= 0.15

            width = width + 1;
            sum_int = sum_int + m(i+1, 2);
            weightR = weightR + m(i+1, 3);

        else % the range is > 0.15

            return_no = return_no + 1;

            if return_no > 0

                z = [z; return_no (sum_int+((threshold-backsig)*width))
width weightR/sum_int ((weightR/sum_int) - z(2,4)) azindex zenindex];
                width = 1;
                sum_int = m(i+1, 2);
                weightR = m(i+1, 3);

            else % this is to make sure that estR = 0 when return_no = 0

                estR = 0;
                z = [z; return_no (sum_int+((threshold-backsig)*width))
width weightR/sum_int estR azindex zenindex];
```

```matlab
                        width = 1;
                        sum_int = m(i+1, 2);
                        weightR = m(i+1, 3);

                    end

                end

        else % the last row of the input matrix is reached

            if return_no < 0

                estR = 0;
                return_no = return_no + 1;
                z = [z; return_no (sum_int+((threshold-backsig)*width)) width
weightR/sum_int estR azindex zenindex];

            else

                return_no = return_no + 1;
                z = [z; return_no (sum_int+((threshold-backsig)*width)) width
weightR/sum_int ((weightR/sum_int) - z(2,4)) azindex zenindex];

            end

        end

end

z = z(2:size(z,1),:); % remove the first row of the output matrix '[0 0 0
0 0 0]'
idx=find(z(:,1)==0); % remove the records for outgoing pulse
z(idx,:)=[];
z(:,4)=[]; % remove column 4 (weightR/intensity sum)

pulse10(listPtr10:listPtr10 + (size(z,1)-1),:) = z;   % store new item
listPtr10 = listPtr10 + (size(z,1));        % increment position pointer

end
end

pulse15(listPtr15:end,:) = [];
pulse10(listPtr10:end,:) = [];

% save('data1063_out.txt', 'pulse10', '-ascii', '-double','-v7')
% save('data1545_out.txt', 'pulse15', '-ascii', '-double','-v7')

% output data:
    % column 1: return number
    % column 2: intensity (sum)
    % column 3: width
    % column 4: range (m)
    % column 5: azimuth index (0-'stop')
    % column 6: zenith index (1-3200)
```

Geom_cuba.m

```matlab
function [xyzdata] = geom_cuba(ScanData, p, res, SquintData);


% Inputs:
    % ScanData = input data file (e.g. data1063_3174)
    % p = last azimuth file to read (4mrad = 749, 1mrad = 3050)
    % res = azimuth resolution in degrees (0.06, 0.12, 0.24)
    % SquintData = geometry data (import 'salcaSquint.mat')

% Designed to run with output from Cuba - i.e.:
    % cols 5 and 6 = azimuth and zenith indices
    % col 4 = range

% Must load 'salcaSquint.mat' which imports as 'data' containing:
    % col 1 = zenith index
    % col 3 = true azimuth
    % col 4 = true zenith

% Make an Azimuth geometry file (AzGeom) to find the true azimuth angle
from the Azmiuth and Zenith Index:

AzIndex = (0:p);
AzindexMatrix = repmat(AzIndex,3200,1);
Azsquint = SquintData(:,3)';
Azsquintdat = repmat(Azsquint,p+1,1);
AzGeom = ((AzindexMatrix*res)+(Azsquintdat'));

% Make a Zenith geometry file (ZenGeom) to find the true zenith angle
from the Azmiuth and Zenith Index:

Zendata = SquintData(:,4); % data from salcasquint
ZenGeom = repmat(Zendata', p+1,1);
ZenGeom = ZenGeom';

indices = [ScanData(:,5)+1,ScanData(:,6)]; % extract indices from input
data

% Find the true Azimuth and Zenith angle for each row of 'indices':

AzAngDeg = AzGeom(sub2ind(size(AzGeom),indices(:,2),indices(:,1))); %
angles in degrees - used to generate foliage profiles
ZenAngDeg = ZenGeom(sub2ind(size(ZenGeom),indices(:,2),indices(:,1)));

AzAng =(AzAngDeg*pi)/180;      % convert to radians
AzAng = (2*pi)-AzAng;          % flip data in azimuth

ZenAng = (ZenAngDeg*pi)/180;   % convert to radians
ZenAng = (pi/2)-ZenAng;        % convert from zenith angle to elevation

newdata=[ScanData AzAng ZenAng AzAngDeg ZenAngDeg];

% Convert to Cartesian coordinates:

[x,y,z] = sph2cart(newdata(:,7),newdata(:,8),newdata(:,4));
xyzdata=[x y z newdata];
```

Ringing.m

```matlab
function [data_noRing] = ringing(xyzdata);


% find high intensity first returns
idx = find((xyzdata(:,5) >= 290) & (xyzdata(:,4)==1));

% separate them out
High1stDN = xyzdata(idx,:);

% remove them from scan data
xyzdata(idx,:) = [];
[tf] = ismember(xyzdata(:,[8:9]),High1stDN(:,[8:9]),'rows');

% remove the remaining returns for those pulses
xyzdata(tf,:) = [];

% concatenate matrices
data_noRing = [xyzdata; High1stDN];

% sort by azimuth and zenith angle
data_noRing = sortrows(data_noRing,[8 9]);
```

match_returns.m

```matlab
function [ratiosout] = match_returns(data1063, data1545);

% inputs:
    % data1063: processed scan data for 1063nm wavelength (geom_cuba
    output)
    % data1545: processed scan data for 1545nm wavelength (geom_cuba
    output)

ratiosout = zeros(1,12);      % preallocate

% chunk data into blocks to speed processing
for s = 0:2:700;
a1063 = data1063;
a1545 = data1545;

idx = find((a1063(:,8)>=s) & (a1063(:,8)<s+2));
a1063 = a1063(idx,:);

idx = find((a1545(:,8)>=s) & (a1545(:,8)<s+2));
a1545 = a1545(idx,:);

% Use zenith and azimuth indices to find where there are hits in both
wavelengths
[tf] = ismember(a1063(:,[8:9]),a1545(:,[8:9]),'rows');
c1063 = a1063(tf,:);
[tf] = ismember(a1545(:,[8:9]),a1063(:,[8:9]),'rows');
c1545 = a1545(tf,:);

% Check same amount of first returns
%idx1=find(c1063(:,1)==1);
%idx2=find(c1545(:,1)==1);

list = unique(c1063(:,[8:9]),'rows'); % generate a list of first return
azimuth and zenith indices

ratios = zeros(1,13); % create an output file which the 'for loop' rows
will be appended to

for i = 1:length(list);

    a = list(i,:); % for each row (az & zen idx) in list
    idx1 = find(c1545(:,8) == a(:,1) & c1545(:,9) == a(:,2)); % extract
all returns for that index in 1545nm data
    c1545_a = c1545(idx1,:);

    idx2 = find(c1063(:,8) == a(:,1) & c1063(:,9) == a(:,2)); % extract
all returns for that index in 1063nm data
    c1063_a = c1063(idx2,:);

        for j = 1:length(c1063_a(:,4));

% find the difference in range between each return in 1063nm and 1545nm,
also add the indices which relates back to c1063 and c1545 data and the
Azimuth and Zenith indices and Range from 1063
```

```matlab
diff = [repmat(c1063_a(j,[1,2,3]),length(idx1),1),(c1063_a(j,7)-
c1545_a(:,7)), idx1(:,1), repmat(idx2(j,1),length(idx1),1),
repmat(c1063_a(j,4),length(idx1),1), (c1545_a(:,4)),
repmat(c1063_a(j,[8,9,7,17]),length(idx1),1), (c1545_a(:,17)) ];

% keep only those pairings with similar range values (+-0.12)
        idx = find((diff(:,4) > -0.12) & diff(:,4) < 0.12);
        new_row = diff(idx,:);

        ratios = [ratios; new_row]; % append the results

        end

end

ratios(1,:)=[]; % remove row of zeros from preallocation

%% Calculate ratios

% normalised ratio
ratios(:,14) = (c1063(ratios(:,6),17) -
c1545(ratios(:,5),17))./(c1063(ratios(:,6),17) + c1545(ratios(:,5),17));

% simple ratio
ratios(:,15) = (c1063(ratios(:,6),17))./ (c1545(ratios(:,5),17));

ratios(:,4:6)=[]; % remove 3 columns (diff, idx1, idx2)

ratiosout = [ratiosout; ratios];

end

ratiosout(1,:) = [];

%save('ratios3181.txt','ratiosout', '-ascii','-double','-v7');

% col 1: x
% col 2: y
% col 3: z
% col 4: Return no 1063nm
% col 5: Return no 1545nm
% col 6: Azimuth index
% col 7: Zenith index
% col 8: Range (m)
% col 9: Apparent reflectance 1063nm
% col 10: Apparent reflectance 1545nm
% col 11: Normalised ratio (r1063-r1545)/(r1063+r1545)
% col 12: Simple ratio (r1063/r1545)

% use azimuth index, zenith index, and return number to find input data
for each ratio
```

Sim_nn.m

```matlab
% First interpolate temperatures

Scandata = data1545_3355;
start = 0;
stop = 3050;

% *** import 'temps' for scan ***

% start and stop are first and last azimuth position (0 and 3050 for high
% res full scan)

az1 = 115/3051;
time = az1*((stop-start));

xi=[start:az1:time]'; % x values for interpolation

xplot=(start:stop)'; % x values to plot High res

x=temps(:,4); % time (mins)
y=temps(:,1); % 1545 temp
yi = interp1(x,y,xi,'linear','extrap'); % linear interpolation with
extrapolation
plot(xi,yi,'r') % plot interpolated values
hold on
scatter(x,y,'pk') % plot original points
temps1545=[yi];

function [AppRef] = Sim_nn(nnInput, net, tempcol);

% *** Ensure correct network is loaded into workspace ***

% Scandata = input scan to be calibrated
% tempcol = column number containing the laser case temps (1063:14,
% 1545:15)

%idx=find(Scandata(:,1)==1); % first returns only
%Scandata=Scandata(idx,:);

InputScan = [nnInput(:,[5,7,tempcol])];

pattern_data = InputScan.';
y = sim(net,pattern_data);
y = sim(net,pattern_data);
AppRef = [nnInput, y']; % all scan data, apparent reflectance
```